DEVELOPMENT OF IMAGE-BASED DENSITY DIAGNOSTICS WITH BACKGROUND-ORIENTED SCHLIEREN AND APPLICATION TO PLASMA INDUCED FLOW

by

Lalit Kishore Rajendran

A Dissertation

Submitted to the Faculty of Purdue University

In Partial Fulfillment of the Requirements for the degree of

Doctor of Philosophy

School of Aeronautics and Astronautics

West Lafayette, Indiana

May 2021

THE PURDUE UNIVERSITY GRADUATE SCHOOL
STATEMENT OF COMMITTEE APPROVAL

Dr. Sally P. M. Bane, Co-Chair
School of Aeronautics and Astronautics

Dr. Pavlos P. Vlachos, Co-Chair
School of Mechanical Engineering

Dr. John P. Sullivan
School of Aeronautics and Astronautics

Dr. Carson D. Slabaugh
School of Aeronautics and Astronautics

Approved by:
Dr. Gregory A. Blaisdell

Dedicated to my family for their constant support and encouragement

ACKNOWLEDGMENTS

I would like to thank my advisors Prof. Sally Bane and Prof. Pavlos Vlachos for providing me the opportunity to pursue graduate studies under their guidance, and for the advice and support on all aspects of this dissertation. I would also like to thank committee members Prof. John Sullivan and Prof. Carson Slabaugh, for their helpful suggestions both on the thesis and other aspects of graduate studies. Thanks are also due to Prof. Gregory Blaisdell and Prof. Steven Schneider, who taught all of my fluid mechanics courses, and also mentored me on the teaching side.

My graduate research has been highly collaborative and I have been fortunate to work with and learn from several talented students. Bhavini Singh has been my major collaborator throughout the PhD, both in the early stages when we were struggling to understand BOS, as well as in all the projects with the spark discharge, which provided the motivation for several developments in this work. Jiacheng Zhang has been the major collaborator in all the projects that involved numerical methods and I have learnt a lot working with him. Sayantan Bhattacharya has helped in nearly all of my projects through his extensive knowledge in all aspects of PIV. I would also like to thank Matthew Giarra for help and guidance during the beginning of my PhD.

I have also had opportunities to collaborate with several students at Purdue in integrating optical diagnostics in their experiments, and in this regard I would like to acknowledge Ravichandra Jagannath, Prashanth Bangalore, Angela Mbugua, James Braun, Javad Eshraghi, Elizabeth Benitez and Mark Frederick. Even though my contributions were minimal in some cases, each of their experiments was novel and challenging, and provided a deeper insight of the measurement techniques. I would also like to thank all other members of Bane and Vlachos groups for many insightful interactions and learning experiences.

I would like to thank all my friends at Purdue, who (in addition to some of the folks mentioned above), have made my time here very enjoyable, especially Harshad Lalit, Shanmukesh Vankayala, Rufat Kulakhmetov, Timo Buschhagen, and Gayathri Shivkumar. Finally, I would like to thank my parents Rajendran and Jayalakshmi, and brother Rahul, for their constant support and encouragement throughout the process.

This work was supported by the U.S. Department of Energy under Award Number DE-SC0018156, and the National Science Foundation through CBET 1706474.

TABLE OF CONTENTS

LIST OF TABLES

LIST OF FIGURES

ABSTRACT

There is growing interest in the use of nanosecond surface dielectric barrier discharge (ns-SDBD) actuators for high-speed (supersonic/hypersonic) flow control. A plasma discharge is created in these actuators using a nanosecond-duration pulse of several kilovolts to deposit energy rapidly in the electrode gap which causes the electrical breakdown. This creates a rapid heat release, which leads to the formation of a shock wave and the development of a complex three-dimensional flow field that is not fully understood.

Actuators based on ns-SDBDs have been applied to high-speed flow control problems such as shock-boundary layer interactions (SBLI), but the results have been mixed and the control authority of the actuator is not well established. This is because, although a general idea of the flow features induced by a ns-SDBD exists, the effect of the actuator geometry (such as the filament spacing) and the operating parameters (such as the pulse frequency) on the induced flow are not well understood and play a critical role in flow control applications.

Even the flow field induced by a single pulse of a ns-SDBD is not entirely understood at a more fundamental level, in contrast to the well-characterized AC-driven SDBD. The flow field induced by ns-DBDs is on much shorter time scales (by almost an order of magnitude) and involves large spatiotemporal gradients in the velocity and temperature fields, posing a significant experimental challenge. Majority of the past work has been limited to qualitative visualizations such as schlieren imaging, and detailed measurements of the induced flow are required to develop a mechanistic model of the actuator performance, such as the heating and vorticity production, and to develop design rules to guide the development and deployment of these actuators.

Background-Oriented Schlieren (BOS) is a recently developed optical flow diagnostic that is a quantitative variant of schlieren imaging and can be used to measure the density and temperature fields of the actuator induced flow. BOS measures density gradients in a flow field by tracking the apparent distortion of a target dot pattern. Since density and refractive index are proportional for fluids, density gradients in a flow are associated with refractive index gradients, and an object viewed through a variable density medium will appear distorted due to the refraction of light rays traversing the medium. The distortion of the dot pattern is typically estimated by cross-correlating an image of the dot pattern without the density gradients (called the reference image) with a distorted image viewed through the density gradients (called the gradient image).

The density gradients can be integrated spatially to obtain the density field, generally by solving the Poisson equation using different computational procedures. Owing to the simple setup and ease of use, BOS has been applied widely in laboratory scale experiments as well as in large scale experiments and rugged industrial facilities, and is becoming the preferred method of density measurement in fluid flows.

However, BOS features several unaddressed limitations with potential for improvement, especially for application to complex flow fields such as those induced by plasma actuators. Some of the limitations are: 1) low spatial resolution due to the large window-sized used in cross-correlation algorithms, 2) lack of an uncertainty quantification methodology, and 3) the density integration procedure using the Poisson solver is very sensitive to noise. Further, since BOS comprises several factors like the dot pattern, illumination, density gradients, optical system and the processing algorithms, each of these factors contribute to the final measurement error/uncertainty in a complex manner.

This thesis presents a series of developments aimed at improving the various aspects of the BOS measurement chain to provide an overall improvement in the accuracy, precision, spatial resolution and dynamic range. A brief summary of the contributions are:

1) a synthetic image generation tool to perform error and uncertainty analysis for PIV/BOS experiments,
2) an uncertainty quantification methodology to report local, instantaneous, a-posteriori uncertainty bounds on the density field, by propagating displacement uncertainties through the measurement chain,
3) an improved displacement uncertainty estimation method using a meta-uncertainty framework whereby uncertainties estimated by different methods are combined based on the sensitivities to image perturbations,
4) the development of a Weighted Least Squares-based density integration methodology to reduce the sensitivity of the density estimation procedure to measurement noise.
5) a tracking-based processing algorithm to improve the accuracy, precision and spatial resolution of the measurements,
6) a theoretical model of the measurement process to demonstrate the effect of density gradients on the position uncertainty, and an uncertainty quantification methodology for tracking-based BOS,

Then the improvements to BOS are applied to perform a detailed characterization of the flow induced by a filamentary surface plasma discharge to develop a reduced-order model for the length and time scales of the induced flow. Filamentary discharges are chosen because they can provide localized heating with minimal power density requirements and provide better control authority as their position on the surface and morphology is known and controllable. While reducing the problem to a single filament and a single pulse is a considerable simplification from practical applications, it allows us to remove the interaction between the flow induced by adjacent filaments and subsequent pulses. A candidate actuator is identified that can be used to create a well-controlled single plasma filament with a single pulse and then perform PIV and BOS measurements to characterize the induced flow for a range of discharge energies. The measurements show that the induced flow consists of a hot gas kernel filled with vorticity in a vortex ring that expands and cools over time. A reduced-order model is developed to describe the induced flow and show that the expansion of the kernel is governed by the vortex ring motion, and the entrainment of cold gas governs the cooling. Applying the model to the experimental data reveals that the vortex ring's properties govern the time scale associated with the kernel dynamics. The model predictions for the actuator-induced flow length and time scales can guide the choice of filament spacing and pulse frequencies for practical multi-pulse ns-SDBD configurations.

Overall this dissertation advances the accuracy, precision, spatial resolution, and dynamic range of image-based density diagnostics using BOS along with the first uncertainty quantification method, and applies these advancements to characterized flow induced by a novel plasma actuator, to develop a reduced-order vortex model for mixing and transport.

1. PIV/BOS SYNTHETIC IMAGE GENERATION IN VARIABLE DENSITY ENVIRONMENTS FOR ERROR ANALYSIS AND EXPERIMENT DESIGN

Lalit K. Rajendran[1], Sally P. M. Bane[1] and Pavlos P. Vlachos[2]
[1] Purdue University, School of Aeronautics and Astronautics, West Lafayette, USA.
[2] Purdue University, School of Mechanical Engineering, West Lafayette, USA.
This chapter has been published in Measurement Science and Technology, and reproduced here with permission. DOI: https://doi.org/10.1088/1361-6501/ab1ca8.

Abstract

We present an image generation methodology based on ray tracing that can be used to render realistic images of Particle Image Velocimetry (PIV) and Background Oriented Schlieren (BOS) experiments in the presence of density/refractive index gradients. This methodology enables the simulation of aero-thermodynamics experiments for experiment design, error, and uncertainty analysis. Images are generated by emanating light rays from the particles or dot pattern, and propagating them through the density gradient field and the optical elements, up to the camera sensor. The rendered images are realistic, and can replicate the features of a given experimental setup, like optical aberrations and perspective effects, which can be deliberately introduced for error analysis. We demonstrate this methodology by simulating a BOS experiment with a known density field obtained from direct numerical simulations (DNS) of homogeneous buoyancy driven turbulence, and comparing the light ray displacements from ray tracing to results from BOS theory. The light ray displacements show good agreement with the reference data. This methodology provides a framework for further development of simulation tools for use in experiment design and development of image analysis tools for PIV and BOS applications. An implementation of the proposed methodology in a Python-CUDA program is made available as an open source software for researchers.

1.1 Introduction

Particle Image Velocimetry (PIV)[1] and Background Oriented Schlieren (BOS)[2] are widely used techniques to investigate complex flows. In PIV, the flow of interest is seeded with particles and the flow velocity is measured by estimating the particle displacements between two successive frames. In BOS (also sometimes referred to as “Synthetic Schlieren”) [3], the density gradients in a flow are measured by the apparent shift of a dot pattern viewed through a variable density medium, where the displacement is evaluated using methods similar to PIV. To assess and improve the accuracy of the displacement estimation algorithms, synthetic particle and/or BOS images are required. For the images to be suitable for testing the algorithms, they must be realistic, i.e., they should display real world artifacts like optical aberrations due to the camera setup, out-of-focus effects, etc. To simulate these effects, current synthetic image generation techniques use empirical models which are too generic to be applied to specific optical systems [1]. In addition, these models cannot be used to simulate effects like ray deflection due to the presence of density gradients, which is an important concern in compressible flow experiments, and several past studies have shown that PIV measurements in environments with refractive index fluctuations can cause measurement errors. [4]–[7].

Ray tracing is a physically realistic alternative, where light rays generated from the particles/dot patterns are traced through the flow under investigation and the optical setup, all the way to the camera sensor. This approach does not require any ad-hoc models and can also naturally handle effects like ray deflection due to density gradients. Although ray tracing tools are ubiquitous across many applications [8]–[10], the methodology presented herein is novel as it is the first to combine density gradients effects with high order numerical schemes, specific user-defined optics without paraxial/thin lens approximations, and camera/sensor parameters with a physical diffraction model along with fluid flow in one package tailored for simulating general aero-thermodynamics experiments.

A significant challenge is that ray tracing is computationally expensive due to the large number of rays required to faithfully reproduce an image. For example, a typical tomographic (Tomo) PIV experiment would have about 100,000 particles inside a laser sheet volume of 300 cm^3. To simulate a particle with sufficient dynamic range, about 10,000 rays are required, which corresponds to a total of 1 billion rays to render a single image, thus posing a significant computational challenge. However, since the path of each light ray is independent of all other rays, this process can be very efficiently parallelized and implemented on Graphics Processing Units (GPUs) which can launch several thousand threads at a time in addition to about a trillion floating point operations (FLOPs) per second. This capability of GPUs is exploited in the current work to significantly accelerate the image generation process.

In the subsequent sections, we first describe in detail the synthetic image generation methodology used to render realistic particle/BOS images in a varying density/refractive-index medium, and then present an application for Background Oriented Schlieren (BOS) experiments. This approach renders images unique to a given optical setup and can be a valuable tool for guiding the choice of optical elements and their placements in the experimental setup to mitigate adverse effects like optical aberrations and steep viewing angles. On the other hand, these effects can be deliberately included for error analysis so that the robustness of an algorithm can be tested for a wide variety of conditions. Some sample particle images generated using the proposed methodology are shown in Figure 1.1.

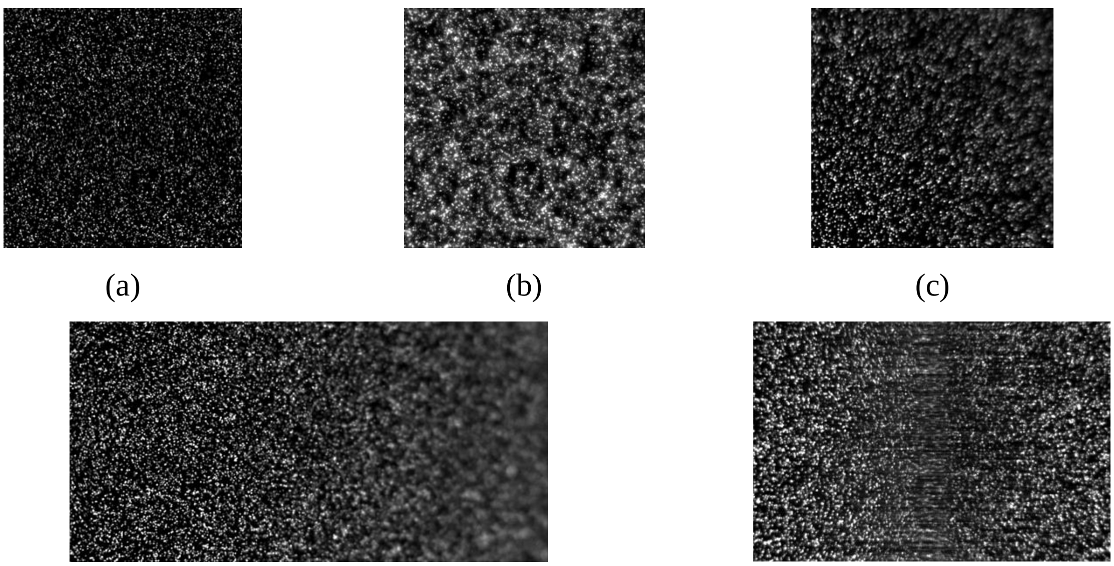

(a) (b) (c)

(d) (e)

Figure 1.1**.** Sample particle images generated using the proposed methodology displaying some common experimental artifacts. (a) Normal Image, (b) Out of focus effects, (c) Lens aberration near edges, (d) Perspective effect, (e) Blurring due to density gradients (normal shock wave in the center of the image).

1.2 Image Generation Methodology

The image generation process, shown schematically in Figure 1.2, is comprised of four steps: (1) generating the light rays, (2) tracing the light rays through density gradients, (3) propagating the light rays through optical elements, and (4) intersecting the rays with the camera sensor to update the pixel intensities. Each of these steps is described in more detail in the following sections.

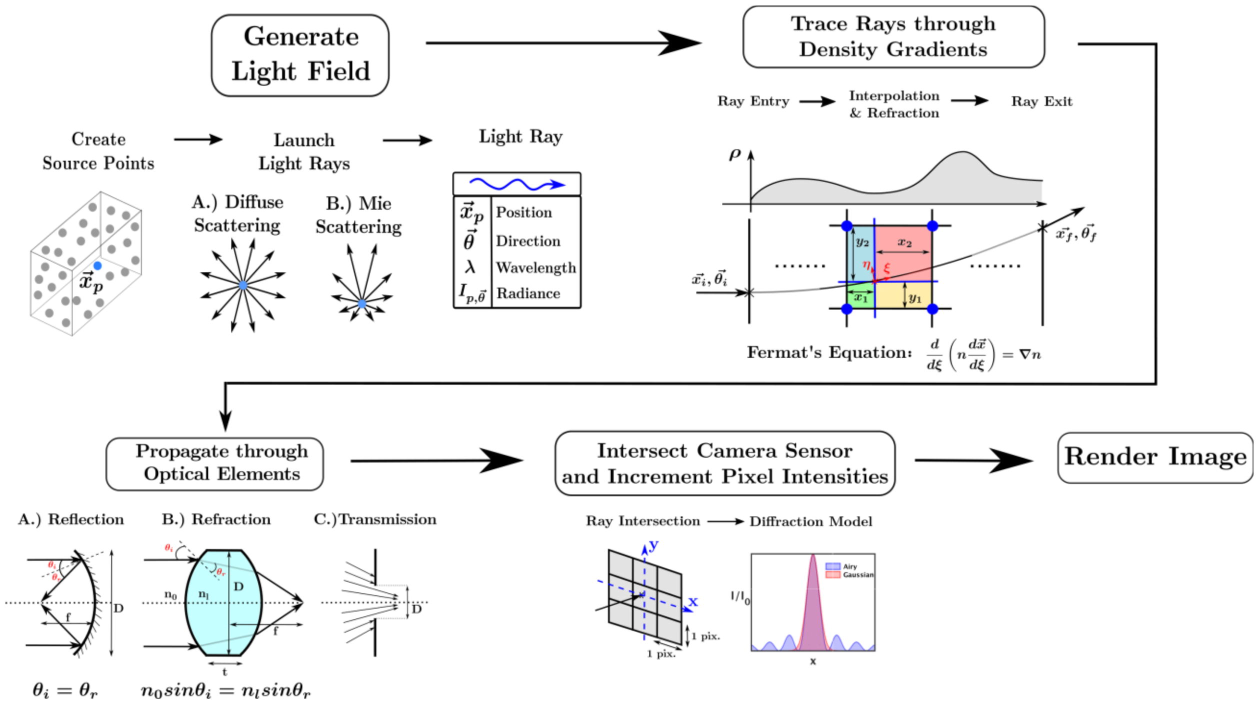

Figure 1.2. Synthetic image generation methodology.

1.2.1 Generating the Light Field

The light rays generated from the particles/dot pattern are considered as vectors connecting source points in the flow field to points of intersection on the camera lens. The source point can be a particle for a PIV experiment or a dot pattern for a BOS experiment. The origin of the light ray vector corresponds to the position of the source point, and its direction corresponds to a unit vector connecting the origin to the point of intersection on the camera lens. Ideally, an infinite number of such light rays can be generated from each source point towards points located on the camera lens. Increasing the number of light rays increases the dynamic range of the generated images but also increases the computational cost.

The radiance of the light ray may have an angular dependence based on the type of scattering associated with the source point. In the case of a PIV particle field where the particle diameters are typically of the same order of the wavelength of the laser, the radiance of the light ray can be estimated using Mie scattering [11]. The scattering cross-section and efficiency depends on the size of the particle, the wavelength of the laser beam, the relative refractive index of the particle with respect to the medium, and the angle between the light ray vector and the direction of propagation of the laser beam. The Mie scattering computations are performed using the method outlined in Bohren & Huffman [12].

1.2.2 Tracing Rays through Density Gradients

A light ray will experience changes in its direction as it passes through a medium containing density gradients due to the dependence of the refractive index on the local density as expressed by the Gladstone-Dale relation:

$$n = K\rho + 1 \tag{1}$$

where n is the refractive index of the medium, ρ is the density, and K is the Gladstone-Dale constant, which has a value of 0.226 cm^3/g for air. Therefore, regions of density gradients also contain refractive index gradients. For a medium containing a continuous change of refractive index, Fermat's principle from geometric optics enables a fast and accurate computation of the trajectory of a light ray through the medium, and the equation for the ray curve is given by [13],

$$\frac{d}{d\xi}\left(n\frac{d\vec{x}}{d\xi}\right) = \nabla n \tag{2}$$

Here $\vec{x}(\xi)$ represents the ray curve and (ξ, η) are the ray-fitted co-ordinates as shown in Figure ***1.2***. Equation (2) is transformed and discretized using a 4th order Runge-Kutta algorithm following the method of Sharma et. al. [14] and the position and direction of the light ray passing through the variable density medium can be updated based on the local refractive index gradient as follows,

$$\begin{aligned} R_{i+1} &= R_i + \left[T_i + \frac{1}{6}(A + 2B)\right]\Delta\xi \\ T_{i+1} &= T_i + \frac{1}{6}(A + 4B + C) \end{aligned} \tag{3}$$

where R, T are 1D arrays representing the position and direction, respectively, and are given by,

$$R = \begin{pmatrix} x \\ y \\ z \end{pmatrix};\ T = n\begin{pmatrix} dx/d\xi \\ dy/d\xi \\ dz/d\xi \end{pmatrix} \quad . \tag{4}$$

The variable n is the refractive index and the subscript i represents the grid point corresponding to the given location of the ray. The constants A, B and C are functions of the refractive index gradients and are given by,

$$A = D(R_i)\Delta\xi \tag{5}$$

$$C = D\left(R_i + \left(T_n + \frac{1}{2}B\right)\Delta\xi\right)\Delta\xi$$

and the function D is given by

$$D = n\begin{pmatrix} \partial n/\partial x \\ \partial n/\partial y \\ \partial n/\partial z \end{pmatrix} = \frac{1}{2}\begin{pmatrix} \partial n^2/\partial x \\ \partial n^2/\partial y \\ \partial n^2/\partial z \end{pmatrix} \quad . \tag{6}$$

An open-source implementation of solving Fermat's equation on a GPU with a piecewise linear approximation (1st order) was provided by SchlierenRay, an artificial schlieren image rendering software developed by Brownlee et. al. [15] Their methodology has been extended to include higher order discretizations and integrated with a full light field-based ray tracing approach for the present application.

1.2.3 Propagating Light Rays through Optical Elements

When light rays pass through optical elements, they can undergo one or more of the following processes: (1) reflection (mirrors), (2) refraction (lenses, windows), and (3) selective transmission (apertures). All of these processes are modeled in the ray tracing methodology, as shown in Figure 1.2. In all cases, the intersection of a ray with the optical element is first computed based on the element's geometry. For example, in the case of a spherical mirror/lens the intersection point is calculated based on the element center, diameter, and radius of curvature. After computing the intersection, the effect of the element is modeled as follows:

1. Reflection due to mirrors is modeled using the law of reflection based on the direction of the light ray with respect to the local surface normal.
2. Refraction due to lenses/windows is modeled using Snell's Law [16], given by

$$n_i \sin(\theta_i) = n_f \sin(\theta_f), \tag{7}$$

where θ_i is the angle of incidence, θ_f is the angle of refraction, and n_i and n_f are the refractive indices of the two media on either side of the refractive surface. For elements with multiple refractive surfaces like a lens, the refraction is performed sequentially on each surface, considering the possibility of total internal reflection if the ray passes from a medium of higher refractive index to a medium of lower refractive index. It should be noted that this approach is quite general and does not require assumptions regarding the paraxial nature of the light rays (as used in matrix methods) or the thickness of the lens, and it is straightforward to include transmittance and dispersive effects of the lens as required.

Further, an array of lenses as in a Plenoptic camera, for example, can also be modeled using this approach.

3. Selective transmission due to apertures is enforced by only allowing light rays that intersect the plane of the aperture and lie within its opening area (or pitch) and blocking the rest.

1.2.4 Intersecting a Ray with the Camera Sensor and Incrementing Pixel Intensities

The final step in the ray tracing process is the intersection of a light ray with the camera sensor, which is solved as a line-plane intersection problem. The diffraction spot is described by an Airy function and is approximated by a Gaussian in this application [17], and the integrated intensity across a pixel is calculated using an error function, as in the case of synthetic PIV image generation [18]. The point of peak intensity is the point of intersection of the light ray with the camera sensor, and the diffraction diameter is a function of the optical system as given by,

$$d_\tau = 2.44\pi f_\#(M+1)\lambda \quad . \tag{8}$$

Here d_τ is the diffraction diameter, $f_\#$ is the f-number of the camera, M is the magnification, and λ is the wavelength of light [17]. For white light illumination in the case of BOS/calibration targets, an effective wavelength corresponding to the green color is used.

This procedure is repeated for all light rays that intersect the camera sensor to obtain an image of the particle field/dot pattern. The dynamic range of the final intensity distribution increases with the number of light rays used to render a particle or dot, but this also increases the computational cost and run time. It was observed from trials that about 10,000 rays are sufficient to provide a 16-bit dynamic range.

1.2.5 Parallelization using CUDA

The ray tracing methodology just described is computationally intensive due to the large number of light rays (~ 1 billion) required to render an image with sufficient dynamic range. Since the trajectories of the light rays are independent of each other, the ray tracing calculations can be parallelized using Graphics Processing Units (GPUs). This methodology was implemented using a CUDA framework with a Python front-end. The images in the present work were generated using an NVIDIA Tesla C2050 GPU, which has 14 streaming multi processors each containing 32 cores for an overall total of 448 cores. Each multi-processor can launch a maximum of 1536 threads amounting to a total of about 21,000 threads at a time.

The details of the parallelization in terms of grids, blocks and threads are as follows. Each thread on the GPU corresponds to a single light ray, and all the computations starting from the ray generation to the intersection with the camera sensor are done independently. All light rays originating from the same particle/dots are organized in blocks, to take advantage of the shared memory in CUDA which has very fast read and write speeds [19]. Thus the information common to all light rays originating from the same particle are stored in shared memory, which frees up the local memory and enables launching a larger number of threads. The number of threads that can be stored in a block and the number of blocks that can be launched are subject to hardware limitations.

In summary, the approach presented in this paper is an integrated implementation of state of the art methods for the various components of the image generation methodology in one package for simulating general aero-thermodynamics experiments. The improvements presented in this approach and their possible applications are:

1. A light field approach for ray generation which lends itself well to simulating Plenoptic experiments, as well as integrated Mie scattering calculations to account for the particle diameter, refractive index, laser wavelength etc. along with a consideration of the laser sheet intensity profile to accurately simulate, for example, forward/backward scatter viewing configurations, among other parameters.
2. Accurate ray tracing through density gradients with higher order Runge-Kutta schemes, which becomes important in simulating flows involving sharp changes in density, such as experiments with shock waves.
3. Non-linear ray tracing through the optical elements without any paraxial or thin lens approximations. This allows us to introduce optical aberrations in a controlled manner, as evident in Figure 1 (c). This is important in simulating experiments where optical aberrations can have a large contribution to the error, such as facilities with curved windows, simulating thick lenses with short radius of curvatures etc.

A physically correct diffraction model for the image formation on the camera sensor. This is critical in assessing cross-correlation/tracking based PIV/BOS algorithms because the subpixel fitting operation is very sensitive to the intensity profile of the particle/dot, and hence dependent on the diffraction diameter of the optical layout.

1.3 Error Analysis

The accuracy of the image generation methodology was simulated using three cases: a) Luneburg lens to test the ray tracing through the density gradients, b) a full Background Oriented Schlieren (BOS) experiment with a known density field and user defined camera optics and comparing the final light ray deflections recorded on the camera sensor to predicted displacements from BOS theory.

1.3.1 Luneburg Lens

The Luneburg lens [20] is a gradient index lens with the refractive index distribution within the lens given by,

$$n(r) = \sqrt{2 - \left(\frac{r}{R}\right)^2} \tag{9}$$

where n is the refractive index, r is the radial co-ordinate, and R is the radius of the lens. The lens has the property that an incoming parallel beam of light rays is focused on to the optical axis at the back surface of the lens, and is a standard benchmark test in the gradient-index optics literature.[14], [21], [22]

This lens is used as the refractive index medium and the light rays are traced through it using the method outlined above. Some sample light ray trajectories are shown in Figure 1.3 (a) and it is seen that rays entering at various heights are focused very close to the exit plane. The positions of the light rays on the exit plane of the lens are recorded and any deviation from zero is considered to be an error. This test enables us to isolate the part of the method used to trace rays through density gradients from the overall image generation methodology and validate it separately.

Monte-Carlo simulations were performed for 1000 light rays entering the lens at random X,Y locations, and the average exit height error was calculated upon leaving the lens. The number of grid points used to represent the refractive index field of the Luneburg lens were varied from 25 to 250, and the average exit height errors are plotted as a function of grid points for a 1st order

Euler method and the 4th order Runge-Kutta (RK4) method in Figure 1.3 (b). It is seen that the error levels are low for both methods and that the RK4 method gives a lower error than the Euler method for any grid point. Further, it is seen that the RK4 method also has a higher rate of decrease of error with increasing grid points due to the higher order of the method. This test serves as a validation for the image generation methodology for tracing rays through the density gradients.

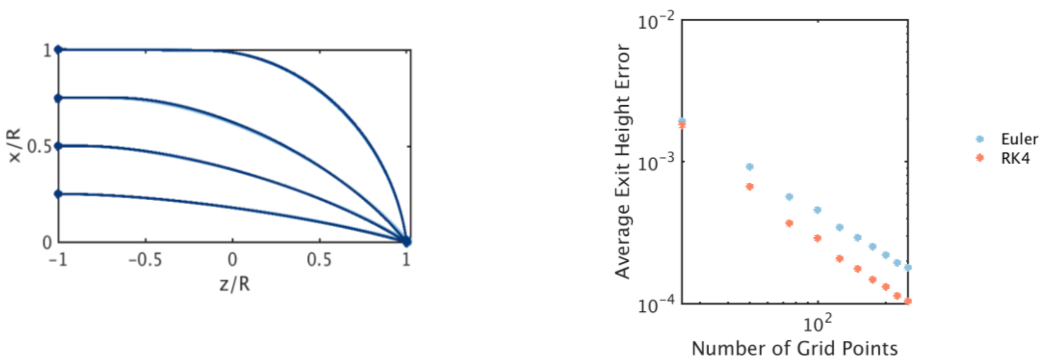

(a) (b)

Figure 1.3. Results of applying the methodology to trace light rays through the Luneburg lens. (a) Sample Trajectories using the Euler scheme and (b) Errors in the exit height for the Euler and RK4 schemes.

1.3.2 Background Oriented Schlieren (BOS) simulation

For the BOS test, two density fields were considered: 1) a constant density gradient field designed to create a uniform displacement of the dot pattern and 2) a more realistic density field taken from a direct numerical simulation (DNS) of homogeneous buoyancy-driven turbulence. The layout of the BOS experimental setup modeled in the image generation software for simulations involving both density fields is shown in Figure 1.4, and the parameters describing the placement of the elements are summarized in

Table 1.1. The refractive index experienced by a light ray is a function of its wavelength, and decreases with increasing wavelength in the visible range. Therefore the angular deflection experienced by a light ray also changes with wavelength, and this issue has been analyzed for synthetic schlieren measurements by Kolaas et. al. [23] A monochromatic light source with a

wavelength of 532 nm was considered in this study and the ambient refractive index is set to be 1.00028.

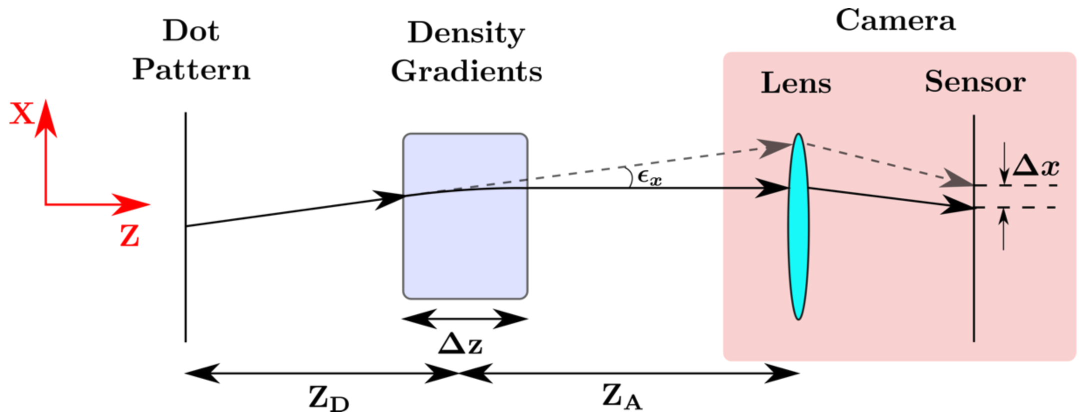

Figure 1.4. Layout of the experimental setup used to simulate a BOS experiment with a known density field.

Table 1.1. Summary of image generation parameters used to simulate the BOS experiment

Z_A	0.75 m
Z_D	0.25 m
L_x x L_y x L_z	32 x 32 x 10 mm
Focal Length	105 mm
Aperture ($f_{\#}$)	11
Magnification	0.12
Pixel Pitch	10 um
Dot density	20 dots / 32x32 pix.

1.3.3 Uniform Density Gradient

For this case, a density field with a constant gradient was simulated, where the density gradient was designed to create a uniform displacement of the light rays emerging from a dot pattern. The magnitude of the density gradient field was calculated from the desired pixel displacement and the optical layout of the system using BOS theory. The theoretical displacement of a light ray for a BOS experiment is given by

$$\Delta\vec{X} = \frac{MZ_D}{n_0}\int_{z_i}^{z_f} \nabla n\, dz \approx \frac{MZ_D K}{n_0} (\nabla\rho)_{avg} L_z \tag{10}$$

where $\Delta\vec{X}$ is the theoretical deflection of a light ray, $(\nabla\rho)_{avg}$ is the path-averaged value of the density gradient, K is the Gladstone-Dale constant, n_0 is the ambient refractive index, and L_z is the depth/thickness of the density gradient field [2]. Using the above equation, a value of $(\nabla\rho)_{avg}$ is calculated using the values of the experimental parameters from

Table 1.1. This test enables us to test the entire simulation chain without the spatial resolution limitations involved with BOS measurements.

Tests were conducted with the theoretical displacement field being varied from 0 to 3 pix. to provide a range representative of typical BOS experiments, and the average displacements of all light rays from the field of view is shown in Figure 1.5. It can be seen that there is good agreement between the theoretical displacements and calculated displacements from the ray tracing simulations.

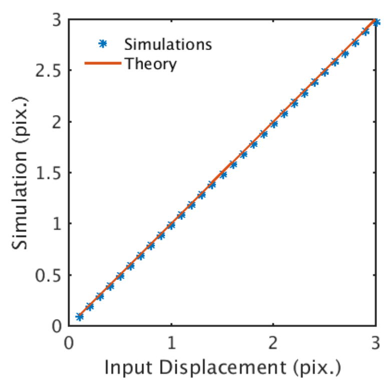

Figure 1.5. Comparison of theoretical and simulated light ray deflections.

1.3.4 Buoyancy Driven Turbulence

The DNS data used for this test are from simulations performed by performed by Livescu et. al. [24]–[26] and downloaded from the Johns Hopkins University Turbulence Database (JHU-TDB) [24], [27], [28]. Two dimensional (x, y) slices of the flow field from two time instants were chosen, and for each time instant, a three-dimensional density volume was constructed by stacking the same two-dimensional slice along the z-direction, thereby ensuring that the gradient of density in the z direction was zero. This was done to account for the depth integration limitation of BOS measurements and to enable a better comparison of the simulated light ray deflections to theory. The refractive index was calculated using Equation (1) using the Gladstone-Dale constant for air, and for the case with the DNS data, the non-dimensional density field was scaled by a factor of 1.225 kg/m^3 to simulate air properties. The values of the experimental parameters were taken from

Table 1.1.

The contours of the input density and density gradients, the theoretical displacements calculated from Equation (9), and the light ray displacements from ray tracing simulations are shown in Figure 1.6. The depth averaged density gradient $(\nabla\rho)_{avg}$ used to calculate the theoretical displacements is taken to be the two-dimensional density gradient field shown in Figure 1.6, as identical 2D slices were stacked to create a 3D density field during the simulations.

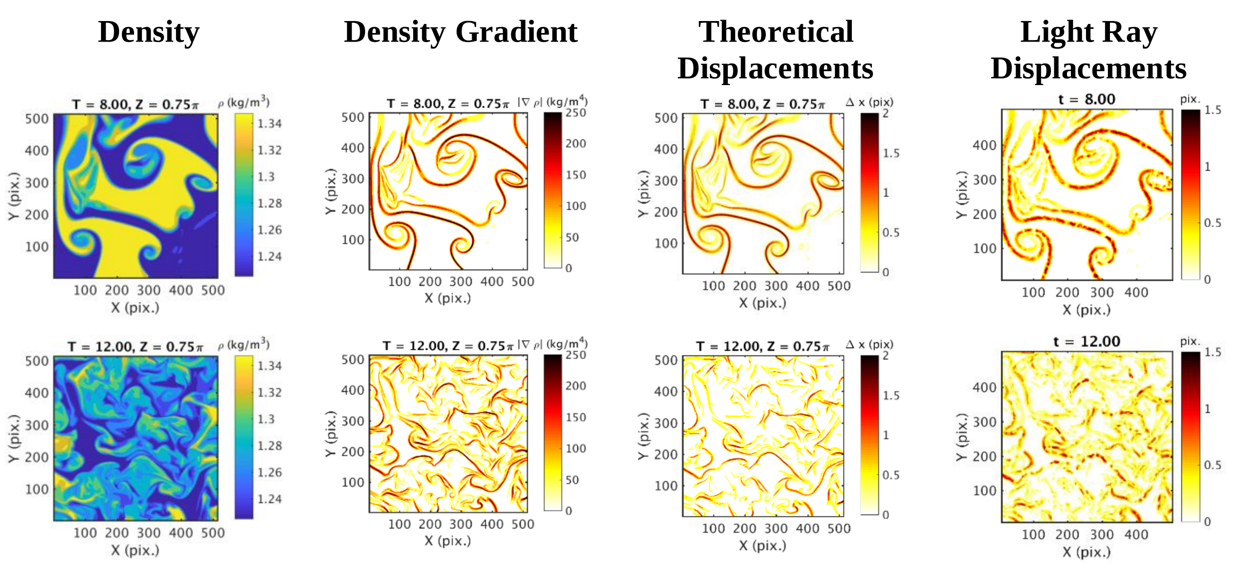

Figure 1.6. Contours of density, density gradients, theoretical displacements, and simulated light ray displacements from the ray tracing simulations using DNS data.

The light ray displacements from the ray tracing simulations will be randomly scattered on the camera sensor due to the random positions of the dots on the target from which the light rays originate. The ray displacements corresponding to a single dot are averaged and interpolated onto a regular grid using a bilinear interpolation and displayed in Figure 1.6. The figure shows that the contours of light ray displacements from the simulations closely correspond to the theoretical displacements except that they are smoothed out. The mismatch between the theoretical and simulated light ray deflections is due to two reasons: (1) the theoretical equation is based on small angle approximations, and (2) the spatial resolution limitation of the BOS experimental setup whereby the light ray deflection of a dot is the average light ray displacement of all rays comprising a ray cone. Both these effects are consistent with well-known characteristics of BOS experiments [2], [29], [30]. Further, it is to be noted that when these two effects are negligible, as in Section 1.3.3 with the uniform density field, the methodology is able to accurately match the theoretical displacements.

Overall, these results show that the proposed methodology is capable of generating accurate synthetic images for user-defined density fields and optical layouts.

1.4 Application: Trade-off between Measurement Sensitivity and Spatial Resolution for BOS experiments

To further illustrate the capability of the proposed image generation methodology to aid in experiment design, we show the application of the methodology for assessing the tradeoff between Measurement Sensitivity and Spatial Resolution for BOS experiments.

In BOS experiments, the relative placement of the density gradient field with respect to the dot pattern and the camera lens is a crucial parameter that determines the measurement quality. In particular, the parameter Z_D which denotes the distance between the dot target and the mid plane of the density gradient field (shown in Figure 1.4), controls both the measurement sensitivity, defined as the apparent displacement of a light ray produced per unit angular deflection, and the spatial resolution of the measurement. This issue has been theoretically analyzed in the past by Gojani et. al. [31] using simplified models for the optics and the density gradient field. Here, we apply the ray tracing methodology to directly evaluate this effect without simplifying assumptions.

The parameter Z_D has a contradictory effect on the sensitivity and spatial resolution because, the measurement sensitivity ($= MZ_D$) increases with Z_D, but for increasing values of Z_D, a ray cone emerging from the dot pattern covers a larger area of the density gradient field. Since the apparent displacement of a dot recorded on the sensor is the average displacement of all light rays within the ray cone, a larger ray cone leads to more averaging and a loss of spatial resolution.

To illustrate this effect, we simulate a BOS experiment with the density field given by a sharp jump designed to represent a normal shock. The density and corresponding density gradient distribution along x are shown in Figure 1.7, and both fields are uniform along y and z $\left(\frac{\partial\rho}{\partial y} = \frac{\partial\rho}{\partial z} = 0\right)$. For a fixed distance Z_B between the camera lens and the dot pattern, three positions of the density gradient field are simulated (Z_D/Z_B = 0.25, 0.5, 0.75). For each case, an image of a dot pattern with and without the density gradient field is rendered, and the apparent displacements of the light rays are calculated.

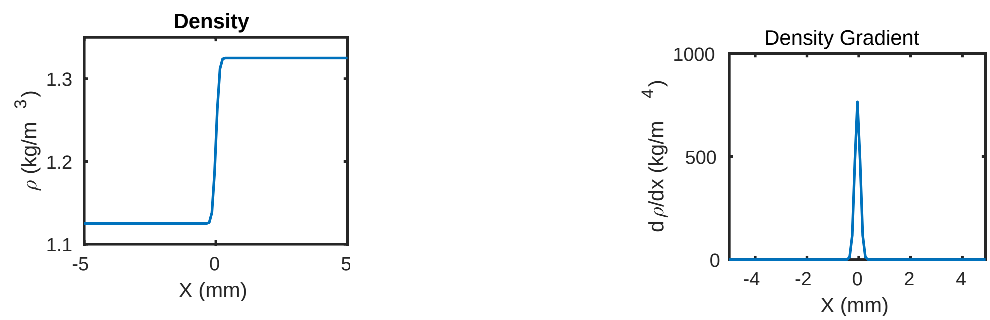

(a) (b)

Figure 1.7. (a) Density and (b) Density Gradient distribution for the sensitivity study

Figure 1.8 (a) shows the density gradient field experienced by all rays emerging from a single dot in the center of the image, and it is seen that as Z_D/Z_B increases, the region of the density gradients covered by the ray cone increases. Since the apparent displacement of a dot on the sensor corresponds to the average of this density gradient distribution, light rays from adjacent dots travel through overlapping regions of the density gradient field, leading to a loss in spatial resolution. This effect is shown in Figure 1.8 (b) showing the average displacements of light rays emerging from a row of dots along x, where it is seen that the displacement field recorded on the sensor has a higher peak displacement for higher values of Z_D/Z_B (corresponding to a higher measurement sensitivity), but more smoothed, corresponding to a lower spatial resolution. Overall, these trends are in agreement with the analysis by Gojani et. al. [31] It is to be noted however, that as Z_D/Z_B increases, the magnification of the density gradient field (different from the magnification of the dot pattern) increases, and hence for the cases with Z_D/Z_B = 0.5 and 0.75, the displacement field appears asymmetric because of clipping due to the finite size of the camera sensor.

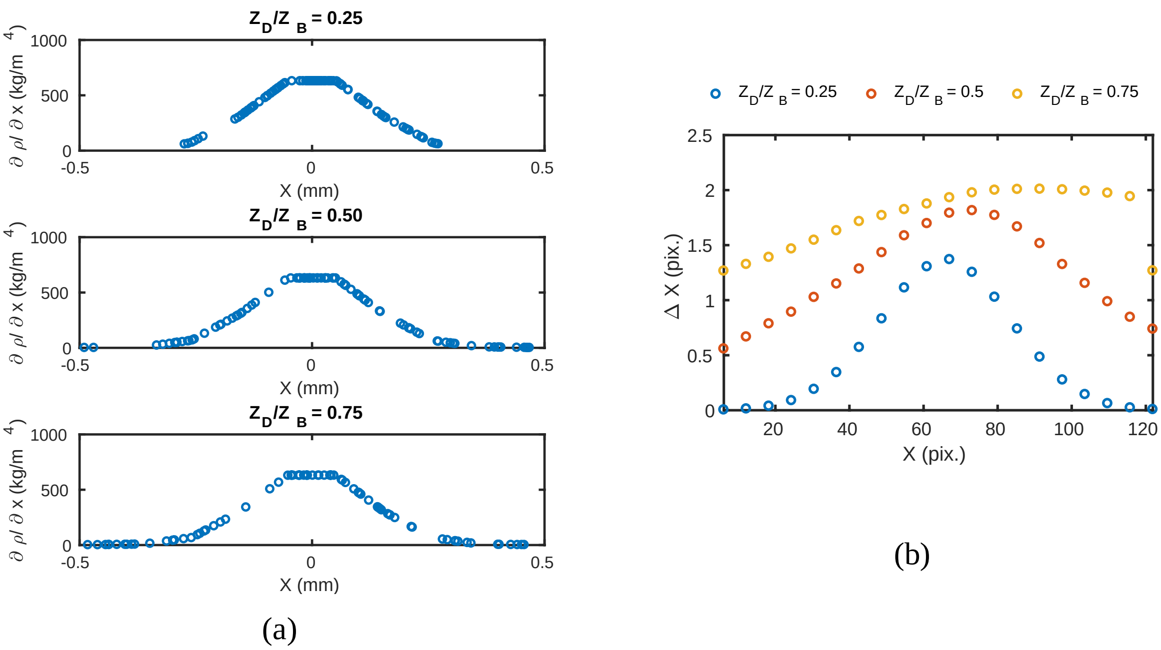

Figure 1.8. Results of the BOS sensitivity study for three positions of the density gradient field (a) Density gradient field experienced by all light rays corresponding to a single dot and (b) Measured displacement field from the whole image.

These results, in addition to the sample particle images shown in Figure 1.1, illustrate the capability of the proposed image generation methodology to accurately generate realistic PIV/BOS images. The methodology enables the introduction of experimental artifacts such as optical aberrations and distortions due to density gradient fields into the image generation process in a deliberate and controlled manner.

1.5 Conclusion

An image generation methodology was proposed and implemented to render realistic PIV and BOS images in variable density environments with a user-defined optical setup. The methodology involves generation of light rays from a particle or dot pattern, propagation of the light rays through density gradients using Fermat's equation and a 4th order Runge-Kutta scheme, reflection/refraction/transmission of the light rays by optical elements, and intersection of the rays with the camera sensor to update pixel intensities using a diffraction model. The computationally intensive ray tracing process was parallelized and implemented on GPUs using CUDA, resulting in a significant acceleration of the computations. The accuracy of the methodology was evaluated using three cases: (1) Luneburg lens, (2) a BOS experiment a uniform density gradient field and (3) a BOS experiment with a density field obtained from DNS of buoyancy-driven turbulence. The light ray deflections from the ray tracing show good agreement with the theoretical estimates. This methodology provides a framework for further development of simulation tools for use in experiment design by incorporating additional features specific to a given experiment. The methodology can also be a valuable tool for error analysis to study the effect of various elements of an optical setup on the final error, and provide directions to improve image analysis tools for PIV and BOS applications.

1.6 Acknowledgment

Rod LaFoy is acknowledged for early efforts in the development of the ray tracing based image generation methodology presented in this work. This material is based upon work supported by the U.S. Department of Energy, Office of Science, Office of Fusion Energy Sciences under Award Number DE-SC0018156. NSF provided support through 1706474.

1.7 References

[1] M. Raffel, C. E. Willert, S. T. Wereley, and J. Kompenhans, *Particle image velocimetry: a practical guide*. Springer, 2013.

[2] M. Raffel, "Background-oriented schlieren (BOS) techniques," *Exp. Fluids*, vol. 56, no. 3, pp. 1–17, 2015.

[3] S. B. Dalziel, G. O. Hughes, and B. R. Sutherland, "Whole-field density measurements by 'synthetic schlieren,'" *Exp. Fluids*, vol. 28, no. 4, pp. 322–335, 2000.

[4] A. Alahyari and E. K. Longmire, "Particle image velocimetry in a variable density flow : application to a dynamically evolving microburst," *Exp. Fluids*, vol. 17, no. 6, pp. 434–440, 1994.

[5] P. Jackson, R. Musalem, C. Rehmann, and D. Hill, "Particle Image Velocimetry Errors due to refractive index fluctuations," in *Hydraulic Measurements and Experimental Methods*, 2002, pp. 1–9.

[6] G. E. Elsinga, B. W. Van Oudheusden, and F. Scarano, “Evaluation of aero-optical distortion effects in PIV,” *Exp. Fluids*, vol. 39, no. 2, pp. 246–256, 2005.

[7] S. B. Dalziel, M. Carr, J. K. Sveen, and P. A. Davies, “Simultaneous synthetic schlieren and PIV measurements for internal solitary waves,” *Meas. Sci. Technol.*, vol. 18, no. 3, pp. 533–547, 2007.

[8] B. Atcheson, I. Ihrke, W. Heidrich, A. Tevs, D. Bradley, M. Magnor, and H.-P. Seidel, “Time-resolved 3d capture of non-stationary gas flows,” *ACM Trans. Graph.*, vol. 27, no. 5, p. 1, 2008.

[9] K. Berger, I. Ihrke, B. Atcheson, W. Heidrich, and M. Magnor, “Tomographic 4D Reconstruction of Gas Flows in the Presence of Occluders,” *Vision, Model. Vis. Work.*, pp. 1–8, 2009.

[10] U. Hartmann and J. R. Seume, “Combining ART and FBP for improved fidelity of tomographic BOS,” *Meas. Sci. Technol.*, vol. 27, no. 9, p. 097001, Sep. 2016.

[11] H. C. Van de Hulst, *Light Scattering by Small Particles*. 1981.

[12] C. F. Bohren and D. R. Huffman, *Absorption and Scattering of Light by Small Particles*. Weinheim, Germany: Wiley-VCH Verlag GmbH, 1998.

[13] M. Born and E. Wolf, *Principles of optics: electromagnetic theory of propagation, interference and diffraction of light*. New York: Pergamon Press, 1950.

[14] A. Sharma, D. V. Kumar, and A. K. Ghatak, “Tracing rays through graded-index media: a new method.,” *Appl. Opt.*, vol. 21, no. 6, pp. 984–987, 1982.

[15] C. Brownlee, V. Pegoraro, S. Shankar, P. McCormick, and C. Hansen, “Physically-based interactive schlieren flow visualization,” *IEEE Pacific Vis. Symp. 2010, PacificVis 2010 - Proc.*, pp. 145–152, 2010.

[16] F. Pedrotti, L. Pedrotti, and L. Pedrotti, *Introduction to optics*. 1998.

[17] R. J. Adrian and C. S. Yao, “Pulsed laser technique application to liquid and gaseous flows and the scattering power of seed materials.,” *Appl. Opt.*, vol. 24, no. 1, pp. 44–52, 1985.

[18] M. Raffel, C. E. Willert, S. T. Wereley, and J. Kompenhans, *Particle Image Velocimetry*. Berlin, Heidelberg: Springer Berlin Heidelberg, 2007.

[19] NVIDIA, *CUDA C Programming Guide*. 2015.

[20] D. Marchand, *Gradient Index Optics*. Academic Press, New York, 1978.

[21] D. Hewak and J. Lit, “Numerical ray-tracing methods for gradient index media,” *Can. J. Phys.*, vol. 63, no. 2, pp. 234–239, 1985.

[22] D. T. Moore, “Gradient-index optics: a review,” *Appl. Opt.*, vol. 19, no. 7, p. 1035, Apr. 1980.

[23] J. Kolaas, B. Hervold, K. Sveen, and A. Jensen, “Bichromatic synthetic schlieren applied to surface wave measurements,” *Exp. Fluids*, vol. 59, no. 8, pp. 1–13, 2018.

[24] D. Livescu, C. Canada, K. Kalin, R. Burns, I. Staff, and Pulido, “Homogeneous Buoyancy Driven Turbulence Data Set,” no. 1, pp. 1–7, 2014.

[25] D. LIVESCU and J. R. RISTORCELLI, “Variable-density mixing in buoyancy-driven turbulence,” *J. Fluid Mech.*, vol. 605, pp. 145–180, 2008.

[26] D. LIVESCU and J. R. RISTORCELLI, “Buoyancy-driven variable-density turbulence,” *J. Fluid Mech.*, vol. 591, pp. 43–71, 2007.

[27] Y. Li, E. Perlman, M. Wan, Y. Yang, C. Meneveau, R. Burns, S. Chen, A. Szalay, and G. Eyink, “A public turbulence database cluster and applications to study Lagrangian evolution of velocity increments in turbulence,” *J. Turbul.*, vol. 9, no. December 2016, p. N31, 2008.

[28] E. Perlman, R. Burns, Y. Li, and C. Meneveau, “Data exploration of turbulence simulations using a database cluster,” *Proc. 2007 ACM/IEEE Conf. Supercomput. (SC ’07)*, 2007.

[29] G. E. Elsinga, B. W. Van Oudheusden, F. Scarano, and D. W. Watt, “Assessment and application of quantitative schlieren methods: Calibrated color schlieren and background oriented schlieren,” *Exp. Fluids*, vol. 36, no. 2, pp. 309–325, Feb. 2004.

[30] M. J. Hargather and G. S. Settles, “A comparison of three quantitative schlieren techniques,” *Opt. Lasers Eng.*, vol. 50, no. 1, pp. 8–17, Jan. 2012.

[31] A. B. Gojani, B. Kamishi, and S. Obayashi, “Measurement sensitivity and resolution for background oriented schlieren during image recording,” *J. Vis.*, vol. 16, no. 3, pp. 201–207, 2013.

2. UNCERTAINTY QUANTIFICATION IN DENSITY ESTIMATION FROM BACKGROUND ORIENTED SCHLIEREN (BOS) MEASUREMENTS

Lalit K. Rajendran[1], Jiacheng Zhang[2], Sayantan Bhattacharya[2], Sally P. M. Bane[1] and Pavlos P. Vlachos[2]

[1] Purdue University, School of Aeronautics and Astronautics, West Lafayette, USA.

[2] Purdue University, School of Mechanical Engineering, West Lafayette, USA.

This chapter has been published in Measurement Science and Technology, and reproduced here with permission. DOI: https://doi.org/10.1088/1361-6501/ab60c8

Abstract

We present an uncertainty quantification methodology for density estimation from Background Oriented Schlieren (BOS) measurements, in order to provide local, instantaneous, a-posteriori uncertainty bounds on each density measurement in the field of view. Displacement uncertainty quantification algorithms from cross-correlation based Particle Image Velocimetry (PIV) are used to estimate the uncertainty in the dot pattern displacements obtained from cross-correlation for BOS and assess their feasibility. In order to propagate the displacement uncertainty through the density integration procedure, we also develop a novel methodology via the Poisson solver using sparse linear operators. Testing the method using synthetic images of a Gaussian density field showed agreement between the propagated density uncertainties and the true uncertainty. Subsequently the methodology is experimentally demonstrated for supersonic flow over a wedge, showing that regions with sharp changes in density lead to an increase in density uncertainty throughout the field of view, even in regions without these sharp changes. The uncertainty propagation is influenced by the density integration scheme, and for the Poisson solver the density uncertainty on average increases on moving away from the regions where the Dirichlet boundary conditions are specified.

Nomenclature

u	Measurement	K	Gladstone-Dale constant
δ_u	Measurement Error	∇	Gradient
σ_u	Measurement Uncertainty	S	Source Term
u_0	True Value	$\bar{\bar{\bar{\nabla}}}$	Mapping matrix
σ	Standard Deviation	$\bar{\bar{L}}$	Label matrix
t_{CI}	Coverage Factor	$\bar{\bar{\Delta}}$	Laplacian operator matrix
ρ	Density	$\bar{\bar{\bar{\Sigma}}}$	Covariance matrix
ρ_p	Projected Density	X_0, Y_0	Centroid
$\Delta\vec{x}$	In-plane Displacement	E	Expectation operator
M	Magnification	n	Refractive index
Z_D	Distance between dot pattern and density gradient field		

2.1 Introduction

Background Oriented Schlieren (BOS) is a flow measurement technique, where the apparent distortion of a dot pattern viewed through a medium with refractive index gradients is measured using cross-correlation, tracking or optical flow based algorithms to estimate the density gradients in the medium [1]–[6] or the surface gradients in a free-surface flow [7], [8]. The density gradients can be integrated spatially to obtain the density field, generally by solving the Poisson equation using different computational procedures [9]. Owing to the simple setup and ease of use, BOS has been applied widely in laboratory scale as well as in large scale and rugged industrial facilities, and is becoming the preferred method of density measurement in fluid flows [10]–[17].

BOS measurements are increasingly used for Computational Fluid Dynamics (CFD) model validation and design [14], [16], [18]–[20]. However, currently there is no framework for quantifying the uncertainties in the density estimation, and inform proper validation of computational models. The BOS measurement chain is complex and subject to several sources of uncertainties ranging from the dot pattern parameters (dot size, dot density), non-uniform illumination, vibrations, blurring/out-of-focus effects, non-linearities (higher order derivatives) and small scale fluctuations in the density field, uncertainties in measurement of the optical layout, as well as the processing and post processing methodologies used to calculate the density from the image displacements. As a result, the uncertainty on the final density measurement is a high-dimensional, coupled, non-linear and non-trivial function of several parameters, and can vary widely across the field of view and across a time series of measurements. Therefore, a comprehensive method for estimating and reporting uncertainties on BOS density measurements is needed. This paper aims to develop and test the first uncertainty quantification methodology to provide a-posteriori, local, instantaneous uncertainty bounds for each density measurement in the field of view for a BOS experiment.

For a measurement u, the uncertainty σ_u is defined as the interval around the measurement in which the true value u_0, and by extension the true error δ_{u_0}, is believed to exist with a predetermined degree of confidence [21]. Following ISO-GUM [22], the standard uncertainty is defined as the range of measurement values that are one standard deviation σ about the true value, for an arbitrary parent population. The expanded uncertainty is defined for an assumed parent distribution for the error, and is specified using a confidence interval at a defined percentage and a coverage factor t_{CI}. This is to indicate that the true value/error lies in an interval $\sigma_u = t_{CI}\sigma$ around the measurement for the pre-defined percentage of samples drawn from the parent distribution. For example, if the errors are drawn from a Gaussian distribution, the expanded uncertainty at 68% confidence interval is equal to the standard uncertainty ($\sigma_u = \sigma$), and the expanded uncertainty at 95% confidence interval is equal to approximately twice the standard uncertainty ($\sigma_u = 1.96\sigma$). The standard uncertainty is reported throughout this paper.
In the related field of Particle Image Velocimetry (PIV) [23]–[26], there have been widespread efforts in the past decade to develop a-posteriori uncertainty quantification methodologies [27], [28], as well as to perform comparative assessment of the existing methods [28]–[30]. As the displacement estimation in BOS is similar to PIV, PIV-based displacement uncertainty methods can be applicable to BOS measurements.

Displacement uncertainty estimation methods for 2D planar PIV can be broadly divided into indirect and direct methods. Indirect methods predict the displacement uncertainty by calibrating the variation of uncertainty to various image parameters and signal to noise ratio metrics, where the calibration is obtained using Monte-Carlo simulations with synthetic images. Timmins et. al. proposed the first PIV uncertainty quantification method termed ‘Uncertainty Surface’ (US) [31], where the uncertainty is calibrated based on four metrics: particle diameter, seeding density, displacement and shear. Charonko and Vlachos [32] proposed the Peak to Peak Ratio (PPR) method, where the uncertainty is calibrated against and calculated using the ratio of the primary to secondary cross-correlation peak heights. This method was later generalized by Xue et. al. [33] to other correlation plane derived metrics such as the Peak to Root Mean Square Ratio (PRMSR), Peak to Correlation energy (PCE), and cross-correlation. The Mutual Information (MI) based uncertainty quantification by Xue et. al. [34], defined as the effective number of correlated particle pairs between two image frames, was also used to estimate PIV uncertainty. The performance of all indirect methods relies on the calibration process, which must be accurate and reflect all possible experimental scenarios in a typical measurement.

On the other hand, direct methods estimate uncertainty directly from the properties of the image or correlation plane and do not require any calibration. Examples of direct uncertainty estimation methods include the Image Matching (IM) method proposed by Sciacchitano et. al. [35], Correlation Statistics (CS) method proposed by Wieneke [36] and the Moment of Correlation (MC) proposed by Bhattacharya et. al. [37]. Each of the direct methods has a different working principle, and in the following, we briefly describe the assumptions, working principles and limitations of the direct methods.

Image Matching (IM) or Particle Disparity (PD) proposed by Sciacchitano et. al. [35], estimates the uncertainty in the displacement using a statistical analysis of the disparity between the measured positions of particles or dots in the two frames after a converged iterative deformation interrogation procedure [38], [39]. This method requires at least six particles to be in the interrogation window for statistical calculations but fails at high seeding densities due to errors in particle identification. This method is also affected by image noise and loss of particles between frames, especially due to out of plane motion [29]. Correlation Statistics (CS) proposed by Wieneke [36], estimates the uncertainty again using the image disparity but at a pixel level. The asymmetry of the correlation peak at the end of a converged window deformation procedure is used as measure of the correlation error and the standard deviation of the error is propagated through the subpixel estimator to estimate the displacement uncertainty. As the method relies on statistics of the correlation plane, it works better with higher seeding densities and larger interrogation windows [29], [36]. Moment of Correlation (MC) proposed by Bhattacharya et. al. [37] predicts the uncertainty by estimating the second order moment of the cross-correlation plane. The estimation process involves the calculation of the Generalized Cross Correlation (GCC) from the inverse Fourier transform of the phase of the complex cross-correlation plane [40]–[42]. The primary peak region of the GCC plane represents the probability density function (PDF) of all possible displacements for the given interrogation window [37]. This PDF is convolved with a Gaussian function, corrected for peak broadening by displacement gradients, and normalized by the effective number of correlating pixels (calculated using MI [34]) to estimate the uncertainty. Similar to Correlation Statistics, this method also works better with high seeding densities and large interrogation windows, as small interrogation windows can lead to an over-prediction of the uncertainty [37].

In two independent comparative assessment of the methods, Sciacchitano et. al. [29] and Boomsma et. al. [30] found the direct methods to be more sensitive to variations in the random error, though Boomsma et. al. [30] found the direct methods to underpredict the standard uncertainty in some cases. Since the indirect methods rely on calibration, only the direct methods will be considered in this work.

There have also been efforts to propagate the displacement uncertainties in PIV derived quantities. Wilson and Smith [43] extended the displacement uncertainties calculated from the Uncertainty Surface method to estimate uncertainties in mean and fluctuating velocity statistics. Sciacchitano and Wieneke [44] provided a framework for calculation of uncertainties for displacement gradient based quantities such as the vorticity, and also identified the importance of spatial correlation of the displacement errors. Bhattacharya et. al. [45] proposed a methodology for stereo-PIV uncertainty quantification by accounting for the uncertainties introduced in the calibration and self-calibration process, along with the planar correlation uncertainty for individual camera image correlation. Azilji et. al. [46] proposed a methodology based on a Bayesian framework to calculate the uncertainties for PIV-based pressure measurement in a three-dimensional flow field, though they calculated the displacement uncertainty from the divergence error of the velocity field and did not use any of the above mentioned displacement uncertainty quantification methods.

In this paper we propose and implement the first comprehensive framework to model and propagate uncertainties from displacement measurements in a BOS experiment onto the final density measurement. To do this, we use methodologies for PIV uncertainty quantification [30]–[32], [47]–[52] and propagate these uncertainties through the BOS measurement chain including the density gradient integration and density reconstruction. We test both the PIV displacement uncertainty schemes as well as the uncertainty propagation framework with synthetic and experimental BOS images.

2.2 Methodology

The proposed uncertainty quantification methodology closely follows the BOS measurement chain and is illustrated in Figure 2.1. First, the raw image pairs and processed displacement fields are used along with PIV-based uncertainty estimation methods to calculate the local, instantaneous uncertainty on each displacement vector as indicated in Figure 2.1 (a). Following this, the optical system parameters such as the magnification and the distance between the dot pattern and the density gradients are used to estimate the uncertainty in the projected density gradient field.

In BOS experiments, the projected density gradient field is related to the apparent displacement of the dot pattern by [2], [3],

$$\nabla\rho_p = \int \nabla\rho \, dz = \frac{\Delta\vec{x}}{Z_D M}\frac{n_0}{K} \qquad \textbf{(11),}$$

where $\Delta\vec{x}$ is the displacement, M is the magnification of the dot pattern, Z_D is the distance between the dot pattern and the mid-point of the density gradient field, n_0 is the ambient refractive index, K is the Gladstone-Dale constant (= 0.225×10^{-3} m^3/kg for air) and $\rho_p = \int \rho \, dz$ is the projected density field.

Similarly, the uncertainty in the projected density gradient field can be expressed by

$$\sigma_{\nabla\rho_p} = \frac{\sigma_{\Delta\vec{x}}}{Z_D M}\frac{n_0}{K} \qquad \textbf{(12),}$$

where $\sigma_{\Delta\vec{x}}$ is the displacement uncertainty and $\sigma_{\nabla\rho_p}$ is the uncertainty in the projected density gradient field (Figure 2.1 (b)). It should be noted that some of the experimental parameters occurring in the above equations can also have their own uncertainties such as the magnification M and the distance Z_D. However, herein, for simplicity we will assume these as known and constant, as our focus is on propagating the displacement-based uncertainties. Any uncertainties in these quantities can be handled in a straightforward manner using the Taylor series propagation model [21].

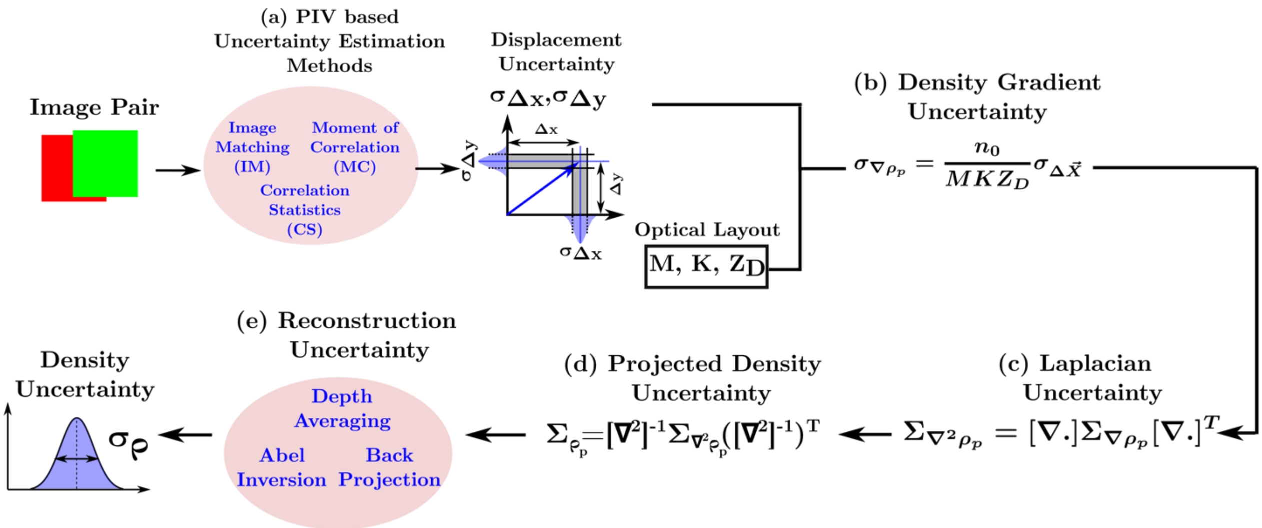

Figure 2.1. Proposed uncertainty quantification methodology for BOS measurements.

The next step in BOS experiments is to calculate the projected density field by solving the Poisson equation:

$$\frac{\partial^2 \rho_p}{\partial x^2} + \frac{\partial^2 \rho_p}{\partial y^2} = S \tag{13}$$

where the source term S denotes the Laplacian of the density field calculated from the projected density gradient field. This equation is then discretized into a system of linear equations using finite difference schemes and solved using appropriate boundary conditions (Dirichlet/Neumann) depending on prior knowledge about regions of the flow field.

The discretization and solution procedure are as follows. The source term S is calculated as

$$\bar{\bar{S}} = \bar{\bar{\nabla}}_x \overline{\frac{\partial \rho_p}{\partial x}} + \bar{\bar{\nabla}}_y \overline{\frac{\partial \rho_p}{\partial y}} \qquad \textbf{(14),}$$

where $\bar{\bar{\nabla}}_x, \bar{\bar{\nabla}}_y$ are the discretized gradient operators (matrices represented by a double overbar) that depend on the finite difference scheme, and $\overline{\frac{\partial \rho_p}{\partial x}}, \overline{\frac{\partial \rho_p}{\partial y}}$ are the density gradients (1D column vector represented by a single overbar). A second order central difference discretization scheme is used for the results reported in this paper.

The source term is combined with points on the boundary to create an augmented matrix $\bar{\bar{R}}$, given by

$$\begin{aligned}\bar{\bar{R}} &= \bar{\bar{\nabla}}_x \overline{\frac{\partial \rho_p}{\partial x}} + \bar{\bar{\nabla}}_y \overline{\frac{\partial \rho_p}{\partial y}} + \frac{1}{h^2}\bar{\bar{L}}\bar{\rho}_{p,L} \\ &= \bar{\bar{S}} + \bar{\bar{S}}_L\end{aligned} \quad \textbf{(15),}$$

where $\bar{L}$ is a label matrix specifying points on the boundary, and h is the grid spacing, and $\bar{\rho}_{p,L}$ is the array of densities of the points corresponding to the label matrix (the Dirichlet boundary condition).

The projected density is calculated by multiplying the augmented matrix $\bar{\bar{R}}$ with the inverse of the augmented Laplacian operator

$$\rho_p = \begin{bmatrix} \bar{\bar{\Delta}} & 0 \\ 0 & \frac{\bar{\bar{L}}}{h^2} \end{bmatrix}^{-1} \begin{bmatrix} \bar{\bar{S}} \\ \bar{\bar{S}}_L \end{bmatrix} \quad \textbf{(16),}$$

where $\bar{\bar{\Delta}}$ (sometimes also represented by ∇^2) is the discretized Laplacian operator for the interior points corresponding to the finite difference schemes used to calculate the Laplacian ($\bar{\bar{\Delta}} = \bar{\bar{\nabla}}_x \bar{\bar{\nabla}}_x{}^T + \bar{\bar{\nabla}}_y \bar{\bar{\nabla}}_y{}^T$). Thus, equation (6) essentially solves the Poisson equation (3) to give the projected density field ρ_p.

The uncertainty calculations are performed in a manner similar to the density integration, by propagating the covariances through the finite difference operators and accounting for the boundary conditions used to calculate the corresponding density field. The covariance in the augmented source term defined in equation (5) is given by

$$\begin{aligned}\bar{\bar{\Sigma}}_R &= \bar{\bar{\nabla}}_x \bar{\bar{\Sigma}}_{\frac{\partial \rho_p}{\partial x}} \bar{\bar{\nabla}}_x^T + \bar{\bar{\nabla}}_y \bar{\bar{\Sigma}}_{\frac{\partial \rho_p}{\partial y}} \bar{\bar{\nabla}}_y^T + \frac{1}{h^2}\bar{\bar{L}}\bar{\bar{\Sigma}}_{\rho_{p_L}} \frac{1}{h^2}\bar{\bar{L}}^T \\ &= \bar{\bar{\Sigma}}_S + \bar{\bar{\Sigma}}_{S_L}\end{aligned} \quad \textbf{(17),}$$

and as shown in Figure 2.1 (c), the covariance in the projected density ($\bar{\bar{\Sigma}}_{\rho_p}$) is calculated using

$$\bar{\bar{\Sigma}}_{\rho_p} = \begin{bmatrix} \bar{\bar{\Delta}} & 0 \\ 0 & \frac{\bar{\bar{L}}}{h^2} \end{bmatrix}^{-1} \begin{bmatrix} \bar{\bar{\Sigma}}_S \\ \bar{\bar{\Sigma}}_{S_L} \end{bmatrix} \left(\begin{bmatrix} \bar{\bar{\Delta}} & 0 \\ 0 & \frac{\bar{\bar{L}}}{h^2} \end{bmatrix}^{-1} \right)^T \quad \textbf{(18).}$$

Finally, the uncertainty in the density is calculated from the square root of the diagonal terms of the density covariance matrix as indicated in Figure 2.1 (d) and is expressed as,

$$\sigma_{\rho_p} = \sqrt{\mathrm{diag}(\Sigma_{\rho_p})} \quad \textbf{(19).}$$

All linear operators in the solution procedure are modeled as sparse matrices to increase computational speed.

The next step is to calculate the 2D density field from the projected density field, either by depth averaging (dividing the projected density field by the thickness of the density gradient field) if the extent of the density field is known, or through an Abel inversion or Filtered Back Projection (FBP) procedure if the flow field is axisymmetric (Figure 2.1 (e)) [12]. While each reconstruction procedure can create a different amplification of the uncertainty, only the depth averaged reconstruction approach will be considered in this paper. For situations which involve the use of Abel inversion, the uncertainty can again be propagated through a matrix representation of the Abel inversion procedure, because all the Abel inversion schemes can be represented by linear operators both for interferometric and deflectometric cases [53], [54]. The final result at the end of all such reconstruction procedures is an estimate of the instantaneous density uncertainty for each grid point.

In the following sections the uncertainty quantification methodology is tested with synthetic BOS images of a Gaussian density field to assess the performance of the various PIV displacement uncertainty schemes and the propagation framework. Subsequently, the potential of the method is demonstrated with experimental BOS images for supersonic flow over a wedge.

2.3 Analysis with synthetic images

The error analysis is performed using synthetic BOS images rendered using a ray-tracing based image generation methodology, where light rays emerging from the dot pattern are traced through the density gradient field and the optical components of the experimental setup, up to the camera sensor to render the final image. This methodology has been validated using analytical solutions for known density field and the rendered images display realistic features of typical BOS experimental setups such as optical aberrations and blurring due to non-linearities in the density field [55].

The density field chosen for the error analysis is a Gaussian density field, described by Equation (20),

$$\rho(X,Y) = \rho_0 + \Delta\rho_0 \exp\left\{-\frac{(X-X_0)^2 + (Y-Y_0)^2}{2\sigma_0^2}\right\} \tag{20}$$

where ρ_0 is the ambient density, $\Delta\rho_0$ is the peak density difference and σ_0 is the standard deviation of the Gaussian field. This field was chosen because it contains significant displacement gradients to test the displacement uncertainty schemes and the density integration procedure. For the simulations reported in this paper, ρ_0 was set to be 1.225 kg/m^3, $\Delta\rho_0$ was set to be 0.3 kg/m^3, and σ_0 was set to be 1/4th of the field of view (= 2.41 mm). The dimensions of the density gradient field were 10 x 10 x 10 mm, and it was located at a distance of 0.25 m from the dot pattern. The optical layout used to image the dot pattern and the density field consisted of a 105 mm lens at a distance of 0.5 m from the dot pattern to provide a magnification of about 40 μm/pix. A 2D slice of the three-dimensional density field is shown in Figure 2.2 (a), and the corresponding light ray displacements are shown in Figure 2.2 (b). A three-dimensional volume was created using the same slice stacked along the Z direction (out of plane) to account for the depth averaging limitation of BOS experiments.

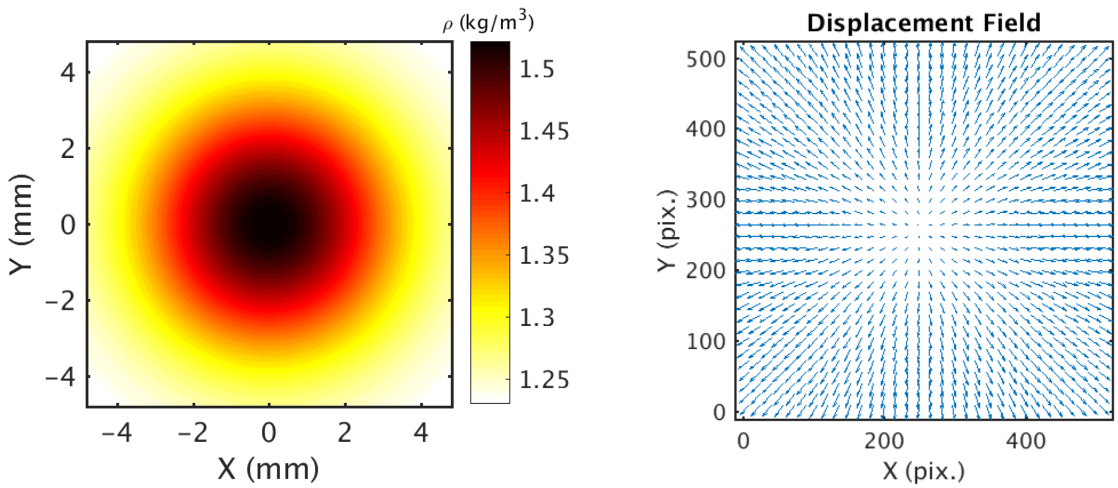

(a) **(b)**

Figure 2.2. (a) 2D slice of the density field used to render the synthetic BOS images, and (b) the corresponding displacement field.

The images were rendered with a dot size of 3 pix. under diffraction limited imaging, with about 20 dots per 32x32 window. The rendered images were corrupted with noise drawn randomly from a zero-mean Gaussian distribution with a standard deviation of 5% of the peak image intensity. A thousand image pairs were rendered in total to create sufficient statistics for the analysis.

The images were processed using a standard cross-correlation procedure for two passes in an iterative window deformation framework [38], [39] with continuous window offset [56]–[58]. The window resolution was 32x32 pix for both passes, which corresponds to a 64x64 pix window size and apodized using a 50% Gaussian window, to minimize edge discontinuities, spectral leakage and wraparound aliasing [59]. The window overlap was set to 0% (grid resolution = 32x32 pix.) for the analysis to avoid introducing covariance on adjacent displacement vectors from the cross-correlation process, as accounting for this covariance in an automatic calibration-free manner is still a subject of ongoing research [44]. The results of the first pass were validated using the Universal Outlier Detection (UOD) method [60] and smoothed, while the results of the second pass were not validated. The displacement uncertainties were calculated using the Image Matching (IM), Correlation Statistics (CS) and Moment of Correlation (MC) methods. For the IM and MC methods, the processing and uncertainty calculation was performed using an open source code PRANA (https://github.com/aether-lab/prana/). For CS, the processing and uncertainty calculation was performed with DaVis 10.0.5 by LaVision. A sample instantaneous displacement field along with the corresponding uncertainty field is shown in Figure 2.3. Sample instantaneous magnitudes of the displacement and uncertainty fields for (a) Prana, IM, MC and (b) DaVis, CS.(a) for results from PRANA processing and uncertainties from IM and MC, and in Figure 2.3. Sample instantaneous magnitudes of the displacement and uncertainty fields for (a) Prana, IM, MC and (b) DaVis, CS.(b) for results from DaVis processing and uncertainties from CS.

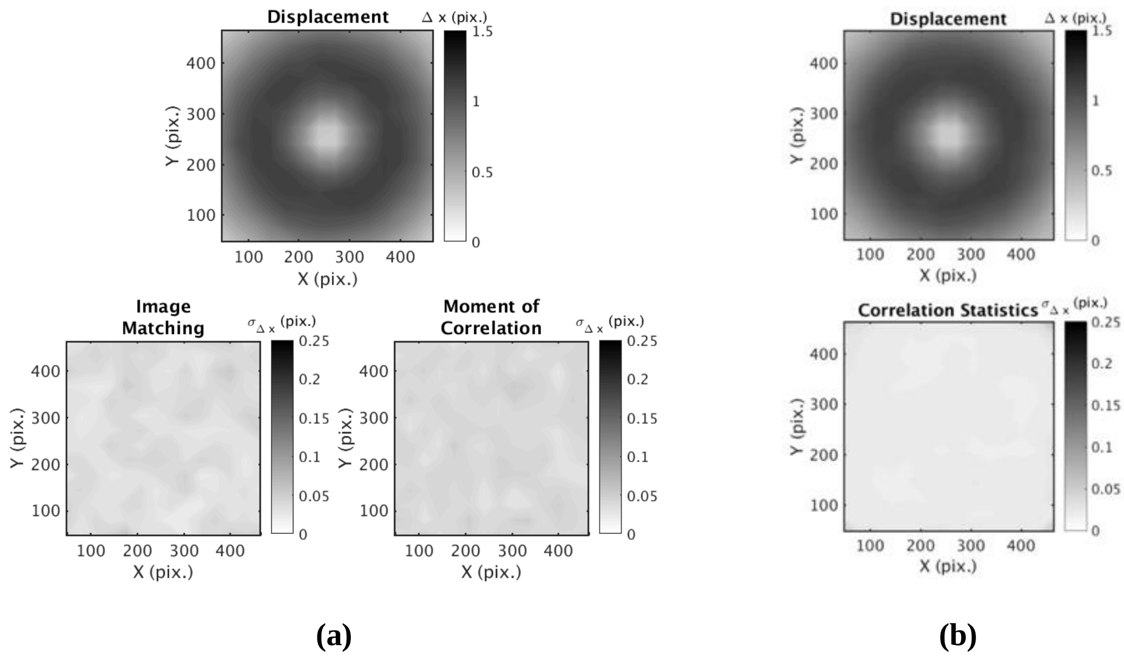

Figure 2.3. Sample instantaneous magnitudes of the displacement and uncertainty fields for (a) Prana, IM, MC and (b) DaVis, CS.

For the error analysis, the displacements obtained from the cross-correlation analysis were compared with the light ray displacements from the ray tracing based image generation procedure to calculate an error for each vector. The final locations of the light rays will be randomly scattered on the image sensor because the dots from which the light rays originate are distributed randomly on the pattern, and the direction of the rays is also varied randomly within the viewing angle of the camera lens. Since the displacements obtained from the cross-correlation analysis is arranged on a regular grid, the true displacements due to the light ray deflections have to be interpolated onto the measurement grid. To achieve this, an interpolation procedure was performed using a natural neighbor interpolation based on Voronoi tessellations [61] to calculate the corresponding true displacement for each vector. Finally, the errors corresponding to all vectors from all image pairs were combined to build a probability density function (PDF) for the error distribution and the corresponding error statistics such as the bias error, the random error and the total error were calculated. As each image pair yielded 256 vectors with the above processing procedure, with a total of 1000 images, we have 256000 vectors to calculate the statistics. The error statistics were split into three main components, the bias/systematic error, the random error, and the total error, defined as:

$$
\begin{aligned}
&\delta_{bias} = E(u - u_{true}), \\
&\delta_{random} = \sqrt{E((u - u_{mean})^2)}, \\
&\delta_{total} = \sqrt{E((u - u_{true})^2)} = \sqrt{\delta_{bias}^2 + \delta_{random}^2},
\end{aligned}
\tag{21}
$$

where δ represents the error statistic, u is the measurement, u_{true} is the ground truth, and u_{mean} is the average of the measurements.

The displacement uncertainty estimates from the three direct schemes were compared to the random error from the analysis to assess the performance of these PIV-based schemes for synthetic BOS images. The spatial distribution of the error statistics as well as the displacement uncertainties are shown in Figure 2.4 (a) for PRANA-IM-MC processing and Figure 2.4 (b) for DaVis-CS processing. It can be seen that the error statistics are fairly uniform throughout the field of view, with negligible bias error from both processing software programs, and that DaVis results in a slightly higher error near the center of the FOV. For the spatial variation of the displacement uncertainty, all three uncertainty schemes result in nearly uniform uncertainty estimates throughout the field of view, and on the same order of their respective random errors. It is important to note that the MC uncertainties reported in this paper are without the bias term in contrast to the original formulation proposed by Bhattacharya et. al. [37]. This is because the bias term in the method is based on an estimate of the local displacement at the end of a converged deformation process, and since the displacement estimation is itself random, the bias estimation itself becomes a random process.

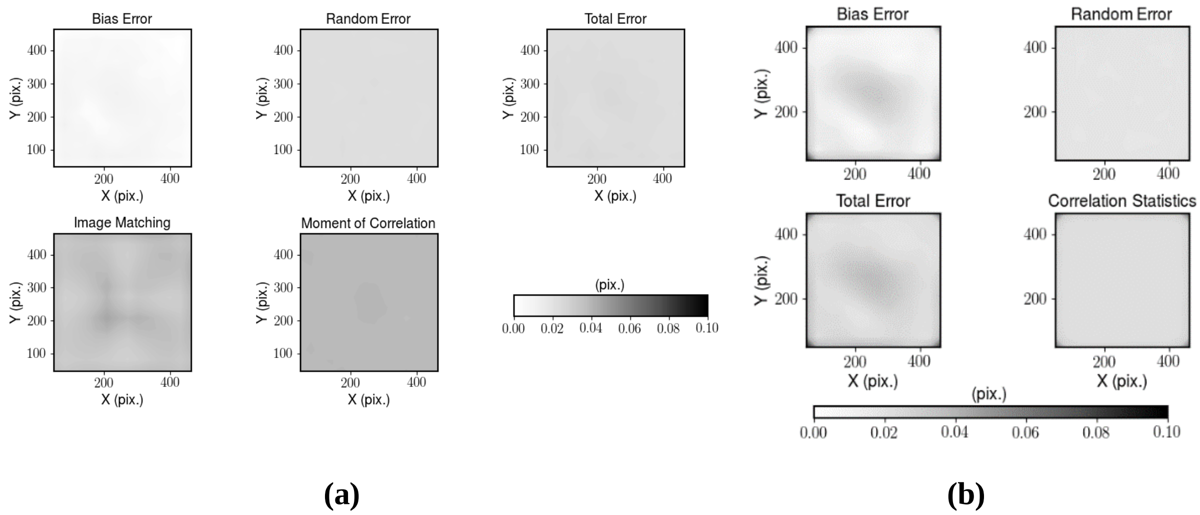

Figure 2.4. Spatial variation of the magnitudes of the displacement error statistics and ensemble averaged uncertainty fields for (a) PRANA, IM and MC, and (b) DaVis and CS methods.

The PDFs of the errors and uncertainties from both software programs are shown in Figure 2.5, along with dashed lines indicating the RMS values of the random error and the RMS values of the corresponding uncertainty schemes. The PDFs were calculated by combining the x and y components of the displacements into a single array. A 0.1 pixel threshold was used to threshold the errors, to reduce the effect of outliers on the reported statistics. This can be confirmed from the error/uncertainty PDF in Figure 2.5, as the PDF has plateaued to nearly zero around 0.05 pix. Therefore any errors on the order of 0.1 pixels are likely outliers, and can be ignored as it is not meaningful to report uncertainties on invalid measurements.

The results for PRANA-IM-MC are shown in Figure 2.5 (a), and the results for DaVis-CS are shown in Figure 2.5 (b). It is expected that for a correct uncertainty prediction, the RMS of the random error should coincide with the RMS of the uncertainty distribution [29]. From the figures it can be first seen that all three displacement uncertainty schemes overpredict the corresponding random error, but the RMS of the uncertainty from CS is closest to the RMS of the random error in Figure 2.5 (b), followed by IM and then MC. Further, CS has a very narrow distribution of the uncertainties compared to IM and MC. The error and uncertainty statistics are summarized in Table 1.

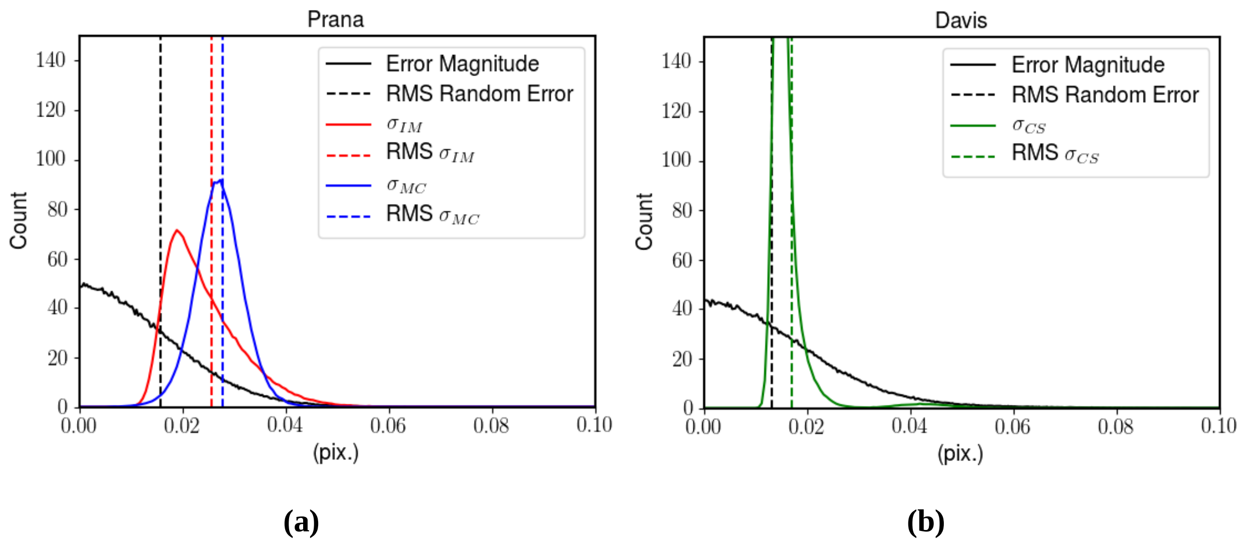

Figure 2.5. Probability density functions (PDF) of the displacement error and uncertainty distributions along with the corresponding RMS values. (a) PRANA, IM and MC, (b) DaVis, CS

Table 2.1. Displacement error and uncertainty statistics from the two software programs and three uncertainty schemes for the Gaussian density field. All values in units of *pix*.

PRANA		**DaVis**	
Bias Error	4.45e-03	Bias Error	1.45e-02
Random Error	**1.58e-02**	**Random Error**	**1.31e-02**
Total Error	1.64e-02	Total Error	1.95e-02
Image Matching	2.56e-02	Correlation Statistics	1.70e-02
Moment of Correlation	2.77e-02		

The displacement fields were also used to calculate the projected density gradient fields using Equation (11), and spatially integrated using the Poisson solver to obtain the projected density field. The thickness of the density gradients from the simulation was then used to calculate the depth averaged density field. Dirichlet boundary conditions were imposed for the density integration procedure, and the density at all four boundaries was set to be values from the true density field used to render the images. Sample results of the depth-averaged density gradient and density fields are shown in Figure 2.6(a).

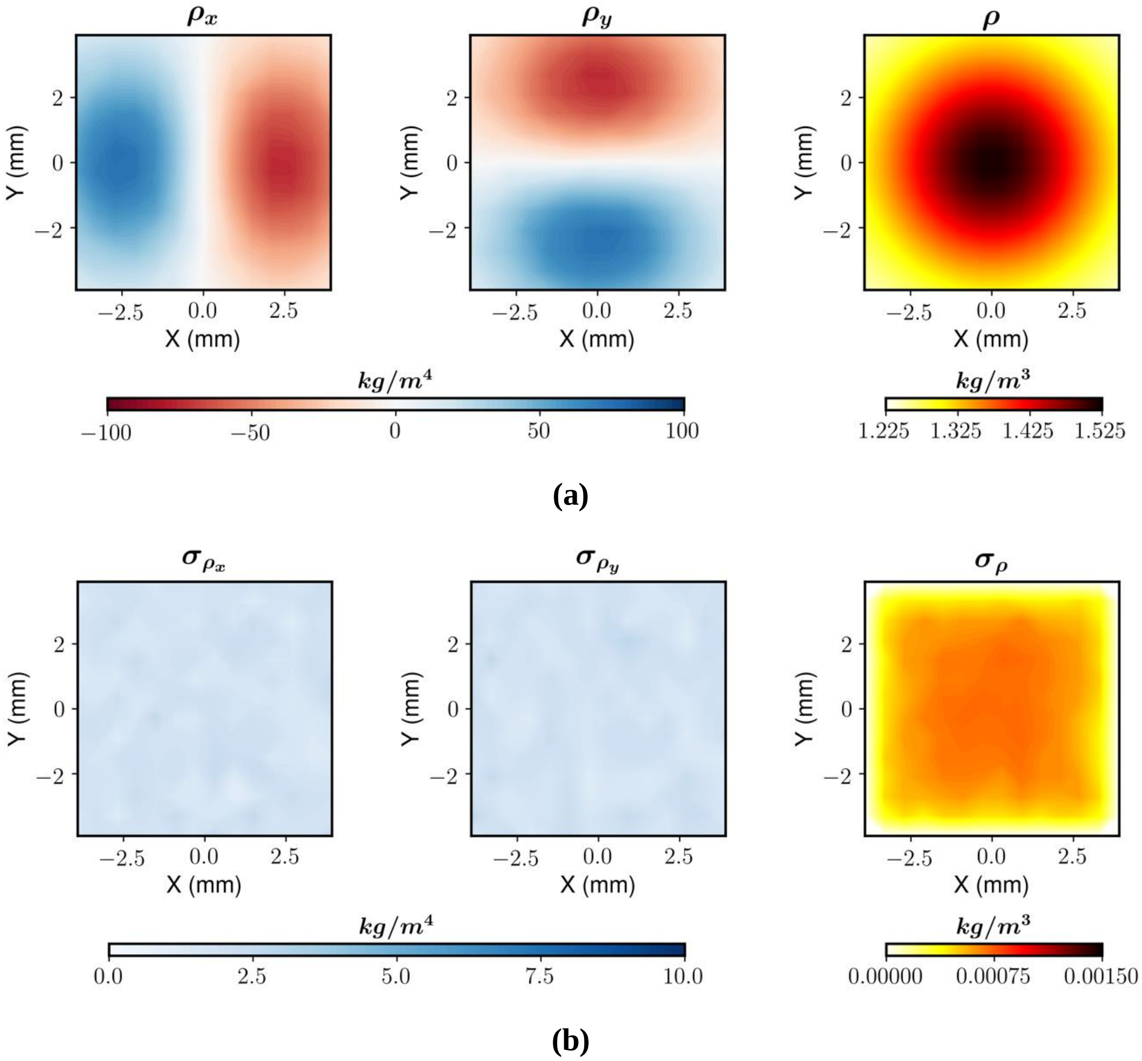

Figure 2.6. Sample instantaneous depth-averaged (a) density gradients and density fields and (b) associated uncertainties obtained from the Poisson solver for PRANA processing.

In addition, the displacement uncertainties from the cross-correlation analysis from each scheme were propagated through the Poisson solver to calculate the density uncertainties. Dirichlet boundary conditions were also used for the uncertainty propagation procedure, with the boundary uncertainties on the four sides set to be 0. In general, the uncertainty in the boundary conditions will have a strong effect on the uncertainty of the resulting field, especially for the Poisson integration method. As the density uncertainty at a point near the boundary is a weighted average of the boundary uncertainty and the gradient uncertainty of the surrounding points, it is expected that if the density uncertainty at the boundary is less than about one order of magnitude (1e-4 kg/m^3) of that in the interior, then its effect should be negligible. Sample instantaneous uncertainties in the depth-averaged density gradient and density fields are shown in Figure 2.6(b).

The calculated density field was then compared with the original density field used to render the synthetic images and the density error was calculated. The resulting density errors from all 1000 images were used to calculate error statistics. The density error statistics and the corresponding ensemble averaged density uncertainties are shown for results from Prana-IM-MC in **Error! Reference source not found.**(a), and for results from DaVis-CS in **Error! Reference so urce not found.**(b).

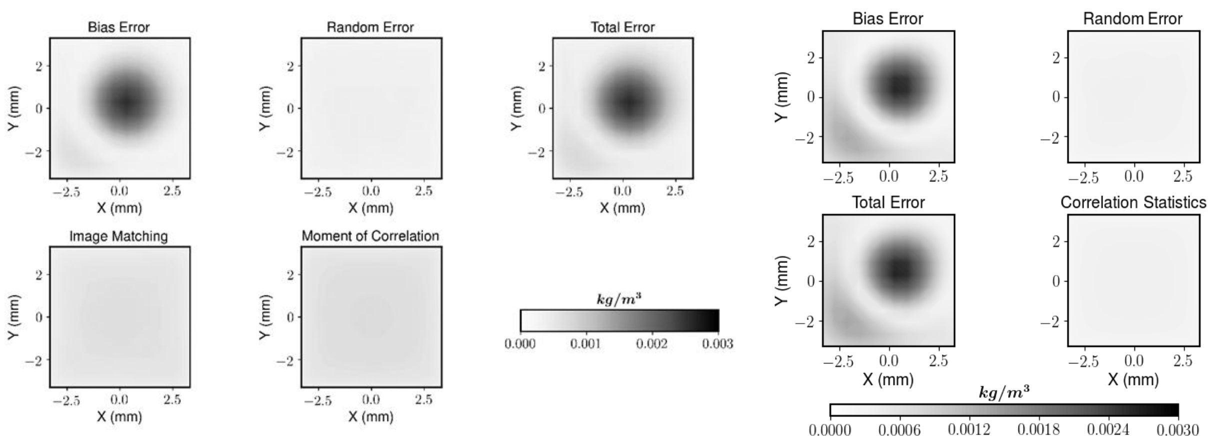

(a) **(b)**

Figure 2.7. Spatial variation of density error and uncertainty statistics from (a) PRANA, IM and MC, and (b) DaVis and CS.

From the figures it can be seen that unlike the displacement error statistics, the density error statistics show a higher bias error component (~ 2e-3 kg/m^3) as compared to the random error. The skew in the spatial distribution of the bias error in Figure 2.7 (b) could be because of a combination of the processing method from the Davis software and the density integration procedure, and given that the small value of the error (0.3% of the density), makes the explanation difficult. It is possibly because the linear system of equations is solved in an iterative procedure beginning at the top right corner and ending with the point on the bottom left corner. Therefore, the bias error in the displacement also propagates from this point to the rest of the field, and this effect is more pronounced in Figure 7 (b), as the displacement errors are higher for Davis processing.

However, since the uncertainty estimated using the proposed methodology is the random uncertainty, the comparison will be performed between the random error and the uncertainty prediction. The density uncertainty predictions however are spatially uniform for all three methods similar to the displacement uncertainty results shown in Figure 2.4, and on the same order as the random error (~ 5e-4 kg/m^3). But overall, the density uncertainties are seen to be very small likely due to the smoothing nature of the Poisson solver and the uncertainty being zero at the boundaries. The PDFs of the density error and uncertainty distributions are shown in Figure 2.8 (a) for PRANA-IM-MC and in Figure 2.8 (b) for DaVis-CS, along with the corresponding RMS values. Due to the strong bias error in the density results, the RMS of the *random error* will be compared to the RMS of the density uncertainty distributions, and a closer match signifies a better performance. As in the displacement uncertainty results, it is again seen that CS gives the best match between the RMS of the random error and the uncertainty, followed by IM and MC. It is also interesting to note that unlike the displacement error PDFs, the density error PDFs are non-Gaussian, and skewed towards the negative values, signifying that the density error is primarily due to under-prediction. The skewness of the error distribution is also consistent with the strong bias error seen in the spatial error maps in **Error! Reference source not found.**. The density errors a nd uncertainties are summarized in Table 2.2.

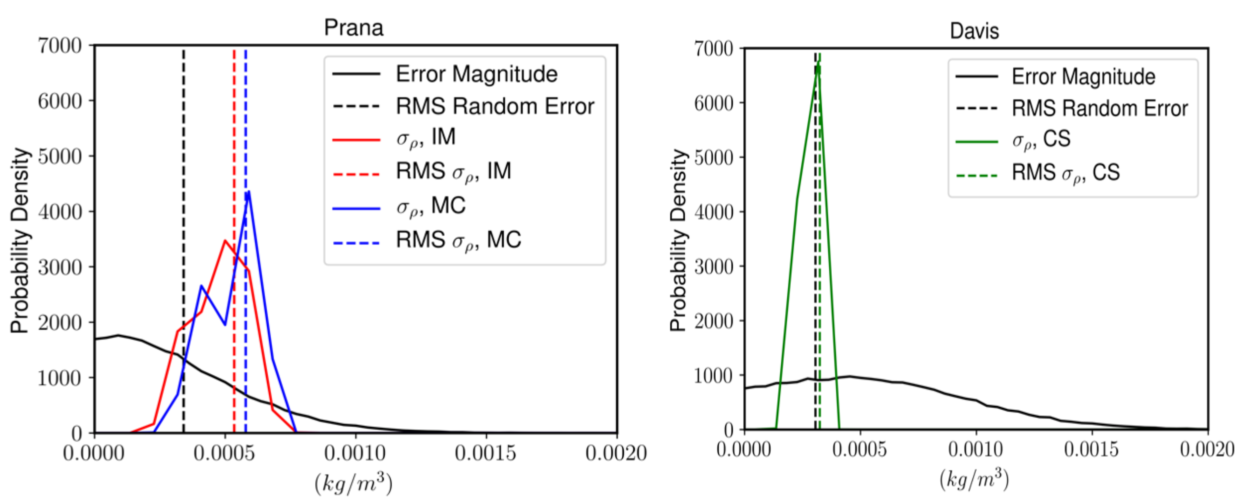

(a) (b)

Figure 2.8. PDFs of the density error and uncertainty distributions for (a) PRANA error, IM, and MC uncertainty, and (b) DaVis error and CS uncertainty.

Table 2.2. Density error and uncertainty statistics from the two software programs and three uncertainty schemes for the Gaussian density field. All values in units of kg/m^3.

PRANA		**DaVis**	
Bias Error	8.65e-04	Bias Error	9.83e-04
Random Error	**3.41e-04**	**Random Error**	**3.06e-04**
Total Error	9.12e-04	Total Error	1.02e-03
Image Matching	5.34e-04	Correlation Statistics	3.25e-04
Moment of Correlation	5.79e-04		

Further, the effect of density uncertainty at the boundaries was investigated by repeating the density integration procedure with a range of density noise levels on the boundaries as a fraction of the peak density offset, and the resulting error and uncertainty statistics are shown in Figure 2.9. It can be seen that as the density noise level increases, all the displacement uncertainty schemes result in a nearly identical density uncertainty, because the noise from the boundaries dominates the density uncertainty. This implies that the performance of the uncertainty quantification methodology is consistent with expectations.

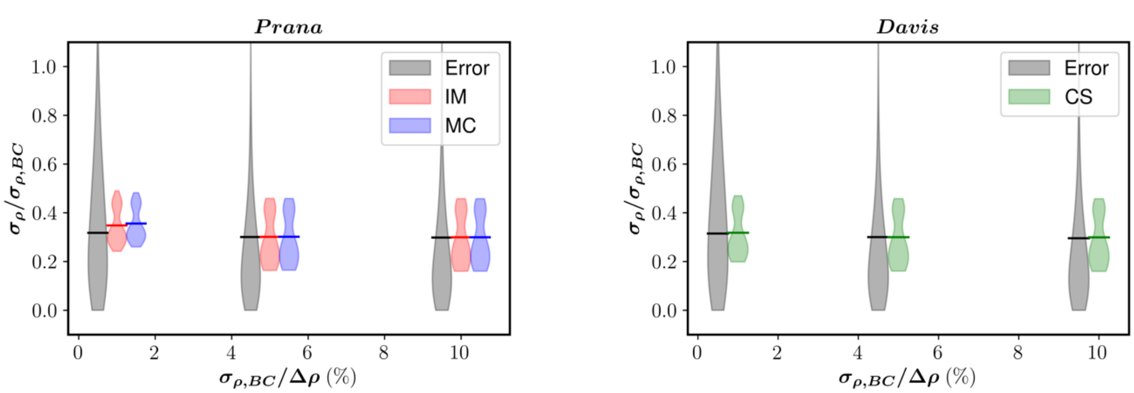

(a) **(b)**

Figure 2.9. Effect of density uncertainty on the boundary on the RMS errors and uncertainties. The violin plots show the error and uncertainty distribution obtained using kernel density estimation, and the solid lines denote the RMS error. The errors/uncertainties on the Y axis are expressed as a fraction of the boundary uncertainty, and the boundary uncertainty is expressed as a percentage of the peak density offset.

Overall, it is seen from the analysis that (1) PIV-based direct displacement uncertainty schemes are also applicable for BOS images, and (2) Correlation Statistics (CS) performs the best in both the displacement and density uncertainty prediction, though the density results showed a strong anisotropic bias error. The sources of uncertainty considered in the synthetic image analysis are due to random positions of the dots, the cross-correlation operator, image noise and density uncertainty at the boundaries.

2.4 Demonstration with Experimental Images

The feasibility of the proposed uncertainty quantification methodology is demonstrated with experimental BOS images taken in a supersonic wind tunnel for Mach 2.5 flow over a $11.5°$ wedge with a base of 1 cm and a height of 2.5 cm. The dot pattern consisted of 0.15 mm diameter dots (corresponding to an image diameter of about 4 pix.) randomly distributed on a transparency with about 25 dots per 32x32 pix. window, and was back-illuminated using an LED with a diffuser plate to obtain uniform illumination. The dot pattern was imaged through the flow with a Photron SAZ camera and a Nikon 105 mm lens at a magnification of 50 um/pix. and an f-number of 32. A total of 5000 images were acquired at 3 kHz for a total/stagnation pressure of 70 psia, corresponding to a free-stream density of 0.49 kg/m^3. The free-stream density is calculated based on isentropic flow theory using the stagnation density and the free-stream Mach number. The stagnation density is calculated using the stagnation pressure in the reservoir assuming an adiabatic compression of air from the atmosphere into the reservoir. A layout of the experimental setup is shown in Figure 2.10 (a), and the wedge geometry is shown in Figure 2.10 (b).

To account for the startup transients in the tunnel, the images are only recorded during the steady state operation of the tunnel. Further, to avoid masking based errors from affecting the analysis, only a small portion from the flow beneath the wedge is considered in this analysis, and a sample image of the dot pattern with the region of interest (ROI) is shown in Figure 2.10 (c).

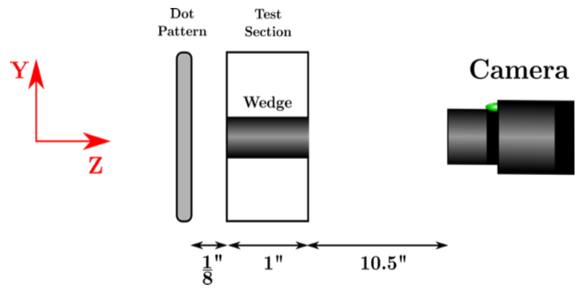

(a)

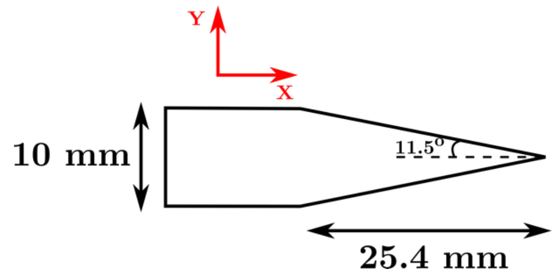

(b)

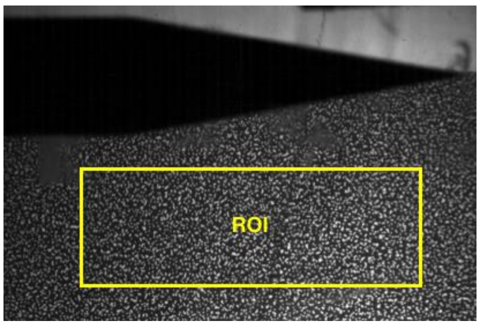

(c)

Figure 2.10. (a) Experimental layout, side view (b) schematic of the wedge, front view, (c) sample image with region of interest (flow is from right to left).

The images were processed using the multi-pass window deformation approach described in the previous section for three passes with identical window sizes and overlap percentages (32x32 pix window size and 0% window overlap), with the intermediate pass results smoothed, but without any outlier detection. This was done to preserve the sharp change in displacement in the shock regions, and to prevent them from being identified as be an outlier. The images were processed using PRANA with displacement uncertainty calculation from IM and MC, and using DaVis with displacement uncertainty calculation from CS.

To reduce the effect of tunnel/camera/dot-pattern vibrations on subsequent calculations, the displacements in the FOV were subtracted by the average displacements measured in the free-stream region. This was done because the free-stream region ahead of the shock does not contain any density gradients and hence any displacements in this region would be a result of vibrations. While the boundary layer on the wind tunnel wall can affect the measured displacement, this is expected to be negligible with respect to the other flow features of interest such as the shock and the expansion fan for the present optical layout. This is because the angular displacement of the light ray due to the boundary layer on the tunnel wall will only be a function of the streamwise ($\partial/\partial x$) and spanwise ($\partial/\partial y$) gradients of density because the wall-normal gradients ($\partial/\partial z$)

coincides with the viewing directions and therefore will not contribute to any angular deflection. Since the streamwise/spanwise density gradients in the boundary layer are much lower than the gradients in the shock/expansion fan, and the displacements in the shock regions are measured to be less than a pixel, the displacements due to the boundary layer is expected to be much lower and hence negligible, especially in comparison with the vibrations which were measured to be on the order of a pixel.

The displacements were then used to calculate the density gradients and density fields using the Poisson solver previously described. For the density integration, Dirichlet boundary conditions were used on the right boundary, where the density was set to be its free-stream value of 0.49 kg/m^3 and Neumann boundary conditions were imposed on the other three boundaries. Sample images of the path averaged density gradients and density fields are shown in Figure 2.11 (a) for PRANA processing, and it can be seen the gradients are highest in the regions corresponding to the shock and expansion fan. The density is seen to increase across the shock followed by a decrease across the expansion fan.

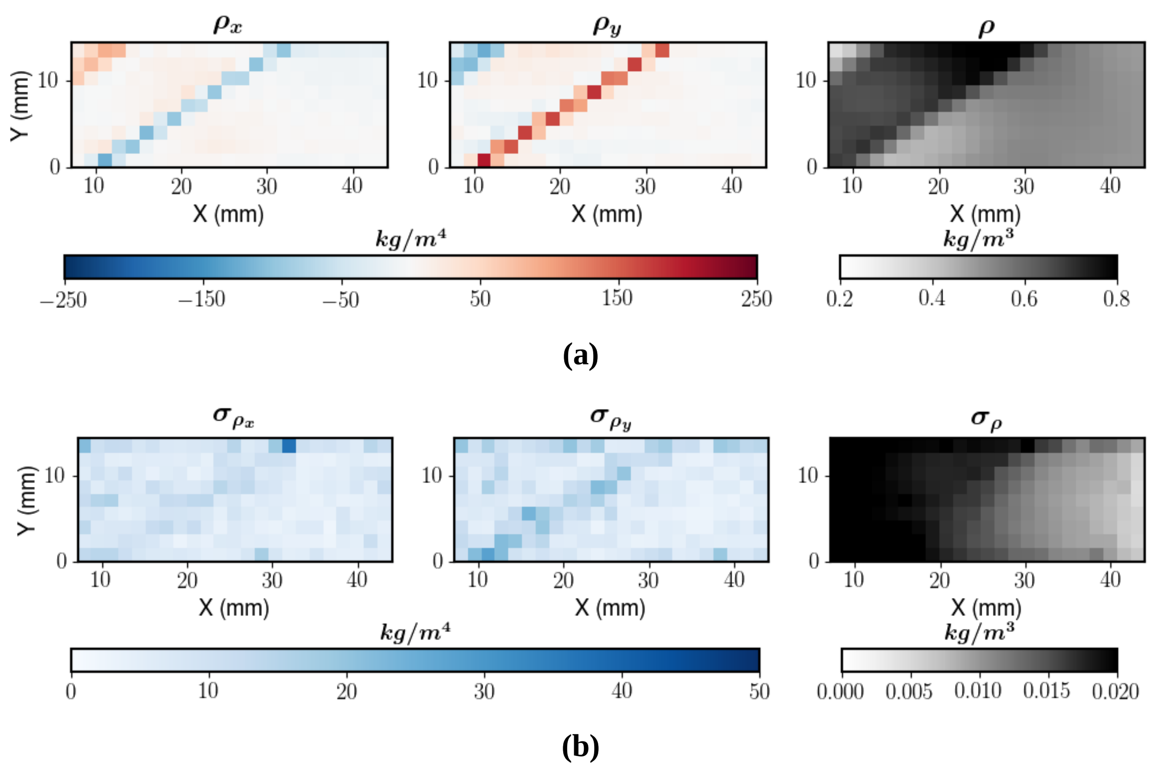

Figure 2.11. (a) Sample density gradient and density fields from PRANA processing and (b) associated uncertainty fields from Image Matching.

A similar approach was also followed for the uncertainty propagation, where a Dirichlet boundary condition was used on the right boundary with an uncertainty of 0.0 kg/m^3 as any fluctuations in the free-stream were much lower than the uncertainties measured from BOS, and Neumann boundary conditions were imposed on the other three sides with the measured density gradients. Sample instantaneous uncertainties in the density gradient and density fields are shown in Figure 2.11 (b) where it seen that the region aft (to the left) of the shock has a higher density uncertainty than the region before (to the right of) the shock, even though these points had similar density gradient uncertainties. This exemplifies the uncertainty propagation characteristics of the Poisson solver used for density integration. As the boundary conditions are only specified on the right boundary, the number of points that affect the density estimation at a given point increases as one moves to the left, and hence the density uncertainty at the given point is also a combination of the uncertainties from an increasing number of points. Since the density gradient uncertainty is always positive, the result is that the density uncertainty field increases, and in general, the density uncertainty for a BOS experiment will increase as one moves away from the Dirichlet boundaries. This is an artifact of the density integration procedure using the Poisson equation, and represents one of the method's limitations.

The uncertainty fields across five thousand images were averaged to calculate the statistics, and the ensemble averaged field is shown in Figure 2.12 for all three uncertainty schemes. Qualitatively, it is seen that the ensemble averaged uncertainty distributions are very similar to the instantaneous fields shown in Figure 2.11 (b), with an increase of uncertainty from right to left. It is also seen that while IM predicts the highest density uncertainty followed by CS and MC.

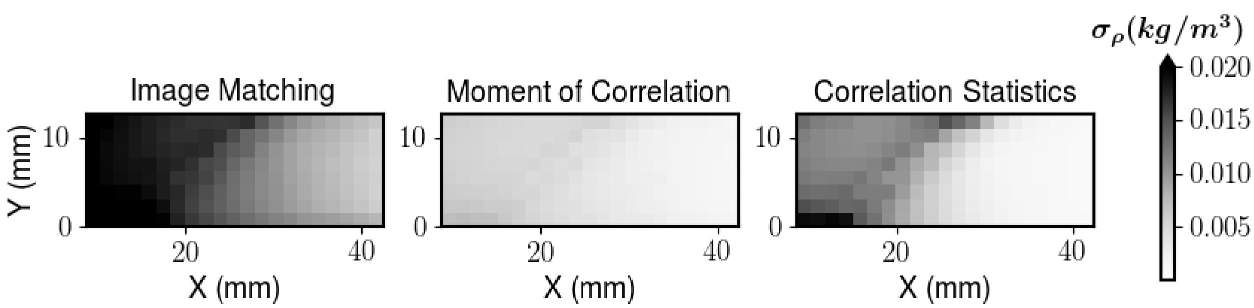

Figure 2.12. Spatial variation of ensemble averaged density uncertainty predictions from Image Matching, Moment of Correlation and Correlation Statistics schemes.

Finally, the uncertainties from all vectors in the time series are combined to calculate the PDFs for the uncertainty distributions. The resulting PDFs are shown in Figure 2.13 along with the RMS values which are 1.51e-2 kg/m^3 for IM, 4.45e-3 kg/m^3 for MC and 8.73e-3 kg/m^3 for CS., It is seen that MC results in the lowest uncertainty and IM results in the highest uncertainty with CS predicting a value slightly lower than IM. Further, all PDFs show a bimodal behavior where each peak corresponds approximately to the density uncertainty ahead of and behind the shock. This is particularly evident for CS having the largest separation between the peaks, and MC with the lowest peak separation. The sources of uncertainty considered in experimental analysis are image noise, the cross-correlation operator and unsteadiness in the flow field. Density noise at the boundaries has not been considered.

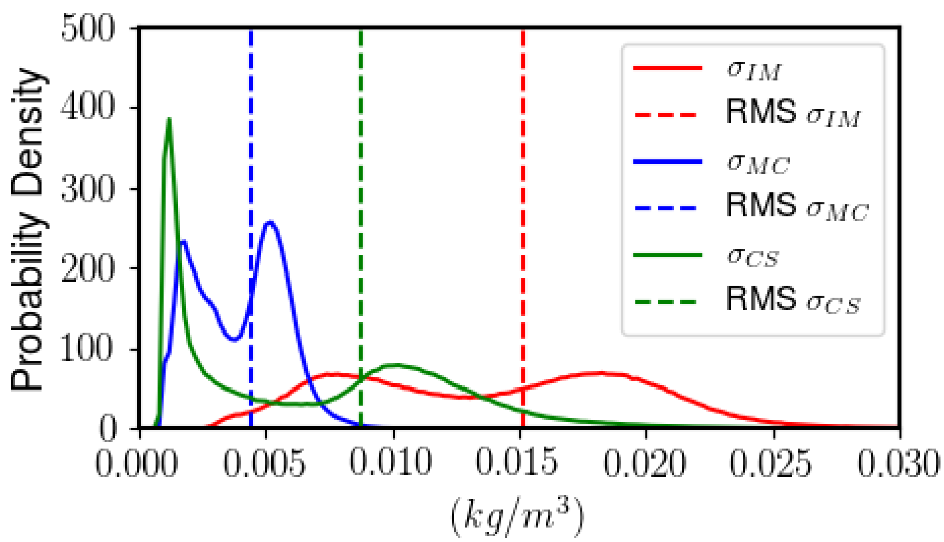

Figure 2.13. PDFs of the density uncertainty distributions for IM, MC, and CS.

2.5 Conclusion

We have implemented and presented the first comprehensive uncertainty quantification framework for density estimation from BOS measurements and tested the method with synthetic and experimental BOS images. The methodology builds upon recent progress in a-posteriori uncertainty quantification in PIV, and direct displacement uncertainty methods are used to also estimate the displacement uncertainty from BOS images. These displacement uncertainties are then propagated to the density gradients using the optical layout and then through the Poisson solver typically used for density integration in BOS to calculate density uncertainties, accounting for the covariances introduced due to the finite differences involved in the calculation of the Laplacian. This method yields instantaneous, local uncertainty bounds for each density measurement throughout the field of view.

The methodology was tested with synthetic BOS images rendered with a Gaussian density field using a ray-tracing based image generation methodology. The images were processed using correlation algorithms with multi-pass window deformation, and the errors were calculated by comparing the measured displacements to the light ray displacements, which are considered to be the ground truth. Processing was done using two different software programs, PRANA and DaVis, and three displacement uncertainty estimation schemes– Image Matching (IM), Moment of Correlation (MC) and Correlation Statistics (CS). Results show that for the displacements, all methods overpredict the true random error, with CS closest to the random error, followed by IM and MC.

When propagated through the Poisson solver for density integration, results from both processing software programs resulted in a stronger bias error in the density field, likely due to truncation errors from the finite differences used in the density integration process. On comparing the random errors with the predicted density uncertainties, CS predicted a density uncertainty closest to the corresponding random error. IM and MC both overpredicted their respective random errors, but IM was closer to the true random error compared to MC.

The method was also demonstrated on experimental BOS images of supersonic flow over a wedge and the processed displacements and the density fields show the presence of a shock wave and expansion fan in the region of interest corresponding to the wedge tip and wedge shoulder respectively. The density gradient uncertainties were highest in close proximity to the shocks and expansion fans, and were sensitive to the boundary condition and the integration procedure. In general, the density uncertainty increased monotonically on moving away from the Dirichlet boundary, with the result that a point downstream of the shock had a higher density uncertainty as compared to a point upstream of the shock, even though they had nearly identical density gradient uncertainties. PDFs of the uncertainty fields from five thousand vector fields showed that IM and CS resulted in very similar uncertainties, and MC under-predicted the uncertainty as compared to the two methods.

A limitation of the proposed methodology is that bias uncertainties are not estimated, and as seen from the analysis with the synthetic images, there is a strong bias error in the density estimation. This is in addition to the bias uncertainties that also exist in the cross-correlation processing which are due to peak-locking and other processing based errors. Developing a similar formulation for the estimation and propagation of the bias uncertainties is still required. Another limitation is that the methodology does not account for covariances introduced between adjacent vectors due to the cross-correlation procedure. This is especially important in situations where window overlap is used in the processing, and is another avenue for future work on this topic. Finally, further work is required to compare these density uncertainty predictions to the measurement error for benchmark BOS experiments, especially for stronger density gradients that can lead to larger image distortions and a corresponding increase in the measurement error and uncertainty.

For complex flows where depth-averaging is not suitable, a volumetric measurement is required to estimate the three-dimensional density field [62]–[64], and in such a measurement the volumetric reconstruction will also have an effect on the uncertainty. First, calibration induced errors can introduce uncertainties in the reconstruction as shown by Bhattacharya et. al. for stereo-PIV measurements [45], and further, the existing uncertainties may be amplified by propagation through the chosen reconstruction algorithms. Therefore, the proposed methodology needs to be extended to account for these effects in volumetric measurements.

Overall, displacement uncertainty methods typically used for PIV experiments are also applicable to BOS data, and the displacement uncertainties can be propagated through the Poisson solver using a sparse linear operator to obtain the density uncertainties. Thus, the method proposed in this manuscript allows for instantaneous spatially resolved uncertainty quantification in density estimates from BOS measurements, and for use in CFD model validation and engineering design.

2.6 Acknowledgements

This material is based upon work supported by the U.S. Department of Energy, Office of Science, Office of Fusion Energy Sciences under Award Number DE-SC0018156. NSF provided support through 1706474.

2.7 References

[1] S. B. Dalziel, G. O. Hughes, and B. R. Sutherland, "Whole-field density measurements by 'synthetic schlieren,'" *Exp. Fluids*, vol. 28, no. 4, pp. 322–335, 2000.

[2] H. Richard and M. Raffel, "Principle and applications of the background oriented schlieren (BOS) method," *Meas. Sci. Technol.*, vol. 12, no. 9, pp. 1576–1585, 2001.

[3] G. Meier, "Computerized background-oriented schlieren," *Exp. Fluids*, vol. 33, no. 1, pp. 181–187, 2002.

[4] M. Raffel, H. Richard, and G. E. A. Meier, "On the applicability of background oriented optical tomography for large scale aerodynamic investigations," *Exp. Fluids*, vol. 28, no. 5, pp. 477–481, May 2000.

[5] L. K. Rajendran, S. P. M. Bane, and P. P. Vlachos, "Dot tracking methodology for background-oriented schlieren (BOS)," *Exp. Fluids*, vol. 60, no. 11, p. 162, Nov. 2019.

[6] B. Atcheson, W. Heidrich, and I. Ihrke, "An evaluation of optical flow algorithms for background oriented schlieren imaging," *Exp. Fluids*, vol. 46, no. 3, pp. 467–476, Mar. 2009.

[7] F. Moisy, M. Rabaud, and K. Salsac, "A synthetic Schlieren method for the measurement of the topography of a liquid interface," *Exp. Fluids*, vol. 46, no. 6, pp. 1021–1036, 2009.

[8] J. Kolaas, B. Hervold, K. Sveen, and A. Jensen, "Bichromatic synthetic schlieren applied to surface wave measurements," *Exp. Fluids*, vol. 59, no. 8, pp. 1–13, 2018.

[9] L. Venkatakrishnan and G. E. a. Meier, "Density measurements using the Background Oriented Schlieren technique," *Exp. Fluids*, vol. 37, no. 2, pp. 237–247, 2004.

[10] M. Raffel, "Background-oriented schlieren (BOS) techniques," *Exp. Fluids*, vol. 56, no. 3, pp. 1–17, 2015.

[11] L. Venkatakrishnan and P. Suriyanarayanan, "Density field of supersonic separated flow past an afterbody nozzle using tomographic reconstruction of BOS data," *Exp. Fluids*, vol. 47, no. 3, pp. 463–473, Sep. 2009.

[12] L. Venkatakrishnan, "Density Measurements in an Axisymmetric Underexpanded Jet by Background-Oriented Schlieren Technique," *AIAA J.*, vol. 43, no. 7, pp. 1574–1579, 2005.

[13] G. E. Elsinga, B. W. Van Oudheusden, F. Scarano, and D. W. Watt, "Assessment and application of quantitative schlieren methods: Calibrated color schlieren and background oriented schlieren," *Exp. Fluids*, vol. 36, no. 2, pp. 309–325, 2004.

[14] D. Ramanah, S. Raghunath, D. J. Mee, T. Rösgen, and P. A. Jacobs, "Background oriented schlieren for flow visualisation in hypersonic impulse facilities," *Shock Waves*, vol. 17, no. 1–2, pp. 65–70, 2007.

[15] T. Mizukaki, K. Wakabayashi, T. Matsumura, and K. Nakayama, “Background-oriented schlieren with natural background for quantitative visualization of open-air explosions,” *Shock Waves*, vol. 24, no. 1, pp. 69–78, 2014.

[16] T. Kirmse, J. Agocs, A. Schröder, M. J. Schramm, S. Karl, and K. Hannemann, “Application of particle image velocimetry and the background-oriented schlieren technique in the high-enthalpy shock tunnel Göttingen,” *Shock Waves*, vol. 21, no. 3, pp. 233–241, 2011.

[17] H. Richard, M. Raffel, M. Rein, J. Kompenhans, and G. E. A. Meier, “Demonstration of the applicability of a Background Oriented Schlieren (BOS) method,” in *Laser Techniques for Fluid Mechanics*, Berlin, Heidelberg: Springer Berlin Heidelberg, 2002, pp. 145–156.

[18] F. Sourgen, J. Haertig, and C. Rey, “Comparison Between Background Oriented Schlieren Measurements (BOS) and Numerical Simulations,” *24th AIAA Aerodyn. Meas. Technol. Gr. Test. Conf.*, vol. 2602, no. July, pp. 1–18, 2004.

[19] B. Singh, L. K. Rajendran, P. Gupta, C. Scalo, P. P. Vlachos, and S. P. M. Bane, “Experimental and Numerical Study of Flow Induced by Nanosecond Repetitively Pulsed Discharges,” *AIAA Scitech 2019 Forum*, no. January, pp. 1–15, 2019.

[20] O. K. Sommersel, D. Bjerketvedt, S. O. Christensen, O. Krest, and K. Vaagsaether, “Application of background oriented schlieren for quantitative measurements of shock waves from explosions,” in *Shock Waves*, 2008, vol. 18, no. 4, pp. 291–297.

[21] H. W. Coleman and W. G. Steele, *Experimentation, Validation, and Uncertainty Analysis for Engineers*. Hoboken,New Jersey: John Wiley & Sons, Inc., 2009.

[22] ISO, “Guide to the Expression of Uncertainty in Measurement,” Geneva, 1995.

[23] R. J. Adrian and J. Westerweel, *Particle image velocimetry*. Cambridge University Press, 2011.

[24] M. Raffel, C. E. Willert, S. T. Wereley, and J. Kompenhans, *Particle image velocimetry: a practical guide*. Springer, 2013.

[25] R. J. Adrian, “Twenty years of particle image velocimetry,” *Exp. Fluids*, vol. 39, no. 2, pp. 159–169, Jul. 2005.

[26] J. Westerweel, G. E. Elsinga, and R. J. Adrian, “Particle Image Velocimetry for Complex and Turbulent Flows,” *Annu. Rev. Fluid Mech.*, vol. 45, no. 1, pp. 409–436, Jan. 2013.

[27] K. T. Christensen and F. Scarano, “Uncertainty quantification in particle image velocimetry,” *Meas. Sci. Technol.*, vol. 26, no. 7, p. 070201, 2015.

[28] A. Sciacchitano, “Uncertainty quantification in particle image velocimetry,” *Meas. Sci. Technol.*, pp. 0–16, Apr. 2019.

[29] A. Sciacchitano *et al.*, “Collaborative framework for PIV uncertainty quantification: comparative assessment of methods,” *Meas. Sci. Technol.*, vol. 26, no. 7, p. 074004, Jul. 2015.

[30] A. Boomsma, S. Bhattacharya, D. Troolin, S. Pothos, and P. P. Vlachos, “A comparative experimental evaluation of uncertainty estimation methods for two-component PIV,” *Meas. Sci. Technol.*, vol. 27, no. 9, 2016.

[31] B. H. Timmins, B. W. Wilson, B. L. Smith, and P. P. Vlachos, “A method for automatic estimation of instantaneous local uncertainty in particle image velocimetry measurements,” *Exp. Fluids*, vol. 53, no. 4, pp. 1133–1147, 2012.

[32] J. J. Charonko and P. P. Vlachos, “Estimation of uncertainty bounds for individual particle image velocimetry measurements from cross-correlation peak ratio,” *Meas. Sci. Technol.*, vol. 24, no. 6, 2013.

[33] Z. Xue, J. J. Charonko, and P. P. Vlachos, “Particle image velocimetry correlation signal-to-noise ratio metrics and measurement uncertainty quantification,” *Meas. Sci. Technol.*, vol. 25, no. 11, p. 115301, Nov. 2014.

[34] Z. Xue, J. J. Charonko, and P. P. Vlachos, “Particle image pattern mutual information and uncertainty estimation for particle image velocimetry,” *Meas. Sci. Technol.*, vol. 26, no. 7, p. 074001, Jul. 2015.

[35] A. Sciacchitano, B. Wieneke, and F. Scarano, “PIV uncertainty quantification by image matching,” *Meas. Sci. Technol.*, vol. 24, no. 4, p. 045302, Apr. 2013.

[36] B. Wieneke, “PIV uncertainty quantification from correlation statistics,” *Meas. Sci. Technol.*, vol. 26, no. 7, p. 074002, Jul. 2015.

[37] S. Bhattacharya, J. J. Charonko, and P. P. Vlachos, “Particle image velocimetry (PIV) uncertainty quantification using moment of correlation (MC) plane,” *Meas. Sci. Technol.*, vol. 29, no. 11, 2018.

[38] F. Scarano and M. L. Riethmuller, “Advances in iterative multigrid PIV image processing,” *Exp. Fluids*, vol. 29, no. 7, pp. S051–S060, 2000.

[39] F. Scarano, “Iterative image deformation methods in PIV,” *Meas. Sci. Technol.*, vol. 13, no. 1, pp. R1–R19, 2002.

[40] M. P. Wernet, “Symmetric phase only filtering: a new paradigm for DPIV data processing,” *Meas. Sci. Technol.*, vol. 16, no. 3, pp. 601–618, Mar. 2005.

[41] A. C. Eckstein, J. Charonko, and P. P. Vlachos, “Phase correlation processing for DPIV measurements,” *Exp. Fluids*, vol. 45, no. 3, pp. 485–500, 2008.

[42] C. Knapp and G. Carter, “The generalized correlation method for estimation of time delay,” *IEEE Trans. Acoust.*, vol. 24, no. 4, pp. 320–327, Aug. 1976.

[43] B. M. Wilson and B. L. Smith, "Uncertainty on PIV mean and fluctuating velocity due to bias and random errors," *Meas. Sci. Technol.*, vol. 24, no. 3, p. 035302, Mar. 2013.

[44] A. Sciacchitano and B. Wieneke, "PIV uncertainty propagation," *Meas. Sci. Technol.*, vol. 27, no. 8, p. 084006, Aug. 2016.

[45] S. Bhattacharya, J. J. Charonko, and P. P. Vlachos, "Stereo-particle image velocimetry uncertainty quantification," *Meas. Sci. Technol.*, vol. 28, no. 1, p. 015301, Jan. 2017.

[46] I. Azijli, A. Sciacchitano, D. Ragni, A. Palha, and R. P. Dwight, "A posteriori uncertainty quantification of PIV-based pressure data," *Exp. Fluids*, vol. 57, no. 5, p. 72, May 2016.

[47] Z. Xue, J. J. Charonko, and P. P. Vlachos, "Particle image velocimetry correlation signal-to-noise ratio metrics and measurement uncertainty quantification," *Meas. Sci. Technol.*, vol. 25, no. 11, 2014.

[48] Z. Xue, J. J. Charonko, and P. P. Vlachos, "Particle image pattern mutual information and uncertainty estimation for particle image velocimetry," *Meas. Sci. Technol.*, vol. 26, no. 7, 2015.

[49] A. Sciacchitano, B. Wieneke, and F. Scarano, "PIV uncertainty quantification by image matching," *Meas. Sci. Technol.*, vol. 24, no. 4, 2013.

[50] B. Wieneke, "PIV uncertainty quantification from correlation statistics," *Meas. Sci. Technol.*, vol. 26, no. 7, 2015.

[51] S. Bhattacharya, J. J. Charonko, and P. P. Vlachos, "Particle Image Velocimetry (PIV) Uncertainty Quantification Using Moment of Correlation (MC) Plane," no. Mc.

[52] A. Sciacchitano *et al.*, "Collaborative framework for PIV uncertainty quantification: Comparative assessment of methods," *Meas. Sci. Technol.*, vol. 26, no. 7, 2015.

[53] C. J. Dasch, "One-dimensional tomography: a comparison of Abel, onion-peeling, and filtered backprojection methods.," *Appl. Opt.*, vol. 31, pp. 1146–1152, 1992.

[54] P. S. Kolhe and A. K. Agrawal, "Abel inversion of deflectometric data: comparison of accuracy and noise propagation of existing techniques.," *Appl. Opt.*, vol. 48, no. 20, pp. 3894–902, Jul. 2009.

[55] L. K. Rajendran, S. P. M. Bane, and P. P. Vlachos, "PIV/BOS synthetic image generation in variable density environments for error analysis and experiment design," *Meas. Sci. Technol.*, pp. 11–14, Apr. 2019.

[56] J. Westerweel, D. Dabiri, and M. Gharib, "The effect of a discrete window offset on the accuracy of cross-correlation analysis of digital PIV recordings," *Exp. Fluids*, vol. 23, no. 1, pp. 20–28, 1997.

[57] F. Scarano and M. L. Riethmuller, “Iterative multigrid approach in PIV image processing with discrete window offset,” *Exp. Fluids*, vol. 26, no. 6, pp. 513–523, 1999.

[58] L. Gui and S. T. Wereley, “A correlation-based continuous window-shift technique to reduce the peak-locking effect in digital PIV image evaluation,” *Exp. Fluids*, vol. 32, no. 4, pp. 506–517, 2002.

[59] A. C. Eckstein and P. P. Vlachos, “Assessment of advanced windowing techniques for digital particle image velocimetry (DPIV),” *Meas. Sci. Technol.*, vol. 20, no. 7, p. 075402, 2009.

[60] J. Westerweel and F. Scarano, “Universal outlier detection for PIV data,” *Exp. Fluids*, vol. 39, no. 6, pp. 1096–1100, 2005.

[61] R. Sibson, “A brief description of natural neighbor interpolation,” in *Interpolating Multivariate Data*, V. Barnett, Ed. Chichester: John Wiley, 1981, pp. 21–36.

[62] E. Goldhahn and J. Seume, “The background oriented schlieren technique: Sensitivity, accuracy, resolution and application to a three-dimensional density field,” *Exp. Fluids*, vol. 43, no. 2–3, pp. 241–249, 2007.

[63] U. Hartmann and J. R. Seume, “Combining ART and FBP for improved fidelity of tomographic BOS,” *Meas. Sci. Technol.*, vol. 27, no. 9, p. 097001, Sep. 2016.

[64] K. Berger, I. Ihrke, B. Atcheson, W. Heidrich, and M. Magnor, “Tomographic 4D Reconstruction of Gas Flows in the Presence of Occluders,” *Vision, Model. Vis. Work.*, pp. 1–8, 2009.

3. META-UNCERTAINTY FOR CORRELATION-BASED DISPLACEMENT ESTIMATION

Lalit K. Rajendran[1], Sayantan Bhattacharya[2], Sally P. M. Bane[1] and Pavlos P. Vlachos[2]
[1] Purdue University, School of Aeronautics and Astronautics, West Lafayette, USA.
[2] Purdue University, School of Mechanical Engineering, West Lafayette, USA.
This chapter has been accepted for publication at Measurement Science and Technology, and reproduced here with permission. DOI: https://doi.org/10.1088/1361-6501/abf44f.

Abstract

Uncertainty quantification for Particle Image Velocimetry (PIV) is critical for comparing experimentally measured flow fields with Computational Fluid Dynamics (CFD) results, and model design and validation. However, PIV features a complex measurement chain with coupled, non-linear error sources, and quantifying the uncertainty is challenging. Multiple assessments show that none of the current methods can reliably measure the actual uncertainty across a wide range of experiments, and estimates can vary. Because the current methods differ in assumptions regarding the measurement process and calculation procedures, it is not clear which method is best to use for an experiment where the error distribution is unknown.

To address this issue, we propose a method to estimate an uncertainty method's sensitivity and reliability, termed the Meta-Uncertainty. The novel approach is automated, local, and instantaneous, and based on perturbation of the recorded particle images. We developed an image perturbation scheme based on adding random unmatched particles to the interrogation window pair considering the signal-to-noise (SNR) of the correlation plane. Each uncertainty scheme's response to several trials of random particle addition is used to estimate a reliability metric, defined as the rate of change of the inter-quartile range (IQR) of the uncertainties with increasing levels of particle addition. We also propose applying the meta-uncertainty as a weighting metric to combine uncertainty estimates from individual schemes, based on ideas from the consensus forecasting literature. We use planar and stereo PIV measurements across a range of canonical flows to assess the performance of the uncertainty schemes. Further, a novel method is introduced to assess an uncertainty scheme's performance based on a quantile comparison of the error and uncertainty distributions, generalizing the current method of comparing the RMS of the two distributions. The results show that the combined uncertainty method outperforms the individual methods, and this

work establishes the meta-uncertainty as a useful reliability assessment tool for PIV uncertainty quantification.

Nomenclature

ϵ	Error	n	Individual method index
Δx	Displacement along the x-direction	N	Number of individual methods
σ	Standard deviation	$\mathcal{N}$	Gaussian/normal distribution
$\sigma_{\Delta x}$	Uncertainty in x displacement	U	Uncertainty
σ_{rat}	Ratio of uncertainties of perturbed and original images	x	Horizontal co-ordinate
f	Probability density function (PDF)	y	Vertical co-ordinate
m	Rate of change of uncertainty ratio with particle addition	w	Weight

3.1 Introduction

Over the past decade, there has been increasing effort in Particle Image Velocimetry (PIV) to develop a-posteriori uncertainty quantification methodologies for local and instantaneous displacement measurements [1]. These efforts aim to provide uncertainties to PIV measurements that can be used for comparison to CFD results and for model design and validation. Parallel efforts included methods for propagating these uncertainties to derived quantities such as turbulence statistics [2], velocity derivatives [3], and pressure [4, 5], as well as to stereo PIV [6] and volumetric PTV [7] measurements. There has also been recent progress in uncertainty quantification in Background Oriented Schlieren (BOS), an image-based density measurement technique. Developments include estimation of displacement uncertainty from dot tracking based processing [8, 9], propagation of both tracking/cross-correlation based displacement uncertainties through the density integration chain [10], and utilizing the uncertainties to improve the density integration process by weighted least squares minimization [11].

The measurement uncertainty of a quantity (e.g., velocity in PIV) represents the interval expected to contain the true value. This uncertainty depends on all the factors in the overall measurement chain. Since PIV involves a complex measurement chain from image recording through processing and post-processing, the final measurement can suffer from a multitude of error sources such as particle size, seeding density, shear, noise, out-of-plane motion, and processing algorithms, to name a few [12]. These error sources can combine in a coupled and non-linear manner to affect the final measurement uncertainty, and also depend on the final quantity of interest, whether the displacement, shear, pressure, or density. Even just for displacement uncertainty, while there have been many methods proposed in the literature, none perform well under all situations.

PIV displacement uncertainty methods are commonly classified into *direct* and *indirect* methods. Indirect methods predict the displacement uncertainty by calibrating the variation of uncertainty to various image parameters (such as particle size, density, shear, noise) and signal-to-noise ratio metrics of the cross-correlation plane (such as the Peak to Peak Ratio (PPR), Mutual Information (MI) and others [13–15]). Monte-Carlo simulations with synthetic images are used to obtain the calibration [13–16]. The performance of all indirect methods relies on the calibration process, which must be accurate and reflect all possible experimental scenarios in a typical measurement.

Direct methods estimate the uncertainty directly based on image or correlation plane properties without calibration. Presently, three direct methods are available to estimate the displacement uncertainty—Image Matching (IM) [17], Correlation Statistics (CS) [18], and Moment of Correlation (MC) [19]. In brief, IM or particle disparity (PD) proposed by Sciacchitano *et al.* [17] estimates the uncertainty in the displacement using a statistical analysis of the disparity between the measured positions of particles in the two frames after a converged iterative deformation interrogation procedure. The performance of this method is sensitive to the accuracy of the particle position estimation and deteriorates with increasing seeding density, noise, and out-of-plane motion. CS, proposed by Wieneke [18], estimates the uncertainty again using the image disparity but at a pixel level. The correlation peak's asymmetry at the end of a converged window deformation procedure is used to measure the correlation error, and propagating the standard deviation of this error through the sub-pixel estimator provides the uncertainty. The CS method relies on the correlation plane statistics and performs better at higher seeding densities and larger interrogation windows. MC, proposed by Bhattacharya *et al.* [19], predicts the uncertainty by estimating the second-order moment of the PDF of displacements contributing to the cross-correlation plane. The PDF is estimated as the generalized cross-correlation (GCC) from the inverse Fourier transform of the phase of the complex cross-correlation plane [20–22], followed by Gaussian filtering, gradient correction, and scaling by the effective number of particles contributing to the cross-correlation. This method also works better with high seeding densities and large interrogation windows, and small interrogation windows can lead to an over-prediction of the uncertainty.

However, multiple previous works show that none of the PIV uncertainty quantification methods perform well under all situations [23, 24]. While the direct methods are sensitive to elemental error sources [23], they can under-predict the random error [24]. In addition, direct methods can predict different uncertainties for the same flow field [10, 19], and as a result, no PIV uncertainty method is universally consistent and robust. Further, it is often impossible to choose the correct estimate in an experiment because the actual random error is unknown, and these potentially incorrect estimates in displacement uncertainty can propagate to derived quantities with detrimental implications for further analysis. Therefore, it is not clear which method to use for an experiment where the error is unknown.

A similar problem also exists in the consensus forecasting literature when assessing the risk/reliability associated with competing models that predict a future quantity based on incomplete information in the present [25–27]. In these applications, the variance of the fluctuations of each model prediction provides the "risk"/"volatility". In this work, we adapt this idea to the problem of PIV uncertainty quantification and develop a method to estimate the robustness/sensitivity of each uncertainty method in a local, instantaneous, and automated manner. We base the method on perturbing the particle images in an interrogation window pair and assessing the variation of the uncertainty estimates to this perturbation. The perturbation should be large enough to provide a variation of the displacement uncertainty *without* significantly affecting the cross-correlation plane and displacement estimate on which we are trying to calculate the uncertainty bounds. We assess this using signal-to-noise ratio metrics of the cross-correlation, such as the peak ratio and mutual information. By repeating the random particle addition over several trials and over different addition amounts, we quantify the response of each uncertainty scheme to the image perturbation. Finally, we use descriptive statistics of the distribution, such as the inter-quartile range (IQR) and the rate of change of the IQR with increasing particle addition, to estimate a reliability metric (the *meta-uncertainty)* for each uncertainty scheme. A broader distribution of uncertainty estimates and a higher meta-uncertainty will characterize schemes that are more sensitive to the perturbations.

Finally, we apply the meta-uncertainty to develop a new uncertainty quantification scheme for PIV that combines the estimates from the individual schemes weighted by the inverse of their meta uncertainty. Similar to consensus forecasting, where the aim is to combine estimates from different models based on a meta-analysis of the individual models [26–28], this approach aims to fuse the prediction from multiple uncertainty models into a new, more robust, and reliable estimate. The hypothesis is that different models utilize different aspects of the information associated with the measurement, and therefore their combination provides a better estimate than each individual model. In the present context, the forecast quantity is the displacement uncertainty, the individual models are the uncertainty quantification methods, and the meta-uncertainty provides the weights for each model. While the proposed framework is general and can apply to many individual uncertainty schemes, here, we will consider only the three *direct* displacement uncertainty schemes—Image Matching (IM) [17], Correlation Statistics (CS) [18], and Moment of Correlation (MC) [19]. We assess the performance of the meta-uncertainty estimation method and the combined uncertainty scheme with synthetic and experimental planar and stereo PIV images.

3.2 Methodology

Figure 3.1 shows the overall meta-uncertainty based combination method whiFigure 3.1ch consists of three major steps: 1) the estimation of the meta-uncertainty for each uncertainty method, 2) calculation of weights based on the response function, and 3) calculating the combined uncertainty. The following sections detail the procedure for each step.

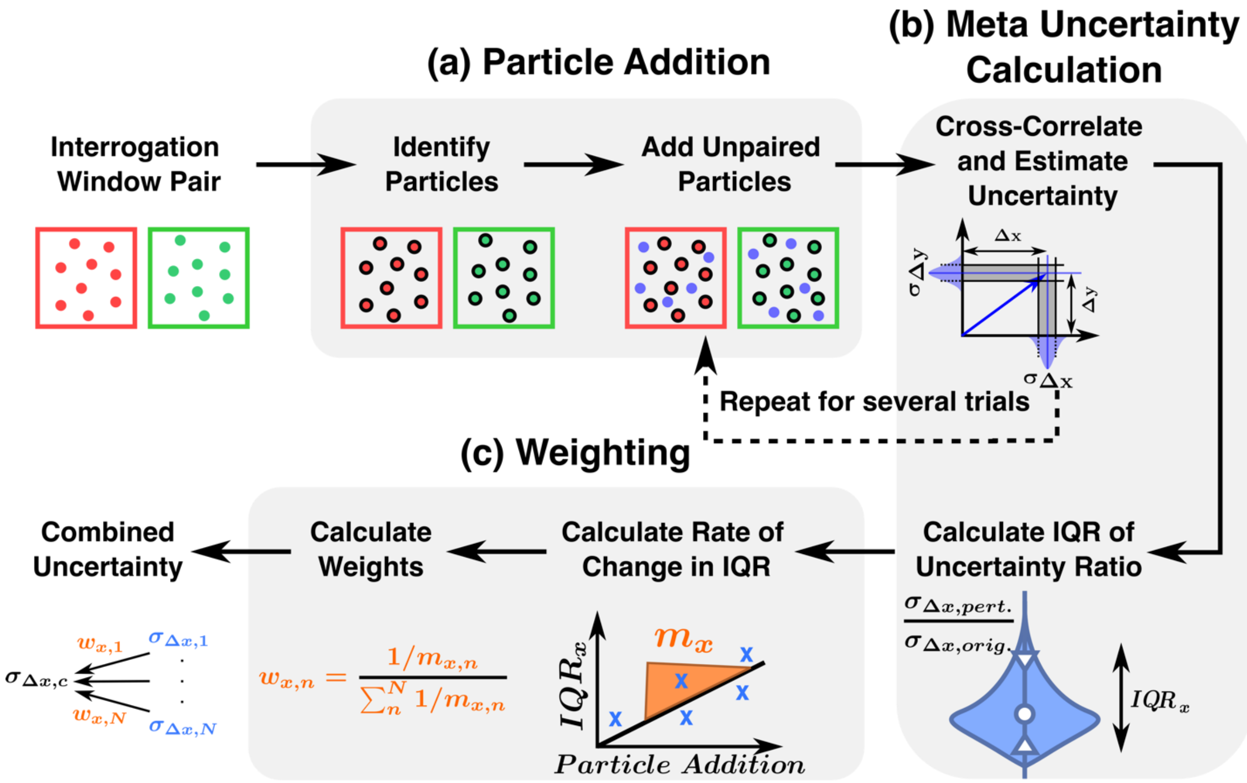

Figure 3.1. Illustration of the meta-uncertainty based combination methodology.

The meta-uncertainty is based on the uncertainty scheme's PDF and describes its response to a perturbation in the input intensity distribution. Since the PIV uncertainty methods rarely have a closed-form expression, we estimate the PDF using a Monte-Carlo simulation procedure. Further, to estimate the *true/parent* PDF requires the knowledge of all inputs—a set of all possible PIV images—which is not possible. Therefore, we perturb the intensity distributions of the interrogation window pair for several trials to generate a local population of particle image pairs and estimate the corresponding uncertainty.

For the image perturbation procedure to be valid, it must be able to provide a variation of the uncertainty estimates without an appreciable change in the underlying signal-to-noise ratio (SNR) metrics of the cross-correlation estimator (such as the Peak to Peak Ratio (PPR), Mutual Information (MI) and others [13–15]) whose uncertainty we are trying to estimate. There are several potential methods to perturb the particle images. We adopt a method of adding random and unpaired particles to the interrogation window pair. Analysis with synthetic and experimental images showed that this method best accomplished perturbing the images with a negligible change in the signal-to-noise ratio metrics.

a) Particle Perturbation

To perform the perturbation, we first identify all the particles on the image using identification and centroid-estimation methods commonly used in Particle Tracking Velocimetry [29, 30]. Following this, we add a set of unpaired particles to the interrogation window pair as shown in Figure 3.1 (a), with the number of unpaired particles specified as a fraction of the seeding density, and the peak intensity and diameter set to be the average of the already identified particles. Figure 3.2 shows a sample particle image pair with the perturbation.

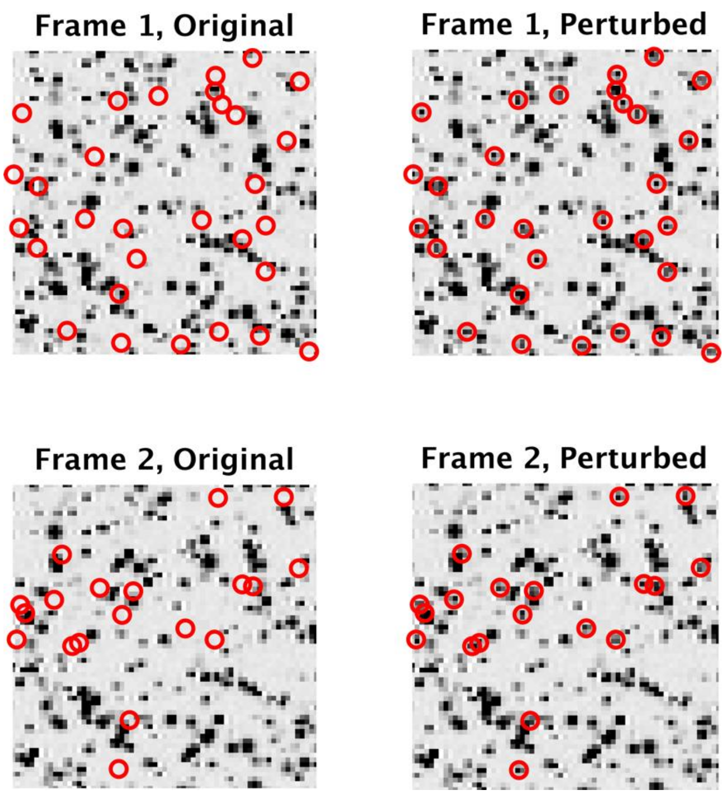

Figure 3.2 Example of a perturbed image pair, with the red circles indicating the location of the added particles.

b) Meta uncertainty calculation

The perturbed window pair is then cross-correlated, and the uncertainty is estimated using all three individual methods as shown in Figure 3.1 (b). We repeat this procedure for several trials to build a PDF of the *ratio* of the perturbed to original uncertainties for each estimator ($\sigma_{rat,\Delta x,n} = \sigma_{\Delta x,n,pert.}/\sigma_{\Delta x,n,orig.}$). Figure 3.3 shows sample distributions of the uncertainty schemes and statistics such as the median and quartilesFigure 3.3. Each level of particle addition results in a *distribution* of uncertainties due to the perturbation. These distributions become wider with increasing level of particle addition at a different rate of increase for each method. The width of the distribution represents the sensitivity of each scheme to particle perturbation, and therefore a scheme with a wider PDF is less reliable compared to a scheme with a narrower PDF. However, the response and relative sensitivity of each scheme will vary with the local image and flow conditions.

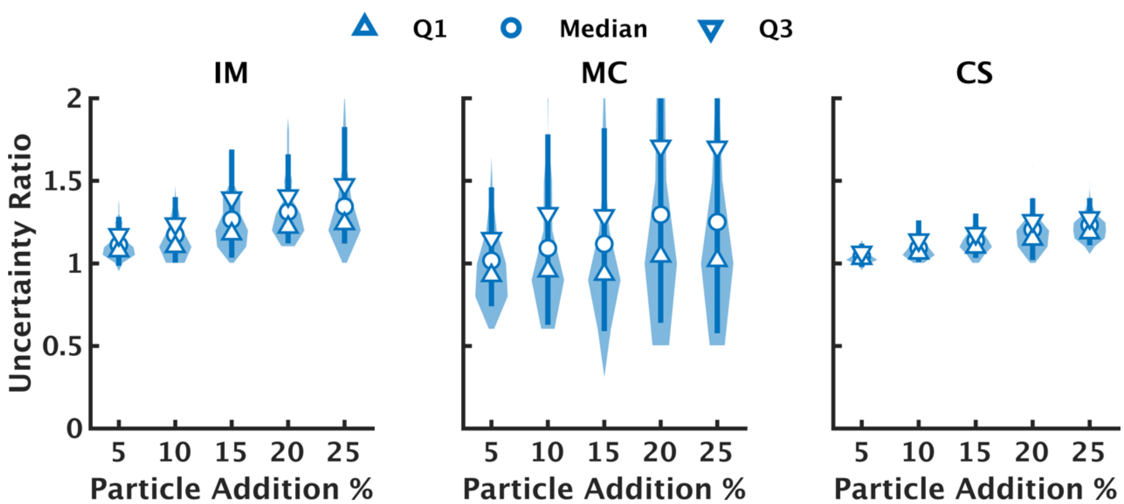

Figure 3.3. Effect of particle addition on the PDF of the ratio of resampled to original uncertainties.

c) Weight calculation

We calculate the IQR for each particle perturbation level from the distributions, and the rate of change of this IQR with particle perturbation (from a linear regression as shown in Figure 3.1 (c)) provides the weight for each scheme. The IQR is used in place of the RMS because it is less sensitive to outliers. Equation (1) provides the weight of the x component(22), with a similar equation for the y component. The slope (and the weight) calculation depends on the number of points used for the regression and the individual scheme's response. Figure 3.4 shows a sample result for the IQR variation with five particle addition levels and the corresponding weightsFigure 3.4. These results are consistent with Figure 3.3 with MC showing the highest rate of increase and therefore assigned the lowest weight, with CS showing the lowest rate of increase and therefore assigned the highest weight. This weight is essentially a local and instantaneous reliability assessment metric for each uncertainty scheme, and the proposed method allows for an automated way to estimate this metric for arbitrary particle images. The relative weights for each scheme can vary across grid points within the same flow field, and across flow-fields.

$$w_x = \left|\left(\frac{\Delta\, IQR_x}{\Delta\, particle\ \%}\right)\right|^{-1} \tag{22}$$

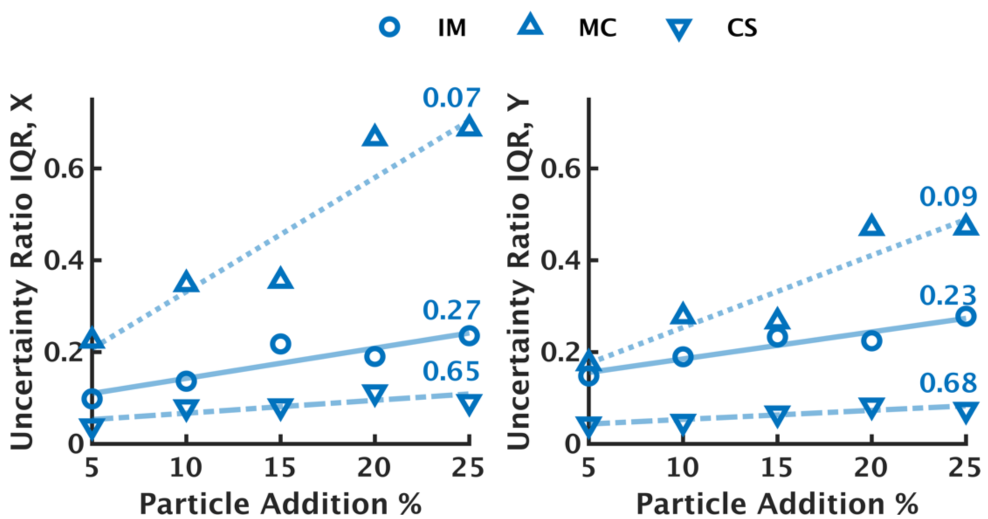

Figure 3.4. Variation of the IQR of uncertainty ratios with particle addition percentage for a grid point, with the corresponding weights obtained from the straight line fit.

d) Combined uncertainty calculation

Finally, we calculate the combined uncertainty as the weighted average of the individual uncertainty schemes as shown in Figure 3.1 (d),

$$\sigma_{x,comb} = \sum_{n=1}^{N} w_{x,n}\sigma_{x,n} \tag{23}$$

for the x-component where σ_x represents the individual uncertainty, w_x represents the corresponding weights, n represents the subscript for each method, and N represents the total number of methods (here, N = 3). In the next section, we will assess the method's performance with synthetic and experimental images from planar and stereo PIV experiments.

3.3 Results

3.3.1 Planar PIV

Planar PIV measurements from several canonical flows are used to test the uncertainty quantification methods over a wide variation of image and flow conditions. The datasets used are: a turbulent boundary layer (PIV Challenge 2003B) [31], a laminar separation bubble (PIV Challenge 2005B) [32], laminar stagnation flow [33], a vortex ring (fourth PIV Challenge) [34], and the unsteady inviscid core of a jet [23]. For each dataset, we processed the images with two processing routines (WS1 and WS2 as listed in Table 3.1) to provide a further variation in the testing, using the open-source PIV code PRANA [35, 36]. Figure 3.5 shows the displacement contours from all flow fields, and foFigure 3.5 each case, the error analysis used a true solution, based on details from the respective publications.

Table 3.1. Summary of processing parameters for all datasets.

	Turbulent Boundary Layer (TBL)	**Laminar separation bubble (LSB)**	**Stagnation flow (SF)**	**Vortex ring (VR)**	**Jet flow (JF)**
WS 1 (% overlap, No. of passes)	64 × 64 (75%, 2) (87.5%, 2)	64 × 64 (75%, 4)	64 × 64 (75%, 4)	64 × 64 (75%, 1) (87.5%, 3)	32 × 32 (87.5%, 4)
WS 2 (% overlap, No. of passes)	64 × 64 (87.5%, 1) 32 × 32 (75%, 3)	64 × 64 (75%, 1) 32 × 32 (50%, 3)	64 × 64 (75%, 1) 32 × 32 (50%, 3)	64 × 64 (87.5%, 1) 32 × 32 (75%, 3)	32 × 32 (75%, 1) 16 × 16 (75%, 3)

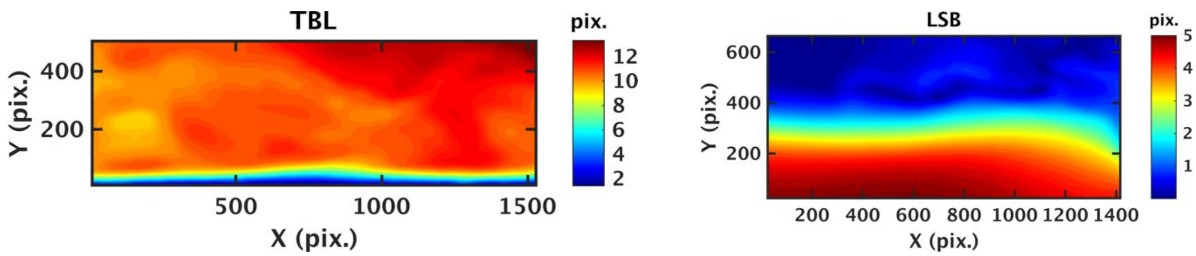

(a) (b)

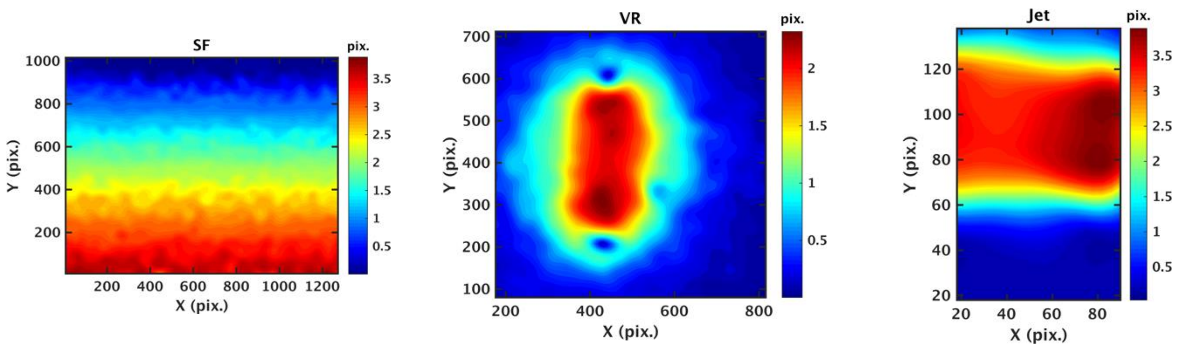

(c) (d) (e)

Figure 3.5. Datasets used for assessment on planar PIV images. (a) Turbulent boundary layer [31], (b) laminar separation bubble [32], (c) laminar stagnation flow [33], (d) vortex ring [34], and (e) jet flow [23].

We test the combination framework shown on the datasets using a Monte-Carlo simulation by randomly choosing a dataset and a processing setting, a snapshot within the dataset, and a grid point within the snapshot. For the chosen grid point, particle addition is used to calculate the meta-uncertainty, and the individual uncertainties are combined using a weighted average using the procedure shown in Figure 3.1. Particle addition was performed for five levels of the seeding density from 5 to 25% and over 100 trials for each perturbation level (as shown in Figure 3.3 and Figure 3.4). This procedure is repeated for 1000 grid points for each dataset and processing setting, and the errors and uncertainties across all datasets (10,000 grid points in total) are merged to calculate the corresponding statistics. This section discusses the merged statistics, and the Appendix contains the individual dataset results.

Figure 3.6 shows the PDFs of the error and uncertainty distributionsFigure 3.6 in the form of violin plots, with the individual schemes in blue, the error in black, and the combined uncertainty scheme in orange. Also shown are the statistics such as the median (circles), quartiles (triangles), and the root mean square (RMS)(straight line) of each distribution. Sciacchitano et al.

[23] showed that when the error distribution for each grid point is modeled as a zero-mean Gaussian random variable with the standard deviation representing the local uncertainty, the RMS of a mixture of these error distributions should match the RMS of the corresponding uncertainty distributions. For these results, the RMS of the error distribution is 0.08 pix., with the combined uncertainty scheme predicting an RMS of 0.07 pix., while the RMS of the individual uncertainty schemes being 0.05 pix. for IM, 0.06 pix. for MC, and 0.1 pix. for CS. Therefore, the combined scheme provides the best estimate of the RMS error and can compensate for the under-prediction by IM and MC and the over-prediction by CS. However, there is still a 0.01 pix. discrepancy between the RMS estimates of the error and the combined scheme, indicating that there is room for further improvement of the method.

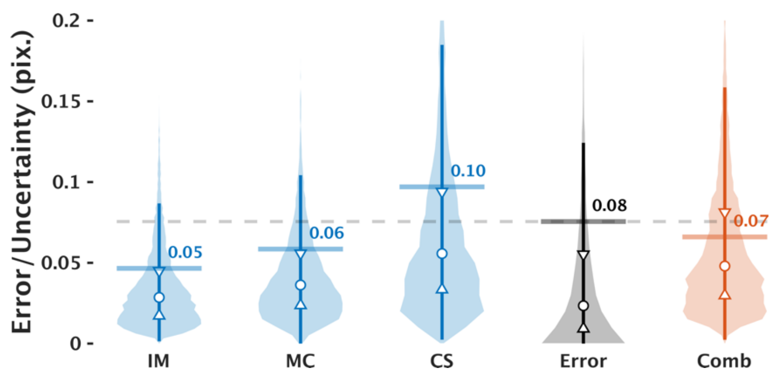

Figure 3.6. PDFs of the error and the individual and combined uncertainty estimates for consolidated results from all datasets.

The PDF of weights assigned to each individual scheme are shown in Figure 3.7 with the individual schemes in blue, and the black dashed line represents the case when all schemes are equally weighted. CS is assigned the highest weights for most cases, followed by IM, and then by MC, consistent with the sample result shown in Figure 3.4. However, even though CS is assigned a higher weight and over-predicts the RMS of the error, the combined effect of IM and MC, which under-predict the error, brings down the RMS of the combined scheme to be close to the RMS of the error. This highlights the advantage of the meta-model as even if one uncertainty scheme (CS) is more robust to perturbations in the correlation plane SNR and hence has a higher weight, the method can compensate with the weighting of other schemes. Finally, the weight distributions are broad, denoting that there are several grid points for which CS could be assigned a lower weight than either IM and MC. Therefore, the meta-uncertainty calculation is also able to capture the variation in the image and flow conditions across the datasets.

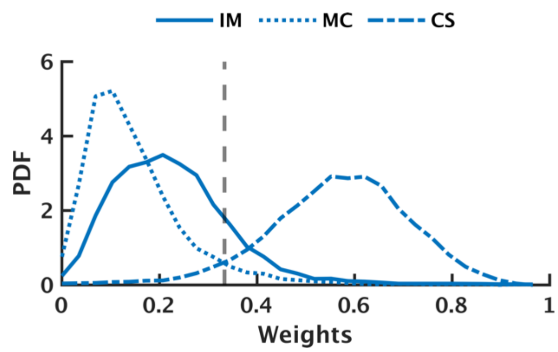

Figure 3.7. Distribution of weights assigned to the individual uncertainty schemes across all the datasets. The grey dashed line represents a case with equal weighting.

We also introduce a new method to compare the error and uncertainty distributions, based on a quantile-quantile comparison of the error and uncertainty distributions. This is a generalization of the method proposed by Sciacchitano et al. [23] for comparing the RMS to address the sensitivity of the RMS calculations to outliers. Consider a set of error measurements ϵ_i , where i represents the grid point under consideration with each error drawn from a corresponding distribution f_{ϵ_i}. Also, let the distribution of all the error measurements be f_ϵ. For each error measurement, we have an estimate of the uncertainty $U_{n,i}$ where n represents an uncertainty method. This uncertainty measurement represents the standard deviation of the error distribution $f_{\hat{\epsilon}_{n,i}}$, with $\hat{\epsilon}_{n,i}$ representing the *estimated* error. Finally, we can also define a combined distribution of each uncertainty scheme's estimated errors as $f_{\hat{\epsilon}_n}$. Our aim then is to compare the distributions of the *true* error distribution, f_ϵ, with that of the *estimated* error distribution, $f_{\hat{\epsilon}_{n,}}$ for each uncertainty scheme. To enable this comparison, we need a model for the individual, estimated, error distributions $f_{\hat{\epsilon}_{n,i}}$. Following the analysis of Sciacchitano et al. [23], if we assume this distribution to be a zero-mean Gaussian random variable, ($f_{\hat{\epsilon}_{n,i}} = \mathcal{N}(0, U_{n,i})$ then the *overall* distribution of the *estimated* error becomes the sum of these individual distributions,

$$f_{\hat{\epsilon}_n} = \sum_i f_{\hat{\epsilon}_{n,i}} = \sum_i \mathcal{N}\left(0, U_{n,i}\right) \ . \tag{24}$$

If the uncertainty estimate $U_{n,i}$ is correct, then the RMS of the above distribution must equal that of the error distribution, consistent with the previous result of Sciacchitano et al. [23]. Therefore, in this work, we compare the *distributions* instead of the RMS values for a more rigorous comparison and to reduce the effect of outliers.

The following procedure is used to estimate $f_{\hat{\epsilon}_n}$. For each grid point and uncertainty method $U_{n,i}$, we draw several (here 1000) random values of $\hat{\epsilon}_{n,i}$ from the corresponding normal distribution. These estimated error values from all grid points provide a pdf of the estimated error distribution $f_{\hat{\epsilon}_n}$. Then the true and estimated error distribution are compared using a quantile-quantile plot.

The results are shown in Figure 3.8, where the x-axis represents the quantiles of f_{ϵ} and the y-axis represents the quantiles of $f_{\hat{\epsilon}_n}$, with each curve corresponding to an uncertainty scheme, and the black line representing the 1:1 variation. The orange curve corresponding to the combined scheme is overall closest to the black line, showing that the combined uncertainty scheme best approximates the true error distributionFigure 3.6.

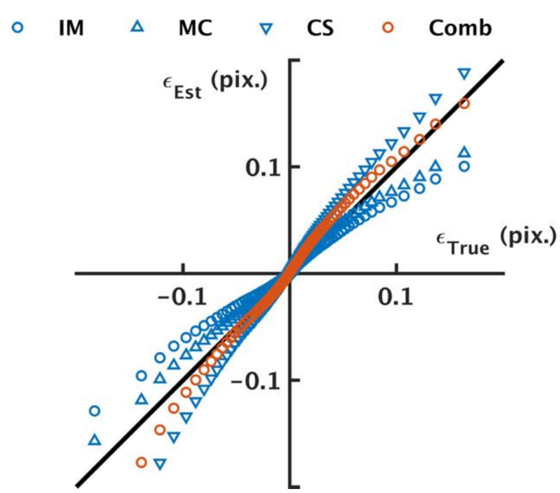

Figure 3.8. Quantile-quantile comparison of the true and estimated error distributions.

To complement the statistical analysis, we investigate the variation of the RMS error and uncertainty as functions of the element error sources such as fractional displacement and shear [16, 37]. To perform the comparison, we bin the errors and uncertainties based on their corresponding values of the displacement and shear, as estimated from the *true solution*. Then we calculate the bin-wise RMS of the error and uncertainties to caFigure 3.9 the variation of these statistics with the elemental error sources. Figure 3.9 shows these results, along with the number of measurements corresponding to each bin. The results show that 1) the errors/uncertainties increase with fractional displacement and (to a lesser extent) with shear, which is consistent with PIV theory [38–40], and 2) the combined scheme provides an RMS uncertainty that is, on average, the closest to the RMS error. However, MC performs better for low values of the velocity gradients, since the large uncertainties predicted by CS for these measurements shift the combined estimates upward.

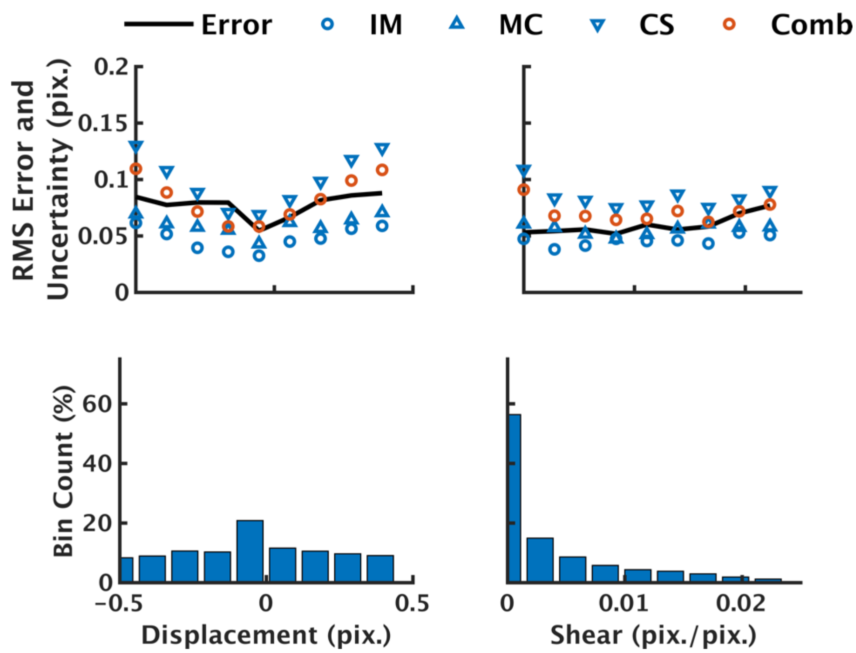

Figure 3.9. Variation of the RMS error and uncertainty as a function of elemental error sources such as displacement and shear, along with the corresponding bin count.

In summary, the analysis on planar PIV datasets showed that the combined uncertainty scheme based on the meta-uncertainty better represented the error distribution in terms of the RMS, quantiles, and the effect of error sources such as fractional displacement and shear. In the next section, we demonstrate the performance of the method for Stereo PIV images of a vortex ring.

3.3.2 Stereo PIV

The performance of the meta-uncertainty-based framework is also tested with Stereo PIV images by utilizing the uncertainty quantification methodology introduced by Bhattacharya et al. [6]. The method propagates the planar PIV uncertainties for each camera through the stereo-reconstruction process, accounting for uncertainties in the mapping function coefficients from the self-calibration procedure [41]. The analysis here uses the vortex ring dataset from Case E of the 4th PIV Challenge [34] (center and left cameras), similar to Bhattacharya et al. [6]. Figure 3.10 shows displacement contours for the three displacement components, with 50 snapshots used for the analysis.

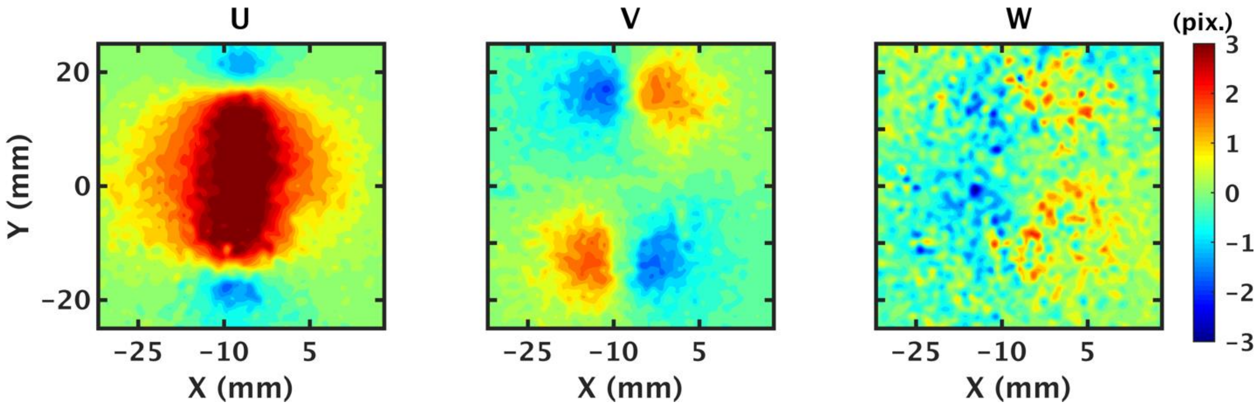

Figure 3.10. Spatial variation of displacement components for the stereo PIV dataset.

We assess the uncertainty schemes using the Monte-Carlo procedure detailed before, with the additional step of propagating the perturbed planar uncertainties through the stereo-reconstruction procedure to calculate the corresponding *stereo* uncertainties, the IQR and the weights. Therefore, the full measurement chain was used to calculate the meta and combined uncertainties.

Figure 3.11 shows the distribution of weights, errors, and uncertainties, and Figure 11Figure 3.11Figure 3.11(a) is consistent with the planar results, with CS being assigned the highest weight, followed by IM and MC. Further, the relative distribution of the weights is nearly identical for the three displacement components. From the error and uncertainty distributions shown in Figure 3.11(b), we see that the RMS of the combined uncertainty method is again the closest to the RMS error for the in-plane component U and V, similar to the planar data, and slightly over-predicts the RMS for the out-of-plane component W. This over-prediction (~ 0.1 pix.) is because of the over-prediction in the CS estimates of the uncertainty.

Finally, the quantile-quantile plots of the true and estimated error distributions in Figure 3.11(c) show that the combined uncertainty best approximates the true error distribution for the in-plane displacement components, while IM and MC perform better for the out-of-plane components.

The deviation of the combined uncertainty closely follows that of the CS curve because of the high weights assigned to CS. Therefore, in situations without an obvious choice for the best individual scheme, the combined scheme offers minor performance improvement. However, the performance of the individual schemes varies for the vast majority of the experiments, and when the error distribution is not available, it is impossible to guess the best method. Therefore, the combined method offers the most robust estimate of the uncertainty for a general experiment without a true solution. Overall, these results establish that the meta-uncertainty based combination framework also performs well for Stereo PIV measurements.

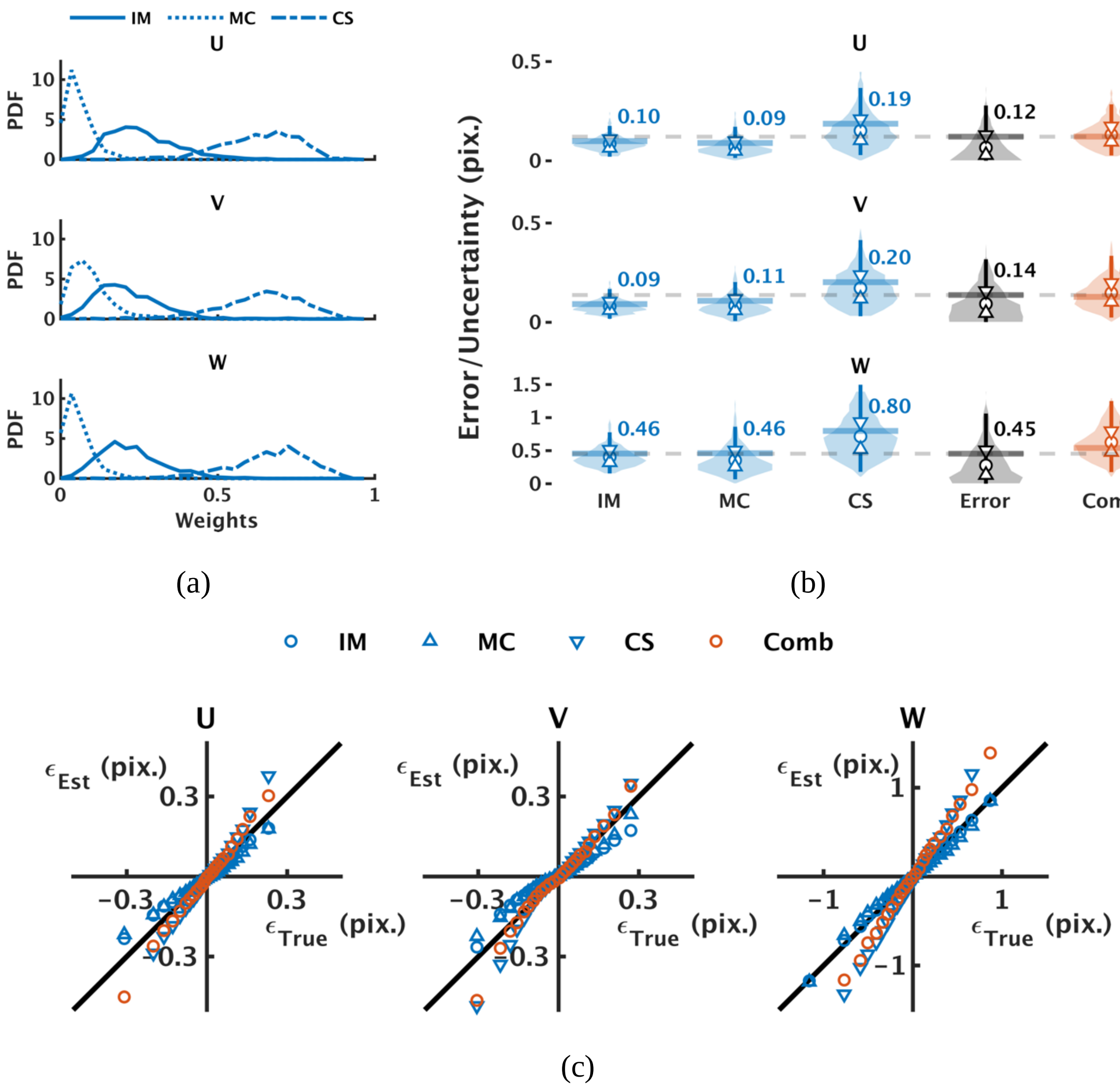

Figure 3.11. Results of applying the meta-uncertainty model to stereo PIV images. (a) PDF of weights, (b) rror and uncertainty distributions, and (c) Quantile-quantile comparison of the true and estimated error.

3.4 Summary and Conclusions

This work introduced a reliability metric of PIV uncertainty quantification methods termed the *meta-uncertainty* and an automated, local, and instantaneous method for its estimation. The meta-uncertainty describes the sensitivity of an uncertainty quantification method to perturbation in the input images, with a more sensitive scheme possessing a higher meta-uncertainty and lower reliability. Random/unpaired particles are added to perturb the images and estimates the uncertainty using each method over several trials and different particle addition levels. The PDF of the uncertainty provides a statistical measure of the response function, and the rate of change of the inter-quartile range (IQR) of the individual uncertainty schemes with particle addition provides the reliability metric.

In addition, this work also introduced a framework for combining individual uncertainty estimates based on the meta-uncertainty, similar to consensus forecasting. Since the uncertainty estimation methods differ in their use of information regarding the displacement estimation process, we hypothesized that combining the individual estimates should provide a better estimate of the uncertainty. The individual estimates were combined using a weighted average, with the weights based on the inverse of the rate of change of IQR, with a more sensitive/less reliable scheme assigned a lower weight.

Both the meta-uncertainty estimation and the combination framework were tested with the direct uncertainty methods - Image Matching (IM), Moment of Correlation (MC), and Correlation Statistics (CS) - with planar and stereo PIV images of several canonical flows, which offer a range of error and uncertainty sources. The planar PIV dataset included a turbulent boundary layer, laminar separation bubble, laminar stagnation flow, vortex ring, and jet flow, two processing settings for each flow field, and the stereo PIV dataset used was a vortex ring. We calculated the individual and combined uncertainties for grid points randomly sampled from these datasets, and results showed that the combined uncertainty best represented the true error distribution in terms of the overall RMS and the variation of RMS with error sources such as displacement and shear.

Further, a new method was introduced to compare the error and uncertainty estimates by generalizing the RMS comparison method of Sciacchitano et al. [23] to quantiles of the error and uncertainty distribution for a more rigorous comparison that is less sensitive to outliers. These results also showed that the error distribution based on the combined method predicts the true error distribution better than the individual uncertainty methods. For the stereo PIV dataset, the meta-uncertainty based combined method showed the best performance for the in-plane components, with a slight over-prediction in the RMS error for the out-of-plane component. However, since an individual uncertainty schemes performance varies significantly for different experiments, the combined method likely provides the best potential estimate of the uncertainty for a general experiment.

The major limitation of the method is the computational cost involved in estimating the meta-uncertainty with approximately 1000 perturbation trials performed for each grid point and uncertainty scheme. Therefore, future work could reduce this computational cost by developing approximate theoretical models of the individual schemes' response functions to accelerate the computations. Machine learning based neural-network models can also improve the combination framework. Finally, the meta-uncertainty can also improve the individual schemes themselves by analyzing their response to particle perturbations. In conclusion, this paper establishes the meta-uncertainty as a useful reliability assessment tool for PIV uncertainty quantification and the combination framework as a successful estimator of the uncertainty for cross-correlation PIV processing, with potential applications to uncertainty propagation, de-noising, and other post-processing routines.

3.5 Acknowledgment

The US Department of Energy, Office of Science, Office of Fusion Energy Sciences supported this work under Award Number DE-SC0018156, and NSF provided support through 1706474.

3.6 References

1. Sciacchitano A (2019) Uncertainty quantification in particle image velocimetry. *Measurement Science and Technology*, 30(9):092001. https://doi.org/10.1088/1361-6501/ab1db8

2. Wilson BM, Smith BL (2013) Uncertainty on PIV mean and fluctuating velocity due to bias and random errors. *Measurement Science and Technology*, 24(3):035302. https://doi.org/10.1088/0957-0233/24/3/035302

3. Sciacchitano A, Wieneke B (2016) PIV uncertainty propagation. *Measurement Science and Technology*, 27(8):084006. https://doi.org/10.1088/0957-0233/27/8/084006

4. Azijli I, Sciacchitano A, Ragni D, Palha A, Dwight RP (2016) A posteriori uncertainty quantification of PIV-based pressure data. *Experiments in Fluids*, 57(5):72. https://doi.org/10.1007/s00348-016-2159-z

5. Zhang J, Bhattacharya S, Vlachos PP (2020) Using uncertainty to improve pressure field reconstruction from PIV/PTV flow measurements. *Experiments in Fluids*, 61(6):131. https://doi.org/10.1007/s00348-020-02974-y

6. Bhattacharya S, Charonko JJ, Vlachos PP (2016) Stereo-particle image velocimetry uncertainty quantification. *Measurement Science and Technology*, 28(1):015301. https://doi.org/10.1088/1361-6501/28/1/015301

7. Bhattacharya S, Vlachos PP (2020) Volumetric particle tracking velocimetry (PTV) uncertainty quantification. *Experiments in Fluids*, 61(9):197. https://doi.org/10.1007/s00348-020-03021-6

8. Rajendran LK, Bane SPM, Vlachos PP (2019) Dot tracking methodology for background-oriented schlieren (BOS). *Experiments in Fluids*, 60(11):162. https://doi.org/10.1007/s00348-019-2793-3

9. Rajendran LK, Bane SPM, Vlachos PP (2020) Uncertainty amplification due to density/refractive index gradients in background-oriented schlieren experiments. *Experiments in Fluids*, 61(6):139. https://doi.org/10.1007/s00348-020-02978-8

10. Rajendran LK, Zhang J, Bhattacharya S, Bane SPM, Vlachos PP (2020) Uncertainty quantification in density estimation from background-oriented Schlieren measurements. *Measurement Science and Technology*, 31(5):054002. https://doi.org/10.1088/1361-6501/ab60c8

11. Rajendran L, Zhang J, Bane S, Vlachos P (2020) Uncertainty-based weighted least squares density integration for background-oriented schlieren. *Experiments in Fluids*, 61(11):239. https://doi.org/10.1007/s00348-020-03071-w

12. Raffel M, Willert CE, Scarano F, Kähler CJ, Wereley ST, Kompenhans J (2018) Particle Image Velocimetry, A Practical Guide. https://doi.org/10.1007/978-3-319-68852-7

13. Charonko JJ, Vlachos PP (2013) Estimation of uncertainty bounds for individual particle image velocimetry measurements from cross-correlation peak ratio. *Measurement Science and Technology*, 24(6):065301. https://doi.org/10.1088/0957-0233/24/6/065301

14. Xue Z, Charonko JJ, Vlachos PP (2014) Particle image velocimetry correlation signal-to-noise ratio metrics and measurement uncertainty quantification. *Measurement Science and Technology*, 25(11):115301. https://doi.org/10.1088/0957-0233/25/11/115301

15. Xue Z, Charonko JJ, Vlachos PP (2015) Particle image pattern mutual information and uncertainty estimation for particle image velocimetry. *Measurement Science and Technology*, 26(7):074001. https://doi.org/10.1088/0957-0233/26/7/074001

16. Timmins BH, Wilson BW, Smith BL, Vlachos PP (2012) A method for automatic estimation of instantaneous local uncertainty in particle image velocimetry measurements. *Experiments in Fluids*, 53(4):1133–1147. https://doi.org/10.1007/s00348-012-1341-1

17. Sciacchitano A, Wieneke B, Scarano F (2013) PIV uncertainty quantification by image matching. *Measurement Science and Technology*, 24(4):045302. https://doi.org/10.1088/0957-0233/24/4/045302

18. Wieneke B (2015) PIV uncertainty quantification from correlation statistics. *Measurement Science and Technology*, 26(7)https://doi.org/10.1088/0957-0233/26/7/074002

19. Bhattacharya S, Charonko JJ, Vlachos PP (2018) Particle image velocimetry (PIV) uncertainty quantification using moment of correlation (MC) plane. *Measurement Science and Technology*, 29(11):115301. https://doi.org/10.1088/1361-6501/aadfb4

20. Knapp C, Carter G (1976) The generalized correlation method for estimation of time delay. *IEEE Transactions on Acoustics, Speech, and Signal Processing*, 24(4):320–327. https://doi.org/10.1109/tassp.1976.1162830

21. Wernet MP (2005) Symmetric phase only filtering: a new paradigm for DPIV data processing. *Measurement Science and Technology*, 16(3):601. https://doi.org/10.1088/0957-0233/16/3/001

22. Eckstein AC, Charonko J, Vlachos P (2008) Phase correlation processing for DPIV measurements. *Experiments in Fluids*, 45(3):485–500. https://doi.org/10.1007/s00348-008-0492-6

23. Sciacchitano A, Neal DR, Smith BL, Warner SO, Vlachos PP, Wieneke B, Scarano F (2015) Collaborative framework for PIV uncertainty quantification: comparative assessment of methods. *Measurement Science and Technology*, 26(7):074004. https://doi.org/10.1088/0957-0233/26/7/074004

24. Boomsma A, Bhattacharya S, Troolin D, Pothos S, Vlachos P (2016) A comparative experimental evaluation of uncertainty estimation methods for two-component PIV. *Measurement Science and Technology*, 27(9):094006. https://doi.org/10.1088/0957-0233/27/9/094006

25. Timmermann A (2013) Forecast Combinations.

26. Bates J, Research C of the (1969) The combination of forecasts. https://doi.org/10.1057/jors.1969.103

27. Clemen RT (1989) Combining forecasts: A review and annotated bibliography. *International Journal of Forecasting*, (5):559–583. https://doi.org/10.1016/0169-2070(89)90012-5

28. Timmermann A (2006) Forecast combinations. *Handbook of economic forecasting*,

29. Marxen M, Sullivan PE, Loewen MR, Jähne B (2000) Comparison of Gaussian particle center estimators and the achievable measurement density for particle tracking velocimetry. *Experiments in Fluids*, 29(2):145–153. https://doi.org/10.1007/s003489900085

30. Cardwell ND, Vlachos PP, Thole KA (2011) A multi-parametric particle-pairing algorithm for particle tracking in single and multiphase flows. *Measurement Science and Technology*, 22(10):105406. https://doi.org/10.1088/0957-0233/22/10/105406

31. Stanislas M, Okamoto K, Kähler CJ, Westerweel J (2005) Main results of the Second International PIV Challenge. *Experiments in Fluids*, 39(2):170–191. https://doi.org/10.1007/s00348-005-0951-2

32. Stanislas M, Okamoto K, Kähler CJ, Westerweel J, Scarano F (2008) Main results of the third international PIV Challenge. *Experiments in Fluids*, 45(1):27–71. https://doi.org/10.1007/s00348-008-0462-z

33. Hubble DO, Vlachos PP, Diller TE (2013) The role of large-scale vortical structures in transient convective heat transfer augmentation. *Journal of Fluid Mechanics*, 718:89–115. https://doi.org/10.1017/jfm.2012.589

34. Kähler CJ, Astarita T, Vlachos PP, Sakakibara J, Hain R, Discetti S, Foy RL, Cierpka C (2016) Main results of the 4th International PIV Challenge. *Experiments in Fluids*, 57(6):97. https://doi.org/10.1007/s00348-016-2173-1

35. (n.d.) PRANA: PIV Research and Analysis. https://github.com/aether-lab/prana/

36. Eckstein A, Vlachos PP (2009) Assessment of advanced windowing techniques for digital particle image velocimetry (DPIV). *Measurement Science and Technology*, 20(7):075402. https://doi.org/10.1088/0957-0233/20/7/075402

37. Raffel M, Willert CE, Wereley ST, Kompenhans J (2007) Particle Image Velocimetry, A Practical Guide. https://doi.org/10.1007/978-3-540-72308-0

38. Westerweel J, Dabiri D, Gharib M (1997) The effect of a discrete window offset on the accuracy of cross-correlation analysis of digital PIV recordings. *Experiments in Fluids*, 23(1):20–28. https://doi.org/10.1007/s003480050082

39. Westerweel J (2000) Theoretical analysis of the measurement precision in particle image velocimetry. *Experiments in Fluids*, 29(Suppl 1):S003-S012. https://doi.org/10.1007/s003480070002

40. Westerweel J (2008) On velocity gradients in PIV interrogation. *Experiments in Fluids*, 44(5)https://doi.org/10.1007/s00348-007-0439-3

41. Wieneke B (2005) Stereo-PIV using self-calibration on particle images. *Experiments in Fluids*, 39(2):267–280. https://doi.org/10.1007/s00348-005-0962-z

Appendix A: Methods for perturbing the particle images

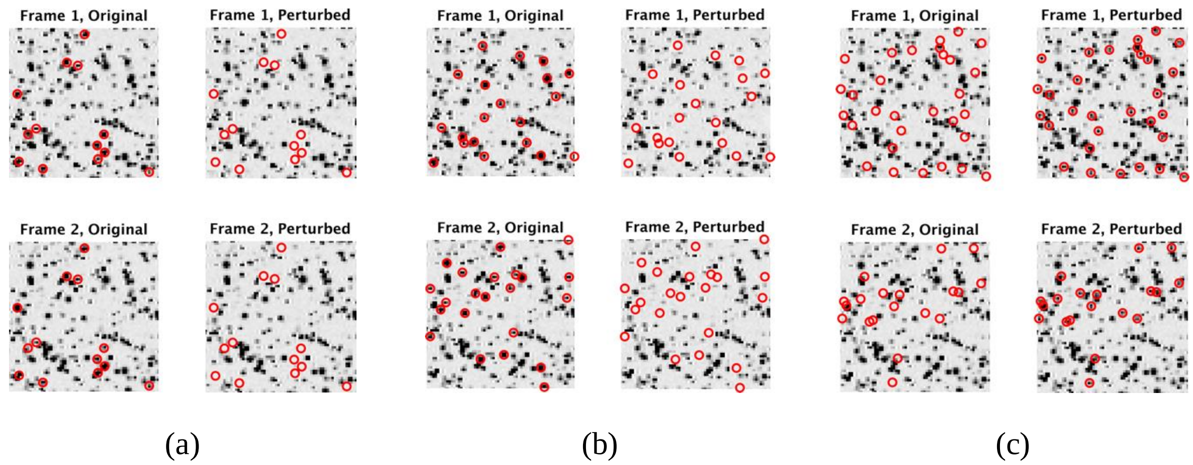

Figure 3.12. Illustration of methods used to perturb the particle images. (a) Removing paired particles, (b) Removing unpaired particles, (c) Adding unpaired particles.

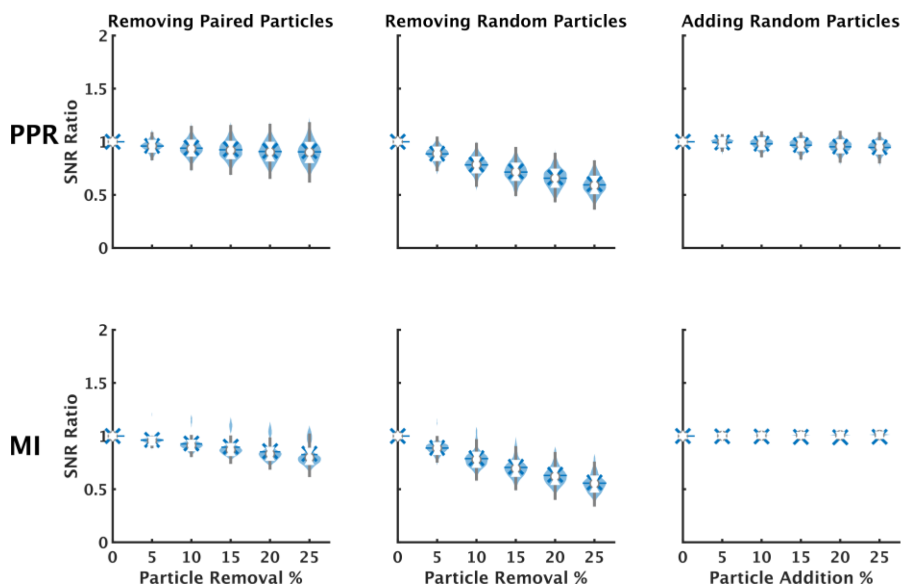

Figure 3.13. Effect of particle perturbation on correlation plane SNR metrics for the three methods.

Appendix B: Planar Uncertainty Distributions for individual datasets

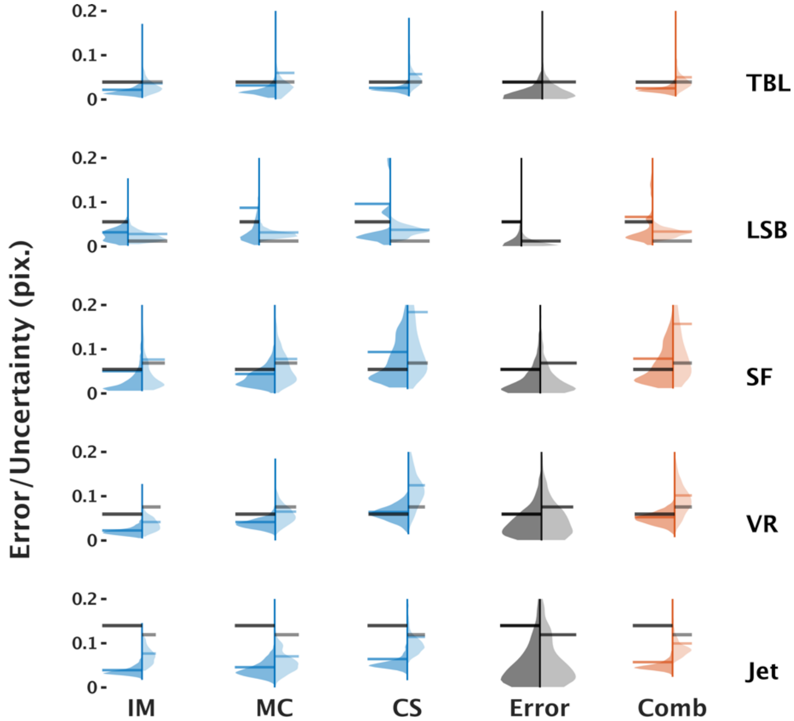

Figure 3.14. Error and uncertainty distributions for each of the planar PIV datasets. For each violin plot, the left (darker) and right (lighter) halves correspond to the results for WS1 and WS2 processing, respectively.

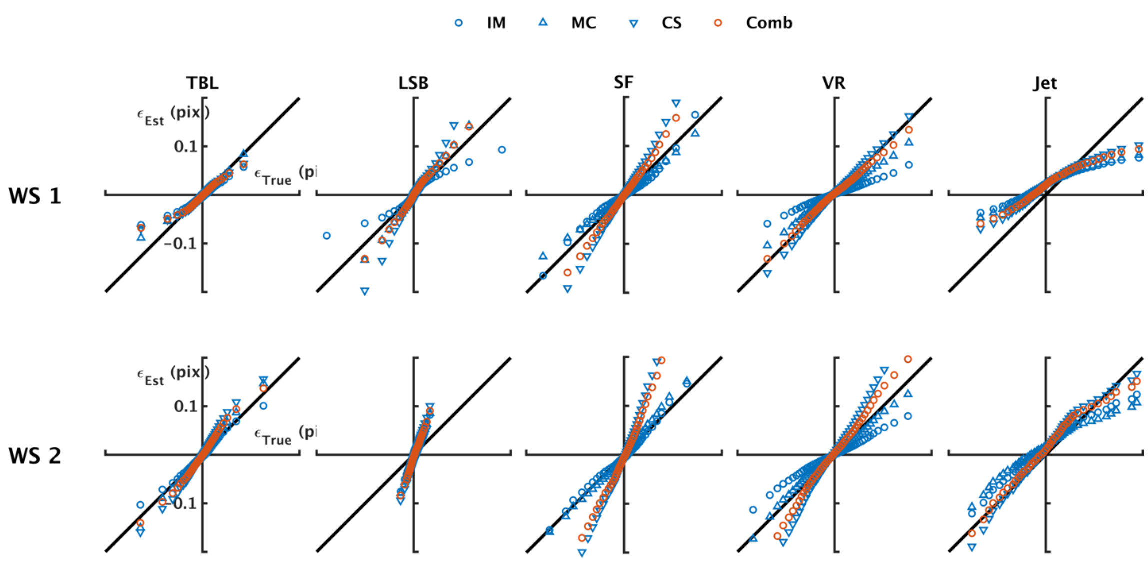

Figure 3.15. Quantile-Quantile comparisons of the true and estimated error distributions based on the individual and combined uncertainty estimates for each planar PIV dataset.

4. UNCERTAINTY-BASED WEIGHTED LEAST SQUARES DENSITY INTEGRATION FOR BACKGROUND ORIENTED SCHLIEREN

Lalit K. Rajendran[1], Jiacheng Zhang[2], Sally P. M. Bane[1] and Pavlos P. Vlachos[2]
[1] Purdue University, School of Aeronautics and Astronautics, West Lafayette, USA.
[2] Purdue University, School of Mechanical Engineering, West Lafayette, USA.
This chapter has been published in Experiments in Fluids, and reproduced with permission.
DOI: https://doi.org/10.1007/s00348-020-03071-w

Abstract

We propose an improved density integration methodology for Background Oriented Schlieren (BOS) measurements that overcomes the noise sensitivity of the commonly used Poisson solver. The method employs a weighted least-squares (WLS) optimization of the 2D integration of the density gradient field by solving an over-determined system of equations. Weights are assigned to the grid points based on density gradient uncertainties to ensure that a less reliable measurement point has less effect on the integration procedure. Synthetic image analysis with a Gaussian density field shows that WLS constrains the propagation of random error and reduces it by 80% in comparison to Poisson for the highest noise level. Using WLS with experimental BOS measurements of flow induced by a spark plasma discharge show a 30% reduction in density uncertainty in comparison to Poisson, thereby increasing the overall precision of the BOS density measurements.

4.1 Introduction and Methodology

Background Oriented Schlieren (BOS) is an optical technique used to measure density gradients by tracking the apparent distortion of a target dot pattern [1]. The apparent displacement is obtained by comparing the distorted image and a reference image without the density gradients, and the estimation can be performed by cross-correlation, tracking, or optical flow algorithms [1]–[3]. This displacement is related to the density gradient field and the optical layout parameters as given by

$$\Delta\vec{X} = \frac{M Z_D K}{n_0} \int \nabla\rho dz \tag{25}$$

where $\Delta\vec{X}$ is the apparent displacement, M is the magnification of the dot pattern, Z_D is the distance between the dot pattern and the mid plane of the density gradient field, K is the Gladstone-

Dale constant (= 0.225×10^{-3} kg/m^3 for air), n_0 is the ambient refractive index, $\nabla\rho$ is the density gradient field and z is the co-ordinate along the viewing axis. The integral is over the depth/thickness of the density gradient field.

Given the apparent displacement from the image processing algorithms, Equation (25) can be used to calculate the projected density gradient field, and then the density field can be obtained by spatial integration [4]. The BOS method provides a robust and simple experimental setup, yields quantitative density information, and can be extended to large scale flows.

The density gradient integration is traditionally performed by solving Equation (26) using a Poisson solver,

$$\begin{aligned} \rho &= (\nabla^2)^{-1}(\nabla \,.\, \nabla\rho) \\ &= (G^T G)^{-1}(G^T \nabla\rho) \end{aligned} \quad . \tag{26}$$

where ρ is the density field, $\nabla\rho$ is the density gradient field, and G is the gradient operator used for discretizing the derivative [4]. However this procedure is sensitive to measurement noise, and the noise can spread from one part of the measurement domain to contaminate other regions [5]. There can be several sources of noise in BOS measurements. For example, non-uniform illumination in the field of view that can increase the effect of image noise, unreliable measurements due to a failure in the displacement estimation algorithm, as well as noise in the boundary condition such as to a pressure/temperature measurement from a probe. Therefore, a robust integration method is required that can withstand and constrain the effect and propagation of measurement noise.

Least Squares (LS) Optimization is an alternate approach that is robust and customizable. It involves formulating the integration as an optimization problem, with the aim of minimizing a pre-defined cost function. For example, the cost function can be defined as the difference between the measured density gradient field and a finite difference approximation of the unknown density field, and the density field can be calculated by minimizing this cost function subject to constraints imposed by the boundary conditions. While solving the least squares problem with the particular cost function defined above is mathematically equivalent to solving the Poisson equation in (26) given the same stencil, the LS-optimization based approach allows the introduction of additional information/constraints about the flow field and flow measurement to improve the density integration procedure.

For example, non-uniform weights can be assigned to grid points to form the Weighted Least Squares (WLS) problem, which can be solved by Equation (27), where W is the "weight matrix".

$$\rho = (G^T W G)^{-1}(G^T W \nabla\rho) \quad . \tag{27}$$

A common approach is to assign weights based on the inverse variance of the measurement error for each point, to ensure that more precise measurements have a greater effect on the result [6][7]. Recently Zhang et. al. [7], [8] showed that WLS can significantly improve the performance of velocity-based pressure integration in incompressible flow, when the weights are assigned based on the accuracy of pressure gradient estimated from velocity error or velocity uncertainty. However, this approach is not applicable to planar BOS in general, due to the compressibility of the flow. Instead, the weights can be assigned based on the uncertainty of the BOS measurement which is directly related to the density gradient.

Recently, Rajendran et. al. [10], [11] made advancements in uncertainty quantification methods for BOS measurements by developing a method to report local, instantaneous, a-posteriori density uncertainty across all points in the field of view. To achieve this, PIV-based displacement uncertainty quantification methods are used to estimate displacement uncertainties from cross-correlation BOS and propagated through the density integration procedure. One of the findings is that displacement uncertainty schemes from PIV are also applicable for cross-correlation BOS, and that result will be used here. Further, the methodology to estimate the density uncertainty will also be utilized in this work.

Therefore, we propose a WLS-based density integration methodology for BOS wherein the displacement/density gradient uncertainty will be used to assign weights for the integration procedure. For a grid point k, the weight is given by,

$$\begin{aligned} W_k &= \left(\sigma_{\nabla\rho,k}\right)^{-2} \\ &= \left(\frac{1}{MKZ_D\Delta z}\sigma_{\Delta X,k}\right)^{-2} \quad , \end{aligned} \tag{28}$$

where $\sigma_{\nabla\rho,k}$ is the density gradient uncertainty at this point and $\sigma_{\Delta X,k}$ is the displacement uncertainty. The pre-multiplying term involves the optical layout parameters described earlier in Equation (1), with the additional parameter Δz denoting the depth/thickness of the density gradient field. This weight matrix is used along with Equation (27) to perform the WLS density integration for BOS. In this manner, the unreliable density gradient data points (with greater uncertainty) are assigned lower weights as defined in Equation (4), and thus have a lower effect on the density integration procedure. Since the state of the art displacement uncertainty estimation methods are sensitive to a wide variety of error and uncertainty sources [12], it is possible identify unreliable measurements in a robust manner, if a reliable uncertainty quantification method is utilized. If the errors in the density gradient are unbiased and uncorrelated, the weight matrix is the inverse of the covariance matrix of the density gradient error, and WLS provides the best unbiased linear estimator for the density integration problem [13].

The following sections detail the assessment of this methodology with synthetic and experimental BOS images, and show that WLS can reduce the density random error/uncertainty and improve the overall precision of the measurement.

4.2 Analysis with synthetic BOS images

We performed error analysis using synthetic BOS images with a known density field, and assessed the performance of three density integration algorithms: (1) Poisson solver, (2) WLS with weights based on the random displacement error, and (3) WLS with weights based on the displacement uncertainty. Further, a patch of high noise was added to one part of the BOS image to assess how the error due this patch propagates to the surrounding field during the density integration procedure. The synthetic BOS images were generated using a ray tracing-based image generation methodology [14]. In this method, light rays are launched from source points on the BOS target, propagated through density gradients by numerically solving Fermat's equation with a 4th order Runge-Kutta method [15], and then through the camera lens until the final intersection with the camera sensor, to generate the dot pattern images.

The density field chosen for the error analysis is a Gaussian density field, described by Equation (20),

$$\rho(X,Y) = \rho_0 + \Delta\rho_0 \exp\left\{-\frac{(X-X_0)^2 + (Y-Y_0)^2}{2\sigma_0^2}\right\} \tag{29}$$

where ρ_0 is the ambient density, $\Delta\rho_0$ is the peak density difference and σ_0 is the standard deviation of the Gaussian field. For the simulations reported in this paper, ρ_0 was set to be 1.225 kg/m^3, $\Delta\rho_0$ was set to be 0.3 kg/m^3, and σ_0 was set to be 1/4th of the field of view (= 2.41 mm). The dimensions of the density gradient field were 10 x 10 x 10 mm, and it was located at a distance of 0.25 m from the dot pattern. The optical layout used to image the dot pattern and the density field consisted of a 105 mm lens at a distance of 0.5 m from the dot pattern to provide a magnification of about 40 μm/pix. These values were chosen to provide a displacement field that was characteristic of a typical BOS experiment (with an expected displacement of ~1-2 pixels), and to also provide displacement gradients for testing the density integration methods. The density field used to render the images is shown in Figure 4.1(a).

The synthetic images featured a random dot pattern with a dot size of 3 pixels and a dot density of 15 dots/32x32 pixel window, and the entire image is corrupted with a noise level that was 1% of the peak image intensity. In addition, a portion of the image was corrupted with image noise higher than the surrounding regions by a specified amplification ratio. Three amplification ratios are considered in this analysis: 1, 10, 20. In all cases, the image noise at a given pixel was drawn randomly from a Gaussian distribution with the standard deviation equal to the imposed noise level. A sample image highlighting the high-noise region is shown in Figure 4.1 (b). A total of 1000 such image pairs were generated with different dot patterns and with each image pair consisting of one image rendered with the density gradient field and a reference image without the field, with the same noise level.

Each image pair is cross-correlated using a multi-pass window deformation procedure with 32x32 pixel windows and 50% overlap to obtain the corresponding displacement field shown in Figure 4.1 (c). Then the displacement error is calculated from the deviation of the measured displacements from cross-correlation with respect to the light ray deflections from ray tracing. Finally, the displacement errors from all image pairs are used to compute the error statistics, and the spatial distribution of the random component of the displacement error (defined as the standard deviation of the error distribution at each grid point) is shown in Figure 4.1 (e), showing, as expected, higher values in the noisy patch.

In addition, the displacement uncertainty is also estimated during the correlation processing using the Moment of Correlation (MC) algorithm developed by Bhattacharya et. al. [16]. In this algorithm, the uncertainty is estimated directly from the PDF of displacements that contribute to the cross-correlation plane. The PDF of displacements is obtained by an inverse fast Fourier transform of the phase plane [17], [18] (also referred to as the Generalized Cross Correlation (GCC)), filtered by a Gaussian to improve subsequent calculations of the peak diameter [19], scaled by the number of correlating particles using the Mutual Information (MI) [20], and corrected for displacement gradients in the interrogation window [21], [22]. The instantaneous displacement uncertainty field is shown in Figure 4.1 (d), and also shows a large increase in the noisy patch, which is consistent with the increase in the random error. Thus, the weights chosen based on the random error/uncertainties are lower in the noisy patch, and thus measurements in the patch would have less effect on the density integration.

However, it is also seen that MC uncertainty is lower than the random error in the noisy patch, and higher in the rest of the field. This is because the displacement uncertainty predicted by MC is an instantaneous estimate of the random error from just a single snapshot, while the true random error is a statistically averaged estimate from several (here 1000) error fields. Despite many recent advances in the development of displacement uncertainty quantification methods, there is no universally accepted method with superior performance across all flow fields [23], [24], and the development of PIV/BOS uncertainty quantification is a young and active research area. While the results reported in this paper utilize MC to estimate the uncertainty, the WLS method is general and can be integrated with any uncertainty quantification method.

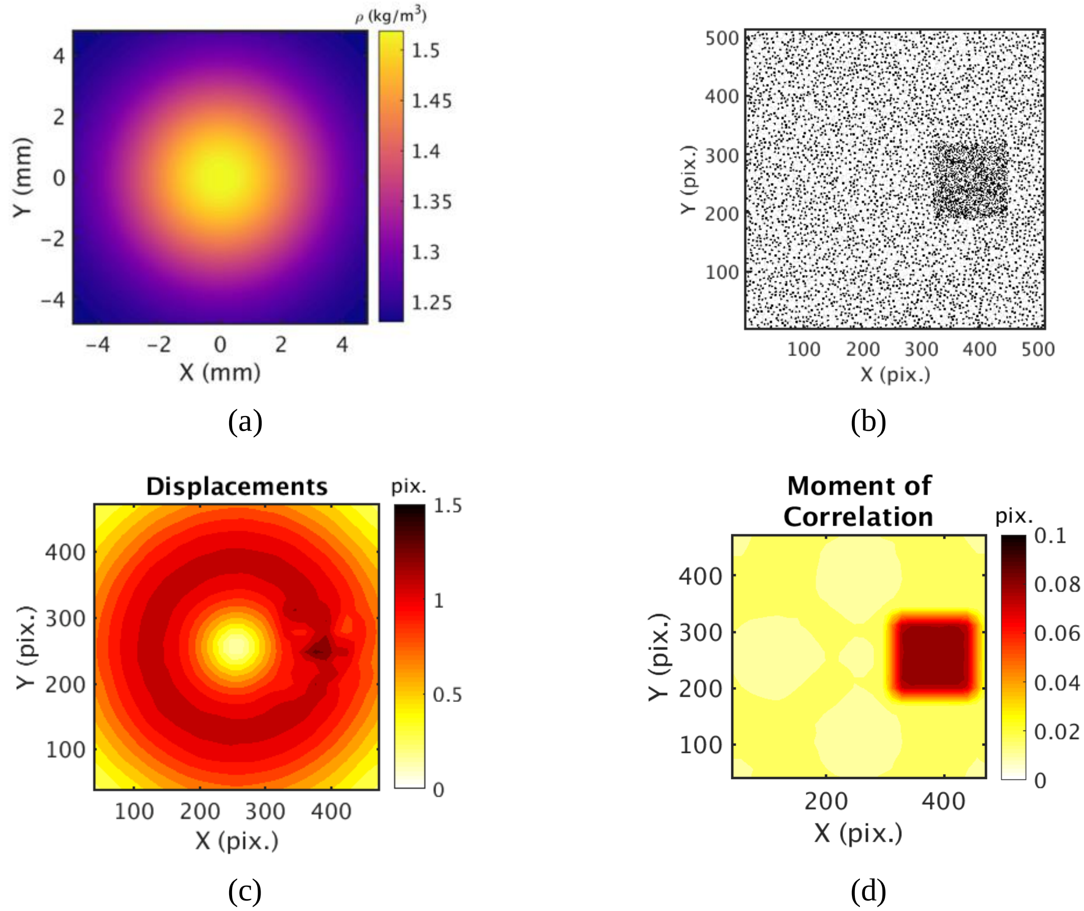

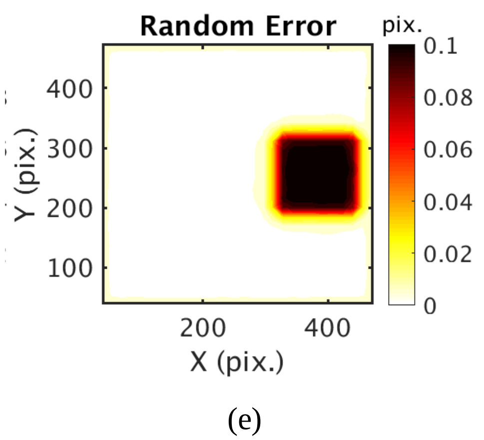

Figure 4.1. Synthetic dataset used for comparing the density integration methods corresponding to an amplification ratio of 20. (a) Gaussian density field, (b) BOS image in false color showing the region of the image corrupted with noise, (c) corresponding displacement field, (d) instantaneous displacement uncertainty from MC, and (e) random error of the displacement from 1000 realizations.

Next, the displacements were used to calculate the density gradients, which were then spatially integrated to calculate the density field using the three integration methods: (a) Poisson, (b) WLS with weights based on the random error, and (c) WLS with weights based on MC uncertainty. A 2[nd] order central difference scheme is used for spatial discretization, with Neumann boundary conditions on all four boundaries and the Dirichlet boundary condition at the midpoint of the top boundary. The density error was then calculated by comparing the integrated density field with the reference field used to render the images, and a snapshot of the instantaneous density field as well as a profile along a vertical line passing through $X = 2.5\ mm$ is shown in Figure 4.2. All three methods show an under-prediction in the density field, potentially due to spatial discretization and truncation errors in the numerical integration. This deviation appears to increase with the noise amplification ratio.

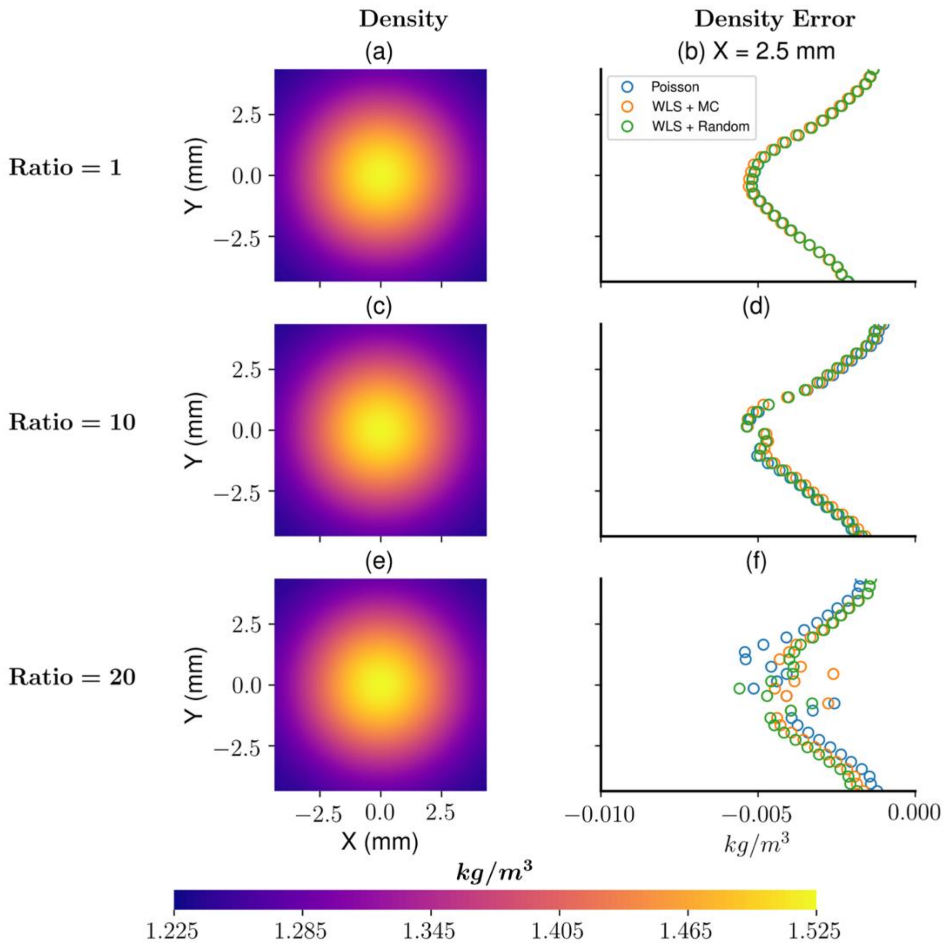

Figure 4.2. Spatial variation of the density field obtained by the Poisson integration method and profiles of the density random error along a vertical line for the three integration methods.

The error statistics from 1000 such fields are calculated, and the resulting random error in the density field obtained from the three integration methods are shown in Figure 4.3. The WLS method (middle and right columns) is able to constrain the spread of the random error from the patch, while the error has a wider spread with Poisson integration (left column), and this difference increases with the patch amplification ratio. Finally, the results show that WLS with weights based on the displacement uncertainty (middle column) performs just as well as the case with weights based on the random error (right column), thereby justifying the use of the displacement/density gradient uncertainty to estimate the weights. This demonstrates the practical value of WLS since the error is not known and only the uncertainty can be estimated in the vast majority of experiments. The variation of the random error along a vertical line located at $X = 2.5\ mm$ is shown in the right most column. With increasing amplification ratio, the WLS method is able to constrain the spread of error and limit the peak error in the patch. The profile of the density random error is seen to be asymmetric with respect to $Y = 0\ mm$ because the Dirichlet boundary condition is imposed at the top mid-point of the field of view, with the rest of the boundaries featuring Neumann boundary conditions.

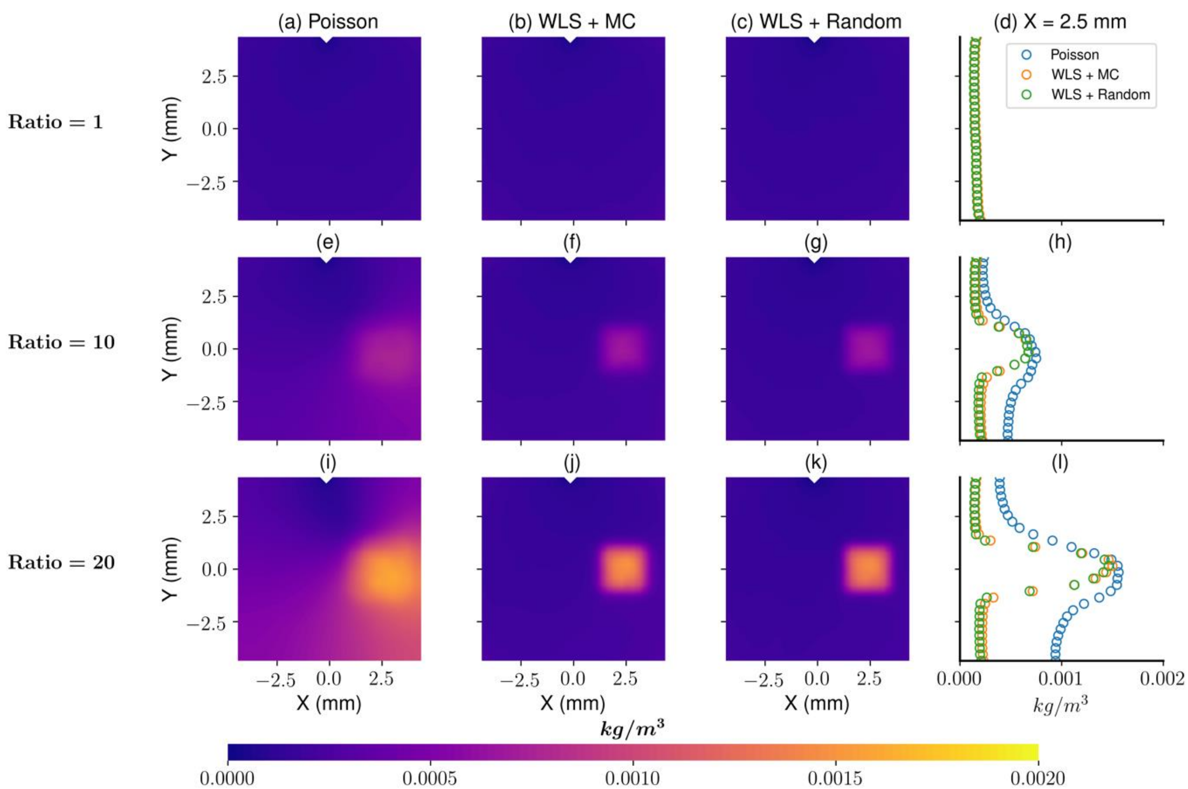

Figure 4.3. Spatial distribution of the density random error associated with the three integration methods: Poisson, WLS + MC, and WLS + Random Error. Each row corresponds to the same patch noise amplification ratio, denoted on the left, and each column corresponds to an integration scheme. The right most column represents a profile of the density random error along a vertical slice.

In addition, the probability density function (PDF) and cumulative density function (CDF) of the density random error distribution was calculated from 250,000 grid points and are shown in Figure 4.4, along with the RMS error for the PDF plot and the 90^{th} percentile error for the CDF plot. As suggested by the PDFs of the random errors in the left column, the modes of the error distributions by WLS methods are less than $1/3^{rd}$ of the error mode by the Poisson (blue) for an amplification ratio of 20. The RMS of the error distributions are shown by dashed lines as a metric to compare the distributions. The RMS values of the WLS methods are about 50% lower than the corresponding RMS for the Poisson.

The right column shows the CDF of the random error distributions for the three integration methods. The dashed lines represent the 90^{th} percentile of the error distribution which is an indication of the noise spreading characteristics. For WLS methods, 90% of the points have errors are less than 3e-4 kg/m^3, whereas the errors by Poisson have a much wider spread and yield a 500% increase in terms of the 90^{th} percentile compared to WLS methods.

It is also seen that the 90^{th} percentile errors from WLS methods are less affected by the noise level. Moreover, the WLS based on MC uncertainty results in a similar error distribution with the WLS based on the random error.

In summary, the error analysis shows that the WLS integration can significantly improve the precision of the density integration procedure in comparison to the traditional Poisson solver.

4.3 Experimental Demonstration

The methodology was also tested using experimental BOS data of the flow induced by a nanosecond spark plasma discharge. A spark discharge of nanosecond duration leads to the rapid deposition of heat in the electrode gap leading to the development of a complex flow field with large thermal gradients. The experimental details corresponding to the dataset used in this assessment are reported in the work by Singh et. al. [25]. The BOS measurements were performed by imaging a random dot pattern (fabricated from sand-blasted aluminum) in the presence of flow induced by a spark across a 5 mm electrode gap. The dot pattern and flow were imaged at a magnification of 0.8 and a frame rate of 20 kHz with a 3.18 cm separation between the target and the electrodes. More details of the experimental setup can be found in Singh et. al. [25].

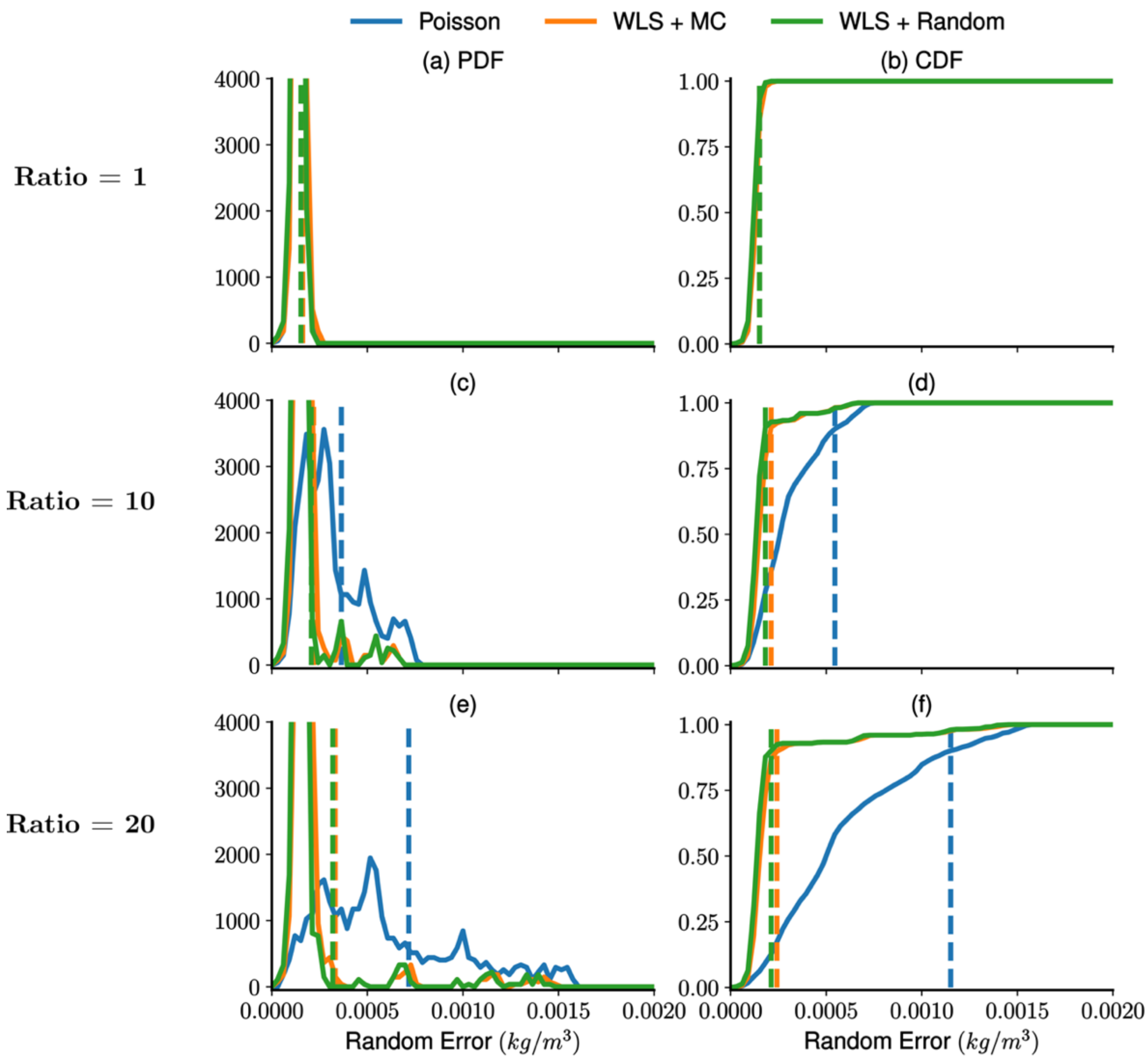

Figure 4.4. PDF (left) and CDF (right) of the density random error associated with the three integration schemes. The dashed lines indicate the RMS error for the left column, and the 90$^{\text{th}}$ error percentile for the right column. Each row corresponds to the same patch noise amplification ratio, denoted on the left.

The dot pattern images were processed using the standard cross-correlation (SCC) method with multi-grid window deformation [26]. The window sizes were varied from 64 to 48 to 32 pixels over 4 passes with an overlap of 50% resulting in a final grid resolution of 16 pixels. The displacement uncertainties were calculated using the MC method described earlier, and the vector field is validated using Universal Outlier Detection (UOD) [27]. A median-based UOD filter was used with a 3x3 grid point neighborhood, and performed in two passes with a normalized residual threshold set to be 3 and 2 respectively. The minimum normalization level (ϵ) was of 0.1 pixels. The detected outliers were replaced by a weighted average of the inverse distance between the invalid vector and the neighboring grid points.

In the case of the experimental data, the extent of the path integration in Equation (25) is not known, as the flow is three-dimensional and only one view is presently available. Therefore, the displacements were used to calculate the *projected* density gradients, $\nabla\rho_p = \int \nabla\rho \, dz$, thereby constituting a 2D simplification of the 3D field. The gradients were then spatially integrated using the Poisson and WLS methods, with the weights assigned based on the projected density gradient uncertainty $\sigma_{\nabla\rho_p}$ for the latter, to yield the *projected* density field $\rho_p = \int \rho dz$. Dirichlet boundary conditions were imposed at the mid-points of the left and right boundaries and Neumann conditions were imposed elsewhere. Further, the Dirichlet density values were set to zero to calculate the 'relative' projected density field with respect to the ambient. During the experiment, the field of view was large enough (= 1 electrode gap on either side of the spark) to ensure that the left and right boundaries were far from the induced flow and truly in the ambient. While the analysis of Singh et. al. employed an Abel inversion procedure to further extract the radial density field, that was not performed here, and instead a direct comparison was performed on the projected density field to avoid introducing additional downstream steps/variables in the comparison.

The dot pattern displacements are shown in Figure 4.5(a) and (b) for two time instants, and the largest displacements occur at the boundary of the hot gas kernel as this corresponds to the largest temperature/density gradients. The kernel is initially cylindrical and deforms into a more complex shape at later times. The corresponding density field calculated using Poisson are shown in (c) and (d), and the density from WLS are shown in (e) and (f) for the same time instants. It is seen that the density is lower inside the gas kernel, corresponding to a higher gas temperature, as expected, and further that the two schemes result in similar density fields. However, it will be seen that there is a significant difference in the density uncertainty field.

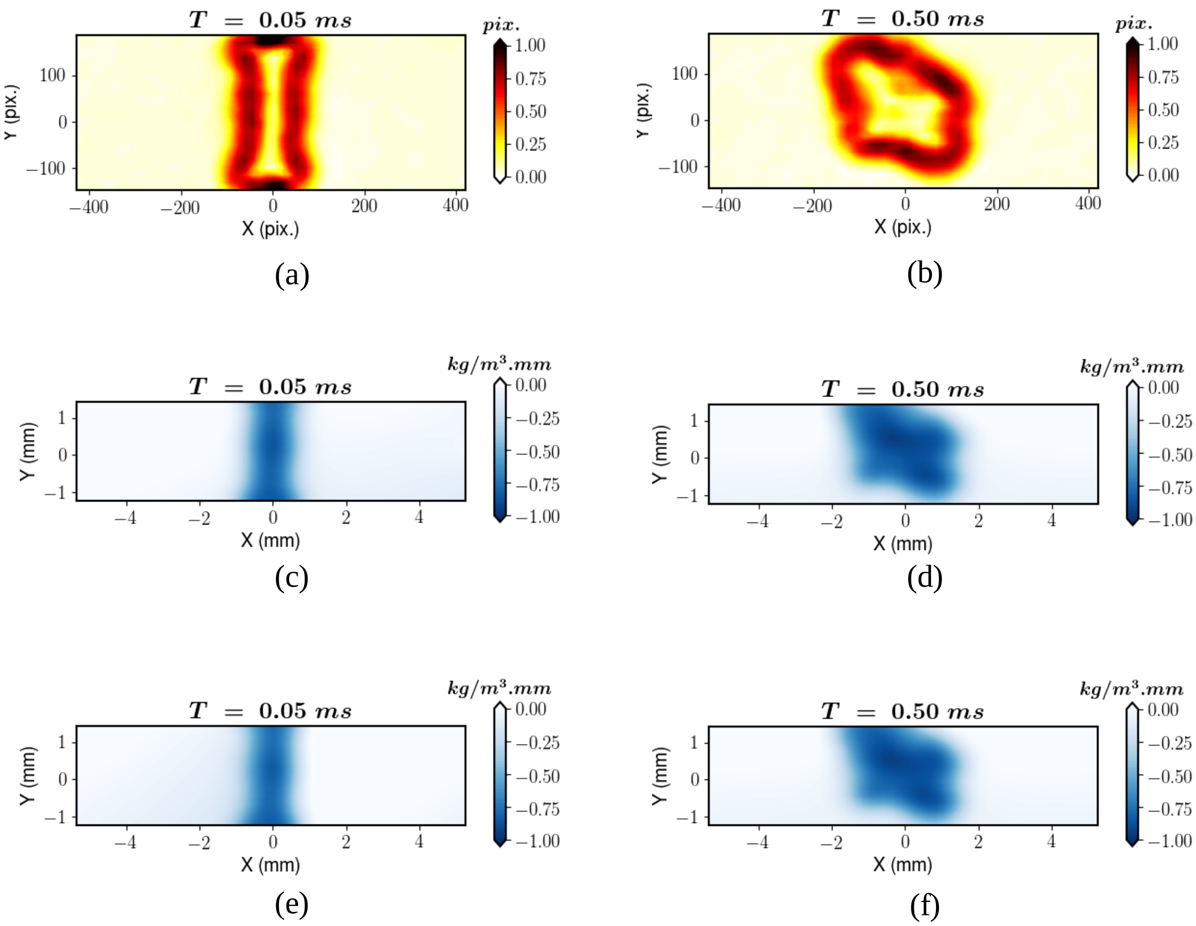

Figure 4.5. Flow induced by a spark discharge at two time instants. (a), (b): Instantaneous displacement fields and (c), (d): density fields obtained using Poisson, and (e), (f): density fields obtained using WLS. Plots (a), (c) and (e) correspond to the same time instant, as do (b), (d) and (f).

The corresponding uncertainties in the displacement fields are shown in Figure 4.6(a) and (b), and the displacement uncertainty is highest within the region occupied by the hot gas kernel, with the noise amplification ratio varying from 5–10 in this region. This is expected because in addition to higher displacements, the displacement gradients are also expected to be higher in this region, leading to a rise in the uncertainty. This uncertainty in the displacement is then propagated through the density integration process using the methodology described in [10], and the density uncertainty fields shown in Figure 4.6 (c) – (f). The uncertainty propagation method is as follows: the displacement uncertainties are used along with the parameters of the optical layout to estimate the density gradient uncertainties. Then the density gradient uncertainties are propagated to the density field through a matrix representation of the density integration process. The computations are performed using sparse linear operators for speed and efficiency. For more details on the method along with the assessment, please refer [10]. Since the true density is not known for this experiment, the density *uncertainty* will be used in place of the density random error as the metric to compare the integration methods. The uncertainty provides the range for the error at a specified confidence level, and is therefore a measure of the 'sensitivity' of the density integration procedure to upstream noise. While estimating the error requires an independent measurement (a ground truth), it is not required for uncertainty quantification. Similar to the analysis with synthetic images, it is again seen that the density uncertainty from WLS is again lower and confined to the region within the hot gas kernel as opposed to that from Poisson where the uncertainty spreads to all regions in the domain. Therefore, WLS integration yields a more robust estimate of the density which is less sensitive noise in the density gradient measurement.

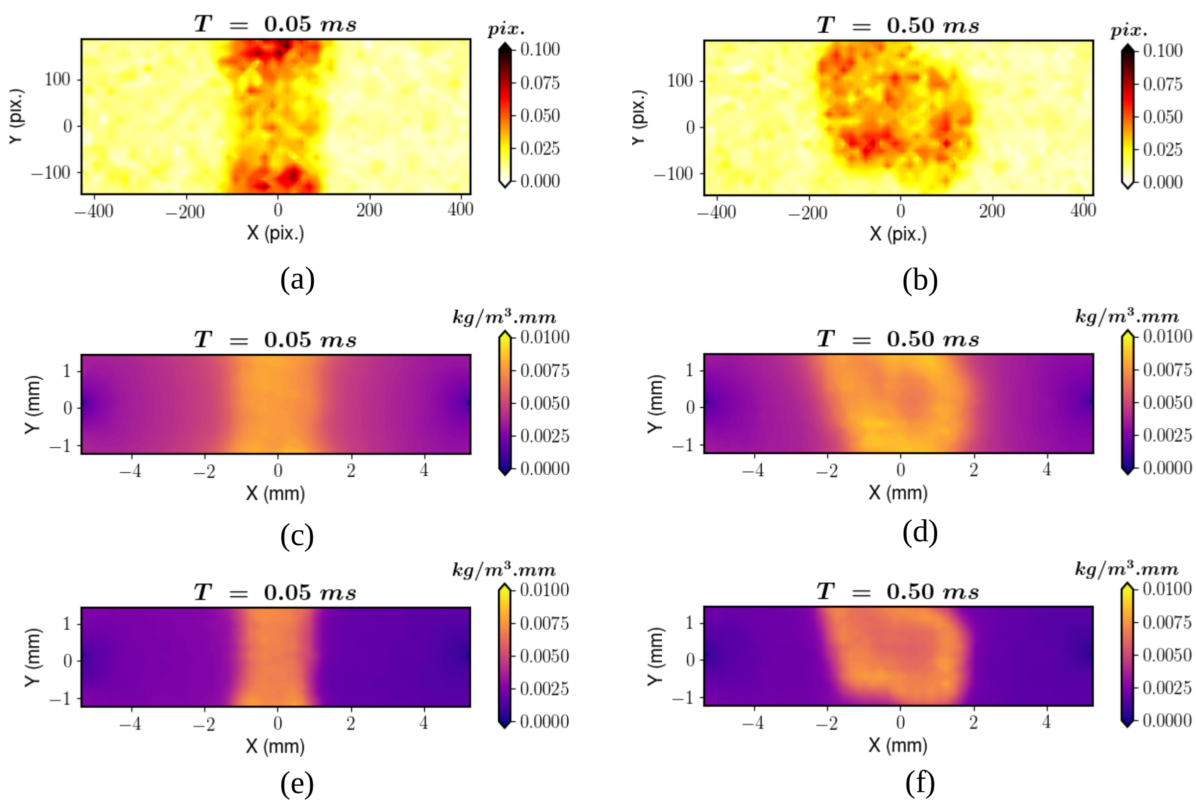

Figure 4.6. Instantaneous spatial distribution of the displacement uncertainty (a), (b) and the density uncertainty fields obtained from Poisson (c), (d) and WLS (e),(f) methods. Plots (a), (c) and (e) correspond to the same time instant, as do (b), (d), and (f).

In addition, the density uncertainty fields from 20 such snapshots of the flow were used to calculate the PDF and CDF distributions for the Poisson and WLS methods. The PDF with RMS of the uncertainty is shown in Figure 4.7(a) and the CDF with the 90th percentile is shown in in Figure 4.7 (b). It is seen that WLS reduces the RMS of the density uncertainty by 30% and the 90th percentile of the density by about 25%, thereby improving the overall precision in the density estimation.

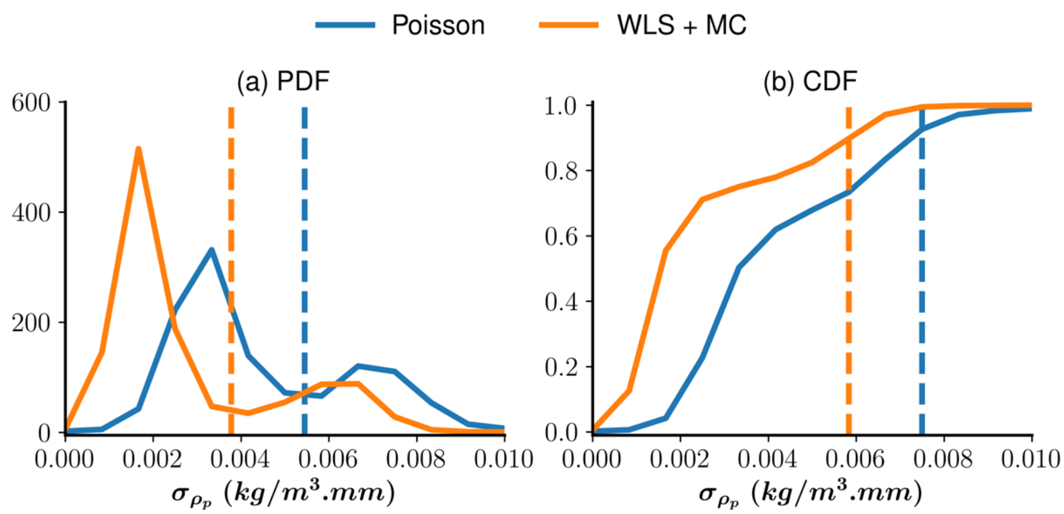

Figure 4.7. (a) PDF and (b) CDF of the density uncertainty associated with the two integration schemes for flow induced by the spark discharge.

4.4 Conclusion

In conclusion, we presented a weighted least squares (WLS) based density integration procedure in which weights are assigned to density gradient measurements based on the corresponding measurement uncertainty to improve the overall precision of the density integration procedure. Results from the synthetic image analysis showed that WLS was able to constrain the spread of the density random error compared to the Poisson solver and reduced the RMS error by 80% for the highest noise level. It was also seen that weights based on the Moment of Correlation uncertainty quantification scheme performed just as well as when weights were based on the displacement random error, thereby demonstrating that the displacement/density gradient uncertainty is a valid reference for assigning the weights. From the experimental images of flow induced by a spark plasma discharge, it was seen that WLS reduced the RMS uncertainty by 30% in comparison to Poisson, thus producing more precise density estimation. However a limitation of this work is that it does not show that the WLS reduced the actual density measurement error in the experiment. An independent measure of density with a benchmark experiment is required in order to perform this assessment. Such an experiment is beyond the scope of this work and will be considered in a future publication.

Further improvement of the method can be achieved by accounting for the covariance in the displacement estimation procedure, to be used for assigning weights in a Generalized Least Squares (GLS) integration framework. Recent work in pressure integration has shown that GLS can further reduce the errors and uncertainties when the covariance information is available [9]. For BOS, the covariance in the density gradient between neighboring grid points arises from the window overlap used in the cross-correlation based displacement estimation. There is currently no method to estimate this covariance in an automated and reliable manner, and this is an avenue for future work. Finally the WLS method can also be combined with tracking based displacement estimation methods for BOS using recent developments on estimating the displacement uncertainty using the ratio of dot diameters in the reference and gradient images [11].

4.5 Acknowledgment

Bhavini Singh is acknowledged for help in conducting the spark discharge experiment. This material is based upon work supported by the U.S. Department of Energy, Office of Science, Office of Fusion Energy Sciences under Award Number DE-SC0018156. This work was also supported by NSF 1706474.

4.6 References

[1] M. Raffel, “Background-oriented schlieren (BOS) techniques,” *Exp. Fluids*, vol. 56, no. 3, pp. 1–17, 2015.

[2] B. Atcheson, W. Heidrich, and I. Ihrke, “An evaluation of optical flow algorithms for background oriented schlieren imaging,” *Exp. Fluids*, 2009.

[3] L. K. Rajendran, S. P. M. Bane, and P. P. Vlachos, “Dot tracking methodology for background-oriented schlieren (BOS),” *Exp. Fluids*, vol. 60, no. 11, p. 162, Nov. 2019.

[4] L. Venkatakrishnan and G. E. a. Meier, "Density measurements using the Background Oriented Schlieren technique," *Exp. Fluids*, vol. 37, no. 2, pp. 237–247, 2004.

[5] J. J. Charonko, C. V King, B. L. Smith, and P. P. Vlachos, "Assessment of pressure field calculations from particle image velocimetry measurements," *Meas. Sci. Technol.*, vol. 21, no. 10, p. 105401, 2010.

[6] J. A. Fessler, "Penalized weighted least-squares image reconstruction for positron emission tomography," *IEEE Trans. Med. Imaging*, vol. 13, no. 2, pp. 290–300, 1994.

[7] D. C. Ghiglia and M. D. Pritt, "Two-dimensional phase unwrapping: theory, algorithms, and software," *Wiely-Interscience, first ed.(April 1998)*, 1998.

[8] J. Zhang *et al.*, "4D Flow MRI Pressure Estimation Using Velocity Measurement-Error based Weighted Least-Squares," *IEEE Trans. Med. Imaging*, vol. 0062, no. c, pp. 1–1, 2019.

[9] J. Zhang, S. Bhattacharya, and P. P. Vlachos, "Uncertainty-based pressure field reconstruction from PIV/PTV flow measurements with generalized least-squares," *arxiv:1912.00130*, pp. 1–33, 2019.

[10] L. K. Rajendran, J. Zhang, S. Bhattacharya, S. P. M. Bane, and P. P. Vlachos, "Uncertainty quantification in density estimation from background-oriented Schlieren measurements," *Meas. Sci. Technol.*, vol. 31, no. 5, p. 054002, 2020.

[11] L. K. Rajendran, S. P. M. Bane, and P. P. Vlachos, "Uncertainty amplification due to density/refractive index gradients in background-oriented schlieren experiments," *Exp. Fluids*, vol. 61, no. 6, p. 139, Jun. 2020.

[12] A. Sciacchitano, "Uncertainty quantification in particle image velocimetry," *Meas. Sci. Technol.*, vol. 30, no. 9, p. 092001, Sep. 2019.

[13] A. C. Aitken, "IV.—On Least Squares and Linear Combination of Observations," *Proc. R. Soc. Edinburgh*, vol. 55, pp. 42–48, Sep. 1936.

[14] L. K. Rajendran, S. P. M. Bane, and P. P. Vlachos, "PIV/BOS synthetic image generation in variable density environments for error analysis and experiment design," *Meas. Sci. Technol.*, vol. 30, no. 8, p. 085302, Aug. 2019.

[15] A. Sharma, D. V. Kumar, and A. K. Ghatak, "Tracing rays through graded-index media: a new method.," *Appl. Opt.*, vol. 21, no. 6, pp. 984–987, 1982.

[16] S. Bhattacharya, J. J. Charonko, and P. P. Vlachos, "Particle image velocimetry (PIV) uncertainty quantification using moment of correlation (MC) plane," *Meas. Sci. Technol.*, vol. 29, no. 11, 2018.

[17] A. C. Eckstein, J. J. Charonko, and P. P. Vlachos, "Phase correlation processing for DPIV measurements," *Exp. Fluids*, vol. 45, no. 3, pp. 485–500, 2008.

[18] C. Knapp and G. Carter, “The generalized correlation method for estimation of time delay,” *IEEE Trans. Acoust.*, vol. 24, no. 4, pp. 320–327, Aug. 1976.

[19] A. C. Eckstein and P. P. Vlachos, “Digital particle image velocimetry (DPIV) robust phase correlation,” *Meas. Sci. Technol.*, vol. 20, no. 5, p. 055401, 2009.

[20] Z. Xue, J. J. Charonko, and P. P. Vlachos, “Particle image pattern mutual information and uncertainty estimation for particle image velocimetry,” *Meas. Sci. Technol.*, vol. 26, no. 7, 2015.

[21] J. Westerweel, “On velocity gradients in PIV interrogation,” *Exp. Fluids*, vol. 44, pp. 831–842, 2008.

[22] S. Scharnowski, R. Hain, and C. J. Kähler, “Reynolds stress estimation up to single-pixel resolution using PIV-measurements,” *Exp. Fluids*, vol. 52, no. 4, pp. 985–1002, 2012.

[23] A. Sciacchitano *et al.*, “Collaborative framework for PIV uncertainty quantification: Comparative assessment of methods,” *Meas. Sci. Technol.*, vol. 26, no. 7, 2015.

[24] A. Boomsma, S. Bhattacharya, D. Troolin, S. Pothos, and P. P. Vlachos, “A comparative experimental evaluation of uncertainty estimation methods for two-component PIV,” *Meas. Sci. Technol.*, vol. 27, no. 9, 2016.

[25] B. Singh, L. K. Rajendran, P. P. Vlachos, and S. P. M. Bane, “Two regime cooling in flow induced by a spark discharge,” *Phys. Rev. Fluids*, vol. 5, no. 1, p. 014501, Jan. 2020.

[26] F. Scarano, “Iterative image deformation methods in PIV,” *Meas. Sci. Technol.*, vol. 13, no. 1, pp. R1–R19, 2002.

[27] J. Westerweel and F. Scarano, “Universal outlier detection for PIV data,” *Exp. Fluids*, vol. 39, no. 6, pp. 1096–1100, 2005.

5. DOT-TRACKING METHODOLOGY FOR BACKGROUND ORIENTED SCHLIEREN (BOS)

Lalit K. Rajendran[1], Sally P. M. Bane[1] and Pavlos P. Vlachos[2]
[1] Purdue University, School of Aeronautics and Astronautics, West Lafayette, USA.
[2] Purdue University, School of Mechanical Engineering, West Lafayette, USA.
This chapter has been published in Experiments in Fluids, and reproduced with permission.
DOI: https://doi.org/10.1007/s00348-019-2793-3

Abstract

We propose a dot-tracking methodology for processing Background Oriented Schlieren (BOS) images. The method improves the accuracy, precision and spatial resolution compared to conventional cross-correlation algorithms. Our methodology utilizes the prior information about the dot pattern such as the location, size and number of dots to provide near 100% yield even for high dot densities (20 dots/32x32 pix.) and is robust to image noise. We also propose an improvement to the displacement estimation step in the tracking process, especially for noisy images, using a "correlation correction", whereby we combine the spatial resolution benefit of the tracking method and the smoothing property of the correlation method to increase the dynamic range of the overall measurement process. We evaluate the performance of the method with synthetic BOS images of buoyancy driven turbulence rendered using ray tracing simulations, and experimental images of flow in the exit plane of a converging-diverging nozzle. The results show that the improved spatial resolution results in a better accuracy of the tracking method compared to correlation based methods in regions with sharp displacement gradients, and the correlation correction step reduces the noise floor of the measurement, resulting in a four-fold improvement in the dynamic range.

5.1 Introduction

Background Oriented Schlieren (BOS) is an optical flow diagnostic technique used to measure density gradients in a flow field by tracking the apparent distortion of a target dot pattern. Since density and refractive index are proportional for fluids, density gradients in a flow are associated with refractive index gradients, and an object viewed through a variable density medium will appear distorted due to the refraction of light rays traversing the medium. The distortion of the dot pattern is typically estimated by cross-correlating an image of the dot pattern without the density gradients (called the reference image) with a distorted image viewed through the density gradients (called the gradient image) using techniques borrowed from Particle Image Velocimetry (PIV) [1]–[5]. Alternatively, the distortion can also be estimated using optical flow algorithms [6].

Low spatial resolution has been traditionally one of the limitations of BOS compared to the traditional schlieren technique, [7], [8] and is due to the large interrogation window sizes required for the PIV-type cross-correlation algorithms to ensure sufficient signal to noise ratio for the measurements [9], [10]. While multi-pass interrogation schemes and window overlap can increase the spatial resolution [11]–[13], adjacent vectors still have some spatial dependence and do not constitute purely independent measurements. Further, correlation methods have been shown in PIV to suffer from bias and random errors in regions with sharp displacement gradients due to peak broadening and peak splitting. [14], [15]

An alternative processing approach that can increase the spatial resolution is tracking individual dots from one image to the next, as done in Particle Tracking Velocimetry (PTV) applications [16]–[25]. Despite the popularity of PTV methods, such analysis has not received attention for BOS images. The primary factor controlling the performance of PTV methods is the ratio of particle displacement across images to inter-particle distance in the same image, because it affects the reliability of matching the same particle between the two frames. Since typical displacements in PTV applications are about 10 pixels, they are traditionally limited to low seeding densities. However, the displacements are typically very low in BOS applications (< 2-3 pixels in most cases), so large dot densities can be used before the accuracy of the dot matching procedure is affected. For example, even with 20 dots in a 32x32 pixel window, the inter-dot distance is still about 3-4 pixels if a dot is about 3 pixels in diameter, so the ratio of dot displacement to inter dot distance is low enough to ensure reliable measurements. Perhaps more importantly, the dot patterns used for BOS experiments are manufactured, and hence all the information about the dots such as their location, size and number are known. In addition, since there is no out of plane motion, the tracking method can be applied in an iterative manner till all the dots in the frame have been tracked, to achieve near 100% vector yield. Due to these reasons, several of the constraints that are typical of standard PTV measurements are not present in BOS, and tracking can be performed with high accuracy and yield even at large dot densities. Finally, the displacement field in BOS is irrotational as opposed to traditional PTV applied to free moving tracer particles in a flow, and hence, it can be described by a single scalar potential. This provides an opportunity to improve BOS measurements, especially in outlier detection, similar to divergence based filtering applied in PIV. The advantage of tracking methods for BOS has also been noted by Charruault et. al. [26] who proposed a tracking algorithm for BOS based on Voronoi cells, and showed that their tracking approach can measure larger image deformations compared to correlation when applied to an air-cavity interface.

One contribution of this paper is to recognize that tracking methods are well suited for BOS measurements due to low displacements typically encountered in these experiments, and also because the dot locations are already known. In addition, the tracking method proposed in this paper is robust to image noise, as it does not require an intensity threshold to detect the peaks, but instead utilizes the prior information about the location of dots on the target. For 15-20 dots in a 32x32 window, dot tracking will result in nearly an order of magnitude more vectors compared to correlation processing, and improve accuracy in displacement estimation in regions involving sharp changes in density.

In the following sections, we will introduce a dot tracking methodology for BOS, and compare its performance with the traditional cross-correlation method using synthetic BOS images of buoyancy-driven turbulence and experimental images of the flow field in the exit plane of a converging-diverging nozzle.

5.2 Dot Tracking Methodology

A schematic of the dot tracking methodology is shown in Figure 5.1. We first describe the standard tracking method, which consists of three steps, (i) particle identification, (ii) sizing and centroid estimation and (iii) tracking.

In standard tracking applications, the particles/dots in the image are isolated from the background using intensity thresholding and segmentation procedures. This can be done using a static intensity threshold or a dynamic threshold using a dilatation-erosion procedure, where the threshold is systematically varied to identify overlapping dots [17] [27]. The main limitation common to all these methods is the choice of the intensity threshold which can either lead to missed particles/dots if the threshold is high or falsely identified particles/dots if the threshold is low. This becomes especially problematic in cases with varying background illumination where the same threshold could be “high” in one part of the image with low illumination, and “low” in other parts of the image with higher background illumination. It also makes the method more error prone in the presence of image noise, due to noisy pixels being falsely identified as particles/dots.

Next in the sizing step, the geometrical properties (centroid and diameter) of the identified particles/dots are estimated to sub-pixel resolution. This can be accomplished using a variety of schemes ranging from a geometrical/intensity-weighted centroid to Gaussian sub-pixel fitting schemes such as the Three/Four Point Gaussian fits and the Least Square Gaussian fit. [28]

Finally in the tracking step, for each dot in the first frame, its corresponding match in the second frame is estimated using a nearest neighbor algorithm. While the nearest neighbor is typically defined as the dot in the second frame that lies closest to the estimated location of the dot in the first frame, it can be generalized using a multi-parametric approach where other properties of the dot such as the peak intensity and diameter can be included to define a weighted residual. The dot in the second frame having the lowest weighted residual and within a pre-defined search radius is defined as the match of the given dot in the first frame, and the dot displacement between the two frames is calculated. [17]

The primary novel contribution of this work is to recognize and utilize in an optimal fashion, the prior information about the dot pattern that is available from the target fabrication, and use this information to improve the overall accuracy and robustness of the method. In the identification step, instead of choosing an intensity threshold to separate from the dots from the background, we use the known location of the dots on the target, and the mapping function of the camera (obtained from calibration) to project the dot locations on the image plane and create a window around this location. The mapping function of the camera can be determined using a calibration process, and a polynomial mapping function as proposed by Soloff et. al. is used in this work. [29] The size of the window is chosen to be slightly larger than the diameter of the dot, where the dot diameter can either be specified beforehand based on the manufacturing details or can be calculated from the diameter of the cross-correlation peak ($d_p = d_{CC}/\sqrt{2}$). [30]

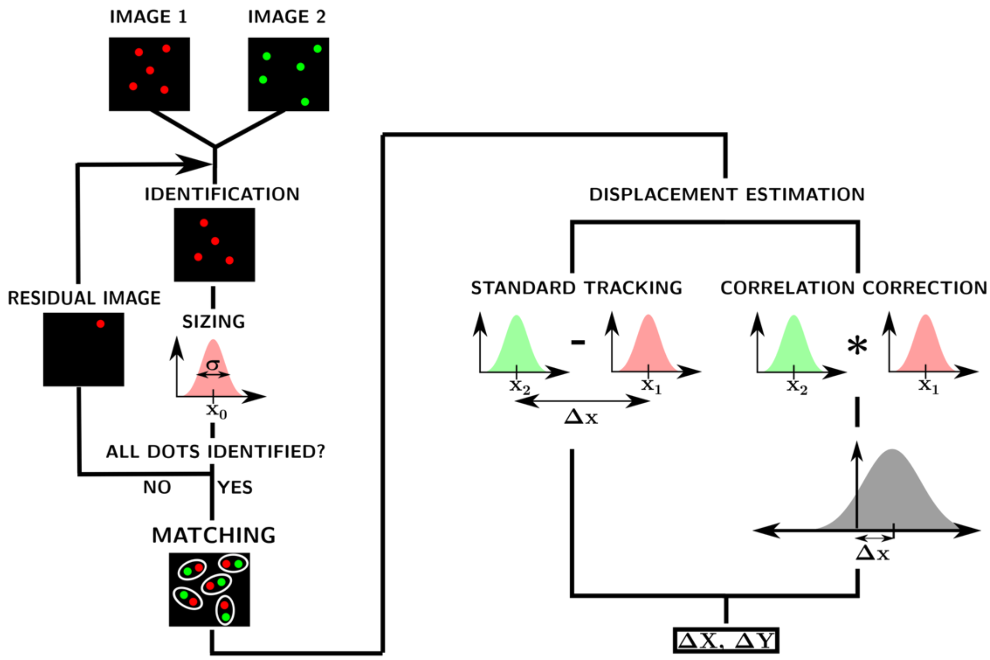

Figure 5.1. Schematic of the proposed Dot Tracking Methodology for BOS.

This window will contain pixels corresponding to the true dot as well as noisy pixels. To separate the dot from the noisy pixels, we use the dynamic segmentation procedure based on erosion-dilatation proposed by Cardwell et. al. [17] to segment the window of pixels to create pixel blobs. In cases where more than pixel blob is detected, we sort the pixel blobs based on their pixel area, peak intensity and distance of the peak from the predicted dot location. We calculate a weighted average of the three properties defined as,

$$C_p = \frac{\left(W_A * \left(\frac{A_p}{max(A_p)}\right) + W_I * \left(\frac{I_p}{max(I_p)}\right) + W_{\Delta x} * \left(1 - \frac{\Delta x_p}{max(\Delta x_p)}\right)\right)}{W_A + W_I + W_{\Delta x}} \quad \textbf{(30)}$$

where $A_p, I_p, \Delta x_p$ are the pixel area, peak intensity and distance respectively for the p^{th} blob, and $W_A, W_I, W_{\Delta x}$ are the associated weights. The pixel blob with the highest weighed average is considered to the true dot and the pixels corresponding to the other blobs are set to zero. For the analysis reported in this paper, the weights were set to 1/3 (equally weighted), but these can be changed for other situations. Once the pixel map for the dot has been extracted, a centroid estimation procedure is performed based on subpixel fitting. An example of this procedure is shown in Figure 5.2.

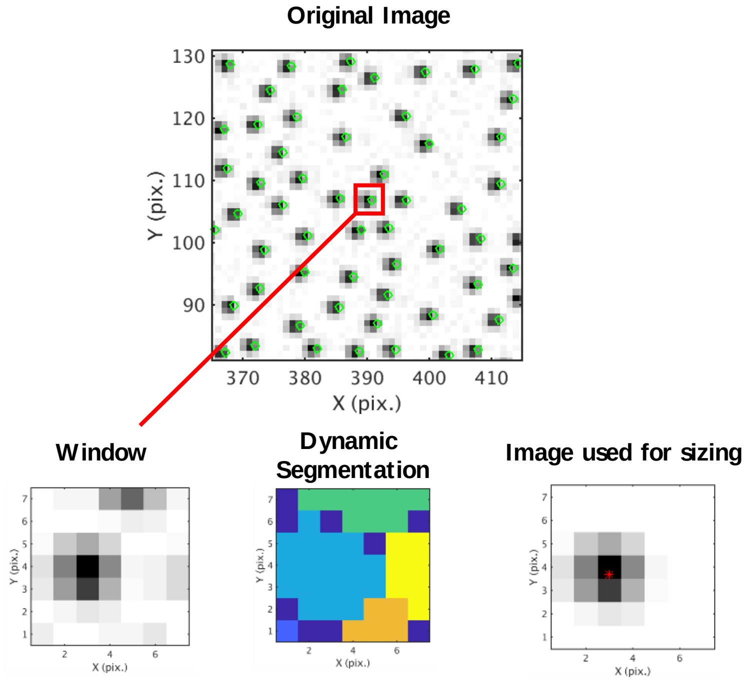

Figure 5.2. Illustration of the dot identification step using prior information about the dot location.

While it is straightforward to see that this approach will work for the reference image (without density gradients), it will also work for the gradient image (with density gradients), because the dot displacements are generally very small (< 2 pix.). Hence the actual location of the dot in the second frame will still be quite close to the predicted location, and since the window is taken to be larger than the dot diameter, it will be large enough to enclose the dot in the second frame as well. In situations where the displacements are greater, a hybrid tracking approach can be used where the displacements obtained from a coarse correlation pass can be used to estimate the location of the dot in the second frame. For the synthetic and experimental images considered this paper, this was not required.

Further, the identification and sizing steps can be performed in an iterative manner to ensure that all the dots on the target have been located. This is done by creating a residual image at the end of each iteration by removing the intensity contribution from the identified dots, as shown in Figure 5.1. The intensity of the residual image is given by,

$$I^{k+1} = I^k - \sum_{p=1}^{N_p^k} I_{0,p} \exp\left[-\left\{\frac{\left(X - X_p\right)^2 + \left(Y - Y_p\right)^2}{2\eta_p^2}\right\}\right] \qquad \textbf{(31)}$$

where I^k is the image intensity after k iterations, p is the dot index, N_p^k is the number of dots identified in the k^{th} iteration, and X_p, Y_p, η_p and $I_{0,p}$ are the positions, diameter and the peak intensity of the p^{th} identified dot. In this way, we are able to improve the accuracy of the method by avoiding incorrect matches and displacement errors due to failed identifications.

We also propose an improvement to the displacement estimation step after the dot matching procedure. Traditionally the displacement is estimated by subtracting the centroids of the two matched particles/dots, but this is error prone because the subpixel fitting procedure is highly sensitive to noise leading to a large position error. This will in turn lead to increased errors in the calculation of the displacements, density gradients and as well as the density field from 2D integration of the density gradients. Further, since the displacements in BOS experiments are typically low, this also severely limits the dynamic range of the measurement. To alleviate this problem, we perform a correlation of the intensity maps of the dots in the two frames to estimate the displacement, as the noise in the pixels is expected to be uncorrelated between the two frames. The intensity maps used are the ones obtained at the end of the identification process where the pixels corresponding to noise/other peaks have been zeroed out, to further improve the correlation signal to noise ratio. In addition, a minimum subtraction operation is also performed where the minimum intensity is taken from the dot window prior to zeroing out the noisy pixels. We refer to this step as a "correlation correction" and in this way we are able to combine the spatial resolution benefit of the tracking method with the noise robustness of the correlation method. As the correlation windows are small (~ 5x5 pix.), we perform this using a direct correlation computation without the use of FFT acceleration, to avoid windowing based artifacts on the processing. This step is illustrated in Figure 5.3.

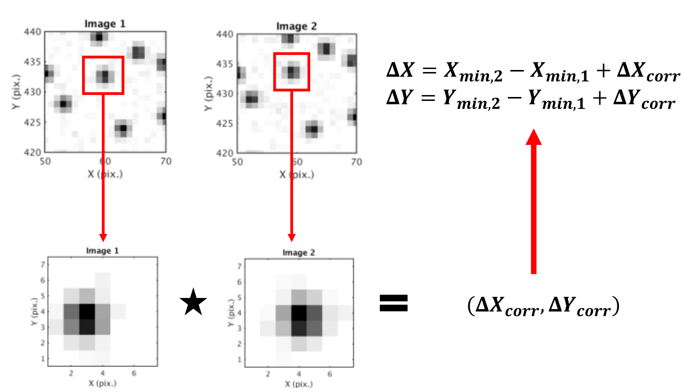

Figure 5.3. Displacement estimation by correlating the intensity maps of the two matched dots.

In the following sections, we will apply this tracking methodology to both synthetic and experimental BOS images and show a substantial improvement in the accuracy, precision and spatial resolution of the results.

5.3 Error Analysis with Synthetic Images

To provide a baseline for comparing the performance of the correlation and tracking methods, an error analysis was first performed using synthetic images rendered with density fields obtained from Direct Numerical Simulation (DNS) data of homogeneous buoyancy driven turbulence performed by Livescu et. al., [31], [32] and available at the Johns Hopkins turbulence database. [33], [34]. The flow involves sharp changes in density over small spatial regions, and hence provides a suitable test case for assessing the spatial resolution of the processing schemes.

5.3.1 Image Generation Methodology

The synthetic BOS images are rendered using a ray tracing-based image generation methodology described in more detail in Rajendran et. al. (2018). [35] The BOS experiment is simulated by generating light rays from the dot pattern and traced through the density gradient field and optical elements to the camera sensor. The trajectory of the light rays through the density gradient field is calculated by solving Fermat's equation:

$$\frac{d}{d\xi}\left(n\frac{d\vec{x}}{d\xi}\right) = \nabla n \tag{32}$$

using a 4th order Runge-Kutta algorithm following established methods in gradient-index optics literature.[36], [37] The refraction through the lens is modelled by Snell's law and the diffraction pattern on the image sensor is modeled using a Gaussian distribution as in synthetic PIV image generation. [38], [39] The computationally intensive ray tracing process is parallelized using Graphics Processing Units (GPUs) and images rendered using this methodology display real world features such as blurring and optical aberrations which can be adjusted in a controlled manner. This methodology has been tested and validated using known density fields. [35] At the end of the ray tracing simulations, the final light ray deflections on the camera sensor for all rays originating from a dot are averaged and used as ground truth for displacement of that dot. This process is repeated for all dots on the pattern to estimate the true displacements throughout the field of view.

Two dimensional (x, y) slices of the flow field from five time instants were chosen, and for each time instant, a three-dimensional density volume was constructed by stacking the same two-dimensional slice along the z-direction, thereby ensuring that the gradient of density in the z direction was zero. This was done to account for the depth integration limitation of BOS measurements and decouple it from the error analysis. Further, the density data was multiplied by 1.225 kg/m^3 to simulate air and enclosed in a three-dimensional volume of size 32 mm x 32 mm x 10 mm.

Images of the density field at these snapshots are shown in Figure 5.4, along with the density gradient, the theoretical light ray displacements and the light ray displacements from the ray tracing simulations. The theoretical displacements were calculated by

$$\begin{aligned} \Delta\vec{X} &= \frac{MZ_D}{n_0}\int_{z_i}^{z_f} \nabla n \, dz \\ &\approx \frac{MZ_D K}{n_0} \, (\nabla\rho)_{avg} \Delta z \end{aligned} \tag{33}$$

where $\Delta\vec{X}$ is the theoretical deflection of a light ray, $(\nabla\rho)_{avg}$ is the path-averaged value of the density gradient, K is the Gladstone-Dale constant, n_0 is the ambient refractive index, and Δz is the thickness of the density gradient field. [1] For the present simulations, the values of the parameters were $M = 0.12$, $Z_D = 0.25$ m, and $\Delta z = 10$ mm.

To ensure that the synthetic image analysis is consistent with the experimental data to be shown in the following sections, we generated BOS images with a regular grid of dots on the target. Due to optical distortions, the final light ray locations will be scattered on a warped grid on the image plane corresponding to the image of the dots. The deflections at these locations are interpolated to a regular grid for displaying the figures shown in Figure 5.4, where the contours of simulated light ray deflections are seen to correspond reasonably well to the theoretical displacements, and in both cases the regions of large displacements correspond to regions of large density gradients. The simulated light ray deflections will not match the theoretical displacements exactly, partly due to 1) small angle approximations used in the theory and 2) the spatial resolution limitation of the experimental setup due to the finite angle of a ray cone emerging from the target. Both of these are well known characteristics of BOS experiments. [7] However, these features are common to the images processed by both the correlation and tracking algorithms, and these simulated light ray deflections are considered as the ground truth for conducting the error analysis.

For the present simulations, the dot diameter was 3 pixels and the dot density was 20 dots per 32x32 pixel window. As dot patterns can be manufactured in a controlled manner for BOS experiments, we use dot patterns without overlapping dots. For each snapshot of the DNS, ten image pairs were rendered, and the images were corrupted with zero-mean Gaussian noise with a standard deviation of 1, 3 and 5% of the peak image intensity.

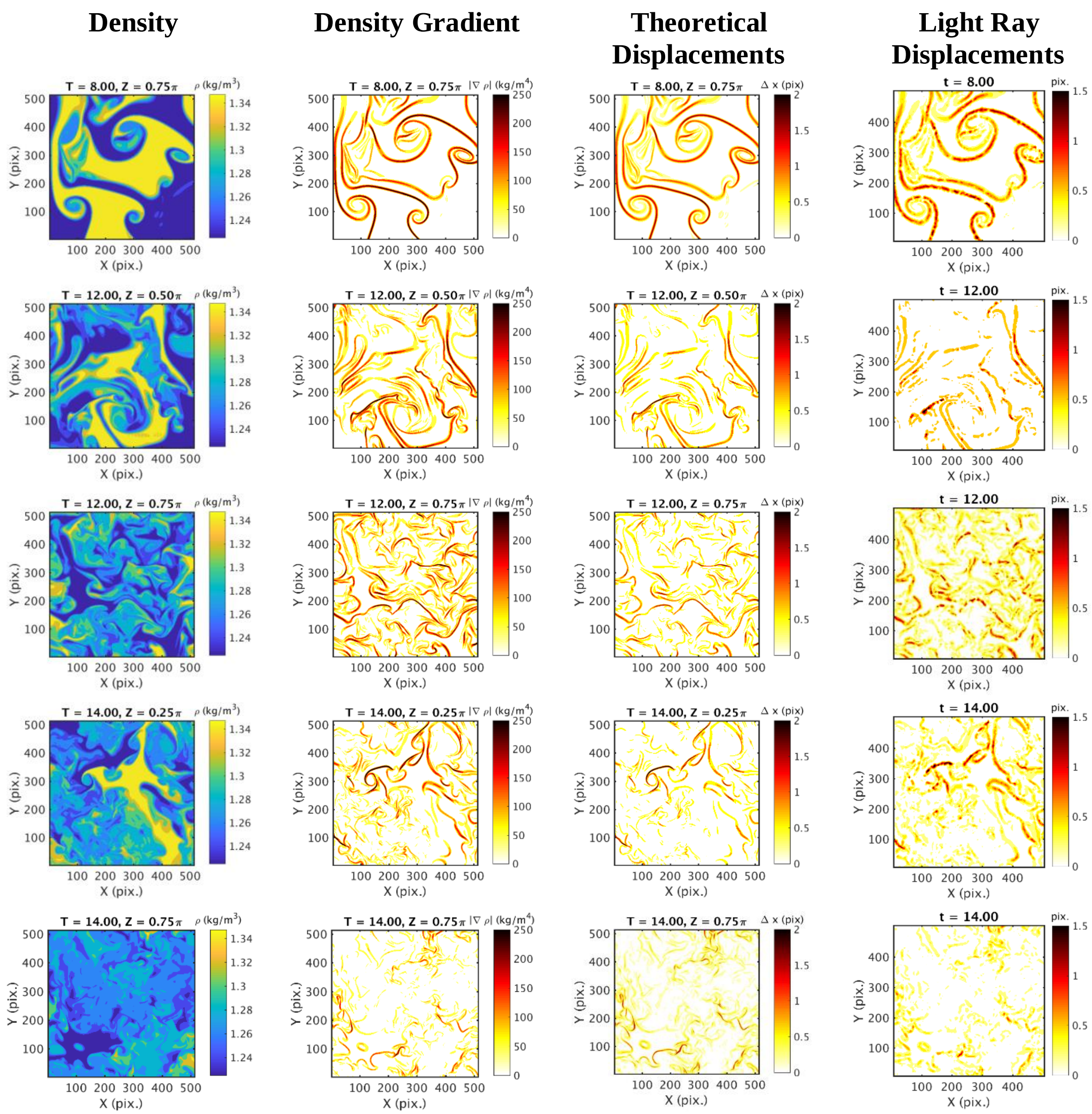

Figure 5.4. Contours of density, density gradients, theoretical displacements and simulated light ray displacements for the five snapshots of DNS data used in the error analysis.

5.3.2 Results

The images were processed using both traditional cross-correlation and the dot tracking method described in Section 3. For the correlation, a multi-grid window deformation method was used with a window size of 32x32 followed by 16x16 pix. without window overlap. For the tracking method a three-point Gaussian subpixel fit was used both for centroid estimation as well as for the displacement estimation using the correlation correction. Then the errors in the final displacements were calculated using the light ray deflection from the ray tracing as the ground truth. Further, the errors were divided into two groups depending on whether the true displacement in that region was above or below a certain threshold. This was done to differentiate the errors due to background image noise, from errors due to lack of spatial resolution. The threshold was chosen to be half the standard deviation of the histogram of *theoretical displacements*. For each noise level, about 500,000 vectors were used in calculating the error distribution, to ensure statistical convergence of the results.

The CDF of the error distribution is shown in Figure 5.5 for all the noise levels. For the case with zero noise, both tracking methods far outperform the correlation method, where nearly all the vectors have an error below 0.01 pixels as opposed to the correlation algorithm, where the error level corresponding to 90% of the vectors is over 0.1 pixels, which is an order of magnitude more than the tracking. Further, the error levels for the correlation are seen to be higher for vectors above the displacement threshold, as these lie in regions with sharp displacement gradients that cannot be captured by the correlation algorithm.

As the noise level increases, the errors for the tracking methods are seen to increase while they remain nearly the same for the correlation method. The main contribution to error in the tracking method is the position error from the centroid estimation, which is sensitive to image noise. However, the correlation method is robust to image noise in general, because the pixel noise across the two frames will be uncorrelated and hence have a lesser effect on the signal to noise ratio of the correlation plane.

The performance of the processing algorithms can be further understood from looking at the error distributions for the vectors above and below the threshold separately. For the higher noise levels, it is seen that the error from tracking approaches the error from correlation for vectors below the threshold, as the error in this region is dominated by position error due to image noise. However, the tracking methods still outperform the correlation method for vectors above the threshold as the error in this region is dominated by spatial resolution requirements due to sharp displacement gradients in the flow field. The tracking methods are seen to be robust to this effect, with nearly the same noise levels for vectors both above and below the threshold.

Finally, it is seen that the tracking method with the correlation correction performs best even for the highest image noise as it combines the spatial resolution benefit of tracking and the smoothing effect of the correlation. This is particularly evident from Figure 5.5 (g) where it is seen that for vectors below the threshold, the noise level is so high that the pure tracking method performs poorer than the correlation, however tracking with correlation correction still maintains the same error level as full correlation. For vectors above the threshold the tracking method with correlation correction is still able to maintain the high spatial resolution and performs best overall. Also shown are the errors in the estimates of the gradient of displacements, corresponding to the second derivative of density. This quantity is needed to perform 2D integration of the density gradient field by solving the Poisson equation, which requires the calculation of the Laplacian of the density field. [40] Again, the dot tracking methods far outperform traditional cross-correlation for all noise levels both above and below the threshold, possibly because the displacement gradient is even more sensitive to the spatial resolution of the schemes.

The results of this analysis using synthetic images of physically realistic flow fields demonstrate that the proposed tracking approach, with non-overlapping dots, apriori identification and correlation correction provides a significant reduction in error compared to the conventional cross-correlation method as well as a large improvement in the spatial resolution for flow fields with sharp density gradients.

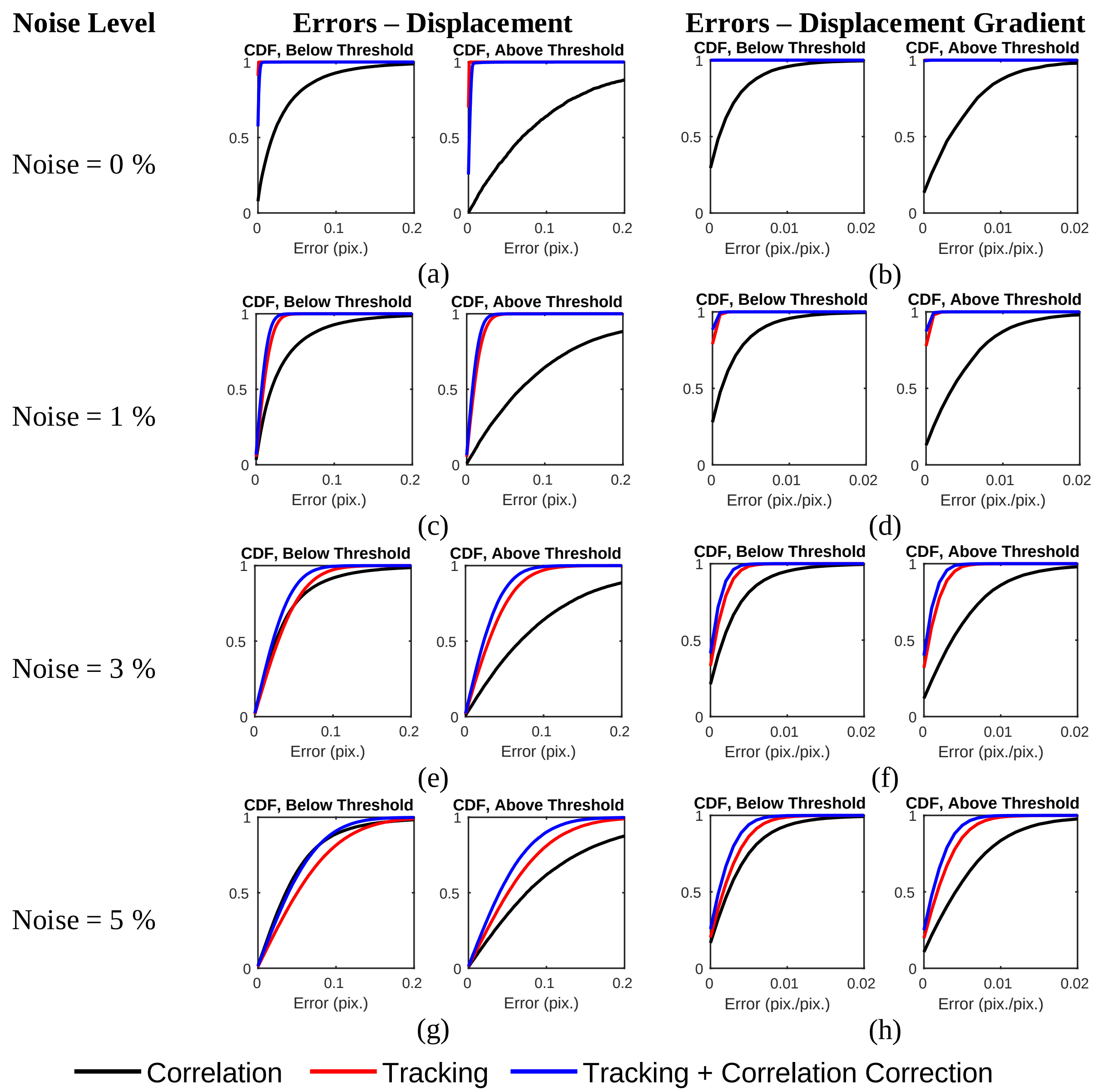

Figure 5.5. Error levels for the displacement and displacement gradient estimates obtained by the correlation and tracking methods.

5.4 Application to experimental images of flow exiting a converging-diverging nozzle

The tracking methodology was also applied to visualize the exit plane of a converging-diverging nozzle for various pressure ratios. This flow field was chosen because of the presence of shocks, expansion fans and other interesting small scale features that appear at high pressure ratios, and serve as a good assessment of the spatial resolution offered by the algorithms. The nozzle geometry along with the experimental layout and a sample image of the target, is shown in Figure 5.6. A regular grid of dots was printed on a transparency and back-illuminated with an LED to serve as the dot pattern. The dots were 0.15 mm in diameter and had a spacing of 0.15 mm, designed to provide a dot diameter of 3-4 pixels to improve the subpixel position estimation, and a dot spacing of about 6-8 pixels to have about 15-20 dots in a 32x32 window for high spatial resolution. The chamber pressure was varied from 0 to 60 psi in steps of 5 psi, while the exit pressure was maintained at atmospheric conditions (14.7 psi). For each pressure condition, the flow was allowed to reach steady state before capturing the images. The images were recorded using a PCO Pixelfly camera and a zoom lens set at a focal length of 32 mm. A sample zoomed-in image of the dot pattern for one of the cases show the sharp displacement gradients involved in this flow field. The changes in displacements happen over a very short length scale, leading to blurring of the dot images. Therefore this case serves as a good test to gauge the spatial resolution increase obtained by the tracking method.

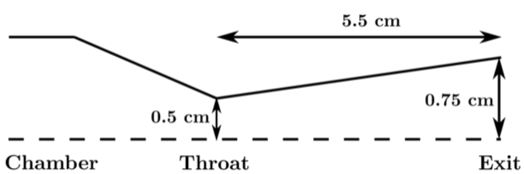

Nozzle Geometry

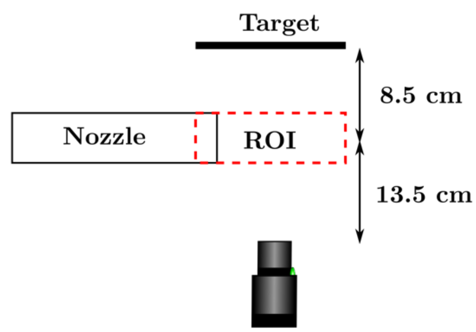

(b) Experimental Layout (Top View)

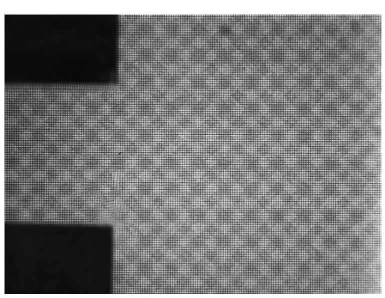

(c) Sample image of the BOS dot pattern

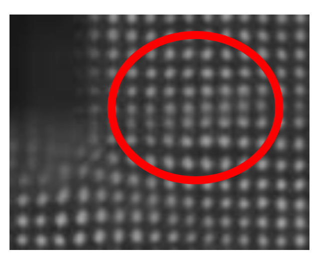

(d) Zoomed-in view of region in the FOV with sharp displacement gradients

Figure 5.6. Details of the experimental setup used to visualize the flow in the exit plane of a converging-diverging nozzle.

The images of the dot pattern with and without the flow were analyzed using the tracking and correlation methods described before. For correlation, the images were processed using a two-pass window deformation approach [12] with 32x32 pix. interrogation windows with 50% overlap, and with smoothing and universal outlier detection (UOD) [41] based validation for the first pass. The final pass results are validated by a threshold validation of 3 pix displacement. The interrogation window size was chosen to 32x32 pix. to ensure that sufficient number of dots were contained in an interrogation window for measurement reliability [9]. For tracking, to initialize the dot identification procedure, the dot locations on the target were calculated using a third order mapping function of the imaging system proposed by Soloff et. al. [29] to account for higher order lens distortions. As the dot pattern used in the experiment resembles a typical calibration target albeit with a higher number of dots, the mapping function of the imaging system was first calculated using the position of every fourth dot in the image, obtained using an intensity-weighted-centroid based subpixel estimation scheme to reduce computational effort. Further, as there is no out of plane motion in BOS measurements, the mapping function was only calculated based on one z-plane. Based on the mapping function, the locations of all the intermediate dots were calculated and used to initialize the multi-parametric dot identification procedure with the dynamic segmentation and the centroids are estimated using a Least Square Gaussian subpixel fit. At the end of the tracking procedure, the correlation correction was performed on the tracks and the subpixel estimation on the correlation plane was again performed using a Least Square Gaussian fit. The displacement contours for two chamber pressures are shown in Figure 5.7.

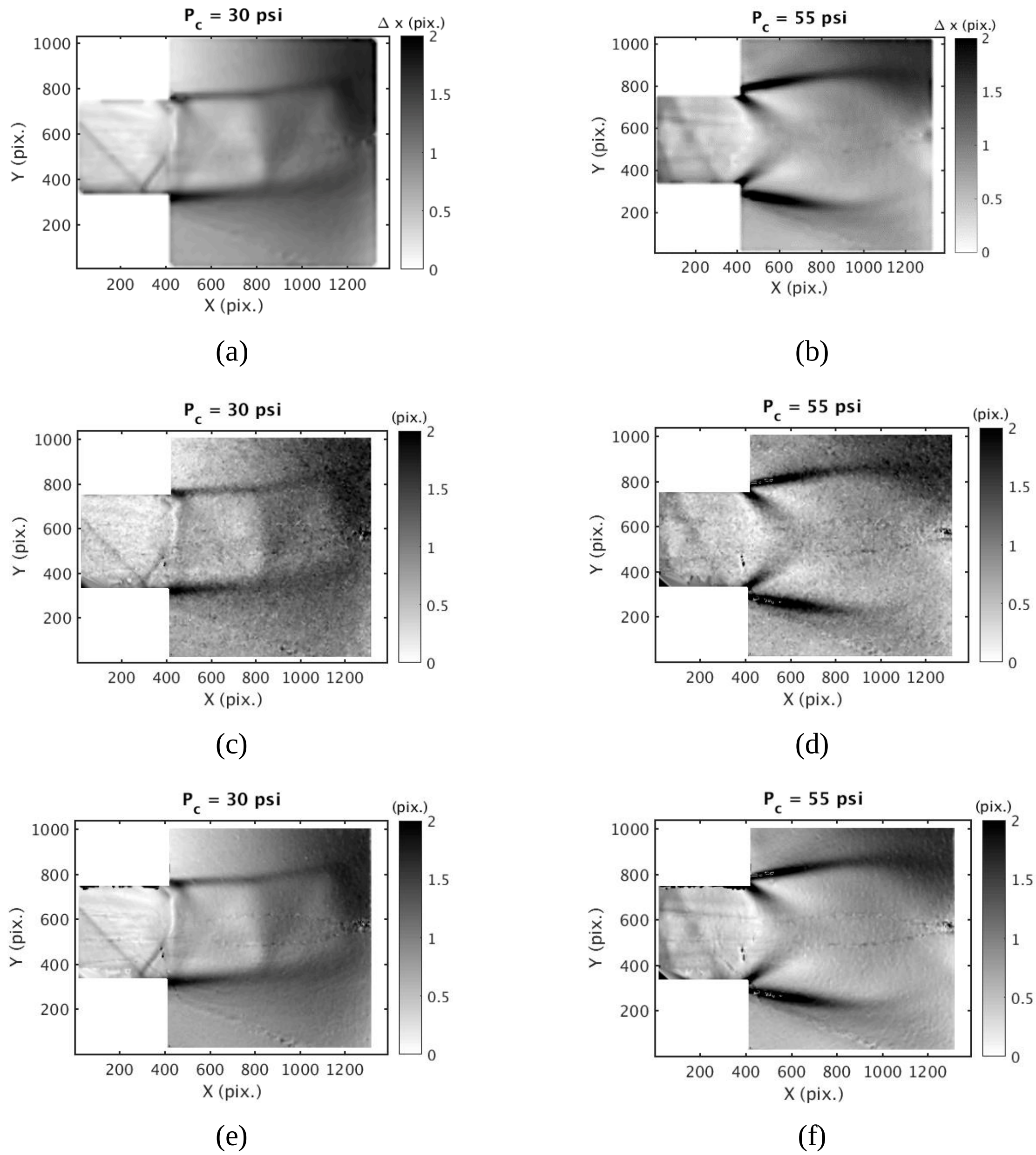

Figure 5.7. Flow in the exit plane of a converging-diverging nozzle obtained from the different processing methods. Left column is for a chamber pressure of 30 psig, and right column is for 55 psig. (a)-(b) Correlation, (c)-(d) Tracking without Correlation Correction, (e)-(f) Tracking with Correlation Correction, (g) Line plot of displacements along X for Y = 600 pix., (h) Line plot of displacements along Y for X = 500 pix.

Figure 5.7 continued

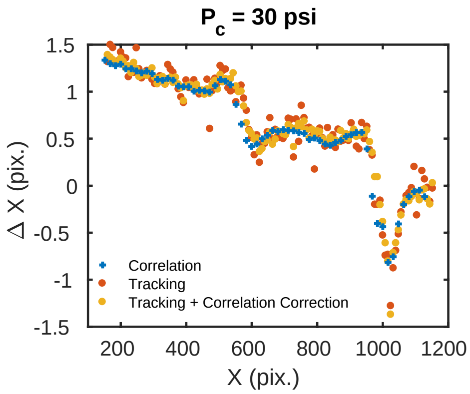

(g)

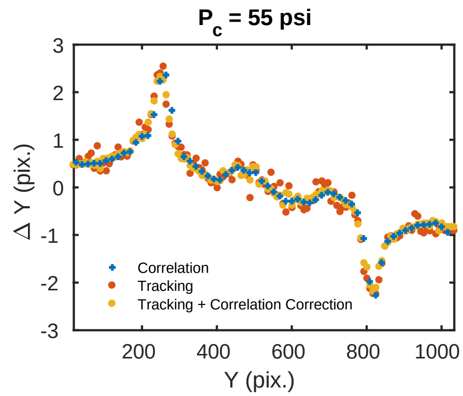

(h)

From the displacement fields it can be seen that the results from the tracking analysis shown in Figure 5.7 (c)-(f) better capture small-scale features of the flow as compared to the correlation results shown in (a)-(b), which appear highly smoothed. Further it is seen that the tracking with correlation correction, shown in Figure 5.7 (e)-(f) provides a smoothing of the noisy displacement field compared to (c)-(d) while maintaining the high spatial resolution. The increase in spatial resolution is also evident from the line plots shown in (g)-(h) where tracking is able to better capture the sharp jumps in the displacement field.

To quantify the improvement offered by the tracking-based methods, statistical analysis was performed to estimate the dynamic range of the displacement gradients measured by the three processing methods. The displacement gradients are calculated in the post-processing of BOS data to perform density integration, and are sensitive to the spatial resolution of the measurements. For the tracking results, the displacements were first interpolated onto a regular grid using a natural neighbor interpolation based on Delaunay triangulation [42], with the grid spacing chosen to be 8 pixels corresponding to the dot spacing in the images. The displacement gradients for all three methods were estimated using a noise optimized 4th-order compact Richardson finite difference scheme proposed by Etebari and Vlachos [43].

Figure 5.8 shows the PDF and CDF of displacement gradients evaluated over the entire field of view for both pressure conditions using the three processing methods. The flow fields considered here exhibit sharp displacement gradients confined to small portions of the field of view. Therefore, a successful processing methodology must capture both the large displacement gradients in the regions with the shocks and expansion fans, as well as the extended zero displacement regions, due to high spatial confinement of these features. Observing both figures, it can be seen that the range of displacement gradients measured by the correlation-based method is lower than the tracking methods due to a lack of spatial resolution. It can be also seen that the pure tracking method results in a very broad histogram with a short peak at 0. This is a direct result of the effect of image noise on the subpixel centroid estimation as well as due to dot blurring, and hence differences in displacements between successive dots due to intensity fluctuations are also being picked up as displacement gradients. On the other hand, the tracking method with correlation correction is able to maintain both a strong peak at 0, and provide a large displacement gradient range at the same time.

Further, the dynamic range of the measurements is also calculated as the ratio of the maximum displacement gradient to the minimum resolvable displacement gradient of the method. The maximum displacement gradient is calculated from the experimental data and the minimum displacement gradient which represents the noise floor of the measurements, is estimated from the error analysis presented in Section 5.3.2 for each processing method. The error analysis results are used to estimate the noise floor because a ground truth of the given flow field is not available for estimating an error. The noise floor is defined as the root mean square (RMS) of the displacement gradient error corresponding to the vectors below the threshold, and the errors corresponding to the highest image noise level (= 5%) are used for this calculation, as this noise level was representative of the experimental images and provides a conservative estimate. The results in Table 5.1 show that the tracking methods offer a large improvement in the dynamic range as compared to the standard cross-correlation method. While the pure tracking method results in an improved spatial resolution as seen in Figure 5.7, it also suffers from a higher noise floor, but the correlation correction is able to minimize this effect and achieve a four-fold improvement in the dynamic range as compared to the standard correlation.

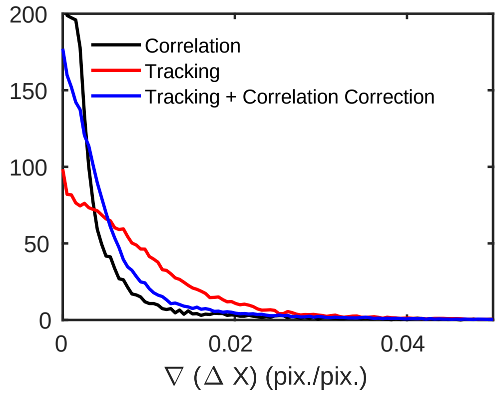

(a) PDF of the displacement gradient distribution

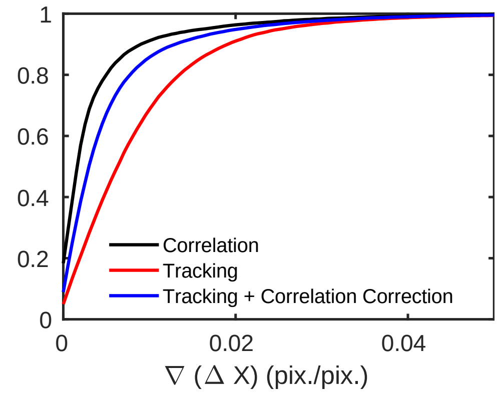

(b) CDF of the displacement gradient distribution

Figure 5.8. Distribution of displacement gradients in the field of view for both flow fields obtained by the three processing methods.

Table 5.1. Dynamic range of the displacement gradients obtained using the three processing methods.

	Min Displacement Gradient (pix./pix.)	Max Displacement Gradient (pix./pix.)	Dynamic Range (= Max/Min)
Correlation	0.01	0.086	8.55
Tracking	0.004	0.123	30.76
Tracking with Correlation Correction	0.003	0.107	35.59

Overall, the dot tracking methodology with identification based on prior dot location and correlation correction appears to be more reliable when applied to BOS experimental data using dot patterns of high dot densities, while also increasing the spatial resolution of the measurements. The method is able to resolve displacements in regions with sharp gradients, while simultaneously maintaining a low noise floor, resulting in a four-fold improvement in the dynamic range. While it is possible that the results from the standard correlation analysis can be improved by using smaller windows and increased window overlap, adjacent vectors will still have overlapping information and do not constitute independent information. Further, the interrogation windows need to be centered on the dot centroids to avoid clipping the dot image and introducing Fourier-transform based errors due to aliasing and spectral leakage [44].

5.5 Conclusions

In this paper we proposed a dot tracking methodology for processing BOS images with high dot density based on two features of BOS experiments: (1) low displacements (2-3 pixels) and (2) availability of prior information about dot locations and size from manufacturing. We use the prior information about the dot locations to perform dot identification and sizing without the need for an intensity threshold, making the method more robust to image noise. We also proposed an improvement to the final displacement estimation, where we correlate the intensity maps of the matched dots instead of subtracting their centroid locations, to improve the performance in high noise situations. In this way we are able to combine the high spatial resolution benefit of tracking with the noise robustness property of correlation methods.

We analyzed the performance of this method and compared it to the conventional cross-correlation algorithm using synthetic and experimental BOS images. For synthetic BOS images of buoyancy-driven turbulence, the tracking methods far outperformed the correlation method especially with low image noise and in regions with a requirement for high spatial resolution. For higher noise levels the errors in the tracking algorithms increased due to the position error from the subpixel fit being sensitive to image noise; however the tracking method with the correlation correction at the end was robust to this effect as the final displacement estimation does not depend on the centroid estimation process, and performed best overall. For experimental BOS images of the flow field in the exit of a converging-diverging nozzle, the tracking methods were able to resolve sharp changes in the density field in the presence of shocks and expansion fans, and improved the dynamic range in the displacement gradient measurement.

The proposed method is applicable to BOS experiments which involve small dot displacements (2-3 pix. or < dot spacing), and where the targets are fabricated in a controlled manner such that the dot locations are known. This opens up a new processing paradigm for BOS measurements using dot tracking methods, and helps in improving the spatial resolution limitation of BOS in comparison to qualitative schlieren measurements. This will enable improved investigation of flows with small scale features such as shocks, expansion fans and small scale compressible turbulence.

A limitation of the spatial resolution improvement offered by the tracking method is in situations where there is strong displacement gradients on a scale equal to or less than the dot diameter itself, which will lead to blurring of the dot image as seen in Figure 5.6 (d). In this case the dot tracking method can only provide an average displacement in this region. Therefore further improvements in the methodology can include a method to extract additional information about the displacement/density gradient field from the blurred shape of the dot. It is likely that the blurring is related to second-order gradients of the density field.

Another limitation of the method is it requires non-overlapping dots to reduce position errors in the identification and sizing process. In situations where the dot pattern cannot be manufactured in a controlled manner, the traditional correlation based approach may be preferable. The correlation based algorithms may also perform better when used with very dense or speckle type dot patterns thus providing the ability to use smaller interrogation windows. However the dot patterns still need to be on the diameter of about 3 pixels for accurate subpixel fitting, and hence this places a limit on the maximum achievable dot density. It is not clear if the correlation algorithms with speckle patterns and small windows can achieve the same spatial resolution as the tracking based method with dense non-overlapping dots.

Finally, a code package implementing the dot tracking method proposed in this paper is available at: https://github.rcac.purdue.edu/lrajendr/dot-tracking-package so that all readers can assess the contribution and benefit from it.

5.6 Acknowledgment

Ravichandra Jagannath is acknowledged for help with the nozzle experiments. This material is based upon work supported by the U.S. Department of Energy, Office of Science, Office of Fusion Energy Sciences under Award Number DE-SC0018156. This work was also supported by NSF 1706474.

5.7 References

[1] M. Raffel, “Background-oriented schlieren (BOS) techniques,” *Exp. Fluids*, vol. 56, no. 3, pp. 1–17, 2015.

[2] G. Meier, “Computerized background-oriented schlieren,” *Exp. Fluids*, vol. 33, no. 1, pp. 181–187, 2002.

[3] S. B. Dalziel, G. O. Hughes, and B. R. Sutherland, “Whole-field density measurements by ‘synthetic schlieren,’” *Exp. Fluids*, vol. 28, no. 4, pp. 322–335, 2000.

[4] H. Richard and M. Raffel, “Principle and applications of the background oriented schlieren (BOS) method,” *Meas. Sci. Technol.*, vol. 12, no. 9, pp. 1576–1585, 2001.

[5] G. S. Settles and M. J. Hargather, “A review of recent developments in schlieren and shadowgraph techniques,” *Meas. Sci. Technol*, vol. 28, 2017.

[6] B. Atcheson, W. Heidrich, and I. Ihrke, “An evaluation of optical flow algorithms for background oriented schlieren imaging,” *Exp. Fluids*, 2009.

[7] M. J. Hargather and G. S. Settles, “A comparison of three quantitative schlieren techniques,” *Opt. Lasers Eng.*, vol. 50, no. 1, pp. 8–17, Jan. 2012.

[8] G. E. Elsinga, B. W. Van Oudheusden, F. Scarano, and D. W. Watt, “Assessment and application of quantitative Schlieren methods: Calibrated Color Schlieren and Background Oriented Schlieren,” *Exp. Fluids*, vol. 36, no. 2, pp. 309–325, Feb. 2004.

[9] R. Keane and R. J. Adrian, “Theory of cross-correlation analysis of PIV images,” *Appl. Sci. Res.*, pp. 191–215, 1992.

[10] J. Westerweel, “Fundamentals of digital particle image velocimetry,” *Meas. Sci. Technol.*, vol. 8, no. 12, pp. 1379–1392, 1997.

[11] F. Scarano and M. L. Riethmuller, “Iterative multigrid approach in PIV image processing with discrete window offset,” *Exp. Fluids*, vol. 26, no. 6, pp. 513–523, 1999.

[12] F. Scarano, “Iterative image deformation methods in PIV,” *Meas. Sci. Technol.*, vol. 13, no. 1, pp. R1–R19, 2002.

[13] F. Scarano and M. L. Riethmuller, “Advances in iterative multigrid PIV image processing,” *Exp. Fluids*, vol. 29, no. 7, pp. S051–S060, 2000.

[14] J. Westerweel, “On velocity gradients in PIV interrogation,” *Exp. Fluids*, vol. 44, pp. 831–842, 2008.

[15] C. J. Kahler, S. Scharnowski, and C. Cierpka, “On the resolution limit of digital particle image velocimetry,” *Exp. Fluids*, pp. 1629–1639, 2012.

[16] M. Marxen, P. E. Sullivan, M. R. Loewen, B. J. Èhne, and B. Jähne, “Comparison of Gaussian particle center estimators and the achievable measurement density for particle tracking velocimetry,” *Exp. Fluids*, vol. 29, no. 2, pp. 145–153, Aug. 2000.

[17] N. D. Cardwell, P. P. Vlachos, and K. A. Thole, “A multi-parametric particle-pairing algorithm for particle tracking in single and multiphase flows,” *Meas. Sci. Technol.*, vol. 22, no. 10, p. 105406, Oct. 2011.

[18] M. Ishikawa, Y. Murai, A. Wada, M. Iguchi, K. Okamoto, and F. Yamamoto, “A novel algorithm for particle tracking velocimetry using the velocity gradient tensor,” vol. 29, 2000.

[19] R. D. Keane, R. J. Adrian, and Y. Zhang, “Super-resolution particle imaging velocimetry,” *Meas. Sci. Technol.*, vol. 6, no. 6, pp. 754–768, Jun. 1995.

[20] T. Fuchs, R. Hain, and C. J. Kähler, “Non-iterative double-frame 2D/3D particle tracking velocimetry,” *Exp. Fluids*, vol. 58, no. 9, pp. 1–5, 2017.

[21] Y. C. Lei *et al.*, “A vision-based hybrid particle tracking velocimetry (PTV) technique using a modified cascade correlation peak-finding method,” *Exp. Fluids*, vol. 53, no. 5, pp. 1251–1268, 2012.

[22] A. V Mikheev and V. M. Zubtsov, “Enhanced particle-tracking velocimetry (EPTV) with a combined two-component pair-matching algorithm,” *Meas. Sci. Technol.*, vol. 19, no. 8, p. 085401, Aug. 2008.

[23] Y. Zhang, Y. Wang, B. Yang, and W. He, “A particle tracking velocimetry algorithm based on the Voronoi diagram,” *Meas. Sci. Technol.*, vol. 26, no. 7, 2015.

[24] C. Cierpka, B. Lütke, and C. J. Kähler, “Higher order multi-frame particle tracking velocimetry,” *Exp. Fluids*, vol. 54, no. 5, 2013.

[25] P. Ruhnau, C. Guetter, T. Putze, and C. Schnörr, “A variational approach for particle tracking velocimetry,” *Meas. Sci. Technol.*, vol. 16, no. 7, pp. 1449–1458, 2005.

[26] F. Charruault, A. Greidanus, and J. Westerweel, “A dot tracking algorithm to measure free surface deformations,” in *18th International Symposium on Flow Visualization*, 2018, p. paper 042.

[27] K. Ohmi and H.-Y. Li, “Particle-tracking velocimetry with new algorithms,” *Meas. Sci. Technol.*, vol. 11, no. 6, pp. 603–616, Jun. 2000.

[28] M. R. Brady, S. G. Raben, and P. P. Vlachos, “Methods for Digital Particle Image Sizing (DPIS): Comparisons and improvements,” *Flow Meas. Instrum.*, vol. 20, no. 6, pp. 207–219, 2009.

[29] S. M. Soloff, R. J. Adrian, and Z.-C. Liu, “Distortion compensation for generalized stereoscopic particle image velocimetry,” *Meas. Sci. Technol.*, vol. 8, no. 12, pp. 1441–1454, 1997.

[30] M. Raffel, C. E. Willert, S. T. Wereley, and J. Kompenhans, *Particle image velocimetry: a practical guide*. Springer, 2013.

[31] D. Livescu, C. Canada, K. Kalin, R. Burns, I. Staff, and Pulido, “Homogeneous Buoyancy Driven Turbulence Data Set,” no. 1, pp. 1–7, 2014.

[32] D. Livescu and J. R. Ristorcelli, “Buoyancy-driven variable-density turbulence,” *J. Fluid Mech.*, vol. 591, pp. 43–71, 2007.

[33] Y. Li *et al.*, “A public turbulence database cluster and applications to study Lagrangian evolution of velocity increments in turbulence,” *J. Turbul.*, vol. 9, no. December 2016, p. N31, 2008.

[34] E. Perlman, R. Burns, Y. Li, and C. Meneveau, “Data exploration of turbulence simulations using a database cluster,” *Proc. 2007 ACM/IEEE Conf. Supercomput. (SC ’07)*, 2007.

[35] L. K. Rajendran, S. P. M. Bane, and P. P. Vlachos, “PIV/BOS synthetic image generation in variable density environments for error analysis and experiment design,” *Meas. Sci. Technol.*, pp. 11–14, Apr. 2019.

[36] A. Sharma, D. V. Kumar, and A. K. Ghatak, “Tracing rays through graded-index media: a new method.,” *Appl. Opt.*, vol. 21, no. 6, pp. 984–987, 1982.

[37] C. Brownlee, V. Pegoraro, S. Shankar, P. McCormick, and C. Hansen, “Physically-based interactive schlieren flow visualization,” *IEEE Pacific Vis. Symp. 2010, PacificVis 2010 - Proc.*, pp. 145–152, 2010.

[38] M. Born and E. Wolf, *Principles of optics*, 6th ed. Pergamon Press, 1980.

[39] M. Raffel, C. E. Willert, S. T. Wereley, and J. Kompenhans, *Particle Image Velocimetry*. Berlin, Heidelberg: Springer Berlin Heidelberg, 2007.

[40] L. Venkatakrishnan and G. E. a. Meier, “Density measurements using the Background Oriented Schlieren technique,” *Exp. Fluids*, vol. 37, no. 2, pp. 237–247, 2004.

[41] J. Westerweel and F. Scarano, “Universal outlier detection for PIV data,” *Exp. Fluids*, vol. 39, no. 6, pp. 1096–1100, 2005.

[42] R. Sibson, “A brief description of natural neighbor interpolation,” in *Interpolating Multivariate Data*, V. Barnett, Ed. Chichester: John Wiley, 1981, pp. 21–36.

[43] A. Etebari and P. P. Vlachos, “Improvements on the accuracy of derivative estimation from DPIV velocity measurements,” *Exp. Fluids*, vol. 39, no. 6, pp. 1040–1050, 2005.

[44] A. C. Eckstein and P. P. Vlachos, “Assessment of advanced windowing techniques for digital particle image velocimetry (DPIV),” *Meas. Sci. Technol.*, vol. 20, no. 7, p. 075402, 2009.

6. UNCERTAINTY AMPLIFICATION DUE TO DENSITY/REFRACTIVE-INDEX GRADIENTS IN BACKGROUND-ORIENTED SCHLIEREN EXPERIMENTS

Lalit K. Rajendran[1], Sally P. M. Bane[1] and Pavlos P. Vlachos[2]
[1] Purdue University, School of Aeronautics and Astronautics, West Lafayette, USA.
[2] Purdue University, School of Mechanical Engineering, West Lafayette, USA.
This chapter has been published in Experiments in Fluids, and reproduced with permission.
DOI: https://doi.org/10.1007/s00348-020-02978-8

Abstract

We theoretically analyze the effect of density/refractive-index gradients on the measurement precision of Background Oriented Schlieren (BOS) experiments by deriving the Cramer-Rao lower bound (CRLB) for the 2D centroid estimation process. A model is derived for the diffraction limited image of a dot viewed through a medium containing density gradients that includes the effect of the experimental parameters such as the magnification and f-number. It is shown using the model that non-linearities in the density gradient field lead to blurring of the dot image. This blurring amplifies the effect of image noise on the centroid estimation process, leading to an increase in the CRLB and a decrease in the measurement precision. The ratio of position uncertainties of a dot in the reference and gradient images is shown to be a function of the ratio of the dot diameters and dot intensities. We termed this parameter the Amplification Ratio (A_F), and a methodology for reporting position uncertainties in tracking-based BOS measurements is proposed. The theoretical predictions of the dot position estimation variance from the CRLB are compared to ray tracing simulations, and agreement is obtained. The uncertainty amplification is also demonstrated on experimental BOS images of flow induced by a spark discharge, where it is seen that regions of high amplification ratio correspond to regions of density gradients. This analysis elucidates the dependence of the position uncertainty on density and refractive-index gradient induced distortion parameters, provides a methodology for accounting its effect on uncertainty quantification and provides a framework for optimizing experiment design.

Nomenclature

α	Image exposure	$I_{0,r}$	Peak image intensity for a single light ray
β	Blurring Coefficient	J_{ij}	Fisher Information matrix
γ	Gray value per unit exposure	K	Gladstone-Dale constant
δ	Dirac delta function	k, l	Pixel indices
$\Delta\theta_0$	Angle of the ray cone	m	Model
ϵ	Angular Deflection	M	Magnification
ζ	Tangential co-ordinate of the light ray trajectory	$\hat{n}$	Thermal Noise
η	Standard deviation of the Gaussian intensity profile on the image plane	n_0	Ambient refractive index
θ	Light Ray angle	$\boldsymbol{N}$	Normal distribution
λ	Wavelength of light	N_R	Number of light rays
ρ	Density	p	Probability Density Function (PDF)
σ	Standard Deviation	r	Light ray index
τ	Point spread function	t	Spatial co-ordinate on the density field
$\boldsymbol{a}$	Model Parameter vector	x, y, z	Coordinates in the object space
AR	Amplification Ratio	X, Y	Spatial co-ordinates on the camera sensor/image space
d_r	Pixel Pitch	z_D	Distance from dot pattern to camera lens
$\boldsymbol{E}$	Expectation operator	z_D	Distance from dot pattern to density gradient field
f	Focal length of the camera lens	Δz	Thickness of the density gradient field

$f_\#$	F-number
g	Image Gray Level or Signal
I	Image intensity

6.1 Introduction

Background Oriented Schlieren (BOS) is an image based flow diagnostic technique used to measure density gradients in a fluid by measuring the apparent displacement of a target dot pattern [1]–[4]. However additional distortions can be introduced to do the dot image due to higher order derivatives in the density/refractive index and due to curved windows in experimental facilities. In situations with very strong spatial variations in the density/refractive index (such as shock waves), the refraction experienced by two light rays emerging from the same dot can be very different, leading to a blurring of the dot image. This blurring is asymmetric and is in the direction of decreasing density. Elsinga et. al. analyzed this problem for 2D planar PIV [5]–[8] and found that this blur leads to a broadening of the cross-correlation peak, along with a small bias error leading to a decrease in measurement accuracy [6]. However, their analysis concerned the effects of aero-optical distortion on the errors/accuracy of the measurement, while the effect on measurement uncertainty/precision is unclear.

Recent work in BOS has shown that tracking-based displacement estimation methods can significantly increase accuracy and spatial resolution in comparison to correlation-based methods [9]. As the dot locations on the target are known from the time of manufacture, this information enables the method to be applied even in images with high dot densities. In tracking-based methods, the centroid estimation process from the dot image controls the measurement accuracy and precision. Therefore, the effect of image noise on centroid estimation is a concern as it can increase the position estimation uncertainty (noise floor) and reduce the dynamic range of the displacement measurement, especially since the maximum displacements in BOS experiments are usually low (< 1 pix.), though some exceptions exist [10]–[12]. The effect of image noise is further amplified for BOS due to the use of small apertures (large f-numbers) in order to keep both the dot pattern and the density field in focus, leading to a decrease in the illumination and a relative increase in the effect of image noise.

We investigate these issues using a theoretical analysis on the effect of density/refractive-index gradients on the measurement precision of the centroid estimation of a dot for a BOS experiment and show that blurring of a dot due to strong refractive index gradients can amplify the effect of image noise on centroid estimation, leading to an increase in the position uncertainty. The analysis is performed using an established theoretical framework called the Cramer-Rao Lower Bound (CRLB), a concept borrowed from the field of parameter estimation [13].

Cramer-Rao Lower Bound (CRLB)

In any experiment, the recorded measurement is a combination of the signal, which is the deterministic aspect of the measurement based on a physical model, and stochastic noise. Given the measurement, one would like to use a model for the measurement process to calculate a parameter of interest, where the particular method/algorithm used to calculate the parameter is called an estimator and the result obtained is the estimate. Based on the choice of the measurement and estimator, the estimates can have a bias (a systematic deviation from the true result) and a variance (due to the presence of noise), where a higher variance implies a lower measurement precision. The CRLB represents the lowest possible variance (or the highest possible precision) that can be achieved in the unbiased estimation of a parameter from a noise- and resolution-limited measurement. In the case of a biased estimation, the CRLB provides the lower bound on the random component of the error. It is a useful tool to study the scaling of error with respect to parameters in an experimental setup [13], [14].

Consider a signal/measurement $\mathbf{g}$, which is composed of a known model signal $\boldsymbol{m}$ defined by a parameter a, and a noise component $\boldsymbol{n}$ such that $\mathrm{g}_k = m_k + n_k, \ \forall\, k$, where k represents the index of the temporal/spatial location at which the measurement is acquired. Further, let the signal be defined by a joint Probability Density Function (PDF) $p(\mathbf{g}, a)$. Then the CRLB for the estimate of a is defined as: [14]

$$\sigma_a^2 = -\frac{1}{\boldsymbol{E}\left[\frac{\partial^2 \ln p(\mathbf{g}, a)}{\partial\, a^2}\right]} \qquad . \tag{34}$$

If the model is defined by a vector of parameters $\boldsymbol{a}$, then the CRLB is defined as the inverse of the diagonal element of the Fisher Information Matrix J_{ij} which is defined as

$$J_{ij} = -\boldsymbol{E}\left[\frac{\partial^2 \ln p(\mathbf{g}, \mathbf{a})}{\partial a_i \partial a_j}\right] \quad \textbf{(35)}$$

with the CRLB for a parameter a_i being given by $\sigma_{a_i}^2 = (J_{ii})^{-1}$ [14].

In the present context, the intensity of the dot recorded on the camera is the *measurement*, contaminated by the thermal noise in the camera, and the sub-pixel fitting procedure is the *estimator*, to obtain the dot centroid which is the *estimate*. We further assume that the only random process in the measurement chain is the thermal noise added to the sensor. In experiments, the true sub-pixel location of the dot can also be a random variable due to the spatial distribution of dots on the target (if a random dot pattern is used for BOS experiments), but this factor will be ignored in the current analysis and the *true centroid* of the dot is assumed to be a constant value.

The CRLB has been derived for 2D PIV/PTV measurements in the past by Wernet and Pline [15], and Westerweel [16]. In both previous analyses, the CRLB was derived for locating the centroid of a Gaussian particle image discretely sampled on a CCD sensor in the presence of noise, but the two approaches differed in their assumptions about the probability density function (PDF) of the noise and thus provide different but complementary results. Wernet and Pline [15] considered the case of low illumination intensity where the noise is dominated by the photon count per pixel, which follows a Poisson distribution. Under this assumption, the CRLB was found to be linearly proportional to the particle diameter and inversely proportional to the photon count. Westerweel [16] considered the case of more recent PIV experiments with high-energy pulsed lasers, where the noise is primarily governed by the thermal noise in the CCD sensor, as well as the resolution and digitization noise, all of which are normally distributed. This assumption resulted in the lower bound being proportional to the square of the particle diameter and inversely proportional to the pixel pitch and illumination intensity.

Our work extends the analysis of Elsinga et. al. [5]–[7] using the theoretical framework of Westerweel [16] to characterize the effect of density/refractive-index gradients on the position uncertainty of a BOS measurement. It will be seen that the effect of density/refractive-index gradients is to *increase the lower bound* (or decrease the precision) of the centroid estimation process, thus decreasing the precision of the overall measurement. The increase in the CRLB is due to non-linearities in the density gradient field which result in blurring of the dot image.

Therefore, the goal of this work is to recognize and demonstrate uncertainty amplification in the presence of density gradients, develop a theory to describe this effect, and to provide scaling relations to aid experiment design. The aim is not to provide quantitative values, but rather general equations that researches can use to design their unique experiments.

In the following sections, we first construct a comprehensive model for the dot pattern image by considering the propagation of light rays through a medium with density/refractive-index gradients. The image model is formulated in terms of the experimental parameters such as the magnification, aperture f-number and the distance between the dot pattern and the density gradient field. The Fisher information matrix is then constructed for the case of normally distributed noise due to the camera sensor to derive the CRLB. Finally, the model predictions are compared to ray-tracing simulations and the uncertainty amplification is demonstrated using experimental BOS images.

6.2 Theory

6.2.1 Image Model

The overall imaging process can be represented using a transfer function approach as shown in Figure 6.1.. Each dot acts as a point source of several light rays which travel through the density gradient field and the optical train and form an image on the camera sensor. The image due to a single light ray can be represented by the convolution of a Dirac delta function centered at the location of the geometric image $\vec{X}_r$ and the point spread function of the optical system $\tau(\vec{X})$. The collective image of the dot formed by all light rays is given by,

$$I(\vec{X}) = \tau(\vec{X}) * \sum_{r=1}^{N_R} I_{0,r}\delta(\vec{X} - \vec{X}_r) \quad . \tag{36}$$

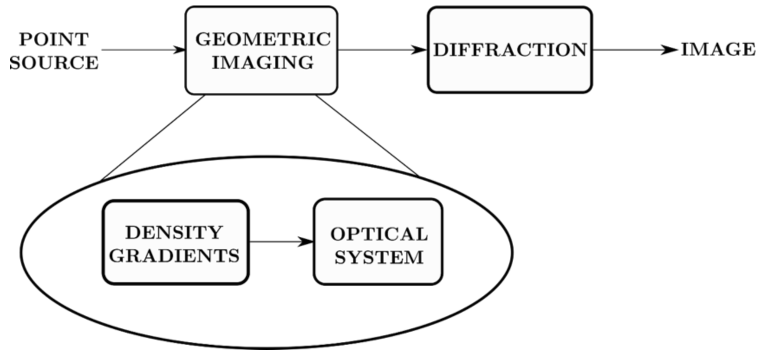

Figure 6.1. Illustration of the imaging process using a transfer function model.

The final location of the light ray $\vec{X}_r$ depends on the density gradients and the optical layout. For BOS, we will consider a head-on viewing configuration in the presence of density gradients, and then model the effect of the aperture.

For the optical setup shown in Figure 6.2., the final location of a light ray $\vec{X}_r$ originating from a dot with initial conditions of $\vec{x}_r, \vec{\theta}_r$, can be expressed as

$$\vec{X}_r = M\vec{x}_r + \Delta\vec{X}_r \tag{37}$$

where the first term is due to magnification of the imaging system, and the second term is the apparent displacement caused by the density gradients. We further use lower case symbols for co-ordinates in the object space and upper case symbols for co-ordinates in the image space on the camera.

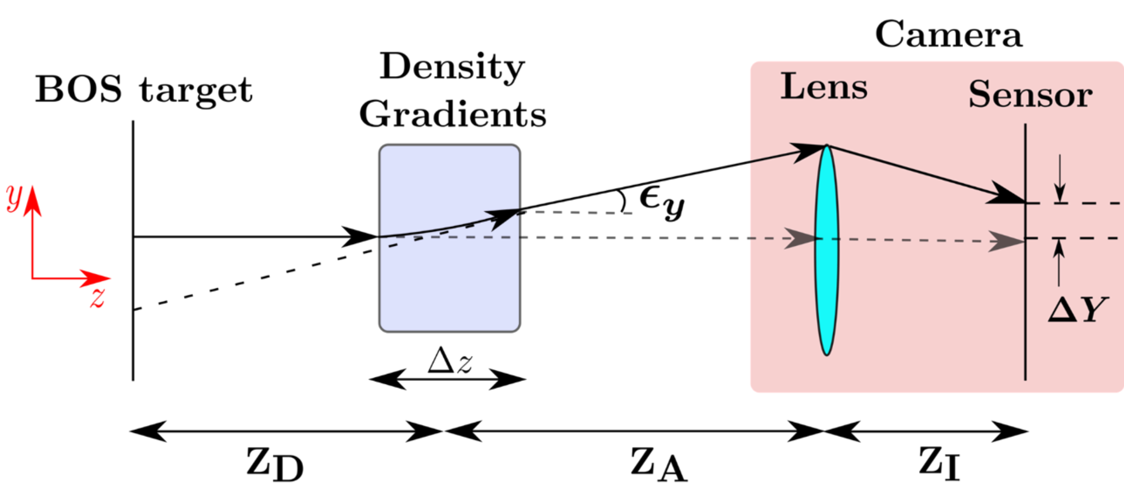

Figure 6.2. Schematic showing the experimental layout for BOS

The magnification M is a function of the object distance and the focal length of the camera lens f, as given by,

$$M = \left(1 - \frac{z_B}{f}\right)^{-1} \tag{38}$$

and the apparent displacement of the light ray as it traverses a density gradient field is given by [4],

$$\begin{aligned} \Delta\vec{X}_r &= M z_D K \int \frac{1}{n} \nabla\rho \, d\zeta \\ &\approx \frac{MK}{n_0} z_D \Delta z_r (\nabla\rho)_{avg,r} \end{aligned} \tag{39}$$

Here K is the Gladstone-Dale constant and n is the refractive index. The major assumptions generally employed for BOS applications are that (1) the light ray deflections are small and hence the tangential ray co-ordinate ζ is approximated by the axial co-ordinate z, (2) the change in the refractive index in the denominator is negligible and is equal to the ambient (n_0), and (3) the integral is replaced by a path averaged value of the density gradient $(\nabla\rho)_{avg,r}$ experienced by each light ray. In the subsequent analysis, the subscript avg will be dropped, with the understanding that the gradient field is always the path averaged value.

Finally, the point spread function of the optical system $\tau(\vec{X})$ is the intensity field created by Fraunhofer diffraction due to a circular aperture and is given by the Airy function. Typically, this is approximated by a Gaussian profile,

$$\tau(\vec{X}) = I_0 \exp\left(-\frac{|\vec{X}|^2}{2\eta^2}\right) \tag{40}$$

where I_0 is the peak intensity and η is related to the diffraction diameter and is given by $\eta = \frac{\sqrt{2}}{\pi} f_\#(1 + M)\lambda$, where λ is the wavelength of light [17]. Therefore, the model for the image of a single dot formed by all the light rays originating from the dot is given by,

$$I(\vec{X}) = \sum_{r=1}^{N_R} I_{0,r} \exp\left[-\frac{\left|\vec{X} - \left(M\,\vec{x}_r + \frac{MK}{n_0} z_D \Delta z_r \nabla\rho|_r\right)\right|^2}{2\eta^2}\right]. \tag{41}$$

Here $I_{0,r}$ is the peak image intensity, and is defined as, $I_{0,r} = \frac{\alpha_r}{2\pi\eta^2}$, where α_r is the total image exposure due to a single light ray.

To simplify further analysis, we rewrite Equation (41) to represent the intensity field due to an “effective Gaussian”, represented by a rotated ellipse, under the assumption that the intensity field formed by several Gaussian distributions will also be a Gaussian distribution. The rotated elliptical Gaussian curve is described by five parameters: (1) X location (X_0), (2) Y location (Y_0), (3) peak intensity (I_0), (4) diameter/standard deviation along x, ($\eta_{0,X}$) and (5) standard deviation along y ($\eta_{0,Y}$) and (6) correlation coefficient (R_0) that controls the tilt of the major and minor axis of the ellipse with the co-ordinate axis of the camera sensor (the word correlation is used in relation to the intensity profiles of the dot along x and y, and is not to be confused with PIV cross-correlation analysis). The dot diameter is defined as four times of the standard deviation, based on the convention in PIV literature [18], [19]. The subscript "0" will be used to distinguish the parameters associated with the dot from those with the light rays, in both the object and image space.

$$I_{eff} = I_0\, exp\left[-\frac{1}{2}\begin{pmatrix} X - X_0 \\ Y - Y_0 \end{pmatrix}^T \frac{1}{1-R^2}\begin{pmatrix} \frac{1}{\eta_{0,X}^2} & -\frac{R_0}{\eta_{0,X}\eta_{0,Y}} \\ -\frac{R_0}{\eta_{0,X}\eta_{0,Y}} & \frac{1}{\eta_{0,Y}^2} \end{pmatrix}\begin{pmatrix} X - X_0 \\ Y - Y_0 \end{pmatrix}\right] . \qquad \textbf{(42)}$$

The effective centroid and diameters can be estimated by equating the moments of the Gaussian distributions expressed in Equations (41) and (42). The main assumption that enables this simplification is that the viewing angle $\Delta\theta_0$ subtended by the dot on the lens is small, and therefore the density gradient field experienced by any arbitrary light ray can be expressed using a Taylor series expansion about the angular bisector of the ray cone, as illustrated in Figure 6.3. The viewing angle is a function of the object distance and the f-number, and for BOS applications, the f-number is generally high to provide a large depth of field, to keep both the dot target and the density gradient field in focus. These requirements result in a very small viewing angle, on the order of 1-2 degrees, which makes the small angle assumption reasonable.

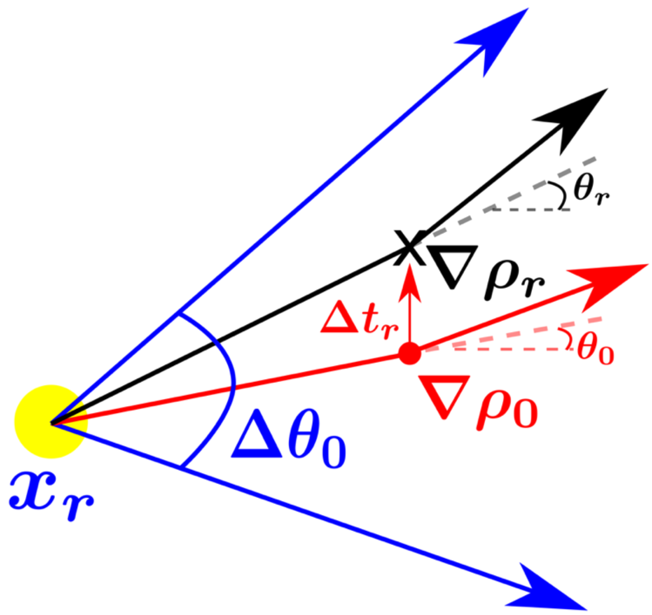

Figure 6.3. Illustration of the Taylor series approximation for the density gradient field showing the ray cone (bounded by the blue rays), the angular bisector (red) and an arbitrary light ray (black). The dashed lines are the light ray trajectories in the absence of a density gradient field.

The effective centroid is described as the first moment of the intensity distribution of the image and is given by,

$$\vec{X}_0 = \frac{\int_{-\infty}^{+\infty}\int_{-\infty}^{+\infty}\vec{X}\, I(\vec{X})dX\, dY}{\int_{-\infty}^{+\infty}\int_{-\infty}^{+\infty} I(\vec{X})dX\, dY} \quad . \tag{43}$$

The above equation will be simplified for the x component in the following analysis, and the procedure for the y component is identical. We have, for $\vec{X}_0 = X_0\hat{\imath} + Y_0\hat{\jmath}$,

$$\begin{aligned} X_0 &= \frac{\int_{-\infty}^{+\infty}\int_{-\infty}^{+\infty} X \sum_{r=1}^{N_R} I_{0,r} \exp\left[-\frac{\left|\vec{X}-\vec{X}_r\right|^2}{2\eta^2}\right] dX\, dY}{\int_{-\infty}^{+\infty}\int_{-\infty}^{+\infty} \sum_{r=1}^{N_R} I_{0,r} \exp\left[-\frac{\left|\vec{X}-\vec{X}_r\right|^2}{2\eta^2}\right] dX\, dY} \\ &= \frac{\sum_{r=1}^{N_R} I_{0,r}\left(\sqrt{2\pi}X_r\eta\right)\left(\sqrt{2\pi}\eta\right)}{\sum_{r=1}^{N_R} I_{0,r}\left(\sqrt{2\pi}\eta\right)\left(\sqrt{2\pi}\eta\right)} \\ &= \frac{1}{N_R}\sum_{r=1}^{N_R} X_r \ . \end{aligned} \tag{44}$$

where we have used the result for Gaussian integrals, that $\int_{-\infty}^{+\infty} \exp\left[-\frac{(x-a)^2}{2b^2}\right] dx = \sqrt{2\pi}b$ and $\int_{-\infty}^{+\infty} x \exp\left[-\frac{(x-a)^2}{2b^2}\right] dx = \sqrt{2\pi}ab$. Further, under the assumption of a small angle of the ray cone, we expect that $I_{0,r} \approx I_0 = constant$ for all light rays emerging from a dot.

Further, for a small cone angle, it is also expected that all light rays travel approximately the same distance from the dot to the edge of the density gradient field ($\Delta z_r \approx \Delta z = constant$). Based on these assumptions, we obtain that

$$\begin{aligned} X_0 &= \frac{1}{N_R} \sum_{r=1}^{N_R} \left(M\, x_0 + \frac{MK}{n_0} z_D \Delta z_r \left.\frac{\partial \rho}{\partial x}\right|_r \right) \\ &= M x_0 + \frac{MK z_D \Delta z}{n_0 N_R} \sum_{r=1}^{N_R} \left.\frac{\partial \rho}{\partial x}\right|_r \quad . \end{aligned} \tag{45}$$

The second term in the above equation represents the *average deflection* of all light rays originating from the dot, where the gradients along z are neglected, because the analysis is performed on the depth averaged density gradient field. and it can be simplified further by using a Taylor series expansion of the density gradient field about the angular bisector of the ray cone. Consider a straight line connecting the dot, the center of the lens and a point on the camera sensor, which represents the case of pinhole imaging. Let the intersection point of this line with the mid-plane of the density gradient field be $\vec{t}_0 = \vec{x}_0 + Z_D \vec{\theta}_0$ and the density gradient at this intersection point be defined as $\nabla\rho|_{t_0}$. Then the density gradient along the x-direction at an arbitrary intersection point $\vec{t}_r$ can be expressed to first order as

$$\left.\frac{\partial \rho}{\partial x}\right|_{\vec{t}_r} = \left.\frac{\partial \rho}{\partial x}\right|_{\vec{t}_0} + \left.\frac{\partial^2 \rho}{\partial x^2}\right|_{\vec{t}_0} \left(t_{r,x} - t_{0,x}\right) + \left.\frac{\partial^2 \rho}{\partial x \partial y}\right|_{\vec{t}_0} \left(t_{r,y} - t_{0,y}\right) + O(|t_r - t_0|^2) \ . \tag{46}$$

The parameter $\left(\vec{t}_r - \vec{t}_0\right) = \Delta\vec{t}_r$ can be expressed in terms of the optical setup as

$$\begin{aligned} \vec{t}_r - \vec{t}_0 &= \left(\vec{x}_0 + z_D \vec{\theta}_r\right) - \left(\vec{x}_0 + z_D \vec{\theta}_0\right) \\ &= z_D\left(\vec{\theta}_r - \vec{\theta}_0\right) \end{aligned} \tag{47}$$

with $\vec{\theta}_r$ being the angle of propagation of a light ray, and $\vec{\theta}_0 = \frac{1}{N_R}\sum_{r=1}^{N_R} \vec{\theta}_r$ being the angle between the bisector of the cone and the horizontal.

Using Equations (46) and (47) in Equation **Error! Reference source not found.** and simplifying, we obtain for the effective centroid along x,

$$
\begin{aligned}
X_0 &= Mx_0 + \frac{MKz_D\Delta z}{n_0 N_R}\sum_{r=1}^{N_R}\left(\left.\frac{\partial\rho}{\partial x}\right|_0 + \left.\frac{\partial^2\rho}{\partial x^2}\right|_0 Z_D\left(\theta_{r,x}-\theta_{0,x}\right) + \left.\frac{\partial^2\rho}{\partial x\partial y}\right|_0 Z_D\left(\theta_{r,y}-\theta_{0,y}\right)\right) \\
&= Mx_0 + \frac{MKz_D\Delta z}{n_0}\left.\frac{\partial\rho}{\partial x}\right|_0 \quad .
\end{aligned}
\tag{48}
$$

where the summations of the ray angles evaluate to zero due to the definition of $\theta_{0,x}$ and $\theta_{0,y}$ as the angles of the bisectors. It is to be noted that in general the dot image will also be skewed as pointed out by Elsinga et. al. [5] and hence θ_0 may no longer be the angular bisector after refraction, leading to small bias errors. However, since the present analysis is concerned with the uncertainty which is expected to scale with the diameter, a second order-accurate approximation of the density gradient field is used. The y component of the centroid can be evaluated in a similar manner, and the 2D centroid of the dot image is given by,

$$
\vec{X}_0 = M\vec{x}_0 + \frac{|M|Kz_D\Delta z}{N_R n_0}\,\nabla\rho|_0 \tag{49}
$$

where the first term on the right hand side is the image location for a dot without the density gradients and the second term is the average displacement of light rays due to the density gradient field, with $\nabla\rho|_0$ representing the depth-averaged density gradient experienced by the angular bisector of the ray cone.

The effective dot diameter can be computed by equating the second moment of the Gaussian distributions. Again, just considering the x-component, the standard deviation (a measure of the diameter) is given by:

$$
\begin{aligned}
\eta_{0,x}^2 &= \frac{\int_{-\infty}^{+\infty}\int_{-\infty}^{+\infty}(X-X_0)^2\, I(\vec{X})dX\,dY}{\int_{-\infty}^{+\infty}\int_{-\infty}^{+\infty} I(\vec{X})dX\,dY} \\
&= \frac{\sum_{r=1}^{N_R} I_{0,r}\int_{-\infty}^{+\infty}(X-X_0)^2\exp\left[-\frac{(X-X_r)^2}{2\eta^2}\right]dX\int_{-\infty}^{+\infty}\exp\left[-\frac{(Y-Y_r)^2}{2\eta^2}\right]dY}{\sum_{r=1}^{N_R} I_{0,r}\int_{-\infty}^{+\infty}\exp\left[-\frac{(X-X_r)^2}{2\eta^2}\right]dX\int_{-\infty}^{+\infty}\exp\left[-\frac{(Y-Y_r)^2}{2\eta^2}\right]dY} \\
&= \frac{\sum_{r=1}^{N_R} I_{0,r}\left(\sqrt{2\pi}\eta(\eta^2+(X_r-X_0)^2)\right)\left(\sqrt{2\pi}\eta\right)}{\sum_{r=1}^{N_R} I_{0,r}\left(\sqrt{2\pi}\eta\right)\left(\sqrt{2\pi}\eta\right)} \\
&= \eta^2 + \frac{1}{N_R}\sum_{r=1}^{N_R}(X_r-X_0)^2.
\end{aligned}
\tag{50}
$$

again using the previously mentioned results for the Gaussian integrals in addition to a new result, that $\int_{-\infty}^{+\infty}(x-c)^2\exp\left[-\frac{(x-a)^2}{2b^2}\right]dx = \sqrt{2\pi}b\{(a-c)^2+b^2\}$.

The second term in the summation can again be simplified using the Taylor series expansion as follows,

$$X_r - X_0 = Mx_0 + \frac{MKZ_D\Delta z}{n_0}\frac{\partial\rho}{\partial x}\bigg|_r - \left(Mx_0 + \frac{MKZ_D\Delta z}{n_0}\frac{\partial\rho}{\partial x}\bigg|_0\right)$$
$$= \frac{MKz_D\Delta z}{n_0}\left(\frac{\partial^2\rho}{\partial x^2}\bigg|_0 Z_D\left(\theta_{r,x} - \theta_{0,x}\right) + \frac{\partial^2\rho}{\partial x\partial y}\bigg|_0 Z_D\left(\theta_{r,y} - \theta_{0,y}\right)\right) \quad . \tag{51}$$

The summation then becomes,

$$\frac{1}{N_R}\sum_{r=1}^{N_R}(X_r - X_0)^2 = \left(\frac{MKz_D\Delta z}{n_0}\right)^2 Z_D^2\left(\left(\frac{\partial^2\rho}{\partial x^2}\bigg|_0\right)^2\frac{1}{N_R}\sum_{r=1}^{N_R}\left(\theta_{r,x} - \theta_{0,x}\right)^2\right.$$
$$+\left(\frac{\partial^2\rho}{\partial x\partial y}\bigg|_0\right)^2\frac{1}{N_R}\sum_{r=1}^{N_R}\left(\theta_{r,y} - \theta_{0,y}\right)^2$$
$$\left. + \frac{\partial^2\rho}{\partial x^2}\bigg|_0\frac{\partial^2\rho}{\partial x\partial y}\bigg|_0\frac{2}{N_R}\sum_{r=1}^{N_R}\left(\theta_{r,x} - \theta_{0,x}\right)\left(\theta_{r,y} - \theta_{0,y}\right)\right) \tag{52}$$

The summations of the angles can be simplified further by modeling the angular distribution of light rays as a uniform random variable, where the angle of propagation of any given light ray is randomly distributed within the total angle of the ray cone $\Delta\theta_{0,x}$. That is,

$$P_{\Theta_x}\left(\theta_{r,x}\right) = \begin{cases}\frac{1}{\Delta\theta_{0,x}} & \theta_{0,x} - \frac{\Delta\theta_{0,x}}{2} \le \theta_{r,x} \le \theta_{0,x} + \frac{\Delta\theta_{0,x}}{2}\\ 0 & \text{otherwise}\end{cases} \tag{53}$$

with a similar expression for the random variable Θ_y corresponding the distribution of the angle of propagation along y, $\theta_{r,y}$, which would depend on the component of the cone angle along y, $\Delta\theta_{0,y}$. Except for highly astigmatic viewing configurations, the components of the cone angle along the two directions will be equal ($\Delta\theta_{0,x} = \Delta\theta_{0,y} = \Delta\theta_0$). By further assuming that the random variables along the two components Θ_x and Θ_y are independent, it can be shown that

a) $\frac{1}{N_R}\sum_{r=1}^{N_R}\left(\theta_{r,x} - \theta_{0,x}\right)^2 = \sigma_{\Theta_x} = \frac{\Delta\theta_0^2}{12}$

b) $\frac{1}{N_R}\sum_{r=1}^{N_R}\left(\theta_{r,y} - \theta_{0,y}\right)^2 = \sigma_{\Theta_y} = \frac{\Delta\theta_0^2}{12}$

c) $\frac{1}{N_R}\sum_{r=1}^{N_R}\left(\theta_{r,x} - \theta_{0,x}\right)\left(\theta_{r,y} - \theta_{0,y}\right) = 0$

and the summation simplifies to,

$$\frac{1}{N_R}\sum_{r=1}^{N_R}(X_r - X_0)^2 = \frac{1}{12}\left(\frac{MKz_D\Delta z}{n_0}\right)^2 Z_D^2\Delta\theta_0^2\left(\left(\frac{\partial^2\rho}{\partial x^2}\bigg|_0\right)^2 + \left(\frac{\partial^2\rho}{\partial x\partial y}\bigg|_0\right)^2\right). \tag{54}$$

The angle of the ray cone $\Delta\theta_0$ can be expressed in terms of the parameters of the optical setup as

$$\Delta\theta_0 = \frac{1}{f_\#}\left(1+\frac{1}{M}\right)^{-1} - \frac{K\Delta z}{2n_0}\left(\left.\frac{\partial\rho}{\partial x}\right|_0 + \left.\frac{\partial\rho}{\partial y}\right|_0\right) \tag{55}$$

where the second term accounts for the mean deflection of the ray cone due to density gradients. The standard deviation (= ¼ diameter) along the x direction is then given by,

$$\begin{aligned}\eta_{0,X}^2 &= \eta^2 + \frac{1}{12}\left(\frac{MKz_D\Delta z}{n_0}\right)^2 z_D^2\Delta\theta_0^2\left(\left(\left.\frac{\partial^2\rho}{\partial x^2}\right|_0\right)^2 + \left(\left.\frac{\partial^2\rho}{\partial x\partial y}\right|_0\right)^2\right) \\ &= \eta^2 + \eta_{b,X}^2\end{aligned} \tag{56}$$

where $\eta_{b,X}$ represents the blurred diameter. A similar analysis yields the standard deviation along the y direction,

$$\begin{aligned}\eta_{0,Y}^2 &= \frac{\int_{-\infty}^{+\infty}\int_{-\infty}^{+\infty}(Y-Y_0)^2\, I(\vec{X})dX\,dY}{\int_{-\infty}^{+\infty}\int_{-\infty}^{+\infty} I(\vec{X})dX\,dY} \\ &= \eta^2 + \frac{1}{12}\left(\frac{MKz_D\Delta z}{n_0}\right)^2 z_D^2\Delta\theta_0^2\left(\left(\left.\frac{\partial^2\rho}{\partial x\partial y}\right|_0\right)^2 + \left(\left.\frac{\partial^2\rho}{\partial y^2}\right|_0\right)^2\right) \\ &= \eta^2 + \eta_{b,Y}^2\end{aligned} \tag{57}$$

Equations (25) and (26) show that non-linearities in the density gradient field increase the effective diameter of the dot leading to *blurring*, consistent with earlier observations by Elsinga et. al. [5] for 2D PIV from experimental data. In the process, we have also modeled the effect of the f-number.

The correlation coefficient R_0 is obtained by equating the covariance of the intensity due to all light rays and the effective intensity distribution.

$$\begin{aligned}R_0 &= \frac{1}{\eta_{0,X}\eta_{0,Y}}\,\frac{\int_{-\infty}^{+\infty}\int_{-\infty}^{+\infty}(X-X_0)(Y-Y_0)\, I(\vec{X})dX\,dY}{\int_{-\infty}^{+\infty}\int_{-\infty}^{+\infty} I(\vec{X})dX\,dY} \\ &= \frac{1}{12}\left(\frac{MKz_D\Delta z}{n_0}\right)^2 z_D^2\Delta\theta_0^2\left.\frac{\partial^2\rho}{\partial x\partial y}\right|_0\left(\left.\frac{\partial^2\rho}{\partial x^2}\right|_0 + \left.\frac{\partial^2\rho}{\partial y^2}\right|_0\right),\end{aligned} \tag{58}$$

and it is seen that the mixed derivative of the density field leads to a covariance or tilt in the effective intensity distribution of the dot.

Finally, the peak image intensity of the effective model can be expressed in terms of the image exposure α_0 defined as,

$$\begin{aligned}\alpha_0 &= \int_{-\infty}^{+\infty}\int_{-\infty}^{+\infty} I(X,Y)dX\,dY \\ &= 2\pi I_0 \eta_{0,X}\eta_{0,Y} \qquad .\end{aligned} \tag{59}$$

Further, since the exposure for the effective model should be equal to that formed by all the individual light rays,

$$\begin{aligned}\alpha_0 &= \sum_{r=1}^{N_R}\int_{-\infty}^{+\infty}\int_{-\infty}^{+\infty} I_r(X,Y)\,dX\,dY \\ &= \sum_{r=1}^{N_R}\alpha_r \ .\end{aligned} \tag{60}$$

Thus, the peak intensity for the effective image model is given by,

$$I_0 = \frac{\alpha_0}{2\pi\eta_{0,x}\eta_{0,y}} \ , \tag{61}$$

thereby completing the formulation of the effective image model.

The final image of the dot sampled on a discrete set of pixels and with a finite number of gray levels is given by,

$$g_{kl} = \gamma d_r^2 I(X_k, Y_l) \quad . \tag{62}$$

Here k, l are the pixel indices along the X, Y directions respectively, γ is the pixel to gray level conversion factor, and $d_r$is the pixel pitch. In addition, all CCD/CMOS sensors have some amount of noise added to the signal due to thermal noise and finite number of gray levels. This will be modeled in the next section when constructing the Fisher Information Matrix.

6.2.2 Noise Model and Fisher Information

The final image of the dot recorded on the sensor is the sum of the sampled intensity profile g_{kl} as given by Equation (62) with some additive noise $\hat{n}_{kl}$:

$$\hat{g}_{kl} = \gamma d_r^2 I(X_k, Y_l) + \hat{n}_{kl} \qquad . \tag{63}$$

Following Westerweel [16], the fluctuations due to thermal noise and finite number of gray levels are assumed to be normally distributed, signal-independent and uncorrelated, with a standard deviation of σ_n. The joint pdf of the measurement then becomes

$$p(\hat{g}, \boldsymbol{a}) = \left(\frac{1}{2\pi\sigma_n^2}\right)^{\frac{MN}{2}} \exp\left[-\frac{1}{2\sigma_n^2}\sum_{k=0}^{M}\sum_{l=0}^{N}(\hat{g}_{kl} - g_{kl})^2\right] \tag{64}$$

where $\boldsymbol{a}$ is the parameter vector and M, N are the number of pixels along X and Y, respectively.

The Fisher information matrix defined earlier represents the total amount of information available about the dot from its intensity profile that can be used to estimate its centroid. For the present scenario, the Fisher Information available to estimate the X component of the centroid becomes [14], [16]:

$$\begin{aligned} J_{X_0X_0} &= \frac{1}{\sigma_n^2}\sum_{k=0}^{M}\sum_{l=0}^{N}\left(\frac{\partial g_{kl}}{\partial X_0}\right)^2 \\ &= \left(\frac{\gamma I_0 d_r}{\sigma_n}\right)^2 \frac{\pi}{2}\frac{\eta_{0,y}}{\eta_{0,x}}\frac{1}{\sqrt{1-R_0^2}}\ . \end{aligned} \tag{65}$$

where the summations are converted into integrals under the assumption that the extent of the dot is small compared to the size of the whole camera sensor. It is to be noted that R_0 lies in the open interval $(-1, 1)$, and is always less than one because the minimum diameter of a dot is 1 pixel. Therefore the term involving the square root is always positive and non-zero.

6.2.3 Cramer-Rao Lower Bound

The Cramer-Rao lower bound for the variance is defined as the inverse of the diagonal elements of the Fisher Information matrix, and therefore the standard deviation for the estimation of the centroid is given by

$$\begin{aligned} \sigma_{X_0} &= \sqrt{\frac{1}{J_{X_0X_0}}} \\ &= \frac{\sigma_n}{\gamma I_0 d_r}\sqrt{\frac{2}{\pi}\frac{\eta_{0,x}}{\eta_{0,y}}\sqrt{1-R_0^2}}\ . \end{aligned} \tag{66}$$

Further, the peak intensity I_0 can be related to the dot diameter using Equation (61) to obtain

$$\frac{\sigma_{X_0}}{d_r} = \frac{2\sqrt{2\pi}\sigma_n}{\gamma\alpha_0}\left(\frac{\eta_{0,X}}{d_r}\right)^{\frac{3}{2}}\left(\frac{\eta_{0,Y}}{d_r}\right)^{\frac{1}{2}}(1-R_0^2)^{\frac{1}{4}}\ . \tag{67}$$

In the absence of blurring, $\eta_{0,x} = \eta_{0,y} = \eta$ and $R_0 = 0$, and the result then simplifies to

$$\frac{\sigma_{X_0}}{d_r} = \frac{2\sqrt{2\pi}\sigma_n}{\gamma\alpha_0}\left(\frac{\eta}{d_r}\right)^2 \tag{68}$$

thereby recovering a result similar to Westerweel [16], that the lower bound increases with the square of the dot diameter. Further, since it was shown previously that the diameter increases due to nonlinearities in the density gradient field, the effect of the density gradients is to *increase* the variance in the measurement of the centroid. It is also seen that the dot tilt introduces a covariance between the dot centroids along the x and y direction, thereby leading to a reduction in the position uncertainty. It should be noted that $R_0^2 < 1$ for a dot with a finite (1 pixel) extent. For a linear density gradient field, there is a uniform translation of the dot and the CRLB is then identical to the result obtained by Westerweel for PIV.

In summary, the Cramer-Rao lower bound associated with the estimation of a 2D dot centroid from a BOS image in the presence of density gradients and thermal noise, is given by Equation (67), and is a function of:

a) Exposure (α_0)
b) Noise level (σ_n)
c) Diffraction Diameter (4η)
d) Magnification (M)
e) Distance between the dot target and the density gradient field (z_D)
f) Extent of the density gradient field (Δz)
g) Non-linearities in the density field ($\nabla^2\rho$)
h) Camera Aperture ($f_\#$)

The parameter Mz_D is defined as the *sensitivity* of a BOS setup, with a larger value being considered better for resolving small scale features in the flow field [20]. However, since it also increases the variance and lowers the precision of the measurement in the presence of blur, an optimal trade-off between sensitivity and precision should be considered when designing an experiment. Further, increasing $f_\#$ tends to reduce the blur and increase the measurement precision, and a large $f_\#$ also helps to keep both the dot pattern and the density gradient field in focus. Therefore, small aperture settings must be favored when designing BOS experiments, which requires the use of high power illumination.

6.2.4 Sensitivity Analysis

It was seen that the position uncertainty given by (67) and the dot diameters given by (56)-(57) are functions of several parameters. To assess the relative importance of these parameters on the final measurement, a sensitivity analysis is performed by a combination of the Taylor series method of uncertainty propagation and Monte-Carlo simulations. The analysis will be presented for σ_{X_0} and $\eta_{0,X}$ but a similar effect is anticipated for the other parameters such as σ_{Y_0}, $\eta_{0,Y}$, and R_0.

a) Position Uncertainty

The position uncertainty σ_{X_0} depends on five parameters, (1) σ_n, (2) α_0, (3) $\eta_{0,X}$, (4) $\eta_{0,Y}$, and (5) R_0. The corresponding sensitivity coefficients are listed in Table 6.1. To assess the relative contributions of these terms, a Monte-Carlo simulation was performed with the parameter values chosen randomly in a pre-defined interval. The intervals were: (1) $\sigma_n = 5 \pm 3$, (2) $\alpha_0 = 1000 \pm 500$, (3) $\eta_{0,X} = 0.75 \pm 0.5\, pix.$, (4) $\eta_{0,Y} = 0.75 \pm 0.5\, pix$ and (5) $R = 0 \pm 1$. A uniform distribution of the parameters was assumed, and the sensitivities and contributions ($\left|\frac{\partial \sigma}{\partial a}\ \Delta a\right|$ where a is the parameter)were calculated over one million trials to build the PDF shown in Figure 6.4.

From the PDFs and median values it is seen that the noise level, exposure and dot diameter along the X direction have the largest effect on the position uncertainty along X. As the dot diameter in turn depends on the derivatives of the density field along x, the orientation of the density field can have a strong effect on the corresponding position uncertainty.

Regarding the contribution of blurring to the position uncertainty, it should be noted that for a fixed amount of blurring, the effect of blur uncertainty will dominate under low illumination/exposure (α) conditions, because the peak intensity of the dot has a first order effect on the position uncertainty as seen in Equation (67). Further, it is also expected to dominate in situations where the blurring itself is large, such as large-scale experiments and flows with large density gradients. In the present simulations, the sum of median uncertainties from all contributing sources is 0.14 pix., and blurring has a 30% contribution.

Table 6.1. Summary of parameters and corresponding sensitivity coefficients for the position uncertainty

Parameter	**Range**	**Sensitivity Coefficient**	**Median Contribution $\Delta\sigma_{X_0}$ (pix.)**
σ_n	5 ± 3	$\frac{\partial\sigma_{X_0}}{\partial\sigma_n} = \frac{2\sqrt{2\pi}}{\alpha_0}\eta_{0,X}^{\frac{3}{2}}\eta_{0,Y}^{\frac{1}{2}}(1-R^2)^{\frac{1}{4}}$	0.041
α_0	$1000 \pm\ 500$	$\frac{\partial\sigma_{X_0}}{\partial\alpha_0} = -\frac{2\sqrt{2\pi}\sigma_n}{\alpha_0^2}\eta_{0,X}^{\frac{3}{2}}\eta_{0,Y}^{\frac{1}{2}}(1-R^2)^{\frac{1}{4}}$	0.032
$\eta_{0,X}$	$0.75 \pm 0.5\,pix.$	$\frac{\partial\sigma_{X_0}}{\partial\eta_{0,X}} = \frac{3\sqrt{2\pi}\sigma_n}{\alpha_0}\eta_{0,X}^{\frac{1}{2}}\eta_{0,Y}^{\frac{1}{2}}(1-R^2)^{\frac{1}{4}}$	0.040
$\eta_{0,Y}$	$0.75 \pm 0.5\,pix$	$\frac{\partial\sigma_{X_0}}{\partial\eta_{0,Y}} = \frac{\sqrt{2\pi}\sigma_n}{\alpha_0}\eta_{0,X}^{\frac{3}{2}}\eta_{0,Y}^{-\frac{1}{2}}(1-R^2)^{\frac{1}{4}}$	0.013
R	0 ± 1	$\frac{\partial\sigma_{X_0}}{\partial R} = -\frac{\sqrt{2\pi}\sigma_n}{\alpha_0}\eta_{0,X}^{\frac{3}{2}}\eta_{0,Y}^{\frac{1}{2}}\frac{R}{(1-R^2)^{\frac{3}{4}}}$	0.011

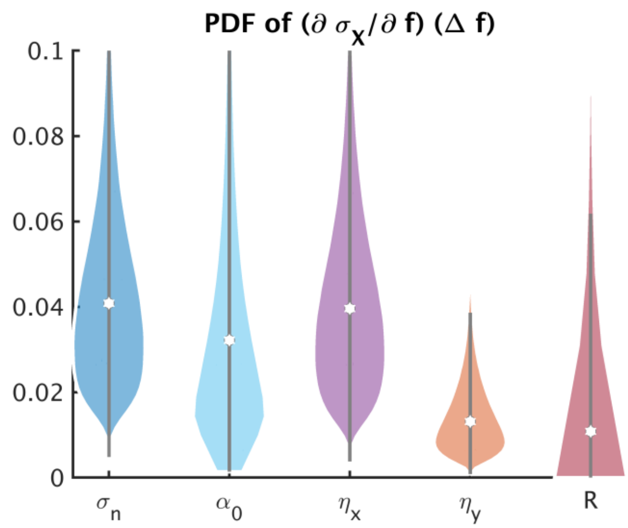

Figure 6.4. PDF of sensitivity of the position uncertainty to changes in the parameters. The median of the distribution is indicated by the white notch.

b) Effective Dot standard deviation

A similar analysis was performed for the effective dot standard deviation $\eta_{0,X}$ as a function of its parameters. The parameters, associated sensitivity coefficients and the range of values used for the Monte-Carlo simulations are summarized in

Table 6.2, and the resulting PDFs and medians are shown in Figure 6.5. The diffraction diameter η is seen to have the largest effect on the effective dot diameter, followed by the distance z_D between the dot pattern and the density field, and the magnification M, with the contributions of the other parameters being similar. While the analysis shows that the contribution from the density gradient terms is the lowest, it should be noted that the blurred diameter η_b is a product of the second derivatives of density with other experimental parameters as shown in Equations (23) and (24). Since all the other parameters are always non-zero and usually uniform throughout the field of view, the density gradient term has a critical effect in 'turning on' the uncertainty amplification. Further, this effect is bound to be more important in flows with sharp discontinuities in the density field, and thereby larger density gradients.

Table 6.2. Summary of parameters and corresponding sensitivity coefficients for the effective dot standard deviation

Parameter	**Range**	**Sensitivity Coefficient**	**Median Contribution $\Delta\eta_{0,X}$ (pix.)**
η	$0.75 \pm 1\ pix.$	$\frac{\partial \eta_{0,X}}{\partial \eta} = \frac{\eta}{\eta_{0,X}}$	0.85
M	1 ± 0.5	$\frac{\partial \eta_{0,X}}{\partial M} = \frac{\left(-\frac{1}{1+M} + \frac{2}{M}\right)\eta_{b,X}^2}{\eta_{0,X}}$	0.35
z_D	0.1 ± 0.05 m	$\frac{\partial \eta_{0,X}}{\partial z_D} = \frac{2\eta_{b,X}^2}{Z_D \eta_{0,X}}$	0.46
$f_\#$	16 ± 8	$\frac{\partial \eta_{0,X}}{\partial f_\#} = -\frac{\eta_{b,X}^2}{f_\# \eta_{0,X}}$	0.23
Δz	0.1 ± 0.05 m	$\frac{\partial \eta_{0,X}}{\partial \Delta z} = \frac{\eta_{b,X}^2}{\Delta z\, \eta_{0,X}}$	0.23
$\partial^2\rho/\partial x^2$	$2500 \pm 1000\ kg/m^3$	$\frac{\partial \eta_{0,X}}{\partial \rho_{xx}} = \frac{\eta_{b,X}^2}{\rho_{xx,0}\eta_{0,X}}$	0.18

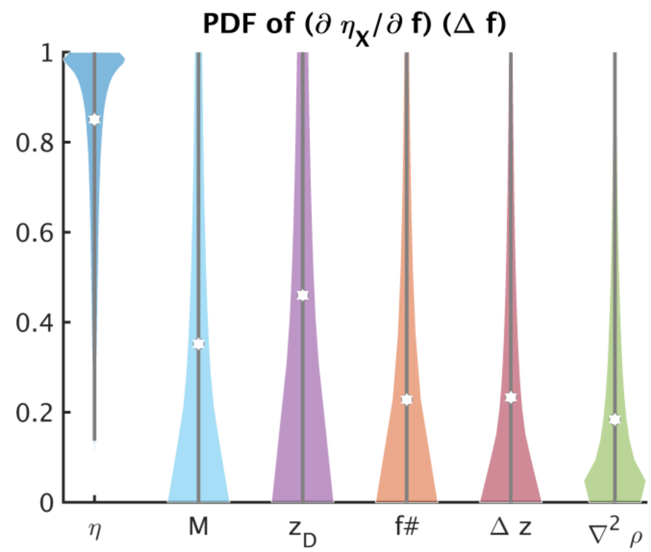

Figure 6.5. PDF of sensitivity of the effective dot diameter to changes in the parameters. The median of the distribution is indicated by the white notch.

Therefore the sensitivity analyses show that though the position uncertainty and the effective diameter are controlled by a large number of experimental parameters, some parameters can have a more dominant effect in comparison to the others.

Finally, a note on the choice of experimental parameters (in particular η_0) for the sensitivity analysis. The effective diameter of the dot η_0 is a combination of the diffraction diameter (η) and blurring due to the density field (η_b). For the former, the range of values were chosen based on the observation from PIV literature that the subpixel estimation both on the cross-correlation plane and the particle intensity profile is optimal for a dot diameter of 3 pix. Since the dot diameter is typically expressed in PIV as four times the standard deviation of the Gaussian intensity profile, the range of diameters considered in the sensitivity analysis is: $4 \times (0.75 \pm 0.5)$ pix., which is 3 ± 2 pix.

The lower end of 1 pix. is chosen to correspond to situations where the dot diameters are really small, though it should be noted that in most BOS experiments, the dot diameter on the reference image can be chosen very precisely because of the ability to manufacture/customize the dot pattern.

The higher end of 5 pix. diameter is chosen to correspond to blurred imaging, with a blurring of 2 pix ($\Delta\eta = 0.5$ pix.), which is typically observed in experiments, including the example shown in Section 6.4. For a similar experimental setup, this would correspond to a magnification $M \approx 1$, the distance $z_D \approx 0.1\ m$, and an $f_{\#} \approx 16$. In fact, these are also the expected values used in the sensitivity analysis reported in Section b), and are chosen to ensure that the analyses for the position uncertainty in Section a) and the blurred diameter in Section b) are consistent with each other.

In summary, the effect of experimental parameters such as η, M, f#, density gradients etc. are assessed in the sensitivity analyses, and the results show how the model predictions would behave for different experiments. It is seen from 2.4.1 that the position uncertainty is most affected by the illumination/exposure (α), the dot diameter (η), and the noise level (σ_n). For the blurred dot diameter in Section 2.4.2, it is seen that the distance between the dot pattern and the density field (z_D) has the largest effect, followed by the magnification (M) and the f-number (f#).

6.2.5 Uncertainty Amplification Ratio

The direct application of Equation (67) to calculate the CRLB for a given experiment is limited by the accuracy in the estimation of the image noise level which can vary across the field of view. In order to isolate the uncertainty amplification due to density gradients on the CRLB, an amplification ratio metric is proposed for BOS experiments that removes the effect of properties that are common to both the reference and gradient images. The amplification ratio, AR, is defined as the ratio of the CRLBs for the same dot in the reference and the gradient images, and it can be shown that this ratio is purely a function of the ratios of the peak intensities and ratios of the dot diameters,

$$AR_X = \frac{\sigma_{X_{0_{grad}}}}{\sigma_{X_{0_{ref}}}} = \sqrt{\frac{\eta_{0,X_{grad}}}{\eta_{0,X_{ref}}}\frac{\eta_{0,Y_{ref}}}{\eta_{0,Y_{grad}}}\frac{I_{0_{ref}}}{I_{0_{grad}}}}\left(\frac{1-R_{0,grad}^2}{1-R_{0,ref}^2}\right)^{\frac{1}{4}}$$
$$AR_Y = \frac{\sigma_{Y_{0_{grad}}}}{\sigma_{Y_{0_{ref}}}} = \sqrt{\frac{\eta_{0,Y_{grad}}}{\eta_{0,Y_{ref}}}\frac{\eta_{0,X_{ref}}}{\eta_{0,X_{grad}}}\frac{I_{0_{ref}}}{I_{0_{grad}}}}\left(\frac{1-R_{0,grad}^2}{1-R_{0,ref}^2}\right)^{\frac{1}{4}} \quad . \qquad \textbf{(69)}$$

In addition, the proposed amplification ratio metric can also be used to report position uncertainties in tracking-based processing for BOS, as these processing methods are shown to significantly improve the accuracy, precision and spatial resolution [9]. First, the position uncertainty for the reference image can be calculated by recording several (e.g. 1000) images of the dot pattern without any flow and estimating the standard deviation of the dot centroids from the subpixel fits. Then, the position uncertainty for a given dot in the gradient image can be calculated by multiplying the position uncertainty for the corresponding dot in the reference image and the amplification ratio. The two position uncertainties can then be combined to calculate a displacement uncertainty for each track, and the uncertainty in the density field can be obtained by propagating the displacement uncertainties through the BOS measurement chain [21].

6.3 Comparison of the model with synthetic BOS images

The theoretical result for the CRLB was tested with synthetic BOS images generated using a ray based synthetic image generation methodology for PIV/BOS experiments in variable density environments, for the purpose of simulating general optical setups as well as for error and uncertainty analysis [22]. Using this methodology, synthetic BOS images were generated for an inviscid supersonic flow over a 11.5° wedge at Mach 2.5 and a free-stream density of 0.46 kg/m^3, corresponding to an experiment described in [21]. The inviscid density field was calculated using shock-expansion theory [23], and discretized on a grid of 234x84x51 points with a spacing of 0.3 mm x 0.3 mm x 0.5 mm along x, y, and z respectively, and is shown in Figure 6.6 (a).

Synthetic BOS images were rendered for a regular dot pattern with a dot diameter of 3 pix. and a dot spacing of 6 pix. The distance between the dot pattern and the mid-plane of the density gradient field was 2.54 mm and the depth of the density gradient field along z was 2.54 mm. The focal length of the camera lens was 105 mm at an aperture setting of f22 to obtain an effective magnification of 0.53 for the dot pattern and 0.57 for the density gradient field. In addition, an image was rendered without the density gradient field to serve as the reference image.

The dots on both the reference and gradient images were identified, sized and tracked using a dot tracking methodology for BOS, that has been shown to significantly improve the accuracy, precision and spatial resolution of the displacement estimation process [9]. The method utilizes prior knowledge of the positions and sizes of the dots on the target to improve the identification and centroid estimation process.

Once all dots have been tracked, each pair of dots from the reference and gradient images are corrupted with zero-mean Gaussian noise. The standard deviation of the normal distribution was set to be 10% of the peak intensity of the reference dot image, to ensure that the same level of absolute noise was added to both images, as the peak intensity of the gradient dot image will be lower in case of blurring.

The dot locations in the noisy image were located using a Least Squares Gaussian (LSG) subpixel fitting scheme, which involves fitting a Gaussian curve to the intensity map of a dot, under the assumption that the diffraction limited image can be approximated by a Gaussian distribution [17], [19]. In this method, the parameters are obtained by minimizing the residual between the predicted intensity from the fit and the actual intensity of the pixels using a non-linear least squares method. The least squares method is initialized by the three-point Gaussian (TPG) fit, which calculates the peak location (referred to as the "centroid" in the following) , peak intensity and standard deviation of a Gaussian curve by fitting it to the intensity values recorded at three points/pixels on the dot intensity map [24]. The three points are taken to be the pixel with maximum intensity and one pixel on either side of the maximum. The centroid estimates are then compared with the ground truth obtained from the final positions of the light rays traced in the simulation to compute the position error. For each dot, the noise addition and centroid estimation procedure was performed 1000 times to calculate the position uncertainty, defined as the standard deviation of the position error. The amplification ratio was then calculated as the ratio of the position uncertainties of the dots in the gradient to the reference image. As noted before, any asymmetrical blur is neglected because, a symmetrical blur is sufficient to elucidate the effect of image blur on the measurement precision. However, the skew due to asymmetrical blurring would need to be considered to account for bias errors.

The LSG fit is the Maximum Likelihood Estimate (MLE) for the centroid estimation in the case of normally distributed image noise. Since the MLE approaches the CRLB in the limit of large number of observations, it is expected that the variance of the centroid estimates from the LSG method would approach the result for the CRLB derived in the previous section [14].

It can be shown that the LSG is the MLE for the centroid estimation problem as follows. For a probability density function defined as $p_\theta(x)$ where x is the signal, and θ is the parameter governing the pdf, the likelihood function is defined as

$$L(\theta|x) = p_\theta(x) \quad . \tag{70}$$

Typically, the likelihood function is replaced by the log likelihood given by

$$l(\theta|x) = \ln L(\theta|x) \quad . \tag{71}$$

The maximum likelihood estimate for the parameter θ given a set of measurements x obeying a known pdf $p_\theta(x)$ is defined as the value that maximizes the likelihood function for the given set of measurements. Since the log function is monotonic, maximizing the log likelihood function is equivalent to maximizing the likelihood function.

$$\hat{\theta} \in \underset{\theta \in \Theta}{\operatorname{argmax}} \, l(\theta|x) \quad . \tag{72}$$

The example we consider here is the Gaussian image of a dot on a camera sensor corrupted with zero-mean noise that is normally distributed with standard deviation σ_n. It was shown earlier that the joint PDF of the image intensity over a M x N pixel region is given by

$$p(\hat{g}, \boldsymbol{a}) = \left(\frac{1}{2\pi\sigma_n^2}\right)^{\frac{MN}{2}} \exp\left[-\frac{1}{2\sigma_n^2}\sum_{k=0}^{M}\sum_{l=0}^{N}(\hat{g}_{kl} - g_{kl})^2\right] . \tag{73}$$

Therefore, the log likelihood function for the parameter $\boldsymbol{a}$ given an intensity measurement $\hat{g}$ becomes

$$l(\boldsymbol{a}|\hat{g}) = -\frac{MN}{2}\ln 2\pi\sigma_n^2 - \frac{1}{2\sigma_n^2}\sum_{k=0}^{M}\sum_{l=0}^{N}(\hat{g}_{kl} - g_{kl})^2 \tag{74}$$

and the MLE becomes

$$\begin{aligned} \hat{\boldsymbol{a}} &\in \underset{\theta \in \Theta}{\operatorname{argmax}} \, l(\boldsymbol{a}|\hat{g}) \\ &\in \underset{\theta \in \Theta}{\operatorname{argmin}} \sum_{k=0}^{M}\sum_{l=0}^{N}(\hat{g}_{kl} - g_{kl})^2 \end{aligned} \tag{75}$$

which is a Least Squares solution. Since g_{kl} is modelled to be a Gaussian, the MLE is a Least Squares Gaussian fit.

The position uncertainty is also estimated from equations (56), (57), and (67) using the specified noise level for the reference and gradient dot images and used to calculate the *theoretical* amplification ratio. Finally, another estimate of the position uncertainty of a dot in the gradient image is obtained by multiplying the amplification ratio from theory with the position uncertainty of the corresponding dot in the reference image. This will be referred to as the *hybrid* uncertainty estimate and is to be a test of the uncertainty quantification methodology introduced in the work.

The spatial variation of the amplification ratio from the theory and simulation are shown in Figure 6.3 (b) and (c) respectively, where it can be seen both results show a rise in the shock region due to blurring of the dot image, with a slight under-prediction in the ratios from the theory. The under-prediction in the theory is expected because it is the lower bound on the measurement uncertainty in the limit of infinite number of observations, infinite sampling and a perfect estimation of the dot diameter in the reference image. However, real measurements deviate from these assumptions, leading to a higher estimated position uncertainty for both the reference and gradient images.

In order to test the amplification ratio calculation separately from the position uncertainty prediction, the hybrid uncertainty is also calculated, and the PDFs of position uncertainties are shown in Figure 6.6 (d) for the theory, simulation, and hybrid estimates, along with the root-mean-square (RMS) estimates. It is seen that while the theoretical position uncertainties underpredict the simulations by about 0.01 pix., the hybrid estimate using the measured position uncertainty from the reference image is used with the theoretical amplification ratio, then the predicted position uncertainty for the gradient image matches the results from simulation. This implies that accurate estimates of the position uncertainty for the gradient image can be obtained using the position uncertainty for the reference image and the amplification ratio. While the position uncertainty for the reference dots are obtained using Monte-Carlo simulations in the synthetic analysis, for experiments they can obtained by recording several reference images and estimating the standard deviation of the positions of the same dot across the time series.

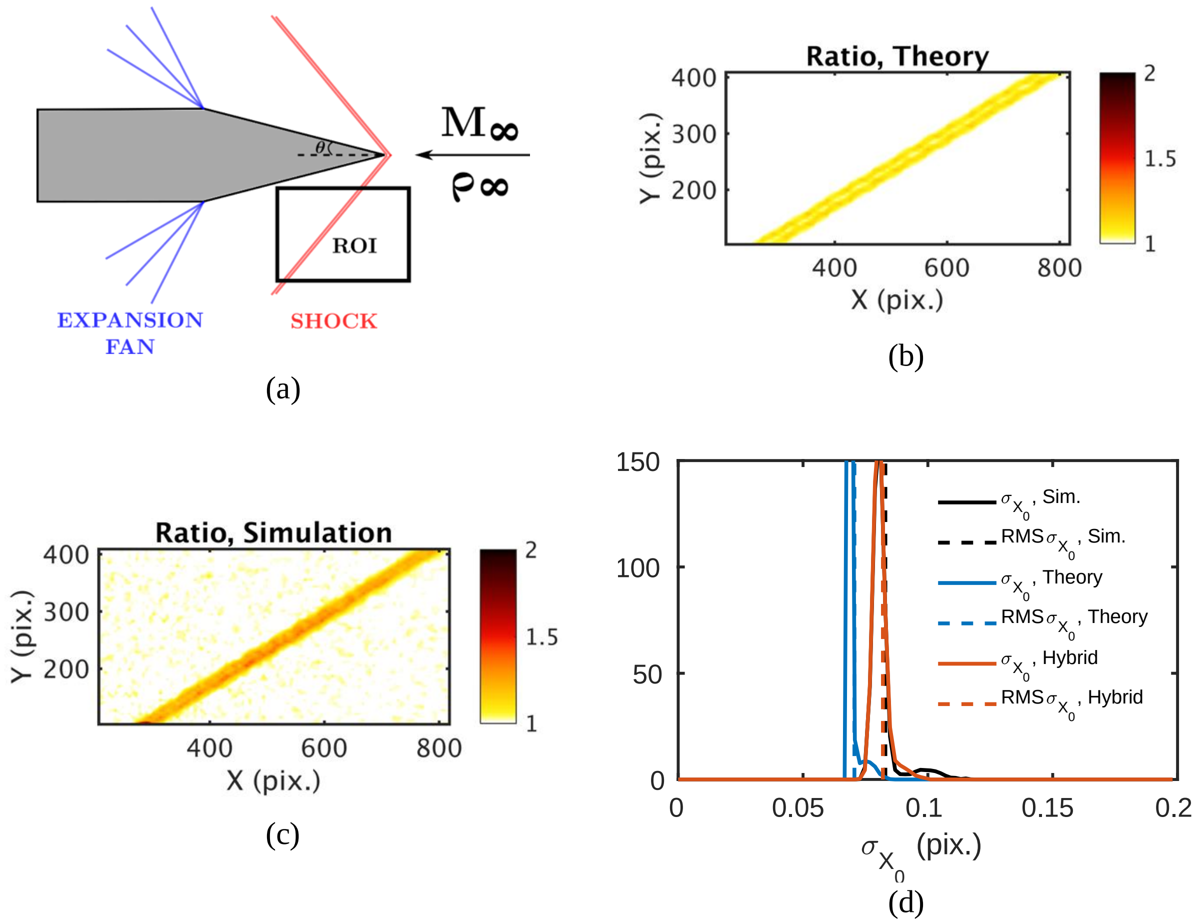

Figure 6.6. Results of the synthetic image analysis for supersonic flow over a wedge. (a) Illustration of the wedge geometry and the region of interest, (b) Spatial variation of amplification ratio from theory and (c) from simulations, (d) PDF and RMS of position uncertainties.

6.4 Demonstration with Experimental Images

The proposed CRLB estimation methodology and the uncertainty amplification is demonstrated on experimental BOS images of flow induced by a nanosecond spark discharge reported by Singh et. al. [25]–[27]. The spark discharge leads to rapid heating of the gas in the electrode gap resulting in a complex three-dimensional flow field. The BOS measurements were performed by recording images of a target dot pattern containing a regular grid of dots in the presence of the spark induced flow field. The images with the flow can be compared to a reference image recorded prior to the discharge to estimate the displacement field and to measure the blurring of the dots in the presence of density gradients. The dot size was about 3 pix., the magnification was 0.8, and the distance between the dot pattern and the spark electrodes was 3.18 cm. More details of the experimental setup can be found in Singh et. al. [25]–[27].

For the experimental images, the Uncertainty Amplification Ratio *AR* defined in Section 6.2.5 was calculated for all the identified dots in both the reference and gradient images using an elliptical Least Square Gaussian fit, and the magnitude of the amplification ratio ($= \sqrt{AR_x^2 + AR_y^2}$) is shown in Figure 6.7.. Also shown are the displacement field which corresponds to the projected density gradients as given by Equation (39) and a histogram of the position uncertainty magnitude for the gradient image calculated using the uncertainty quantification methodology outlined in Section 6.2.5. As the flow-field involves a large number of points in the ambient, only vectors with displacements larger than the 20th percentile (~ 0.05 pix.) are plotted in the histogram. The dot identification and displacement estimation is performed using the same tracking methodology used for the synthetic image analysis.

The figures show that regions corresponding to the displacement gradients are coincident to regions with large values of the ratio metric. However, in the present flow field, the regions of high displacements and displacement gradients coincide because of the sharp density gradient interface, and hence the amplification ratio appears to increase with displacement. A value of the ratio metric greater than 1 implies that the CRLB for the gradient image will be higher than the reference image in this region. While the regions greater than 1 mostly occur in regions with large second gradients of the density (first derivative of displacement), there are still some stray values in regions without density gradients, that are most likely due to intensity fluctuations between the reference and gradient images from the Xenon arc lamp light source used for the experiments.

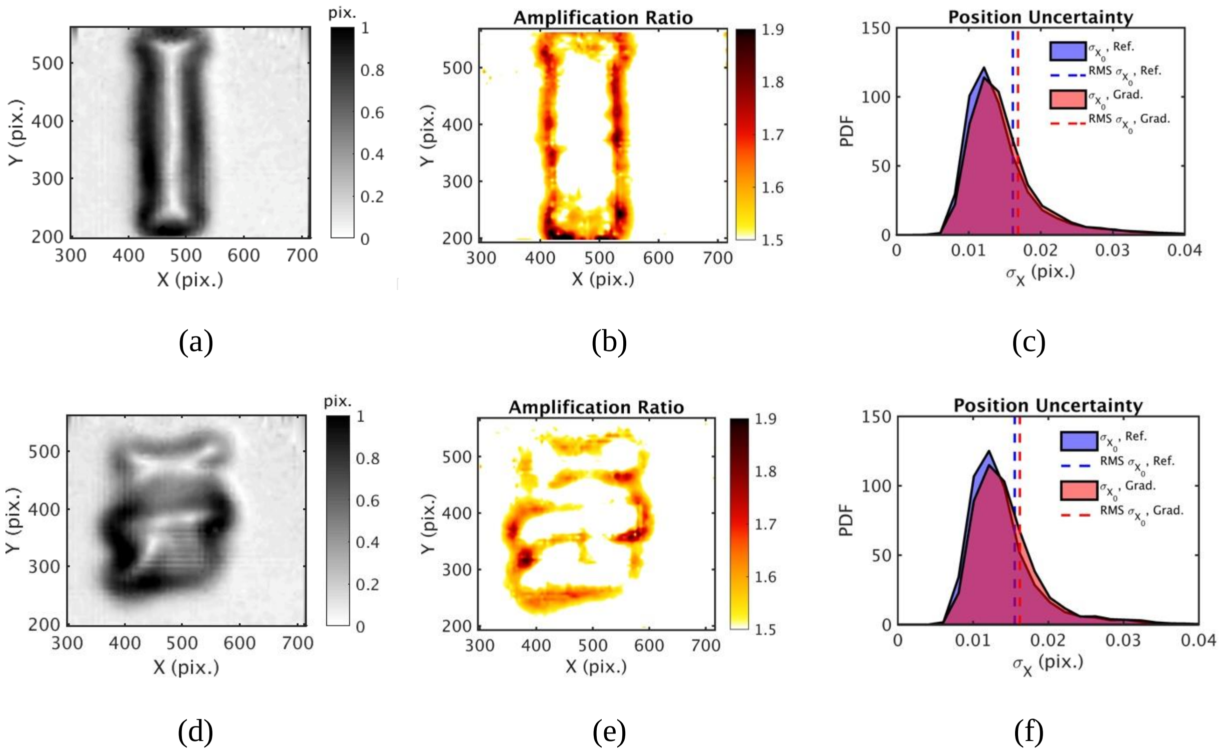

Figure 6.7. Snapshots of the displacements (a), (d), amplification ratios (b), (e), and histogram of position uncertainties for the gradient image (c), (f) for two time instants of the spark induced flow field.

6.5 Conclusions

The effect of density/refractive-index gradients on the precision of BOS experiments was theoretically analyzed using the Cramer-Rao lower bound of the 2D centroid estimation process. To perform the analysis, a model for the diffraction limited image of a dot viewed through a non-linear density gradient field was derived under the assumption of a small ray cone angle which is expected to be reasonable given the requirement of a large depth of field to focus on both the target and the flow field. Under the further assumption that the effective model of a dot imaged through density gradients can be described by a Gaussian profile, it was shown that the effective centroid can be expressed as the original centroid of the image in addition to a shift corresponding to the average deflection of light rays, and that the effective diameter is a root mean squared sum of the diffraction diameter and a blurring due to the second derivatives of the density field. As a result of the increase in the diameter due to blurring, the effect of density gradients is to *increase* the Cramer-Rao lower bound and to lower the measurement precision in the centroid estimation process. It was also seen that the ratio of the CRLBs of the dots in the reference and gradient images, termed the Uncertainty Amplification Ratio (AR), is a function of the ratio of their diameters and the peak intensities. Based on this ratio, a methodology was proposed to report position uncertainties for tracking-based BOS measurements.

The theoretical amplification ratio predicted by the imaging model was compared with ray tracing simulations for synthetic BOS images of supersonic flow over a wedge. The dot images were corrupted with Gaussian noise and the centroid was estimated using a Least Square Gaussian fit, and the corresponding position error was calculated for 1000 trials to estimate the position uncertainty. This procedure was repeated for all pairs of dots in the reference and gradient images, and the ratio of the position uncertainty was used to calculate the AR. In addition, these quantities were also calculated from the theory, and the AR from the theory was combined with the position uncertainty in the reference image from the simulations to calculate the uncertainty for the gradient image. The results show a rise in the amplification ratio in the shock region due to blurring of the dot image and the AR predictions from theory slightly under-predict the simulations. In addition, it was seen that position uncertainties for the gradient image that were estimated using the theoretical amplification ratio and the position uncertainty from the reference image obtained from simulations, accurately predict the true uncertainty from the simulations. This signifies that the AR is a valid metric to report uncertainties for tracking based BOS measurements. The implications of the model of the CRLB were also demonstrated with experimental BOS images of flow induced by a nanosecond spark discharge. Analysis of the images showed that the CRLB for the gradient image is amplified with respect to the reference image particularly in regions of strong density gradients. While the experimental demonstrations are qualitatively consistent with the model, benchmark experiments over a wider parameter space are required to further test the model proposed in this work.

One of the limitations of this work is that small-scale setups were used in both the simulations and experiments corresponding to typical laboratory settings. However, the theoretical analysis shows that the blurring scales as Z_D^4, therefore the blurring effect will be more significant for large-scale industrial facilities. In contrast, the magnification M and the angle of the ray cone $\Delta\theta$ would also be lower for a large-scale facility, so the effect would be somewhat mitigated. Therefore, uncertainty amplification for large-scale BOS setups is an interesting avenue deserving further analysis.

Beyond BOS, the image model presented in this work can also be extended to the analysis of position estimation uncertainties in a multi-camera volumetric PTV setup and propagated through the measurement chain accounting for uncertainties introduced in the calibration and reconstruction procedures to elucidate the effect of distortions due to density/refractive-index gradients on the 3D centroid estimation process [28]. Another area of future work is to apply this methodology to assess the effect of curved windows on the position uncertainty. Further, the possible utility of the uncertainty amplification factor for uncertainty quantification for correlation-based PIV/BOS similar to the peak-to-peak ratio and signal to noise ratio metrics [29]–[31] is an avenue for further work.

6.6 Acknowledgement

This material is based upon work supported by the U.S. Department of Energy, Office of Science, Office of Fusion Energy Sciences under Award Number DE-SC0018156. Bhavini Singh is acknowledged for help with the spark discharge experiment. Jiacheng Zhang, Javad Eshraghi and Adib Ahmadzadegan are acknowledged for reviewing the manuscript drafts. This work was also supported by NSF 1706474.

6.7 References

[1] H. Richard and M. Raffel, "Principle and applications of the background oriented schlieren (BOS) method," *Meas. Sci. Technol. Meas. Sci. Technol*, vol. 12, no. 12, pp. 1576–1585, 2001.

[2] G. Meier, "Computerized background-oriented schlieren," *Exp. Fluids*, vol. 33, no. 1, pp. 181–187, 2002.

[3] S. B. Dalziel, G. O. Hughes, and B. R. Sutherland, "Whole-field density measurements by 'synthetic schlieren,'" *Exp. Fluids*, vol. 28, no. 4, pp. 322–335, 2000.

[4] M. Raffel, "Background-oriented schlieren (BOS) techniques," *Exp. Fluids*, vol. 56, no. 3, pp. 1–17, 2015.

[5] G. E. Elsinga, B. W. Van Oudheusden, and F. Scarano, "Evaluation of aero-optical distortion effects in PIV," *Exp. Fluids*, vol. 39, no. 2, pp. 246–256, 2005.

[6] G. E. Elsinga, B. W. van Oudheusden, and F. Scarano, "The effect of particle image blur on the correlation map and velocity measurement in PIV," in *Proceedings of SPIE*, 2005, vol. 5880, p. 588010.

[7] G. E. Elsinga, B. W. van Oudheusden, and F. Scarano, “Modeling of particle imaging through shock waves,” *Opt. Model. Perform. Predict. II*, vol. 5867, pp. 58670M-58670M–11, Aug. 2005.

[8] G. E. Elsinga and G. C. Orlicz, “Particle imaging through planar shock waves and associated velocimetry errors,” *Exp. Fluids*, vol. 56, no. 6, p. 129, Jun. 2015.

[9] L. K. Rajendran, S. P. M. Bane, and P. P. Vlachos, “Dot tracking methodology for background-oriented schlieren (BOS),” *Exp. Fluids*, vol. 60, no. 11, p. 162, Nov. 2019.

[10] M. M. Clem, C. A. Brown, and A. F. Fagan, “Background Oriented Schlieren implementation in a jet-surface interaction test,” *51st AIAA Aerosp. Sci. Meet. Incl. New Horizons Forum Aerosp. Expo. 2013*, no. January, pp. 1–14, 2013.

[11] F. Sourgen, F. Leopold, and D. Klatt, “Reconstruction of the density field using the Colored Background Oriented Schlieren Technique (CBOS),” *Opt. Lasers Eng.*, vol. 50, no. 1, pp. 29–38, 2012.

[12] F. Nicolas *et al.*, “A direct approach for instantaneous 3D density field reconstruction from background-oriented schlieren (BOS) measurements,” *Exp. Fluids*, vol. 57, no. 1, pp. 1–21, 2016.

[13] A. van den Bos, *Parameter estimation for scientists and engineers*. Wiley and Sons, 2007.

[14] H. Nobach and C. Tropea, “Fundamentals of Data Processing,” in *Springer Handbook of Experimental Fluid Mechanics*, Berlin, Heidelberg: Springer Berlin Heidelberg, 2007, pp. 1399–1417.

[15] M. P. Wernet and A. Pline, “Particle displacement tracking technique and Cramer-Rao lower bound error in centroid estimates from CCD imagery,” *Exp. Fluids*, vol. 15, no. 4–5, pp. 295–307, 1993.

[16] J. Westerweel, “Theoretical analysis of the measurement precision in particle image velocimetry,” *Exp. Fluids*, vol. 29, no. 7, pp. S003-S012, 2000.

[17] R. J. Adrian and C. S. Yao, “Pulsed laser technique application to liquid and gaseous flows and the scattering power of seed materials.,” *Appl. Opt.*, vol. 24, no. 1, pp. 44–52, 1985.

[18] M. Willert, C.E. and Gharib, “Digital Particle Image Velocimetry”, Experiments in Fluids,” *Exp. Fluids*, vol. 3, pp. 181–193, 1991.

[19] M. R. Brady, S. G. Raben, and P. P. Vlachos, “Methods for Digital Particle Image Sizing (DPIS): Comparisons and improvements,” *Flow Meas. Instrum.*, vol. 20, no. 6, pp. 207–219, 2009.

[20] E. Goldhahn and J. Seume, “The background oriented schlieren technique: Sensitivity, accuracy, resolution and application to a three-dimensional density field,” *Exp. Fluids*, vol. 43, no. 2–3, pp. 241–249, 2007.

[21] L. K. Rajendran, J. Zhang, S. Bhattacharya, S. Bane, and P. Vlachos, "Uncertainty quantification in density estimation from background oriented schlieren (BOS) measurements," *Meas. Sci. Technol.*, no. December 2016, pp. 0–22, Dec. 2019.

[22] L. K. Rajendran, S. P. M. Bane, and P. P. Vlachos, "PIV/BOS synthetic image generation in variable density environments for error analysis and experiment design," *Meas. Sci. Technol.*, pp. 11–14, Apr. 2019.

[23] J. D. Anderson, *Fundamentals of Aerodynamics*, 4th ed. McGraw-Hill, 2004.

[24] C. Willert and M. Gharib, "Digital particle image velocimetry," *Exp. Fluids*, vol. 193, pp. 181–193, 1991.

[25] B. Singh, L. K. Rajendran, P. Gupta, C. Scalo, P. P. Vlachos, and S. P. M. Bane, "Experimental and Numerical Study of Flow Induced by Nanosecond Repetitively Pulsed Discharges," *AIAA Scitech 2019 Forum*, no. January, pp. 1–15, 2019.

[26] B. Singh, L. K. Rajendran, P. P. Vlachos, and S. P. M. Bane, "Two regime cooling in flow induced by a spark discharge," *Phys. Rev. Fluids*, 2019.

[27] B. Singh, L. K. Rajendran, P. Vlachos, and S. P. M. Bane, "Study of cooling and the effect of energy deposited in a single nanosecond spark plasma discharge using simultaneous 50 kHz PIV and BOS," in *AIAA Scitech 2020 Forum*, 2020.

[28] S. Bhattacharya and P. P. Vlachos, "Uncertainty Quantification in Volumetric PTV," in *13th International Symposium on Particle Image Velocimetry*, 2019.

[29] J. J. Charonko and P. P. Vlachos, "Estimation of uncertainty bounds for individual particle image velocimetry measurements from cross-correlation peak ratio," *Meas. Sci. Technol.*, vol. 24, no. 6, p. 065301, Jun. 2013.

[30] Z. Xue, J. J. Charonko, and P. P. Vlachos, "Particle image velocimetry correlation signal-to-noise ratio metrics and measurement uncertainty quantification," *Meas. Sci. Technol.*, vol. 25, no. 11, 2014.

[31] Z. Xue, J. J. Charonko, and P. P. Vlachos, "Particle image pattern mutual information and uncertainty estimation for particle image velocimetry," *Meas. Sci. Technol.*, vol. 26, no. 7, 2015.

7. FILAMENTARY SURFACE PLASMA DISCHARGE FLOW LENGTH AND TIME SCALES

Lalit K. Rajendran[1], Bhavini Singh, Pavlos P. Vlachos[2] and Sally P. M. Bane[1]
[1] Purdue University, School of Aeronautics and Astronautics, West Lafayette, USA.
[2] Purdue University, School of Mechanical Engineering, West Lafayette, USA.
This chapter has been published in Journal of Physics D: Applied Physics, and reproduced here with permission. DOI: https://doi.org/10.1088/1361-6463/abe66a

Abstract

Nanosecond Surface Dielectric Barrier Discharge (ns-SDBDs) are a class of plasma actuators that utilize a high-voltage pulse of nanosecond duration between two surface-mounted electrodes to create an electrical breakdown of air, along with rapid heating. These actuators usually produce multiple filaments when operated at high pulse frequencies, and the rapid heating leads to the formation of shock waves and complex flow fields. In this work we replicate a single filament of the ns-SDBDs and characterize the induced flow using velocity measurements from particle image velocimetry and density measurements from background-oriented schlieren. The discharge is produced by a high voltage electrical pulse between two copper electrodes on an acrylic base. A hot gas kernel characterizes the flow field formed close to the electrodes that expands and cools over time and a vortex ring that propagates away from the surface while entraining cold ambient fluid. The gas density deficit inside the kernel displays a power-law decay over time. Based on the observations, we develop a simplified theoretical model based on vortex-driven cooling and perform a scaling analysis to obtain the induced flow length and time scales. The results show that the cooling process's time scales correspond to a circulation-based time scale of the vortex ring, and the length scale of the kernel corresponds to the vortex ring radius. These findings can guide the choice of optimal filament spacing and pulse frequencies in the design, deployment, and operation of nanosecond surface dielectric barrier discharges (ns-SDBDs) for flow control.

7.1 Introduction

There is growing interest in the use of nanosecond surface dielectric barrier discharge (ns-SDBD) actuators for high-speed (supersonic/hypersonic) flow control. A plasma discharge is created in these actuators using a nanosecond-duration pulse of several kilovolts to deposit energy rapidly in the electrode gap [1–3]. The electrical breakdown leads to a two-step ultra-fast heating mechanism characterized by (1) the electronic excitation of gaseous nitrogen molecules by electron impact and (2) subsequent dissociative quenching of the excited N_2 by oxygen molecules producing oxygen atoms and excess thermal energy [4–6]. The rapid heat release leads to the formation of a shock wave and the development of a complex three-dimensional flow field near the actuator surface characterized by coherent vorticity and a hot gas kernel [7–13].

Past work studying the flow induced by ns-SDBDs has shown that the initial strength of the induced shock increases with the peak voltage and that the shock rapidly decays to an acoustic wave on moving away from the actuator surface [7, 8, 14, 15]. High-speed schlieren visualization of the post-shock stage of the induced flow has shown the presence of a hot gas kernel near the electrodes, which expands and cools to ambient [11, 13, 15, 16]. Actuators based on ns-SDBDs have also been applied to control the shock-boundary layer interaction (SBLI) on a wedge, and it was found that the actuator can perturb the low-frequency unsteadiness in the separation bubble [17]. Interactions between the shock generated by the actuator and the incident oblique shock have also been observed in the study by Kinefuchi et al. [18, 19], who found an optimal pulse frequency for the actuator, corresponding to a time scale based on the boundary layer thickness and the flow velocity. Although a general idea of the flow features induced by a ns-SDBD exists, the effect of the actuator geometry (such as the filament spacing) and the operating parameters (such as the pulse frequency) on the induced flow are not well understood and play a critical role in flow control applications. Further, a knowledge of the intrinsic frequency of the flow induced by the actuator and its relation to the time scales associated with an oncoming flow is also critical for flow control applications.

Even the flow field induced by a single pulse of a ns-SDBD is not entirely understood at a more fundamental level, in contrast to the well-characterized AC-driven SDBD. The flow field induced by ns-DBDs is on much shorter time scales (by almost an order of magnitude) and involves large spatiotemporal gradients in the velocity and temperature fields, posing a significant experimental challenge. However, detailed measurements of the induced flow are required to develop a mechanistic model of the actuator performance, such as the vorticity production, heating, penetration depth, etc., and to develop scaling rules that relate the actuator design and operating conditions to its performance.

In this work, we perform the first detailed characterization of the flow induced by a single filamentary surface discharge produced by a single nanosecond-duration pulse in a quiescent medium using Particle Image Velocimetry (PIV) and Background Oriented Schlieren (BOS) measurements and develop a reduced-order model for the flow field. Filamentary discharges are preferred because they can provide localized heating with minimal power density requirements and provide better control authority as their position on the surface and morphology is known and controllable [10, 11, 13]. Further, Leonov et al. [13] have observed that when ns-SDBD actuators are operated in high Reynolds number flows, they almost always transform to a filamentary discharge due to ionization instabilities. While reducing the problem to a single filament and a single pulse is a considerable simplification from practical applications, it allows us to remove the interaction between the flow induced by adjacent filaments and subsequent pulses.

We first identify a candidate actuator that can be used to create a well-controlled single plasma filament with a single pulse and then perform PIV and BOS measurements to characterize the induced flow for a range of discharge energies. The measurements show that the induced flow consists of a hot gas kernel filled with vorticity in a vortex ring that expands and cools over time. We also develop a reduced-order model to describe the induced flow and show that the expansion of the kernel is governed by the vortex ring motion, and the entrainment of cold gas governs the cooling. Applying the model to the experimental data reveals that the vortex ring's properties govern the time scale associated with the kernel dynamics. The model predictions for the actuator-induced flow length and time scales can guide the choice of filament spacing and pulse frequencies for practical multi-pulse ns-SDBD configurations.

7.2 Experimental Methods

7.2.1 Actuator Geometry, Plasma Generation and Electrical Measurements

A saw-tooth actuator consisting of copper electrodes on an acrylic base was used for the measurements and is shown in Figure 7.1 (a). The electrodes tips were 2 mm apart, and the thickness of the copper tape was approximately 0.1 mm. This particular actuator was chosen because it could produce a single discharge filament for a single pulse, thereby providing a controlled line deposition of energy, as shown in Figure 7.1 (b). These choices were based on direct imaging of the discharge produced by several actuator designs with varying tip geometries, and with some candidates also featuring Kapton tape to provide higher dielectric strength. Since the candidates with Kapton tape could not produce a single filament with a single pulse, which is the main objective of this study, this particular actuator was chosen even though it is not a traditional DBD. The actuator designs were based on previous work by Devarajan et al. [11], and the details on the design study are summarized in [20].

The plasma discharge was generated by an Eagle Harbor Technology NSP-300 high voltage nanosecond pulser connected to the electrodes by high voltage cables soldered to the electrodes. The electrical properties of the discharge were measured using two Tektronix P6015A high voltage probes (in a differential measurement configuration) and a Magnelab CT-D1.0 current transformer. The probes were connected to an Agilent DSO9104A oscilloscope, and the voltage and current traces were used to calculate the discharge power and energy deposited. The displacement current was measured for a case without a breakdown to calculate the lag between the voltage and the current [6]. The energy was varied by changing the DC voltage and the pulse duration to obtain a range of 1 – 5 mJ. Sample measurements of voltage, current, and electrical energy are shown in Figure 7.1 (c).

7.2.2 Background-Oriented Schlieren (BOS)

Background-Oriented Schlieren (BOS) was used to measure the density of the hot gas kernel and to characterize the cooling process [21–27]. A schematic of the experimental setup is shown in Figure 7.1 (d). The induced flow was imaged perpendicular to the electrode axis (in the Y-Z plane in Figure 7.1). The dot pattern used was a photomask with a regular grid of dots manufactured by FrontRange Photomask with dot diameters of 42 μm and center-to-center dot spacing of 42 μm. The photomask was back-illuminated by an arc lamp, and a diffuser plate was placed between the lamp and the dot pattern to provide uniform illumination over the field of view. The images were acquired using a Photron SA-Z camera recording at 20 kHz at 1024 x1024 pixels. The camera was equipped with a 200 mm focal length Nikon lens and a 2X teleconverter and operated at an aperture stop of f16 to achieve a magnification of 10 μm/pixels and a field of view of 10 mm x 10 mm. The distance between the dot pattern and the density gradients (Z_D) was 25.4 mm, and the distance between the camera and the dot pattern ($Z_B = Z_D + Z_A$) was 267 mm. A sample magnified image of the dot pattern at the first time instant with the plasma filament is shown in Figure 7.1 (b). It should be noted that this particular image is not used for the displacement estimation, and the image analysis begins from the 2nd frame.

The dot pattern images with and without the plasma-induced flow were processed using a dot tracking methodology that has been shown to provide an order of magnitude improvements in the accuracy, precision, and spatial resolution of the displacement estimation for BOS [28]. The method utilizes prior information about the dot pattern design, such as the location, size, and the number of dots, to provide near 100% yield. A correlation correction is performed after the tracking to improve the dynamic range for subpixel displacement estimation. The displacement estimates were validated with a Universal Outlier Detection (UOD) method for unstructured measurements using Delaunay triangulation [29]. The displacement uncertainties were calculated using a recently developed methodology for uncertainty amplification in BOS, based on the ratio of the cross-correlation plane diameters of the dot intensity maps in the reference and gradient images [30].

The displacement fields were used to calculate the density gradients using Equation (11),

$$\frac{\partial \rho_p}{\partial x} = \int \frac{\partial \rho}{\partial x} dz = \frac{\Delta x}{Z_D M} \frac{n_0}{K} \tag{76}$$

where $\partial\rho/\partial x$ is the density gradient along the x direction, Δx is the pixel displacement on the camera sensor, M is the magnification, Z_D is the distance between the density gradient and the dot pattern, n_0 is the refractive index of the undisturbed medium, and K is the Gladstone-Dale constant. The displacements were interpolated onto a regular grid (with the grid spacing based on the target dot spacing) along with the uncertainties, and a 2D integration was performed using a Weighted Least Squares density integration procedure [31] to obtain the projected density field ρ_p *relative* to the ambient [27]. Dirichlet boundary conditions were used on the left and right boundaries with zero relative projected density, as these points correspond to the ambient. The final spatial resolution of the measurements was 0.08 mm. The displacement uncertainties were propagated through the density integration procedure to estimate the density uncertainty [32], and the maximum uncertainties in the projected density were about 3% of the peak density deficit with respect to the ambient.

Following the density integration, a *projected density deficit* ($\rho_d = \rho_{p,\infty} - \rho_p$) was calculated where $\rho_{p,\infty} = 0$, and the hot gas kernel was identified as the set of points with a projected density deficit greater than 5% of the peak density deficit. Then the mean density deficit of all points in the kernel was calculated for each time instant, and this procedure was performed at each time step for all tests.

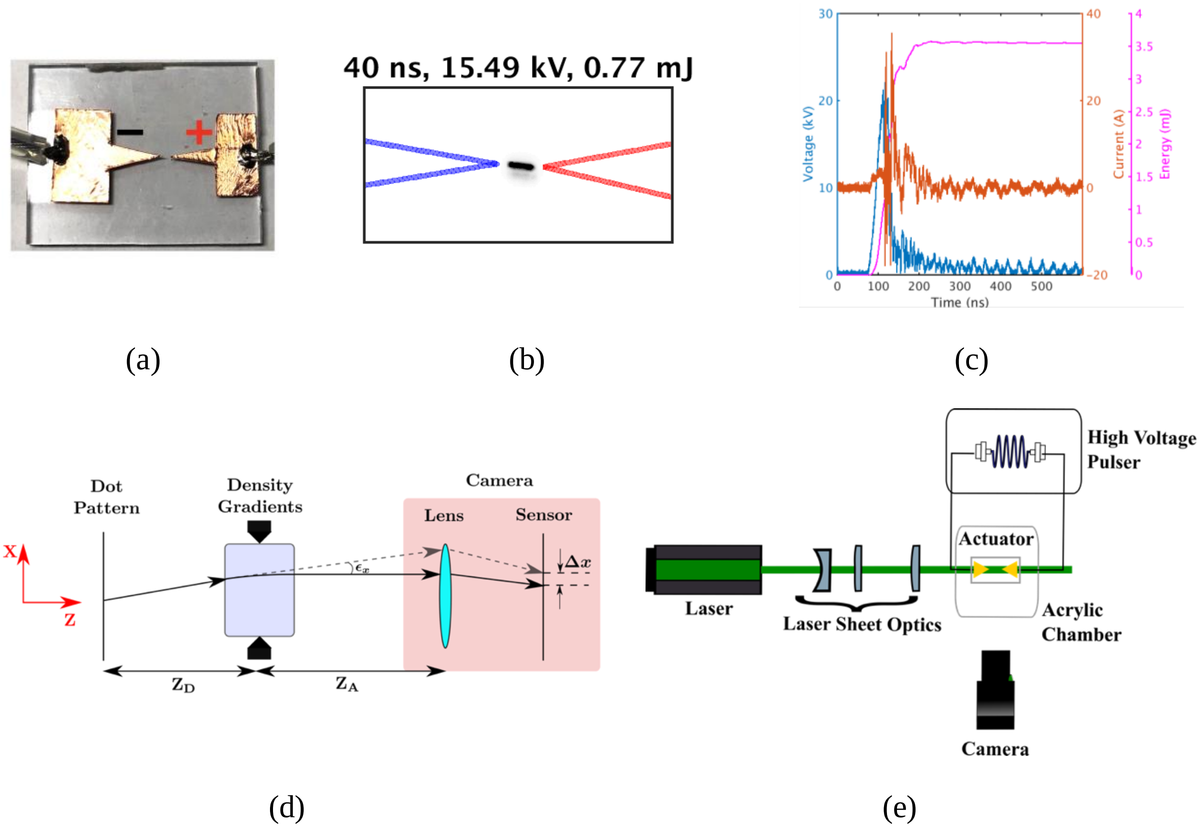

Figure 7.1. (a) Saw-tooth actuator used for the experiments, (b) false-color image of the discharge filament, (c) sample waveform for a discharge (d) schematic of the BOS experimental setup (top view), and (e) schematic of PIV experimental setup (top view).

7.2.3 Particle Image Velocimetry (PIV)

Time-resolved planar Particle Image Velocimetry (PIV) was used to measure the velocity and vorticity fields induced by the surface discharge. A schematic of the PIV system is shown in Figure 7.1 (e). The setup consists of an enclosed acrylic test section containing the surface discharge actuator, a Photron SA-Z camera, and an EdgeWave Nd:YAG laser operating at 20 kHz. The laser sheet optics produced an approximately 1 mm thin waist in the region of interest where the plasma was generated. A Quantum Composer Model 575 delay generator was used to synchronize and trigger the laser, cameras, and high voltage pulse generator. A fluidized bed seeder was used to inject aluminum oxide particles with diameters of about 0.3 µm and estimated Stokes number of approximately 0.002 into the chamber. Particle images were recorded at 20,000 fps at a resolution of 1024 x 1024 pixels using the Photron camber with a Nikon Nikorr 105 mm lens.

PRANA (PIV Research and ANAlysis) software was used to process the recorded particle images [33]. The correlation method used was the Robust Phase Correlation (RPC) [34, 35] in an iterative multigrid framework using window deformation [36, 37], with each pass validated by universal outlier detection (UOD) [38]. A total of four passes was used, and a 50% Gaussian window was applied to the original window size [39], resulting in window resolutions of 64 x 64 pixels in the first pass to 32 x 32 pixels in the last pass, with 50% window overlap in all passes. Between successive passes, velocity interpolation was performed using bicubic interpolation, and the image interpolation was performed using a sinc interpolation with a Blackman filter. The subpixel displacement was estimated using a three-point Gaussian fit [40], and the displacement uncertainty was calculated using the Moment of Correlation method [41]. The final spatial resolution was 0.16 mm, and the average uncertainty was approximately 0.02 m/s, about 20% of the mean velocity.

The velocity measurements were de-noised based on Proper Orthogonal Decomposition (POD) before post-processing [42]. The vorticity was calculated from the velocity field using the 4^{th} order noise-optimized compact-Richardson scheme [43]. As the vorticity calculations cannot differentiate between shear and swirl regions, coherent structures (vortex cores) identification was performed using a λ_{CI} criterion, or the swirl strength [44]. Regions in the flow field characterized by a swirl greater than the instantaneous 95^{th} percentile were considered coherent/swirling. The vorticity in the other regions was set to zero to ensure that spurious and shear-based vorticity measurements did not affect the subsequent calculation of the vortex ring properties.

The vortex ring parameters, such as the circulation and ring radius, were then calculated based on integral relations [45]. Instead of explicit tracking of the vortex cores, this method was used to minimize errors induced by coherent structure identification due to the complex distribution of vorticity. Further, the integral relations derived initially for an axisymmetric vortex ring were modified to account for the general experimental case, which may violate these assumptions because of tilting, three-dimensionality, etc. Therefore, the *net circulation* Γ was defined as half of the area integral of the magnitude of the vorticity field as given by (77), and the ring centroid was defined as the first moment of the magnitude of the vorticity field as given by (78). Finally, the *ring radius* R was defined as the first moment of the magnitude of the vorticity distribution about the ring centroid and is given by (79).

$$\Gamma = \frac{1}{2}\iint |\omega_z(x,y)|\, dx\, dy \tag{77}$$

$$x_0 = \frac{\iint x\, |\omega_z(x,y)| dxdy}{\iint |\omega_z(x,y)| dxdy} \tag{78}$$

$$R = \frac{\iint\ |x - x_0||\omega_z(x,y)| dxdy}{\iint |\omega_z(x,y)| dxdy} \tag{79}$$

These definitions reduce to the standard definition of the vortex ring properties for a perfectly axisymmetric flow field [45].

7.3 Results

In this section, we present observations of the density and vorticity fields to show that the discharge induces a hot gas kernel and a vortex ring, both of which move away from the surface over time. To describe the cooling process and the vortex dynamics, we develop a model relating the time variation of the mean kernel density to the vortex ring properties and use the model to develop characteristic length and time scales of the induced flow. The results presented in this work correspond to measurements on an actuator with an electrode gap of 2 mm, viewed from the side, obtained from a set of 15 tests for PIV, and another separate set of 15 tests for BOS.

7.3.1 Measurements of the plasma-induced flow field

The density and velocity measurements of the flow field from a single test are presented in Figure 7.2, though it should be noted that the two measurements are obtained from different realizations of the induced flow. The density measurements show a torus-shaped hot gas kernel close to the discharge location. Over time, the kernel propagates upwards, expands, and cools. In addition, the vorticity/swirl measurements show the formation of a vortex ring that propagates upwards from the surface. The ring is seen to entrain ambient fluid from the side and ejects this fluid vertically away from the surface. For these discharges the flow is induced by the outward expansion of a shockwave at early times (~ 1 μs), followed by the formation and propagation of the vortex rings at later times (~ 1 ms). The measurements reported in this work are in the late stages, where the gas velocity is induced by the vortex ring. While the direction of the inward flow induced by the rings is opposite to the direction of the kernel expansion, the two motions are distinct. The kernel expansion is a result of the mixing induced by the vortex rings and does not represent the flow velocity. However, the vorticity distribution at the early times is complex and the measurements are noisy, thereby limiting efforts at centroid estimation and tracking of the vortex cores.

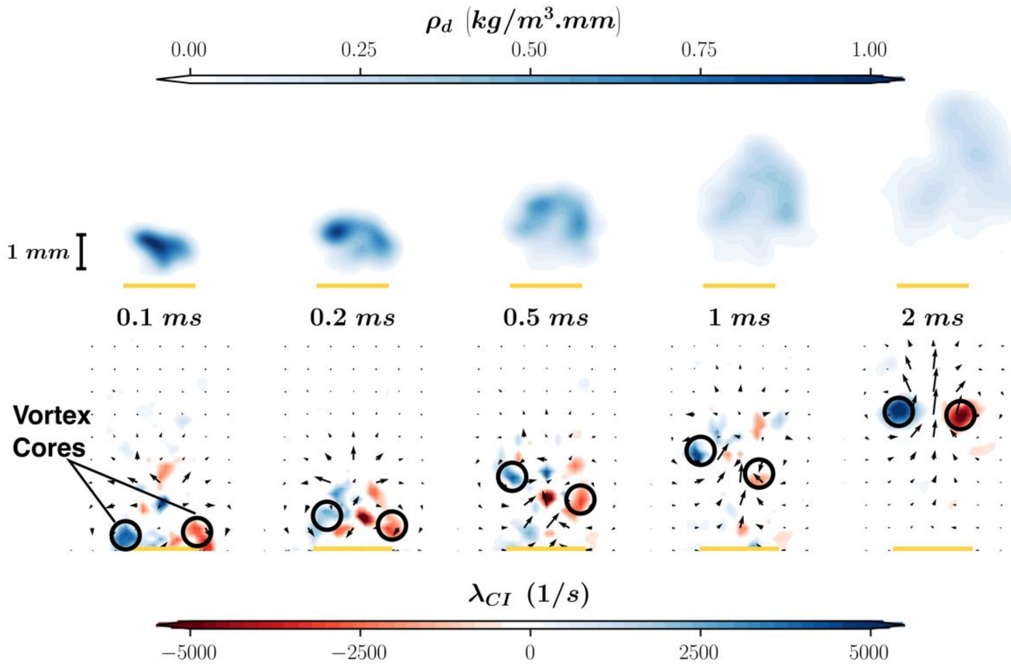

Figure 7.2. Density and swirl fields induced by the surface discharge from 0.1 to 2 ms. The top row shows the projected density deficit, and the bottom row shows the swirl contours and velocity vectors (every 4th vector shown). The two sets of measurements correspond to different realizations of the induced flow, with a peak to peak voltage of about 19 kV for the BOS measurement, and 13.5 kV for the PIV measurement.

The time histories of the bulk properties of the hot gas kernel and the vortex ring are shown in Figure 7.3 (a) and (b), respectively. Figure 7.3(a) shows that the mean density deficit of the kernel increases at early times, followed by a cooling period, and the simultaneous increase in area denotes the kernel expansion. Both the density deficits and the kernel areas increase with energy deposited in the plasma. For the vortex ring properties, shown in Figure 7.3(b), there is no such apparent effect of energy deposited, and the time series of the measurements is quite noisy.

The results show that the density deficit of the hot gas kernel decreases with time, and since the cooling process is essentially a surrogate for passive scalar mixing, we are interested in the time scale of this process and its relation to other flow parameters. In the case of a filamentary discharge produced between two pointed electrodes far away from a surface, the cooling rate of the hot gas kernel is controlled by cold gas entrainment due to a pair of vortex rings induced near the electrode tips [46, 47]. As the current flow induced by the surface discharge also features a vortex ring and a hot gas kernel, we are interested to know if a similar coupling exists between them. We examine these issues in the next section by reducing a simplified model for the induced flow.

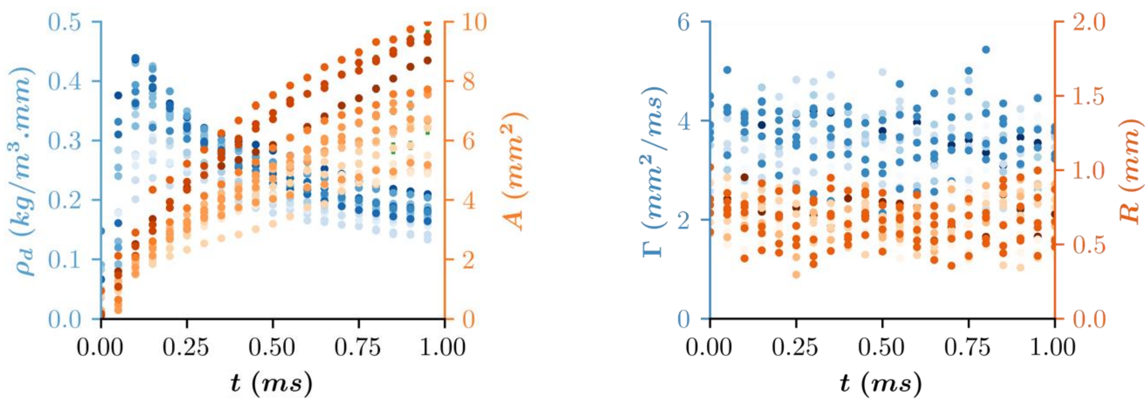

(a) (b)

Figure 7.3. Time histories of kernel and ring properties. (a) Density deficit of the kernel (left axis) and kernel area (right axis). (b) Net circulation (left axis) and radius (right axis) of the vortex ring. The darker markers represent a case with higher energy deposited.

7.3.2 A simplified model for the induced flow

This section develops a reduced-order model for the cooling induced by the vortex ring and performs a scaling analysis. A sketch of the flow field is shown in Figure 7.4 with a hot gas kernel near the wall and a vortex ring inside the kernel. The kernel is modeled as a cylindrical control volume denoted by the gray dashed line in the figure, and it is further assumed that this cylinder expands purely along the vertical direction due to the ring motion to simplify the analysis. The vortex ring entrains cold fluid along the hot gas kernel's sides and ejects warm, mixed fluid through the top boundary. Further, the radius of the control volume is approximated to be the radius of the vortex ring under the assumption that majority of the kernel will be confined within the rings, based on observations of a related flow in pin-to-pin discharges [47]. Under this framework, and following the analysis of Singh. et al. [46, 47], the relation between the density of the hot gas kernel and the entrainment can be expressed by,

$$\frac{\rho_\infty - \rho_k}{\rho_\infty - \rho_{k,i}} = \exp\left(-\int_{t_i}^{t} \frac{\dot{V}_{in}}{V_k} dt\right) \tag{80}$$

where ρ_∞ is the ambient density, ρ_k is the mean kernel density, V_k is the kernel volume, $\dot{V}_{in}$ is the entrainment of gas into the kernel, and the subscript i represents the initial conditions. Equation (80) is derived by combing the inviscid mass and energy conservation equations in the low Mach number limit. Details of the derivation are given in [46].

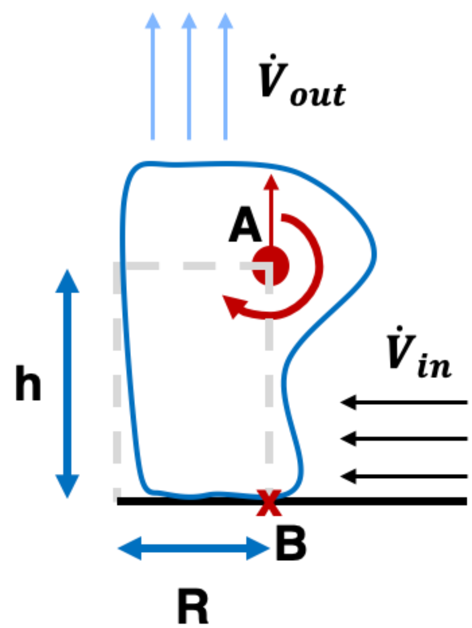

Figure 7.4. Schematic of a simple model for the flow field induced by the surface filament discharge.

In this analysis, we evaluate Equation (80) for the present geometry by modeling the vortex ring as a thin-core ring with a uniform vorticity distribution [51] and simplify the equation based on a scaling analysis. A scaling analysis is used because the goal of the theoretical analysis presented in this section is to estimate the length and time scales of the induced flow for applications with multi-filament and multi-pulse configurations. The uniform vorticity distribution is used because it is the most common model for a vortex ring for which analytical expressions for the streamfunction are available. However, the validity of this assumption is limited by the nature of the ring formation, which may be different from a traditional piston-driven vortex ring. This flow field has an added feature due to the presence of the wall, which can potentially affect the vortex ring dynamics and the cooling process. As shown by Walker et. al. [48], a vortex ring can be affected by a nearby wall due to the (1) no-penetration (inviscid), and (2) no-slip (viscous) boundary conditions. The inviscid effect is accounted for by modeling an image vortex below the wall, affecting properties such as the ring diameter, entrainment, etc. The viscous effects influence the velocity profile in the boundary layer near the wall and the shear stress distribution. Walker et al. noted from both computations and experiments that both the effect of the image vortex and viscous effects are negligible when the distance of the primary vortex from the wall is greater than one ring radius. In this situation, the entrainment can then be ascribed purely to the primary vortex ring, and the contribution from wall effects is negligible. In the flow field measurements shown in Figure 7.2, it is seen that the ring is approximately one radius away at 0.2 ms, and the ring integral parameters in Figure 7.3 (b) are also nearly constant after this time.

Under this condition, the entrainment through the right side of the control volume can be expressed as the difference between the value of the streamfunction ψ at the core of the ring (point A) and at the wall (point B). Further, since the streamfunction due to a vortex ring decays rapidly away from the core, its value at B when h > R will be negligible. The entrainment can then be expressed as

$$\begin{aligned} \dot{V}_{in} &= 2\pi(\psi_A - \psi_B) \\ &= \mathit{\Gamma} R\left[log\left(\frac{8R}{a}\right) - \frac{3}{2}\right] \approx \Gamma R. \end{aligned} \tag{81}$$

where Γ is the net circulation, R is the ring radius, and a is the vortex core radius. Therefore, it is seen that when the ring is far away from the wall ($h > R$), the entrainment is constant because the ring properties will not change. This is also observed in Figure 7.3 (b).

The volume V_k in Equation (80) can be calculated from the cylindrical control volume properties, which expands due to the ring motion. When the distance between the ring and the wall is larger than the ring radius, $h > R$, the ring can be approximated to have constant properties, and the volume of the ring as a function of time can be expressed as,

$$\begin{aligned} V_k(t) &= \pi R^2 h(t) \\ &= \pi R^2 V_{R,y} t \\ &= \frac{\pi R^2 \Gamma}{2\pi R} t \approx \Gamma R t \end{aligned} \tag{82}$$

where $V_{R,y}$ is ring velocity along the vertical direction.

Under these assumptions, the cooling equation in (80) can be simplified to obtain

$$\frac{\rho_\infty - \rho_k}{\rho_\infty - \rho_{k,i}} = \frac{\rho_{d,k}}{\rho_{d,k_i}} = \exp\left(-\int_{t_i}^{t} \frac{\alpha}{t} dt\right) = \left(\frac{t}{t_i}\right)^{-\alpha} \tag{83}$$

where $\rho_{d,k}$ is the average density deficit for the points within the hot gas kernel, ρ_{d,k_i} is the kernel deficit at the start of the cooling process (taken to be the maximum across the time series), and α is a constant of proportionality in the scaling analysis. The coefficient α is introduced to account for unsteady, three-dimensional effects that are neglected in this model, and which will vary from one realization to another. Physically, it represents the deviation of the entrainment from the inviscid vortex ring theory, as well as an expansion of the hot gas kernel that is not strictly vertical. The value of the α is determined from a power law fit to the kernel density deficit shown in Figure 7.3 (a). The time t_i is the initial condition for the cooling analysis, and since the analysis is only valid once $h > R$, t_i is taken as the time instant corresponding to when the vortex ring is one radius away from the wall ($h = R$). This time t_i can be related to the vortex ring properties, and it can be shown to that $t_i = \frac{R^2}{\Gamma} = \tau$.

From this simple model, we obtain the result that (1) the cooling of the hot gas kernel is described by a power-law process over time, and (2) the time scale of this process is determined by the vortex ring properties such as the circulation and ring radius. In the next section, we compare these model results to the experimental measurements.

7.3.3 Length and time scale analysis

To test the model result that the cooling follows a power law process, we replot Figure 7.3 (a) with a normalized density deficit and time scale. The density deficit is normalized by the peak value $\left(\frac{\rho_{d,k}}{\rho_{d,k,0}}\right)$ and the time is normalized based on the time scale obtained from a power-law fit of equation (83) to the raw measurements τ_k. The quantity τ_k represents the time scale of the kernel cooling process, and is expressed as $\tau_k = (t_i)^\alpha$, where the variables t_i and α represent the time of peak density deficit and the correction factor respectively, and are both obtained from a power law fit to the variation of the kernel density deficit with time. $\tau_k = (t_i)^\alpha$. This is shown in Figure 7.5 (a), and we observe a near-collapse of the normalized density deficit time series from all tests, thereby showing that a universal power-law process may describe the cooling of the kernel, with a correction factor α. Next, we also compare the time scale from the power-law fit τ_k to that from the vortex ring properties ($\tau_r = R^2/\Gamma$) in Figure 7.5 (b), and observe a close agreement between the two estimates (~ 0.1 – 0.2 ms), thereby showing that there is indeed an effect of the vortex ring on the cooling process. The variability in the results may be because the two measurements correspond to different realizations of the induced flow.

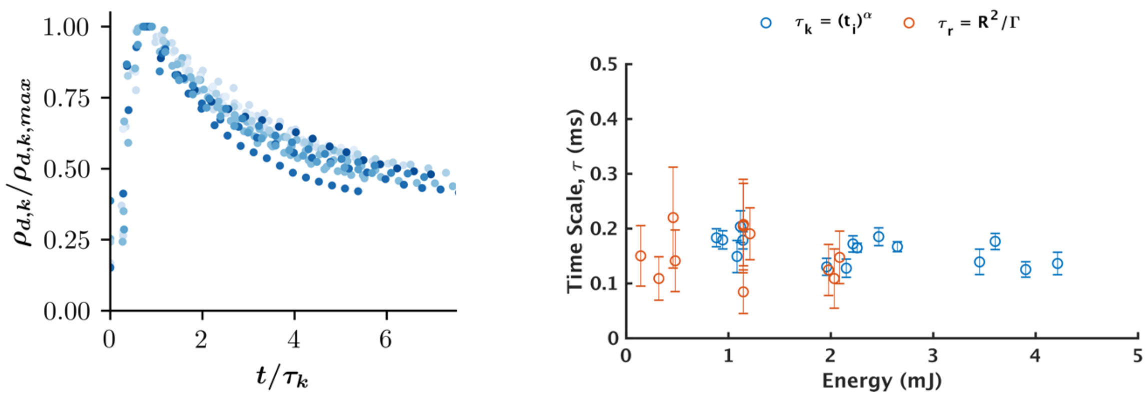

(a) (b)

Figure 7.5. (a) Time history of the normalized density deficit shows a near-collapse of all cooling curves. (b) Comparison of time scales obtained from the kernel and ring properties.

Next, we also compare the length scale of the hot gas kernel to the vortex ring radius. Figure 7.6 (a) shows the time history of the kernel area (previously shown in Figure 7.3 (a)) normalized by its mean value across time, and we again see a collapse of the area curves across all tests. In Figure 7.6 (b), we compare a representative length of the kernel based on the time average area $\lambda_k = \frac{1}{2}\sqrt{A_k}$, (with the factor of two to account for the assumed axisymmetry of the model) to the vortex ring radius, and again observe that both estimates take similar values over the energy range from about 0.5 – 1 mm. The area used to calculate λ_k corresponds to the projected area of the kernel that is directly measured from BOS based on kernel identification, and includes points that contain a density deficit within 95% of the peak value. The square root of the area is to create a representative length scale, and the factor of 2 is to account for the axisymmetry. For the case of a cylinder this would be $\sqrt{Rh/2}$ which is approximately R when the ring is near one diameter away from the wall.

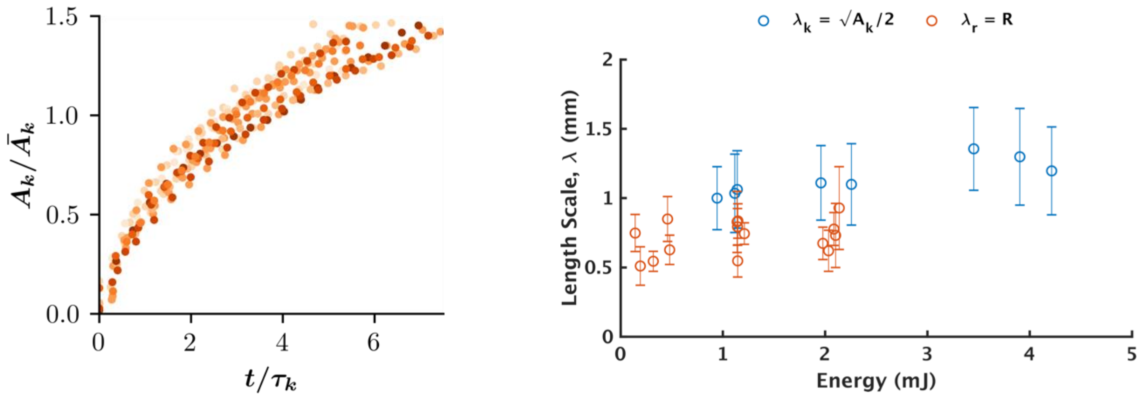

(a) (b)

Figure 7.6. (a) Time history of the normalized kernel area. (b) Comparison of length scales from the kernel properties to the ring radius.

7.4 Conclusions

The results of this work show that a vortex ring-based cooling model is able to predict the length and time scales of the flow induced by a nanosecond surface discharge. This is consistent with recent findings that vortex rings drive entrainment and cooling in flow induced by pin-to-pin spark discharges [47]. While the present analysis is about the cooling of the hot gas kernel, the fluid density is just one example of a passive scalar, and the results can be generalized to the mixing of any quantity in the induced flow. For example, in a situation where the actuator is placed in the presence of an oncoming flow, the vortex ring may also introduce mixing of momentum. In the case of a chemically reacting flow, the actuator may result in the mixing of chemical species in addition to temperature.

The model predictions of the inherent length and time scales of the induced flow also provide useful guidelines on the optimal spacing and pulse frequency for a multi-filament, multi-pulse ns-SDBD actuator, which are more commonly used in flow control applications. For example, to ensure optimal mixing, the spacing of the plasma filaments is to be one vortex ring diameter, and the optimal frequency/time interval between pulses should be based on the vortex ring circulation and diameter. As the decay of the kernel follows a power-law variation, one can specify the time interval required for a specified decay/mixing percentage (say 50%), and use this percentage to determine the optimal inter-pulse interval. This is because, in a power-law process, the rate of mixing reduces with time, so it may be more beneficial to pulse the actuator repeatedly after 50% mixing, with longer wait times yielding diminishing returns.

The present work only concerns the flow induced by a single filament, and the results show that the filament can induce velocity through a shock wave at early times (~ 10 μs) and a vortex ring at later times (~ 1 ms). If multiple filaments are used, then each filament may also affect the flow induced by the adjacent ones and this can be manifested in both the formation and propagation of the vortex ring, along with entrainment, expansion and cooling of the kernel. The nature and extent of this interaction would be controlled by the filament spacing, energy deposited, orientation of the filaments and phase difference between adjacent pulses. This is an interesting problem for future work. Further, the simplified theoretical analysis can also be extended to higher dimensions via numerical analysis. Equation (5) is obtained by an energy balance analysis on the low Mach number conservation equations derived in [46] this equation can be solved using more complex vorticity distributions and finite element analysis.

A primary limitation of the present work is that the BOS and PIV experiments are from different experiments, thereby limiting a direct instantaneous comparison of the vorticity and density fields. Therefore, simultaneous measurements are required to ascertain both the relative positions of the vortex ring and the hot gas kernel, as well as for a direct test of Equation 6. Further, one of the unanswered questions in this work is the origin of the vorticity and formation of the vortex ring, and this was also limited by the noise in the vorticity measurements at early times, limiting the centroid estimation and tracking of the vortex cores. It is possible that the vorticity may be controlled by the properties of the shock wave (such as curvature and speed) that is observed at early times [49]. Suppose a model for predicting this vorticity is available, and the formation mechanism of the vortex ring is understood. In that case, one can use the analysis in this work to estimate the desired vortex ring properties for a given operating condition (such as filament spacing and pulse frequency) and estimate the required energy and electrode gap. On the other hand, if there is a specified power budget, one can estimate the vortex ring properties and then design the filament configuration. Such a model for the vortex ring formation would also help connect the early and late stages of the induced flow.

Finally, it was observed during the experimental campaign that the flow was highly three-dimensional. Volumetric measurements of the velocity and density fields using a tomographic PIV and BOS measurement system are required to investigate the flow's three-dimensionality further.

This might also help characterize the orientation of the vorticity and heat flux transport and their effect on flow control, as reported by Kinefuchi et al. for SBLI [18], where they observed that the orientation of the actuator (filaments) with respect to the free-stream affected the size of the separation bubble, which they hypothesized a due to competing effects of heat and vorticity generation by the plasma.

7.5 Acknowledgment

This material is based upon work supported by the U.S. Department of Energy, Office of Science, Office of Fusion Energy Sciences under Award Number DE-SC0018156. Ravichandra Jagannath and Nick Schmidt are acknowledged for help with the actuator design and conducting the experiments.

7.6 References

1. Little J (2018) Localized thermal perturbations for control of turbulent shear flows. *AIAA Journal*, 57(2):655–669. https://doi.org/10.2514/1.J056826

2. Wang L, Luo Z, Xia Z, Liu B, Deng X (2012) Review of actuators for high speed active flow control. *Science China Technological Sciences*, 55(8):2225–2240. https://doi.org/10.1007/s11431-012-4861-2

3. Russell A, Zare-Behtash H, Kontis K (2016) Joule heating flow control methods for high-speed flows. *Journal of Electrostatics*, 80:34–68. https://doi.org/10.1016/j.elstat.2016.01.004

4. Popov NA (2001) Investigation of the mechanism for rapid heating of nitrogen and air in gas discharges. *Plasma Physics Reports*, 27(10):886–896. https://doi.org/10.1134/1.1409722

5. Pai DZ, Lacoste DA, Laux CO (2010) Nanosecond repetitively pulsed discharges in air at atmospheric pressure—the spark regime. *Plasma Sources Science and Technology*, 19(6):065015. https://doi.org/10.1088/0963-0252/19/6/065015

6. Rusterholtz DL, Lacoste DA, Stancu GD, Pai DZ, Laux CO (2013) Ultrafast heating and oxygen dissociation in atmospheric pressure air by nanosecond repetitively pulsed discharges. *Journal of Physics D: Applied Physics*, 46(46):464010. https://doi.org/10.1088/0022-3727/46/46/464010

7. Zheng J, Zhao Z, Li J, Cui Y, Khoo B (2014) Numerical simulation of nanosecond pulsed dielectric barrier discharge actuator in a quiescent flow. *Physics of Fluids*, 26(3):036102. https://doi.org/10.1063/1.4867708

8. Zhao Z, Li J-M, Zheng J, Cui Y, Khoo B (2014) Study of Shock and Induced Flow Dynamics by Nanosecond Dielectric-Barrier-Discharge Plasma Actuators. *AIAA Journal*, 53(5):1336–1348. https://doi.org/10.2514/1.J053420

9. Dawson R, Little J (2013) Characterization of nanosecond pulse driven dielectric barrier discharge plasma actuators for aerodynamic flow control. *Journal of Applied Physics*, 113(10):103302. https://doi.org/10.1063/1.4794507

10. Newnam K, Jagannath R, Stockett P, Wu P, Rajendran LK, Bane SP (2017) Shock Wave/Boundary Layer Control Using Nanosecond Reptitively Pulsed Dielectric Barrier Discharges. (January)https://doi.org/10.2514/6.2017-1805

11. Devarajan A, Jagannath R, 2019 … R-L (2019) Shock Wave/Boundary Layer Control Using Nanosecond Repetitively Pulsed Dielectric Barrier Discharges. https://doi.org/10.2514/6.2019-1351

12. Zhang C, Huang B, Luo Z, Che X, Yan P, Shao T (2019) Atmospheric-pressure pulsed plasma actuators for flow control: shock wave and vortex characteristics. *Plasma Sources Science and Technology*, 28(6):064001. https://doi.org/10.1088/1361-6595/ab094c

13. Leonov SB, Adamovich IV, Soloviev VR (2016) Dynamics of near-surface electric discharges and mechanisms of their interaction with the airflow. *Plasma Sources Science and Technology*, 25(6):063001. https://doi.org/10.1088/0963-0252/25/6/063001

14. Starikovskii YA, Nikipelov A, Nudnova M, Roupassov D (2009) SDBD plasma actuator with nanosecond pulse-periodic discharge. *Plasma Sources Science and Technology*, 18(3):034015. https://doi.org/10.1088/0963-0252/18/3/034015

15. (Udagawa) K, Zuzeek Y, Lempert WR, Adamovich IV (2011) Characterization of a surface dielectric barrier discharge plasma sustained by repetitive nanosecond pulses. *Plasma Sources Science and Technology*, 20(5):055009. https://doi.org/10.1088/0963-0252/20/5/055009

16. Liu Q, Zhang Y (2014) Shock wave generated by high-energy electric spark discharge. *Journal of Applied Physics*, 116(15):153302. https://doi.org/10.1063/1.4898141

17. Nishihara M, Gaitonde D, Adamovich I (2013) Effect of Nanosecond Pulse DBD Plasma Actuators on Oblique Shocks and on Shock/Boundary Layer Interaction. :461.

18. Kinefuchi K, Starikovskiy AY, Miles RB (2018) Control of Shock-Wave/Boundary-Layer Interaction Using Nanosecond-Pulsed Plasma Actuators. *Journal of Propulsion and Power*, 34(4):909–919. https://doi.org/10.2514/1.B36530

19. Kinefuchi K, Starikovskiy AY, Miles RB (2018) Numerical investigation of nanosecond pulsed plasma actuators for control of shock-wave/boundary-layer separation. *Physics of Fluids*, 30(10):106105. https://doi.org/10.1063/1.5051823

20. Rajendran LK, Singh B, Jagannath R, Schmidt GN, Vlachos PP, Bane SP (2020) Experimental Characterization of Flow Induced by a Nanosecond Surface Discharge. *AIAA Scitech Forum*, https://doi.org/10.2514/6.2020-1164

21. Raffel M (2015) Background-oriented schlieren (BOS) techniques. *Experiments in Fluids*, 56(3)https://doi.org/10.1007/s00348-015-1927-5

22. Richard H, Raffel M (2001) Principle and applications of the background oriented schlieren (BOS) method. *Measurement Science and Technology*, 12(9):1576. https://doi.org/10.1088/0957-0233/12/9/325

23. Meier G (2002) Computerized background-oriented schlieren. *Experiments in Fluids*, 33(1):181–187. https://doi.org/10.1007/s00348-002-0450-7

24. Elsinga GE, Oudheusden BW van, Scarano F, Watt DW (2004) Assessment and application of quantitative schlieren methods: Calibrated color schlieren and background oriented schlieren. *Experiments in Fluids*, 36(2):309–325. https://doi.org/10.1007/s00348-003-0724-8

25. Hargather MJ, Settles GS (2012) A comparison of three quantitative schlieren techniques. *Optics and Lasers in Engineering*, 50(1):8–17. https://doi.org/10.1016/j.optlaseng.2011.05.012

26. Goldhahn E, Seume J (2007) The background oriented schlieren technique: sensitivity, accuracy, resolution and application to a three-dimensional density field. *Experiments in Fluids*, 43(2–3):241–249. https://doi.org/10.1007/s00348-007-0331-1

27. Venkatakrishnan L, Meier GEA (2004) Density measurements using the Background Oriented Schlieren technique. *Experiments in Fluids*, 37(2):237–247. https://doi.org/10.1007/s00348-004-0807-1

28. Rajendran LK, Bane SPM, Vlachos PP (2019) Dot tracking methodology for background-oriented schlieren (BOS). *Experiments in Fluids*, 60(11):162. https://doi.org/10.1007/s00348-019-2793-3

29. Duncan J, Dabiri D, Hove J, Gharib M (2010) Universal outlier detection for particle image velocimetry (PIV) and particle tracking velocimetry (PTV) data. *Measurement Science and Technology*, 21(5):057002. https://doi.org/10.1088/0957-0233/21/5/057002

30. Rajendran LK, Bane SPM, Vlachos PP (2020) Uncertainty amplification due to density/refractive index gradients in background-oriented schlieren experiments. *Experiments in Fluids*, 61(6):139. https://doi.org/10.1007/s00348-020-02978-8

31. Rajendran L, Zhang J, Bane S, Vlachos P (2020) Uncertainty-based weighted least squares density integration for background-oriented schlieren. *Experiments in Fluids*, 61(11):239. https://doi.org/10.1007/s00348-020-03071-w

32. Rajendran LK, Zhang J, Bhattacharya S, Bane SPM, Vlachos PP (2020) Uncertainty quantification in density estimation from background-oriented Schlieren measurements. *Measurement Science and Technology*, 31(5):054002. https://doi.org/10.1088/1361-6501/ab60c8

33. PRANA: PIV Research and Analysis. https://github.com/aether-lab/prana/

34. Eckstein A, Vlachos PP (2009) Digital particle image velocimetry (DPIV) robust phase correlation. *Measurement Science and Technology*, 20(5):055401. https://doi.org/10.1088/0957-0233/20/5/055401

35. Eckstein AC, Charonko J, Vlachos P (2008) Phase correlation processing for DPIV measurements. *Experiments in Fluids*, 45(3):485–500. https://doi.org/10.1007/s00348-008-0492-6

36. Scarano F, Riethmuller ML (2000) Advances in iterative multigrid PIV image processing. *Experiments in Fluids*, 29(Suppl 1):S051–S060. https://doi.org/10.1007/s003480070007

37. Scarano F (2002) Iterative image deformation methods in PIV. *Measurement Science and Technology*, 13(1):R1. https://doi.org/10.1088/0957-0233/13/1/201

38. Westerweel J, Scarano F (2005) Universal outlier detection for PIV data. *Experiments in Fluids*, 39(6):1096–1100. https://doi.org/10.1007/s00348-005-0016-6

39. Eckstein A, Vlachos PP (2009) Assessment of advanced windowing techniques for digital particle image velocimetry (DPIV). *Measurement Science and Technology*, 20(7):075402. https://doi.org/10.1088/0957-0233/20/7/075402

40. Willert CE, Gharib M (1991) Digital particle image velocimetry. *Experiments in Fluids*, 10(4):181–193. https://doi.org/10.1007/bf00190388

41. Bhattacharya S, Charonko JJ, Vlachos PP (2018) Particle image velocimetry (PIV) uncertainty quantification using moment of correlation (MC) plane. *Measurement Science and Technology*, 29(11):115301. https://doi.org/10.1088/1361-6501/aadfb4

42. Brindise MC, Vlachos PP (2017) Proper orthogonal decomposition truncation method for data denoising and order reduction. *Experiments in Fluids*, 58(4):28. https://doi.org/10.1007/s00348-017-2320-3

43. Etebari A, Vlachos PP (2005) Improvements on the accuracy of derivative estimation from DPIV velocity measurements. *Experiments in Fluids*, 39(6):1040–1050. https://doi.org/10.1007/s00348-005-0037-1

44. ZHOU J, ADRIAN RJ, BALACHANDAR S, KENDALL TM (1999) Mechanisms for generating coherent packets of hairpin vortices in channel flow. *Journal of Fluid Mechanics*, 387:353–396. https://doi.org/10.1017/s002211209900467x

45. Shariff K, Leonard A (1992) Vortex Rings. *Annual Review of Fluid Mechanics*, 24(1):235–279. https://doi.org/10.1146/annurev.fl.24.010192.001315

46. Singh B, Rajendran LK, Vlachos PP, Bane SPM (2020) Two regime cooling in flow induced by a spark discharge. *Physical Review Fluids*, 5(1). https://doi.org/10.1103/PhysRevFluids.5.014501

47. Singh B, Rajendran LK, Zhang J, Vlachos PP, Bane SPM (2020) Vortex rings drive entrainment and cooling in flow induced by a spark discharge. *Physical Review Fluids*, 5(11):114501. https://doi.org/10.1103/physrevfluids.5.114501

48. Walker JDA, Smith CR, Cerra AW, Doligalski TL (1987) The impact of a vortex ring on a wall. *Journal of Fluid Mechanics*, 181(1):99–140. https://doi.org/10.1017/s0022112087002027

49. Singh B, Rajendran LK, Vlachos PP, Bane SPM (2021) Shock generated vorticity in spark discharges. *Journal of Fluid Mechanics (under review)*.

8. CONCLUSIONS AND RECOMMENDATIONS

8.1 Conclusions

This thesis presented a series of advancements to the BOS technique to improve the overall accuracy, precision, spatial resolution, and dynamic range through the development of advanced algorithms for all aspects of the measurement chain. The advancements to the technique were then applied to characterize flow induced by a filamentary surface plasma discharge, and a reduced order model was developed to describe the flow length and time scales.

All the developments to the BOS method were guided by a synthetic image generation methodology developed to generating realistic PIV/BOS images using ray-tracing. This allowed the controlled variation of BOS experimental parameters such as the dot pattern, density gradients, and optical layouts over a large parameter space. This method was used to perform detailed error and uncertainty analysis of the BOS measurement chain, to propose and evaluate the advancements.

In particular, the first uncertainty quantification methodology for BOS was developed to provide local, instantaneous, uncertainty bounds on density measurements, by estimating the displacement uncertainties using PIV methods, and propagation through the measurement chain. The results showed good agreement between the various PIV displacement uncertainty methods for the synthetic analysis, but a large variation for the experimental data.

This motivated the development of a meta-uncertainty based combination framework where uncertainty estimates from different models were combined based on their sensitivities to image perturbations – referred to as the meta-uncertainty. An automated method was developed to estimate the meta-uncertainty using random particle addition, and this method showed an improvement in displacement uncertainties when applied to planar and stereo PIV measurements.

In addition to quantifying the uncertainty, the use of the uncertainty as a signal-to-noise ratio metric was explored in the development of an uncertainty-based weighted least squares density integration method to address the noise sensitivity of the traditional Poisson solver. The density gradient estimates were weighted by their respective uncertainties to ensure that more reliable measurements are weighted higher in the integration process. The new method showed a large reduction in the density uncertainty, thereby increasing the dynamic range of BOS.

A new approach to BOS processing was developed based on dot tracking to provide order of magnitude improvement in the spatial resolution of the measurements, as well as the accuracy in region with large displacement gradients. This method was based on PTV but adapted to the unique features of BOS, where all properties of the dots are known – such as their position, size, and density – and the displacements are small, often less than the dot diameter. A method was developed to use prior information about the dot pattern to guide the identification, sizing, and tracking of the dots, as well as a correlation correction procedure to estimate the subpixel estimations, and resulted in an overall improvement in the robustness of the procedure to image noise.

Since the only source of error in the dot tracking procedure stems from image noise, a theoretical model was developed to quantify the effect of image noise on the position uncertainty, by deriving the Cramer-Rao lower bound (CRLB) for BOS measurements. This was performed by extending the CRLB framework for PIV/PTV measurements to account for density gradient effects in BOS imaging. The results showed that the position uncertainty is amplified by density gradients especially in situations that lead to dot blurring. Based on this model, a displacement uncertainty quantification method was developed for BOS-tracking measurements.

Finally, these methods were applied to characterize flow induced by a nanosecond surface plasma discharge. High-speed PIV/BOS measurements revealed the presence of a hot gas kernel and a vortex ring close to the actuator surface. The vortex ring was seen to propagate upwards due to self-induction while entraining cold ambient gas towards the actuator surface, and accompanied by the expansion and cooling of the hot gas kernel. A reduced-order model was developed to describe the kernel expansion and cooling, using an energy balance and an inviscid vortex model. The results showed that the normalized kernel expansion and cooling follow a universal power law behavior across all the tests, and that the length and time scales of the kernel dynamics are related to the vortex ring properties. While the analysis was in regards to the cooling procedure, it is just one example of a scalar mixing process and it can be extended to the mixing of other properties such as momentum, temperature or chemical species. Further, the length and time scales can also be used to guide the filament spacing and pulse frequency of multi-filament multi-pulse ns-SDBDS.

8.2 Recommendations

There are several avenues for extending the work reported in this thesis, and work in ongoing to explore these avenues. A brief summary is provided below.

8.2.1 Numerical uncertainty for BOS

Application of the uncertainty quantification method to synthetic images showed that the density uncertainty estimates compared well with the random error in the density measurement, but could not account for the bias error which was almost an order of magnitude higher. This is because the uncertainty quantification method only accounted for the errors/uncertainties in the displacement estimation and propagated them through the density integration procedure, whereas the density integration can introduce additional errors primarily through the truncation error due to the finite difference discretization.

This truncation error is also commonly encountered in CFD simulations, and methods have been proposed to estimate this error a-posteriori. The estimation is based on the Richardson extrapolation procedure whereby the discretization error of a numerical estimation can be estimated based on the residual between two sets of results with different grid levels as:

$$\bar{\epsilon}_h = -\frac{f_h - f_{rh}}{r^p - 1}, \tag{1}$$

Where $\bar{\epsilon}_h$ is the estimated numerical error of the result obtained on a grid with spacing h, f_h and f_{rh} are the results obtained on the grids with spacing h and rh, respectively, with r being the downsampling factor (usually $r = 2$), and p is the order of accuracy of the discretization scheme. In this study, p is 2 since the second-order central differencing scheme was used for carrying the numerical integration. The estimated error is then employed as the *numerical uncertainty* ($U = |\epsilon_h|$).

Therefore, if the random density uncertainty obtained using the previous method is interpreted to be the standard deviation of the density random error distribution, and the numerical uncertainty interpreted as the standard deviation of the density bias error distribution, the *standard total* uncertainty can be expressed as

$$U_{total}^2 = U_{bias}^2 + U_{random}^2, \tag{2}$$

thereby providing a framework for combining the random uncertainty estimates to estimate the overall uncertainty in the density integration.

A synthetic sinusoidal scalar field is used to test the proposed uncertainty estimation method, as described in equation (3), where f represents the scalar field, and λ represents the wavelength.

$$f(X,\ Y) = sin\left(\frac{2\pi}{\lambda}X\right) sin\,\frac{2\pi}{\lambda}Y,$$
$$\frac{df}{dX}(X,\ Y) = \frac{2\pi}{\lambda} cos\,\frac{2\pi}{\lambda}X\, sin\,\frac{2\pi}{\lambda}Y,$$
$$\frac{df}{dY}(X,\ Y) = \frac{2\pi}{\lambda} sin\,\frac{2\pi}{\lambda}X\, cos\,\frac{2\pi}{\lambda}Y. \tag{3}$$

The combination framework for the total uncertainty was tested with the sinusoidal fields corrupted with noise, where the noise was drawn from a zero-mean Gaussian distribution of a prescribed noise level. One thousand (1000) realizations of the corrupted field were generated, and for each realization, the integration was performed with the noisy gradient fields to estimate the error. The results are shown in Figure 1 for two noise levels: 1% and 10% of the peak value of the scalar field. It is seen in both levels that the spatial variation of the total uncertainty matches that of the total error, and the RMS of the total uncertainty coincides with the RMS of the error distribution. This validates the total uncertainty estimation framework, and efforts are ongoing to test the method with synthetic BOS images and experimental data.

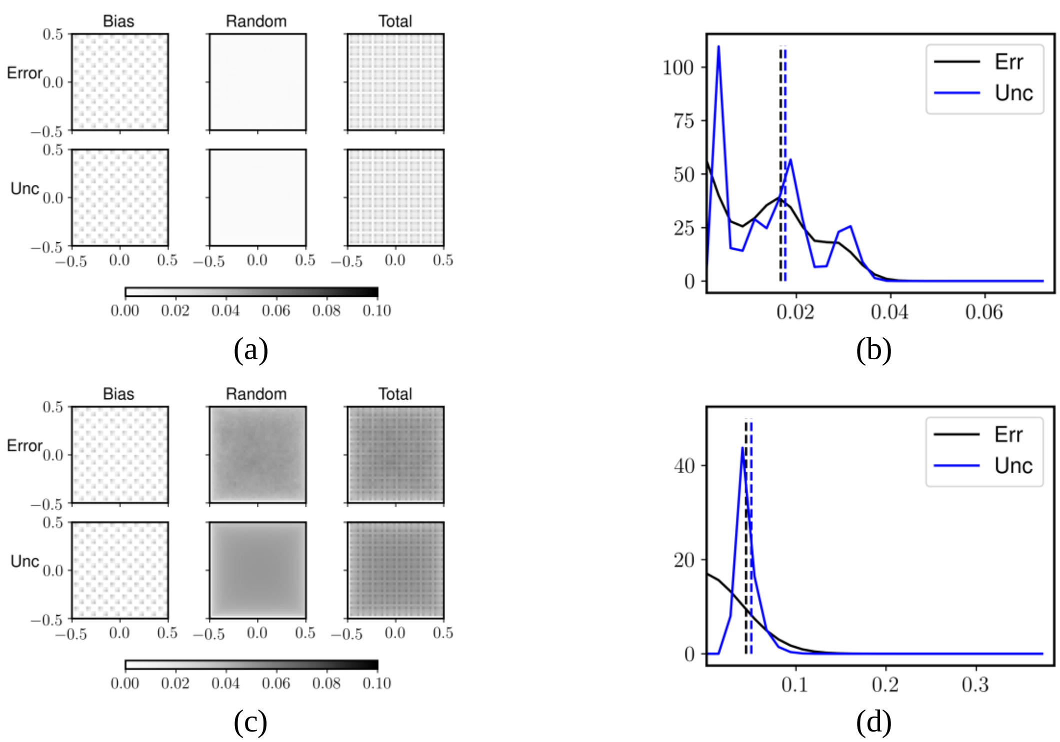

Figure 8.1. Error and uncertainty statistics for two noise levels. (a) and (b) represent the spatial variation and probability density functions respectively for a 1% noise level, with (c) and (d) representing the corresponding results for the 10% noise level.

8.2.2 High-Speed Tomographic BOS

Conventional BOS measurements of the plasma-induced-flow showed that the flow field is three-dimensional, and therefore volumetric measurements of the density are required, both for fundamental flow characterization and for actuator design/deployment in a background three-dimensional flow. Tomographic BOS is the common approach used to perform volumetric BOS measurements from multiple views. While several procedures have been proposed to perform Tomo BOS, the commonly used method involves the following steps: 1) 2d displacement estimation from each view, 2) 3d reconstruction of the gradient field and 3) 3d integration to obtain the scalar field. Since the reconstruction and integration steps can be expressed as linear operators, the two steps can be combined, and the system of linear equations can be solved as a least squares optimization problem with regularization based constraints, and the cost function is given by,

$$J = \sum_{2D\ BOS\ Vectors} \left\| \bar{d}_{meas} - \bar{T}\bar{D}\rho \right\|^2 + \alpha^2 \sum_{3D\ grid\ points} \|q\|^2 \tag{84}$$

where J is the cost function $\bar{d}_{meas}$ represents the measured 2D displacements from each view, $\bar{T}$ is the camera projection matrix containing the angle and distance information, $\bar{D}$ is the gradient matrix representing the x, y, and z derivatives, and ρ is the three-dimensional density. The least squares minimization problem is under-constrained because the number of measurements ($= MN^2$ for $N \times N$ grid vectors from M views) is lower than the number of unknowns ($= N^3$). Therefore, a regularization term is added to the cost function to provide additional constraints, and is represented by q in the equation. The form of the regularization term depends on the problem, with common choices being the gradient, the second derivative, or the Laplacian, with all choices resulting in a smoothing effect on the resulting field.

The primary challenge with Tomo BOS is the dense nature of the density field, and as a result the experiments reported in literature often utilize 10 views or more for a successful reconstruction. This is a major impediment for high-speed experiments, because high frame-rate cameras are very expensive (~$100,000), and therefore advancements are required on both the hardware and the reconstruction sides to enable high-speed Tomo BOS imaging. The following sections describe efforts and recommendations in addressing these challenges using: a) quadscope imaging to provide multiple views on the same camera, and b) dynamic vision sensors to reduce cost associated with high-speed imaging.

a) Quadscope Imaging

A quadscope is an optical device consisting of a set of flat and triangular mirrors that allows the imaging of an object from 4 directions onto a single camera sensor. This is accomplished by dividing the camera sensor area into four (imaginary) quadrants, and aligning the system of mirrors to project each views onto a corresponding quadrant. Therefore it allows volumetric imaging from a single camera. Some limitations include reduced spatial resolution and the need to use smaller viewing angles, due to the depth of field required to ensure all the different views are in focus on the same camera sensor. Further, the setup and alignment of the quadscope is fairly complex and requires a high-level precision on the 3d position and angle adjustments on the mirrors.

The quadscope apparatus was applied to volumetric BOS imaging of a Helium jet to assess its performance, and to establish a workflow for data acquisition and processing. The experimental apparatus is shown in Figure 8.2(a), and images of a Helium jet exiting from a 20 psi reservoir pressure into ambient air were acquired, with a sample image shown in Figure 8.2 (b). Volume calibration was performed using a grid of 0.25 mm dots of with 0.5 mm spacing traversed through the volume at 0.635 mm increments, at 7 planes. The BOS images were processed using cross-correlation, with a subset size of 32 pixels, and a 50% overlap to provide a final grid resolution of 16 pixels. The displacements are shown in Figure 8.2 (c) with highest displacements in the jet boundary, which is expected as it features the largest density gradients. Efforts are underway to perform tomographic reconstruction on the data, and in using multiple quadscopes to perform measurements on the plasma induced flow.

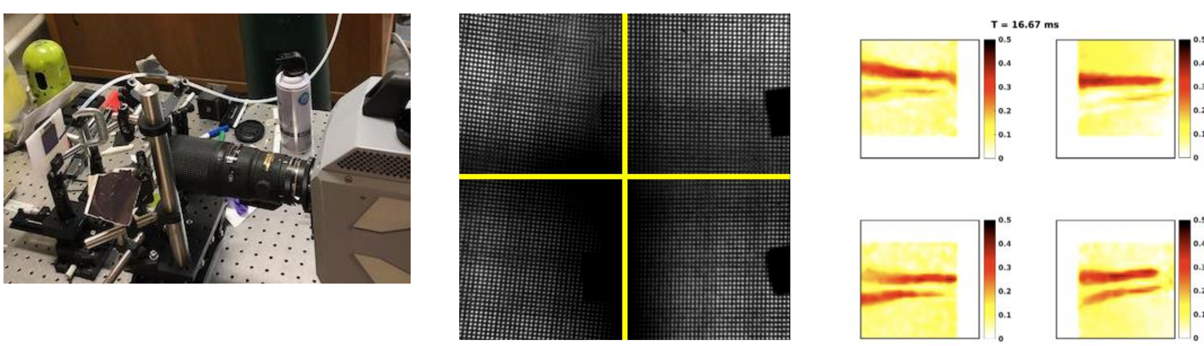

(a) (b) (c)

Figure 8.2. (a) Quadscope imaging setup, (b) sample image of the BOS target with the yellow lines indicating the quadrants, and (c) 2D displacements from preliminary processing.

b) Dynamic Vision Sensors

Dynamic vision sensors are a type of camera sensors that respond to changes in illumination, in contrast to traditional frame-based cameras that record the illumination directly. Each pixel on the camera responds asynchronously when the current intensity exceeds a reference intensity level, termed an ‘event’. Each event is represented by the pixel location (x, y), the time (t), and the polarity of the intensity change ($p = \pm 1$). Therefore the ‘recording’ is a 3D space-time point cloud which require novel algorithms for processing. These cameras enable a sparse representation of the scene, leading to high temporal resolution (1 μs), reduced power consumption, high dynamic range (120 dB) at a low cost (~ $5000). Due to these reasons, these cameras are attractive for high-speed tomographic imaging, since it is possible to deploy 10s of these cameras in place for a single high-speed camera for the same overall cost. However, the temporal resolution has not been well characterized, and the 1 μs metric only refers to the resolution of the ‘time-stamping’ circuit which is at the end of the sensing chain. Therefore errors and uncertainties introduced in upstream steps such as the recording of the illumination and the event detection, along with bandwidth constraints, can drastically reduce the overall temporal resolution.

To characterize the temporal resolution, a pulsed LED light source (HardSoft ILM-501CG) was triggered at a frequency of 10 kHz, and the events were recorded using a Prophesee EVK-Gen4 camera. Since the temporal resolution inversely depends on the number of pixels recording events due to bandwidth constraints, only a small (10x10 pixel) neighborhood was illuminated with the led to provide the 'best' possible performance. A sample frame is shown in Figure 8.3(a) to illustrate the ROI, and a time series of events are shown in Figure 8.3 (b) for an LED frequency of 10 kHz. It is seen that the response is band-limited at 1 kHz, and the camera cannot respond to any faster intensity changes. A variety of low-level settings were explored on the camera but this was the best performance achievable. Therefore, the camera is presently unsuitable for ultra-high-speed imaging required for flow fields such as the plasma discharge, but given the rapid development in hardware, this may be possible in the near future. Efforts are ongoing to explore the use of these cameras for low-speed imaging applications.

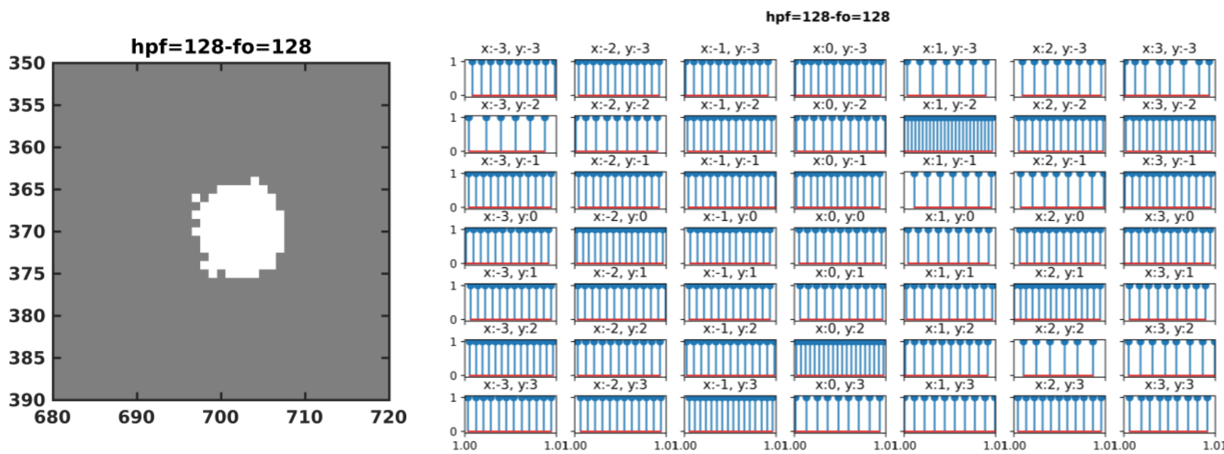

(a) (b)

Figure 8.3. Response of the event camera for an LED pulse train of width 20 μs and a frequency of 10 kHz. (a) Accumulated frame showing the ROI, (b) Time Series.

VITA

EDUCATION

Purdue University *West Lafayette, IN* May 2021*
Ph.D. in Aeronautics & Astronautics
Thesis Title: "Development of Image-based Density Measurements with Background-Oriented Schlieren and Application to Flow Induced by a Nanosecond Surface Plasma Discharge"
Advisors: Prof. Sally P. M. Bane and Prof. Pavlos P. Vlachos

Purdue University *West Lafayette, IN* July 2015
M.S. in Aeronautics & Astronautics
Thesis Title: "Skin Friction Measurement on the NASA Common Research Model with Global Luminescent Oil Film Skin Friction Meter"
Advisor: Prof. John P. Sullivan

Indian Institute of Technology (IIT), Kharagpur *Kharagpur, West Bengal, India* June 2012
B.Tech (Hons). in Aerospace Engineering
Thesis Title: "Numerical Investigation of Supersonic Combustion in a SCRAMJET Engine"
Advisor: Prof. Arnab Roy

RESEARCH

Purdue University, **Aerospace Sciences Laboratory** August 2015 - present
Graduate Research Assistant (Ph.D.)

- Developed methods for image-based fluid velocity and density measurements (PIV/BOS/Schlieren) to achieve large performance improvement in accuracy, precision, spatial resolution and dynamic range.
- Implemented the methods as open source software tools in Python, C/C++, CUDA and MATLAB.
- Deployed the methods in several fluid mechanics and combustion facilities through collaborative research.
- Characterized a novel plasma flow control actuator with advanced flow diagnostic techniques.

Purdue University, **Aerospace Sciences Laboratory** August 2012 – July 2015
Graduate Research Assistant (M.S.)

- Manufactured a wind-tunnel scale model of a passenger aircraft using a 5-axis CNC machine.
- Performed full-field skin friction measurements on the swept wing and fuselage using a luminescent oil film based skin friction technique.

- Studied leading edge separation which induced transition over 50% the wing surface, as well as the effect of trips on the skin friction field.

Indian Institute of Technology (IIT), Kharagpur August 2011 – June 2012
Undergraduate Thesis

- Completed a thesis titled "Numerical Investigation of Supersonic Combustion in a SCRAMJET Engine".
- Computationally investigated the flow field in a supersonic dump combustor with ANSYS Fluent.
- Developed a finite volume solver for compressible flows towards the development of an inhouse CFD code.

TEACHING

Purdue University, **School of Aeronautics and Astronautics** June 2017 - Aug 2017
Instructor

- Delivered 4 lectures/week on undergraduate Fluid Mechanics to a class of junior/senior level students.
- Held 2 additional sessions every week for focused help on clarifying concepts taught in class and assignments.
- Developed and graded questions for weekly assignments, mid-term and final examinations.
- Obtained excellent reviews from students (4.1/5) including repeat takers.

Purdue University, **School of Aeronautics and Astronautics**
Graduate Teaching Assistant

- Served as TA for undergraduate, graduate and advanced-graduate level courses on fluid dynamics.
- Assisted the instructor in delivering lectures, grading homework problems and exams.
- Held help sessions with students to clarify concepts and help with assignments.
- **Undergraduate:**
  AAE 334: Aerodynamics (Fall 2014, Spring 2015)
- **Graduate:**
  AAE 511: Introduction to Fluid Mechanics (Fall 2013, Fall 2016)
  AAE 512: Computational Aerodynamics (Spring 2014, Spring 2016)
  AAE 519: Hypersonic Aerothermodynamics (Fall 2015, Fall 2017)
- **Advanced Graduate:**
  AAE 624: Laminar-Turbulent Transition (Fall 2016)
  AAE 626: Turbulence & Turbulence Modeling (Spring 2017)

Purdue University, **Brees Student-Athlete Academic Center** August 2012 – July 2013
Tutor

- Held help sessions for student athletes for a variety of undergraduate courses in mechanical engineering and freshman calculus.

PUBLICATIONS

a) Journal Articles

Eshraghi, J., **Rajendran, L. K.,** Yang W., Stremler, M., & Vlachos, P. P. "On flowing soap films as experimental models of 2D Navier-Stokes flows." *Experiments in Fluids (under review).*

Singh, B., **Rajendran, L. K.,** Vlachos, P. P., & Bane, S. P. M. "Shock Generated Vorticity In Spark Discharges". *Journal of Physics D: Applied Physics (under review).* arXiv:2101.07358

Rajendran, L. K., Bhattacharya. S, Bane, S. P. M., and Vlachos, P. P., "Meta Uncertainty for Particle Image Velocimetry". *Measurement Science and Technology (**Special Issue on PIV Uncertainty Quantification**).* https://doi.org/10.1088/1361-6501/abf44f

Rajendran, L. K., Singh, B., Vlachos, P. P., & Bane, S. P. M. "Filamentary Surface Plasma Discharge Flow Length and Time Scales". *Journal of Physics D: Applied Physics*, ***54**, 205201*. doi.org/10.1088/1361-6463/abe66a

Singh, B., **Rajendran, L. K.,** Zhang, J., Vlachos, P. P., & Bane, S. P. M. (2020). "Vortex rings drive entrainment and cooling in flow induced by a spark discharge" *Physical Review Fluids, 5(11), 114501*. doi.org/10.1103/PhysRevFluids.5.114501

Rajendran, L. K., Zhang, J., Bane, S. P. M., & Vlachos, P. P. (2020). Uncertainty-based weighted least squares density integration for background-oriented schlieren. *Experiments in Fluids*, 61(11), 239. doi.org/10.1007/s00348-020-03071-w

Rajendran, L. K., Bane, S. P., & Vlachos, P. P. (2020). Uncertainty amplification due to density/refractive index gradients in background-oriented schlieren experiments. *Experiments in Fluids*, *61*(139), 139. doi:10.1007/s00348-020-02978-8

Singh, B., **Rajendran, L. K.**, Vlachos, P. P., & Bane, S. P. M. (2020). Two regime cooling in flow induced by a spark discharge. *Physical Review Fluids*, *5*(1), 014501. ***(Selected for Editor's highlights)*** doi:10.1103/physrevfluids.5.014501.

Rajendran, L. K., Zhang, J., Bhattacharya, S., Bane, S. P. M., & Vlachos, P. P. (2020). Uncertainty quantification in density estimation from background oriented schlieren (BOS) measurements. *Measurement Science and Technology*, *31(5), 054002*. *(**Invited Article**)*. doi:10.1088/1361-6501/ab60c8

Rajendran, L. K., Bane, S. P. M., & Vlachos, P. P. (2019). Dot tracking methodology for background-oriented schlieren (BOS). *Experiments in Fluids*, *60(11)*. doi:10.1007/s00348-019-2793-3

Rajendran, L. K., Bane, S. P. M., & Vlachos, P. P. (2019). PIV/BOS synthetic image generation in variable density environments for error analysis and experiment design. *Measurement Science and Technology*, *30(8), 085302*. doi:10.1088/1361-6501/ab1ca8

Singh, B., **Rajendran, L. K.**, Giarra, M., Vlachos, P. P., & Bane, S. P. M. (2018). Measurement of the flow field induced by a spark plasma using particle image velocimetry. *Experiments in Fluids*, *59(12)*. doi:10.1007/s00348-018-2632-y

b) Conference Proceedings

Rajendran, L. K., Singh, B., Jagannath, R., Schmidt, G. N., Vlachos, P. P., & Bane, S. P. (2020). Experimental Characterization of Flow Induced by a Nanosecond Surface Discharge. *AIAA Scitech 2020 Forum*. doi:10.2514/6.2020-1164

Singh, B., **Rajendran, L. K.,** Vlachos, P. P., & Bane, S. P. (2020). Study of cooling and the effect of energy deposited in a single nanosecond spark plasma discharge using simultaneous 50 kHz PIV and BOS. In *AIAA Scitech 2020 Forum* (p. 1885). https://doi.org/10.2514/6.2020-1885

Rajendran, L. K., Bhattacharya, S., Zhang, J., Bane, S. P., & Vlachos, P. P. (2019). Assessment of Uncertainty Quantification methods for density estimation from Background Oriented Schlieren (BOS) measurements. In *13th International Symposium on Particle Image Velocimetry* (pp. 377-395).

Singh, B., **Rajendran, L. K.,** Gupta, P., Scalo, C., Vlachos, P. P., & Bane, S. P. (2019). Experimental and Numerical Study of Flow Induced by Nanosecond Repetitively Pulsed Discharges. *AIAA Scitech 2019 Forum*. doi:10.2514/6.2019-0740

Devarajan, A., Jagannath, R., **Rajendran, L. K.,** Newnam, K., & Bane, S. P. (2019). Shock Wave/Boundary Layer Control Using Nanosecond Repetitively Pulsed Dielectric Barrier Discharges. *AIAA Scitech 2019 Forum*. doi:10.2514/6.2019-1351

Rajendran, L. K., Bane, S. P. M., & Vlachos, P. P. (2018). Dot tracking and Cramer-Rao Lower Bound for Background Oriented Schlieren measurements. In *19th International Symposium on Application of Laser and Imaging Techniques to Fluid Mechanics, Lisbon.*

Singh, B., **Rajendran, L. K.,** Bane, S. P., & Vlachos, P. (2018). Characterization of Fluid Motion Induced by Nanosecond Spark Plasmas: Using Particle Image Velocimetry and Background Oriented Schlieren. *2018 AIAA Aerospace Sciences Meeting*. doi:10.2514/6.2018-0680

Rajendran, L. K., Singh, B., Giarra, M., Bane, S. P., & Vlachos, P. P. (2017). PIV/BOS Synthetic Image Generation in Variable Density Environments for Error Analysis and Experiment Design. *55th AIAA Aerospace Sciences Meeting*. doi:10.2514/6.2017-0254

Newnam, K., Jagannath, R., Stockett, P., Wu, P., **Rajendran, L. K.,** & Bane, S. P. (2017). Shock Wave/Boundary Layer Control Using Nanosecond Repetitively Pulsed Dielectric Barrier Discharges. *55th AIAA Aerospace Sciences Meeting*. doi:10.2514/6.2017-1805

Singh, B., **Rajendran, L. K.,** Giarra, M., Bane, S. P., & Vlachos, P. (2016). Fluid Motion Induced by Spark Plasma: Development of Particle Image Velocimetry Measurements. *54th AIAA Aerospace Sciences Meeting*. doi:10.2514/6.2016-1214

Husen, N. M., **Rajendran, L. K.,** Liu, T., & Sullivan, J. (2016). The Luminescent Oil-Film Flow-Tagging (LOFFT) Skin-Friction Meter. *54th AIAA Aerospace Sciences Meeting*. doi:10.2514/6.2016-2015

c) Conference Abstracts

Rajendran, L.K., Bhattacharya, S., Bane, S., Vlachos, P. (2020). Meta Uncertainty for Particle Image Velocimetry. *In APS Division of Fluid Dynamics Meeting Abstracts.*

Singh, B., **Rajendran, L.K.,** Vlachos, P. P., & Bane, S. (2020). Estimation of vorticity generated due to shock curvature in spark induced flow. *In APS Division of Fluid Dynamics Meeting Abstracts.*

Rajendran, L.K., Singh, B., Jagannath, R., Schmidt, G.N., Vlachos, P., Bane. S. (2019). Experimental Characterization of Flow Induced by a Nanosecond Surface Discharge. *In APS Division of Fluid Dynamics Meeting Abstracts.*

Rajendran, L.K., Zhang, J., Bane, S., Vlachos, P. (2019). Weighted Least squares density reconstruction for Background Oriented Schlieren (BOS). *In APS Division of Fluid Dynamics Meeting Abstracts.*

Singh, B., **Rajendran, L.K.,** Vlachos, P. P., & Bane, S. (2019). Vorticity Generation in a Single Nanosecond Spark Discharge Due to Shock Curvature. *In APS Division of Fluid Dynamics Meeting Abstracts.*

Rajendran, L.K., Bhattacharya, S., Bane, S., Vlachos, P. (2018). Effect of density gradients on the Cramer-Rao lower bound for volumetric PIV/PTV measurements. *In APS Division of Fluid Dynamics Meeting Abstracts.*

Singh, B., **Rajendran, L.K.,** Vlachos, P. P., & Bane, S. (2018). Characterization of early stages of flow induced by spark plasma discharges using high-speed PIV and BOS. *In APS Division of Fluid Dynamics Meeting Abstracts.*

Rajendran, L.K., Singh, B., Giarra, M., Bane, S., & Vlachos, P. (2016). Assessment of sources of error in Background Oriented Schlieren (BOS) measurements. *In APS Division of Fluid Dynamics Meeting Abstracts.*

Singh, B., **Rajendran, L.K.,** Giarra, M., Bane, S., & Vlachos, P. (2016). Study of shock shape and strength as a function of plasma energy using background oriented schlieren and shadowgraph. *In APS Division of Fluid Dynamics Meeting Abstracts.*

SYNERGISTIC ACTIVITIES

Membership: American Institute of Aeronautics and Astronautics (AIAA), American Physical Society (APS)

Reviewer: Measurement Science and Technology, Experiments in Fluids, Journal of Physics D: Applied Physics. Publons: https://publons.com/a/3243017

Session chair for Purdue Summer Undergraduate Research Fellowship (SURF) symposium in July 2019.